université de bretagne occidentale

THÈSE / UNIVERSITÉ DE BRETAGNE OCCIDENTALE
sous le sceau de l'Université européenne de Bretagne

pour obtenir le titre de
DOCTEUR DE L'UNIVERSITÉ DE BRETAGNE OCCIDENTALE
Mention : Océanographie Physique
École Doctorale des Sciences de la Mer

Présentée par
Luis Quaresma dos Santos

Préparée au Service Hydrographique et Océanographique de la Marine

Super-inertial tides over irregular narrow shelves

Soutenance de la thèse le 9 juillet 2012
devant le jury composé de :

Chantal STAQUET
Professeur, Université de Grenoble / *rapporteur*

Theo GERKEMA
Professor, Royal Netherlands Institute for Sea Reearch / *rapporteur*

Paulo RELVAS
Professor, Universidade do Algarve / *examinateur*

Xavier CARTON
Professeur, Université de Bretagne Occidental / *examinateur*

Bernard LE CANN
Chargé de Recherche CNRS, Laboratoire de Physique des Océans / *examinateur*

Yves MOREL
Directeur de Recherche CNRS, Laboratoire d'Etude en Géophysique et Océanographie Spatial / *directeur de thèse*

Annick PICHON
Ingénieur de Recherche, Service Hydrographique et Océanographique de la Marine / *codirectrice de thèse*

SUPER-INERTIAL TIDES OVER IRREGULAR NARROW SHELVES

L. S. QUARESMA

Divisão do Oceanografia
Instituto Hidrográfico – Marinha Portugal

The present document is a PhD thesis proof, delivered the 25th May 2012, to the selected Jury. It results from a study developed from January 2009 to July 2012 at **Service Hydrographique et Océanographique de la Marine – DOPS/HOM/REC** (France). It is submitted to **Université de Bretagne Occidentale** and co-supported by **Instituto Hidrográfico** (Marinha -Portugal) and **Fundação para a Ciência e Tecnologia**.

Para o Afonso, Manuel e António

SUPER-INERTIAL TIDES OVER IRREGULAR NARROW SHELVES

CONTENTS

Preface 3

PART I

Barotropic tide along narrow continental margins 7

Chapter I: Tides and tidal flows 8

Chapter II: Tidal solutions along continental margins 13

Chapter III: Modelling the barotropic tide along the West-Iberian margin 19

PART II

Barotropic tide over idealized bathymetry shelf features 45

Chapter I: 1D Kelvin wave distortion 46

Chapter II: Building 2D academic simulations 57

Chapter III: Super-inertial tides over abrupt continental shelf features 61
Part I: Barotropic solution.

Appendix A: Bottom friction 95

Appendix B: 1D barotropic tide solutions across regular margins 105

PART III

Baroclinic tide over idealized bathymetry shelf features 117

Chapter I: Internal tides 118

Chapter II: Super-inertial tides over abrupt continental shelf features 129
Part II: Internal waves.

Appendix A: Three-dimensional reflection 165

Discussion and perspectives 169

Preface

This thesis results from a straight collaboration between the Portuguese Hydrographic office and its homologous French institution. Both HIDROGRAFICO and SHOM share a common national responsibility to map and observe the ocean and, naturally, they have met again to work together in this specific project. Seven year ago, as a young Portuguese navy officer I took the opportunity to embark in a French research cruise, leaded by Dr. Yves Morel. This was the beginning of a fascinating journey, which brought me to France in 2009 to develop my PhD studies with Dr. Annick Pichon. So, since 2005, my research work as been shared with them, taking place between Brest and Lisbon, where the shorter and safer root was always the northeast Atlantic Ocean.

The internal tide activity, observed along the west-Iberian margin, is the starting problem of the present study. Numerous satellite observations, taken during the past twenty years in the vicinity of the Portuguese and Spanish Atlantic coast, show complex patterns of internal wave surface signatures. Such features result primarily from tidal forcing over irregular topography and are observed worldwide near continental margins and ocean rifts. Probably the most simple and successful method to identify the origin of these internal tide waves is the ray tracing technique, linking waves to their slope of origin, based on remote sensing interpretation, stratification profiles and topography analysis. Despite the simplicity of the method, coherent results are obtained and allow to trace regional maps of the internal tide generation sites, kindly called “hotspots”. Along continental margins, these “hotspots” are located over the shelf-break isobaths and are stronger along the rim of geomorphic structures such as submarine canyons and submarine promontories. Yet, internal tide surface signatures are sometimes observed far from this “hotspot” belt, over the deep-ocean or close to the coast, in strange spatial configurations that become difficult to address to specific generation sites. The present work pretends to contribute with an integrated comprehension of the origin and creation of such complex internal wave patterns, observed over irregular narrow shelves, as it is the west-Iberian margin.

The internal tide forcing mechanism relies on the gravitational pull promoted by asters orbiting nears the earth (notably the moon and the sun), which apply into the ocean body forces acting over the entire volume of the sea. Consequently, propagating surface waves are generated with periods ranging from few hours to 18.5 years. The water movements directly associated to these waves are barotropic and acquire vertical velocity component whenever they cross irregular seabed reliefs. Produced cyclically, with tidal frequencies, these oscillations become internal wave-makers inside the stratified ocean. Density gradients are the waveguide of such internal vibrations and for that stratification structure determines their waveform and dispersion mechanism.

The internal tide patterns observed over the sea surface become then a problem of assembling accurate topography relief and water column stratification to correct barotropic tidal flow solutions. This was the working plan in the beginning of my thesis, but soon, the apparent straightforward task diverged to an academic study to evaluate the role of each variable in the linear internal tide solution, over irregular narrow shelves. Three scientific papers, submitted during the past 3 years, result from this study and express the analytical interpretation of both realistic and academic tide/internal tide solutions. The thesis is though organized in correspondent Parts, where short introductions integrate each paper to describe the adopt theory, methods and to include adjacent analysis.

Chapter I, presents a new realistic barotropic tide solution obtained over the west-Iberian margin by the use of a finite-difference primitive equations numerical model and validated by local observation datasets. It resulted from the need of an accurate tidal flow solution, missing in literature with regional scale and fine resolution, out coming from reliable bathymetry. Although the present study is focused on super-inertial tides, the sub-inertial harmonics are also included, showing the generation of continental shelf waves (already reported in this region by other authors). The originality of the published solution is the identification of a surprising super-inertial tide wave distortion “trapped” along the irregular shelf. The frequency domain and the wavelength of such features put aside any possible coastal bounded wave modes, steering to a different interpretation. In conclusion, a topographic effect is suggested to justify the tidal ellipses intensification and inversion over abrupt geomorphic structures, such as submarine canyons and promontories present along this narrow shelf.

In Chapter II, the previous topographic effect hypotheses is tested and validated by the use of the same numerical model, in frictionless linear configuration, forced with idealized topographies and monochromatic super-inertial tidal harmonic. Similar trapped solutions are obtained over single submarine canyon configuration (negative shelf width anomaly) and promontory (positive shelf width anomaly). Results are discussed under the principle of angular momentum conservation, which can justify the observed depth-integrated tidal flow distortion, with consequent tidal ellipses inversion and intensification.

Finally in Chapter III, stratification is added to the problem introduced above. Three-dimensional tide solutions are obtained and interpreted over idealized submarine canyons and promontories. The two-layers and constant buoyancy profiles are forced by the same semi-diurnal monochromatic surface tide. The solutions reproduce the complex internal tide patterns usually observed over irregular continental margins and help its interpretation. These patterns are described by 2D geometric wave interferences and 3D internal tide bottom reflections, occurring in the vicinity of each abrupt geomorphic shelf feature.

By gathering all the results and analysis developed within the present thesis, the reader can formulate a better comprehension of the origin and physical mechanisms behind the intricate internal wave patterns observed along the west-Iberian margin and near other worldwide irregular narrow shelves.

Agradecimentos

Permita-me o leitor de escrever este parágrafo na minha língua materna para agradecer a todos aqueles a quem eu devo esta tese e que sem eles não teria chegado a bom porto. Aos meus filhos, que sempre imaginaram o pai a trabalhar na terra dos piratas e que por isso aceitaram a minha ausência com naturalidade e paciência. À minha mulher, pela tolerância e apoiado neste desafio. À minha família, por toda a confiança depositada em mim. Ao Yves por ter arquitectado esta aventura e à Annick por ter sido o pilar e guia por bons ventos, águas safas e mar calmo. Por fim, e não em último, quero agradecer a todos os amigos que fiz em Brest e que sempre estiveram do meu lado e me fizeram sentir em casa.

Muito Obrigado!

PART I

Barotropic tide along narrow continental margins

***CONTENTS*:**

Chapter I: Tides and tidal flows 8

1. Historical background
2. Laplace tidal Equations

Chapter II: Continental shelves tide solutions 13

1. Free inertial gravity waves
2. Kelvin mode
3. Trapped modes

Chapter III: Modelling the barotropic tide along the West-Iberian margin. . .19
Quaresma L.S. & A. Pichon, 2011.
Published on Journal of Marine Systems, Available online 10 October 2011,
doi: 10.1016/j.jmarsys.2011.09.016.

1. **Introduction** 21

2. **Materials and methods** 23

2.1 Data analysis
2.2 Numerical model
2.3 Bathymetry
2.4 Tidal forcing

3. **Model accuracy** 25

3.1 Sea-surface height
3.2 Tidal currents

4. **Results** 29

4.1 Semi-diurnal tide
4.2 Diurnal tide

5. **Analysis** 35

5.1 Diurnal continental shelf waves
5.2 Semi-diurnal waves shelf variability

6. **Barotropic forcing term** 40

7. **Summary** 42

Chapter I
Tides and tidal flows

" Time and tide wait for no man "
old proverb

1. Historical background

This is an old proverb that expresses the uninterrupted periodic oscillation of the sea-surface as if it was itself a timeline reference. The word "time" derives from the Saxon "*tid*" that expresses a seasonal character or periodicity. In fact, since ancient times, man got the perception that there is a regular pattern in the vertical displacement of the sea-surface and in the related backward and forward motion of the water flow in coastal regions. Moreover, he soon understood that this cycle is correlated with the position and phases of the sun and moon, and from that he constructed empirical formulations to predict this phenomenon. Even if the ancients justified this behavior as a terrestrial manifestation of the power of the celestial gods, the study of the tides can be assumed as the oldest subject in oceanography.

References to oceanic tidal movements date at least from reports of the army of Alexander the Great (325 B.C.), where Pytheus identified the relation between the half-monthly variation in the tide amplitude and the phases of the moon. Later, the roman Pliny the Elder noted in his *Natural History* compilation that the maximum tidal amplitude occurs a few days after the new or full moon and that amplitude is higher during the equinoxes periods and smaller during the solstices. Explanations for these movements started to be associated with supernatural phenomenons, like the Chinese idea that tidal flow is the blood circulation of the earth, pulsing in a regular beating. Or, the poetic approach that claims to be the manifestation of a footstep of angel, raising the water when he places his foot on the ocean, followed by the tidal ebb when he lifts it. More scientifically, Galileo (1564-1642) proposed that tides result from seawater movements over the ocean relief, when pushed by the earth rotation while spinning annually around the sun and daily around its own axis. Contemporaneously, Kepler (1571-1630) introduced the idea of a gravity force, induced by the moon, pulling the water of the ocean. He also proposed that this force is balanced by the earth attraction (applied to the same water masses), which prevents the oceans to flow towards the moon. These historical facts and theories can be found in Cartwright (1999) or summarized in Deacon (1971).

The present knowledge of tides and tidal flows are based on theoretical studies dating back to Newton's *Mathematical Principles of Natural Philosophy* (1679–1687). The unbalanced sum of two different classes of forces causes a change in the fluid momentum: superficial forces acting at the fluid boundaries (such as pressure and friction) and body forces acting over the entire volume of the fluid (such as gravity and tidal forces). Laplace introduced in 1774 a dynamical theory in his *Mechanique Celeste* work to explain the periodic motion of the sea surface elevation and fluid motion. According to Laplace, tides are harmonic waves induced by gravity forces, associated with flows of the same periods of oscillation. Since then, many authors explored this theory and their work is summarized in Lamb (1932), Proudman (1953) and Defant (1961).

During the past four decades, the development of new instrumentation, including precise tide gauges, satellite altimeters and computers, enabled further developments. These new tools made possible the systematic observation and the long-period recording of the worldwide sea-surface oscillations, allowing the validation of the Laplace tidal equations as well the parameterization of frictional forces. The latter is critical over continental margins, where tidal flows are controlled by variable topography and bottom friction.

2. *Laplace tidal equations* (LTE)

Pierre-Simon Laplace assembled important physical concepts and mathematical approaches, developed by contemporary researchers, to formulate a group of linear partial differential equations able to reproduce the observed tidal phenomena. The dynamical response of the ocean to gravity forces, induced by the earth and other celestial bodies, was expressed taking the Euler's equation of motion for a fluid in a rotating frame of reference,

$$\frac{D\mathbf{u}}{Dt} + \frac{1}{\rho}\nabla p = \underbrace{-g\hat{\mathbf{z}}}_{\textit{Gravity force}} + \underbrace{-2\Omega \times \mathbf{u}}_{\textit{Coriolis acceleration}} + \underbrace{-\Omega \times \Omega \times \mathbf{r}}_{\textit{Centrifugal acceleration}} + \underbrace{F}_{\text{Friction}} \quad (1)$$

where **u** (u, v, w) is the fluid velocity vector in the Cartesian coordinate system x, y, z (eastward, northward, upward) and D/Dt its rate of change subject to a time and space dependent velocity field, $\mathrm{D}\mathbf{u} / \mathrm{Dt} = (\partial \mathbf{u} / \partial t) + (\mathbf{u} \cdot \nabla)\, \mathbf{u}$. ρ is the density of the fluid, p the pressure, g the gravity, $\hat{\mathbf{z}}$ the unit vector in the upward direction, $\mathbf{\Omega}$ the earth angular velocity vector, **r** the distance normal to the rotating axis and F the frictional force per unit mass. The rotating frame introduces two apparent forces: the centrifugal acceleration ($-\ \mathbf{\Omega}$ x $\mathbf{\Omega}$ x $\mathbf{r}$) radially pointing outward and the Coriolis acceleration ($-\ 2\ \mathbf{\Omega}$ x $\mathbf{u}$) pointing 'to the right' of the velocity vector (if $\mathbf{\Omega}$ is anticlockwise).

By convenience, the gravity force and the centrifugal acceleration are combined in a single term, expressing the gravitational potential modified by the centrifugal force, $\nabla\phi$ ("measured" gravity) as

$$\phi = gz - \frac{\Omega^2 r^2}{2} \qquad (2)$$

In addition, the Coriolis acceleration is replaced for the earth system by a straightforward term $f \times \hat{\mathbf{z}}u$, where $f = 2\ \Omega\ sin\ \varphi$ is known as the Coriolis frequency (function of the latitude, φ). This expression shows that, when variability of vertical velocity is neglected, the only earth angular velocity component that can have impact on the motion of a geo-fluid is the vertical one ($\Omega\ sin\ \varphi$). This conclusion reveals also that rotational effects are negligible at the equator ($f \rightarrow 0$) and maximum at the earth poles. The previous rearrangements simplify the Euler momentum equation to

$$\frac{\mathrm{D}\mathbf{u}}{\mathrm{D}t} + f\,\hat{\mathbf{z}} \times \mathbf{u} = -\nabla\phi - \frac{1}{\rho}\nabla p + F \qquad (3)$$

As they stand, these equations are much too difficult to solve and since Laplace's time they are traditionally simplified when applied to earth tides. The usual approach (Laplace tidal Equations) transforms the depth-averaged Euler's equations in a compact form with the following assumptions (critically examined by Miles, 1974):

(i) ***Homogeneous incompressible fluid.*** This assumption implies a barotropic motion and neglects all the other baroclinic modes present in real stratified oceans. The incompressibility ignores fluid motions due to sound waves, as they are relatively unimportant when compared with gravity waves.

$$\frac{\partial \rho}{\partial t} + \mathbf{u} \cdot \nabla\rho = 0 \qquad (4)$$

(ii) ***Small disturbances relative to a state of uniform rotation***. It allows the linearization of the equations and is justified for tidal motion, except for very shallow waters flows,

$$(\mathbf{u} \cdot \nabla)\mathbf{u} = 0 \qquad (5)$$

(iii) ***Uniform gravitational field***. It assumes a spherical Earth and neglects tidal self-attraction (mutual gravitational attraction associated with free-surface displacement). Self-attraction can be significant for tides and may be formally incorporated in LTE either through the introduction of a linear operator (Platzman, 1971) or through the expansion of the solution in spherical harmonics (Lamb, 1932).

(iv) ***Rigid ocean bottom.*** It ignores the bottom elasticity of the ocean floor.

(v) ***Shallow hydrostatic ocean***. Both the Coriolis acceleration associated with the horizontal component of the Earth's rotation and the vertical component of the fluid acceleration are neglected. Variations in pressure are due to variations of the sea-surface slopes, $\nabla p = \rho g \nabla \eta$.

In addition to the Laplace simplifications listed above, the nature of tidal dynamics over small regions of interest, such as continental shelves, allows other simplifications, as:

(vi) ***Plane earth coordinate system***. The *f-plane* approximation is usually adopted for modeling the dynamics of small-scale oceanic processes. It takes into account that *Coriolis frequency* varies slowly as a function of the latitude φ and that the study region is limited to small latitude ranges.

(vii) ***Friction reduced to horizontal planes***. In the Euler's equation the 3D frictional forces are assumed to be applied as horizontal stress gradients (τ_x ,τ_y). In the ocean, forces due to turbulent friction are known to dominate molecular viscous stresses (exception in processes restricted to very thin layers near boundaries). At the seabed the bottom friction component is also usually expressed by horizontal drag related-stresses (τ_{bx} ,τ_{by}).

(viii) ***Tidal forcing term***. The astronomical potential that generates tides can be replaced by an equivalent sea-surface displacement, η_e. On other hand, tidal phenomena on the shelf are generally assumed to be independent of the direct forcing of the astronomical potential (Defant, 1961). Tides are then so-termed

"co-oscillating" (generated by the inertial movements of the deep ocean, acting through continuity, at the edge of the continental shelf), and are usually treated as freely propagating waves.

All the previous assumptions are usually used to derive the Laplace tidal equations (LTE), whose original form was written in rotating coordinates. In the chapter III, these equations are used in a vertical integrated compact form (6), written in Cartesian coordinates, under the *f*-plane approximation and by taking into account non-linear and tidal forcing terms. The pressure, p, is replace by free surface elevation, η, using the hydrostatic assumption.

$$\begin{cases} u_t + u u_x + v u_y - f v = -g(\eta - \eta_e)_x + \tau_{bx}/\rho H \\ v_t + u v_x + v v_y + f u = -g(\eta - \eta_e)_y + \tau_{by}/\rho H \\ \eta_t + \left[(H+\eta)u\right]_x + \left[(H+\eta)v\right]_y = 0 \end{cases} \quad (6)$$

where the *x, y* subscripts represent the derivative with respect to the longitudinal latitudinal directions, and *t* the derivative with respect to time. *H* stands for the depth at rest. The first two equations express the horizontal fluid momentum conservation and the last equation is the fluid continuity condition.

Chapter II

Tidal solutions along continental margins

The periodical rise and fall of the sea surface and associated horizontal displacements of the water masses, usually called tidal currents, express the tide phenomenon. Since Laplace theory, this ocean process became a fluid motion problem, for which other variables than the periodic generating forces are involved, as the earth rotation, friction and the ocean basin configuration (including the varying ocean depth). Although these motions result from a forced wave, the solution must meet the boundary conditions associated with the ocean limits. The tide-bounded solution of LTE is the subject of many theoretical and observational studies, initiated one century ago by Proudman and Doodson. Several analytical solutions where obtained, as we will see next.

Continental margins introduce lateral boundary effects that constraint the dynamics of long gravity waves, as tides (Mysak & Tang, 1974), reflecting free waves and guiding a wide set of trapped modes (Huthnance, 1975). Each mode has different dispersion relations, as a function of distinct boundary conditions, topographic configurations and latitude location (changes in f). The polychromatic tidal wave becomes a particular case given that it assembles different harmonic constituents, whose frequencies are close to f. At latitudes higher than 30ºN, the principal tidal harmonics can be split in sub-inertial (e.g. diurnal constituents) and super-inertial waves (e.g. semi-diurnal constituents). The lateral boundary effect is then different for each frequency range: the super-inertial constituents are generally reflected as free-modes (Poincaré waves) and the sub-inertial are usually trapped as continental shelf waves. However, a fundamental mode does also exists and is unaffected by the changing f, co-existing in both frequency domains (Kelvin mode). In chapter III, realistic barotropic tide modelling will reveal a complex tide solution, along the west-Iberian margin, which results from the combination of different wave modes such as the ones listed above (and described next).

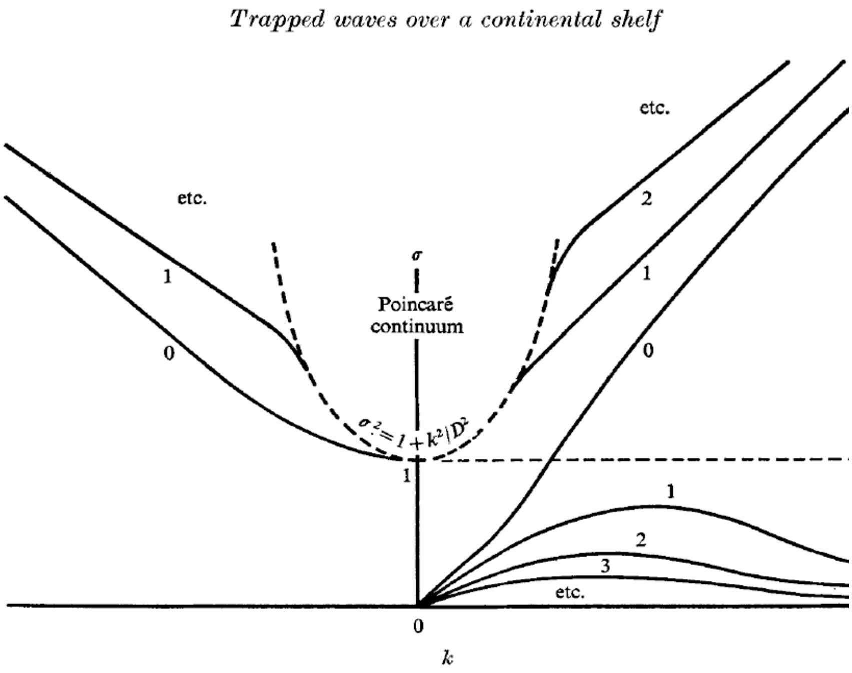

Figure 1. Dispersion relations of different barotropic wave modes along bounded oceans. Mode numbers equal the numbers of offshore nodes. The mode dispersion curves are traced as function of the horizontal wavenumber (k) and frequency ($\sigma = \omega / f$). $D^2 = f^2L^2/gH$ is a non-dimensional parameter that compares a shelf-width scale W with a Rossby radius of deformation. *From Huthnance (1975).*

1. Free inertial gravity waves

Lord Kelvin (1824-1907) introduced the hypothesis of a uniform rotating framework (f-plane) to simplify the Laplace tidal equation (1). By considering small disturbances relative to a deep flat ocean bottom ($H >> \eta$), at rest in this reference frame of uniform rotation, non-linear terms (including friction) can be neglected and the previous Laplace tidal equations reduce to :

$$\begin{cases} u_t - fv = -g\eta_x \\ v_t + fu = -g\eta_y \\ \eta_t + H(u_x + v_y) = 0 \end{cases} \quad (7)$$

These equations can be solved by successive term substitution, using x, y or t derivation of each equation. Deriving 7.1 in order to the x variable, 7.2 in order to y, allows the replacement of the terms u_{xt} and v_{yt} in the time derivative of 7.3. By rearranging this new equation and taking the resulting vorticity term $(v_x - u_y) = \zeta = \eta f / H$ one gets an equation for the single variable η :

$$\eta_{tt} - gH(\eta_{xx} + \eta_{yy}) + f^2\eta = 0 \quad (8)$$

The solution of equation (8) is then hunted in the form of a free plane wave $(\eta, u, v) = [\eta, u, v]\ exp\ \{i\ (\omega t - kx - ly)\}$, where (k, l) are the longitudinal and latitudinal wave numbers and ω the wave frequency. This allows the replacing of the time variability, $\partial^2/\partial t^2$ by $-\omega^2$, $\partial^2/\partial x^2$ by $-k^2$ and $\partial^2/\partial y^2$ by $-l^2$, to yield the relation dispersion for the so-called Poincaré modes:

$$\omega^2 = f^2 + (k^2 + l^2)\, gH \quad (9)$$

The Poincaré solution shows dispersive propagation since its phase velocity is also a function of the wavenumber. In other words, different wavelength propagates with different phase velocities over the same ocean depth. One can also verify from (9) that these unbounded wave modes are limited in frequency, $\omega^2 > f^2$ (super-inertial modes). These two statements define the so-called Poincaré continuum, which defines a region in the wavenumber-frequency plane where unbounded inertial gravity waves solutions exist (Figure 1). When propagating towards a coastline bounding a flat ocean, these free waves will be reflected, in a classic "optical" way (the reflected wave will preserve the incident angle relatively to the direction perpendicular to the coast and change sign of one wavenumber component), since the solution does not impose any boundary trapping condition. The reflection of obliquely incident Poincaré waves over continental shelves is subject of analytical work published by Webb (1976), Buchwald (1980), Middleton & Bode (1987), Garreau (1992) and Das & Middleton (1997).

2. Kelvin mode

A different solution is obtained if one imposes as boundary condition the vanishing of the velocity component perpendicular to the coastline, represented by a strait vertical wall. This condition reduces the governing equations (7) to the following form (when taking a north-south coastline, $u = 0$), also called the semi-geostrophic equilibrium,

$$\begin{cases} g\eta_x &= -fv \\ v_t &= -g\eta_y \\ \eta_t &= -Hv_y \end{cases} \quad (10)$$

As for the previous case, the solution comes out by similar manipulation of the momentum and continuity equation. When (10.3) is derived relative to time and (10.2) relative to *y*, one can eliminate v_{ty} to obtain $\eta_{tt} - gH\eta_{yy} = 0$. Again, the free wave form solution, $(\eta, v) = [\eta, u]\ exp\ \{i\ (\omega t - ly)\}$ is used to obtain the dispersion relation for the so-called Kelvin mode,

$$\eta\,(\omega^2 - gH\,l^2) = 0 \qquad (11)$$

The Kelvin waves are non dispersive, with a phase velocity $C = \omega / l = \pm\ (gH)^{1/2}$. Since the solution is independent from f, the Kelvin mode is valid for both super and sub-inertial tidal forcing frequencies (Figure 1). From (10) one can also get the structure of this wave by eliminating v between (10.1) and (10.2) equations, to obtain

$$\eta_x = -\frac{f}{C}\eta \qquad (12)$$

This equation has an exponential decay solution along x, given by $\eta = \eta\ \exp(-f\,x/C)$. Therefore, the sea surface slope and the velocity field for a Kelvin wave has respectively the form

$$\eta = \eta_0\ e^{(-f\,x/C)}\cos\,(ly - \omega t) \qquad (13)$$

$$v = \eta_0\,\sqrt{g/H}\ e^{(-f\,x/C)}\cos\,(ly - \omega t) \qquad (14)$$

The transverse decay scale C/f is called the external Rossby radius of deformation, which sets the offshore length of the Kelvin wave: λ ~2000 km for H = 4000 m and at mid-latitude ($f = 1.0\text{x}10^{-4}\ \text{s}^{-1}$).

3. Trapped modes

When topographic variations, normal to the coast, are introduced to the previous bounded condition, other solutions become also possible. Stokes (1819-1903) discovered the classical solution for the fundamental-mode edge wave, on a uniform sloping beach. Again, this and other "trapped" modes can be derived from the barotropic long wave equations (7).

Assuming that the bottom slope is uniform along-shelf and sufficiently small in order to neglect vertical fluid motions, one can derive a general amplitude equation, in the wave form (see Part II, Chapter I, for details), to the cross-shelf section (x-direction) as,

$$\eta_{xx} + \frac{H_x}{H}\eta_x + \left(\frac{\omega^2 - f^2}{gH} - \frac{H_x}{H}\frac{f}{\omega}l - l^2\right)\eta = 0 \qquad (15)$$

Solution of (15) can be found by imposing similar boundary condition as to the Kelvin wave, i.e. $\eta(0)$ and u(0) = 0 (amplitude and velocity at the coast) and an uniform slope (α), where $H_x = \alpha\, x$. The result is a dispersion relation for the *n-th* mode of the progressive edge wave as (e.g. LeBlond and Mysak, 1978):

$$\omega^2 = (2n+1)\,\alpha\, g\, l \qquad (16)$$

The solution shows that edge waves are discrete modes that can travel in either direction along the coast, with phase velocity of

$$C = \sqrt{(2n+1)\,\alpha\, g\,(\lambda/2\pi)} \qquad (17)$$

Where $\lambda = 2\pi/l$ is the along-shore edge wavelength. From (16) one can verify the wavelength range, for edge wave solutions, if the forcing frequency is taken as semidiurnal ($\omega = 1.4\text{x}10^{-4}\ \text{s}^{-1}$). When considering typical continental shelf bottom slopes (< 0.02) one will get edge waves length smaller than $3\text{x}10^{\,3}$ m for the first mode and smaller for higher modes. Although there exists possible tide wave solutions in the form of edge modes, in situ observations do not show energy in this frequency/wavenumber domain and for that they should not be considered in the next sections.

Another root of (15) is the step-topography configuration, where a simplified flat shelf (H_1) is bounded by deeper ocean region of constant depth (H_2). The dependent variable in (15) is now set to $F = \psi$, $\partial\psi / \partial x = Hv$, and the solution is pursuit in the principle of flux conservation in both sides of the shelf break. By taking the shelf-break distance from the coast as L, the solutions around x = L (shelf break) are,

$$\begin{cases} \psi_{H2} = A_1 \sinh lx & , L < x \le 0 \\ \psi_{H1} = A_1 \sinh lL\, e^{-l(x-L)} & , x < L \end{cases} \qquad (18)$$

Equation (15) must be verified at each side of the shelf break, which condition gives by integration of (15) over a small neighbourhood about $x = L$,

$$\left(\frac{1}{H_2} - \frac{1}{H_1}\right)\psi_x = -\left(\frac{1}{H_2} - \frac{1}{H_1}\right)\frac{l f}{\omega}\,\psi(x=0) \qquad (19)$$

The solution of (18), when using (19) will yield the dispersion relation for the bounded step-topography modes, which solutions are usually called Continental shelf modes.

The disperse relation (20) was first obtained by Larsen (1969) and shows that continental shelf wave modes must be sub-inertial, since for any configuration its absolute value is always $\omega / f < 1$ (Figure 1).

$$\frac{\omega}{f} = -\frac{h_2 - h_1}{h_1 + h_2 \coth(l\,L)} \qquad (20)$$

All the previsions solutions are derived with flat bottom, linear slopes or step bathymetry conditions. Yet, in nature, where the ocean relief is far from monotonous, these modes coexist in distorted solutions, function of the bathymetry configuration and forcing frequencies. Many one-dimensional solutions can be found in literature for different simplified bathymetry functions.

References

Buchwald, V. T., 1980: Resonance of Poincaré waves on a continental shelf. Aust. J. Mar. Freshwater Res., 31, 451–457.

Cartwright, D.E., 1999: *Tides – A Scientific History*. Cambridge University Press, Cambridge, 293pp.

Das, P., **Middleton**, J., 1997. Obliquely Incident Poincaré waves on a sloping continental shelf. Journal of Physical Oceanography 27, 1274-1285.

Deacon, M., 1971: *Scientists of the Sea 1650-1900: A Study of Marine Science*. Academic press, London and New York, 445 pp.

Defant, A., 1961: *Physical Oceanography*, Volume II, Pergamon Press, New York, 590 pp.

Garreau, P., 1992. Passage de la marée au-dessus d'un talus **-** Etude des processus linéaires et non linéaires **-** Application au golfe de Gascogne, Thèse de Doctorat, Université de Bretagne Occidentale, Brest.

Huthnance, J. M., 1975: On trapped waves over a continental shelf. *Journal of Fluid Mechanics*, 69, 689–704.

Lamb, H., 1932: *Hydrodynamics*, 6th ed. Dover, New York, 738 pp.

Middleton, J. H., and L. **Bode**, 1987: Poincare´ waves obliquely incident to a continental shelf. Contin. Shelf Res., 7, 177–190.

Miles, J.W., 1974: On Laplace’s tidal equations, *Journal of Fluid Mechanics*, 68, 241-260.

Mysak, L. A., & C. L. **Tang**, 1974: Kelvin wave propagation along an irregular coastline. *Journal of Fluid Mechanics*, 64, 241–261.

Platzman, G. W., 1971: Ocean tides and related waves. *Mathematical Problems in the Geophysical Sciences*. Am. Math. Soc., Rhode Island, Vol. 2, 239-291.

Proudman, J., 1953: Dynamical Oceanography, Methuen, London, and John Wiley & Sons, New York, 409 pp.

Webb, D. J., 1976: A model of continental-shelf resonances. Deep-Sea Res., 23, 1–15.

Chapter III

Modelling the barotropic tide along the West-Iberian margin*

LUIS S. QUARESMA
Instituto Hidrográfico - Marinha, Lisboa, Portugal.

ANNICK PICHON
Service Hydrographique et Océanographique de la Marine, Brest, France.

* *Article publish online, Journal of Marine Systems (2011)*

Abstract

[1] The present work explores the use of a numerical model to predict the barotropic tide along the West-Iberian region, extending from the Gulf of Cadiz to the Bay of Biscay and from the shelf to nearby seamounts (Gorringe and Galicia banks). The model is used, in a single isopycnal layer, to simulate the 2D propagation of the following eight principal tidal constituents: M2, S2, N2, K2, K1, O1, P1 and Q1. Astronomical tide-raising force is introduced into the equations of motion in order to improve model results. Recently updated global tide solutions are optimally combined to force a polychromatic tidal spectrum at the open boundaries. New bathymetry is built from hydrographic databases and used to increase the accuracy of the model, especially over the Portuguese continental shelf. Data from several tide gauges and acoustic Doppler current profilers are used to validate the numerical solution. Tidal amplitude and tidal current velocity solutions are evaluated by classical harmonic analysis of in situ and simulated time-series. Model outputs demonstrate the improvement of the regional hydrodynamic tide solution from earlier references. The harmonic solutions highlight small-scale variability over the shelf, and over nearby seamounts, due to the generation of diurnal continental shelf waves and topographic modulation of the semi-diurnal tidal ellipses. The barotropic forcing term is calculated over the study region and themain internal tide generation “hotspots” are revealed.

[2] Key words: barotropic tide, barotropic forcing term, numerical model, tide-gauges ADCP data.

Journal of Marine Systems xxx (2011) xxx–xxx

Contents lists available at SciVerse ScienceDirect

Journal of Marine Systems

journal homepage: www.elsevier.com/locate/jmarsys

Modelling the barotropic tide along the West-Iberian margin

Luis S. Quaresma [a,*], Annick Pichon [b]

[a] INSTITUTO HIDROGRAFICO, Divisão de Oceanografia, Rua das Trinas, nº49, 1249–093 Lisboa, Portugal
[b] SHOM, HOM/REC, 13 rue du Chatellier, 29200 Brest, France

ARTICLE INFO

Article history:
Received 1 October 2010
Received in revised form 5 August 2011
Accepted 21 September 2011
Available online xxxx

Keywords:
Barotropic tide
Barotropic forcing term
Numerical model
Tide-gauge
ADCP data

ABSTRACT

The present work explores the use of a numerical model to predict the barotropic tide along the West-Iberian region, extending from the Gulf of Cadiz to the Bay of Biscay and from the shelf to nearby seamounts (Gorringe and Galicia banks). The model is used, in a single isopycnal layer, to simulate the 2D propagation of the following eight principal tidal constituents: M2, S2, N2, K2, K1, O1, P1 and Q1. Astronomical tide-raising force is introduced into the equations of motion in order to improve model results. Recently updated global tide solutions are optimally combined to force a polychromatic tidal spectrum at the open boundaries. New bathymetry is built from hydrographic databases and used to increase the accuracy of the model, especially over the Portuguese continental shelf. Data from several tide gauges and acoustic Doppler current profilers are used to validate the numerical solution. Tidal amplitude and tidal current velocity solutions are evaluated by classical harmonic analysis of *in situ* and simulated time-series. Model outputs demonstrate the improvement of the regional hydrodynamic tide solution from earlier references. The harmonic solutions highlight small-scale variability over the shelf, and over nearby seamounts, due to the generation of diurnal continental shelf waves and topographic modulation of the semi-diurnal tidal ellipses. The barotropic forcing term is calculated over the study region and the main internal tide generation "hotspots" are revealed.

1. Introduction

The West-Iberian margin is marked by a narrow continental shelf shaped by submarine canyons, promontories and capes (Fig. 1). Its major topographic feature is the Estremadura promontory, extending 200 km offshore and forming a wide shallow plateau (Tagus Plateau). Two important submarine canyons (Nazaré and Setúbal) delimit this structure and increase its slope at the north and south faces. These topographic features divide a wider shelf to the north from an almost absent shelf to the south. Other smaller canyons, seamounts (Gorringe and Galicia banks) and islands increase the intricacy of this region.

Different oceanographic processes occur in the region, varying in spatial and time scales. A common shelf/slope current velocity power spectrum shows an energetic band at tidal frequencies, bounded by low-frequency circulation and energetic high-frequency activity. The low-frequencies domain highlights the deep/subsurface poleward thermohaline flows, as well as frequent wind-driven transport. During winter, the short-period processes are dominated by storm gravity waves and during summer by non-linear internal tide dynamics (Quaresma et al., 2007).

As far as tidal dynamics are concerned, the M2 semi-diurnal constituent is dominant over the study region. The S2 is the next-largest constituent and consequently introduces Spring-Neap tidal modulation along the continental shelf. N_2 and K_2 harmonics are also very energetic, being responsible for longer period modulation. While being less energetic, the O_1 and K_1 diurnal constituents are also present and are responsible for the observed diurnal inequality of the tide. These six principal tidal harmonics are then followed by five semi-diurnal waves ($2N_2$, MU_2, NU_2, L_2, T_2) and by two other diurnal constituents, Q_1 and P_1 (Fig. 2). Within the same order of amplitude, the study region also reveals long-period radiational harmonics (SA, SSA and MM). Although the observed tidal currents are small (rarely above 0.2 $m.s^{-1}$), when compared with other coastal regions, they are the driving force of the strong high-frequency baroclinic activity, recorded over this margin (Azevedo et al., 2006; Da Silva et al., 1998; Jeans and Sherwin, 2001; Quaresma et al., 2007; Sherwin et al., 2002; Small, 2002).

To understand and predict the complex dynamics of the regional internal tidal features, the MITIC research project (Modelling of the Internal Tide over the West-Iberian Coastal margin) was put together in a partnership between the Portuguese and the French hydrographic offices (HIDROGRAFICO and SHOM). The study of the internal tide dynamics requires knowledge and accurate forecasting of the barotropic tidal solution. This task was explored in the present work by the use of HYCOM (HYbrid Coordinate Ocean Model), in a 2D tidal hydrodynamic regional configuration.

Other authors have dedicated work to model the barotropic tide over this continental margin. Among them, it is important to point out studies performed by Fanjul et al. (1997), who applied a 3D Z-coordinate model (HAMSOM) with a variable grid size scheme.

* Corresponding author. Tel.: +351 210943000.
E-mail address: luis.quaresma@hidrografico.pt (L.S. Quaresma).

0924-7963/$ – see front matter © 2011 Elsevier B.V. All rights reserved.
doi:10.1016/j.jmarsys.2011.09.016

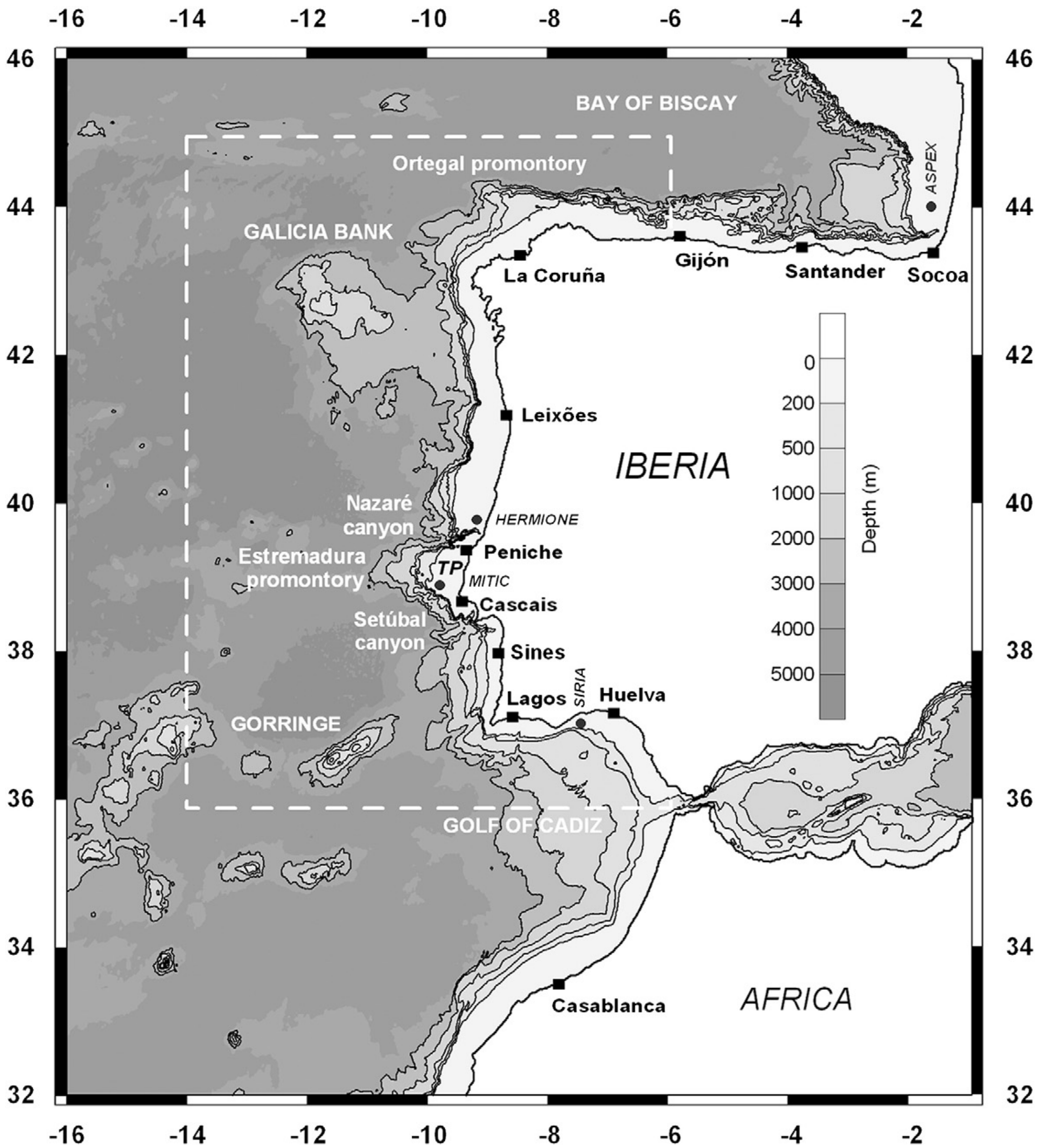

Fig. 1. The West-Iberian region (numerical model domain). Global tide solutions were forced at the open boundaries. These limits were selected in order to guarantee a homogeneous deep-ocean condition (distant from important topographic structures). Black squares indicate tide-gauges and gray circles the current-profile dataset locations, used to validate model results. The white dashed line delimits the study domain.

Monochromatic tidal waves, derived from the first TOPEX/POSEIDON datasets, were forced at the open boundaries. The simulation suggests Kelvin wave mode propagation, from south to north with amplitudes increasing towards the coast. Extensive solution validation was performed by tide-gauge data. Sauvaget et al. (2000) used TELEMAC-2D to model these structures, zooming the northern Portuguese shelf. A special attention was given to M2 and K1 constituents, revealing the generation of diurnal continental shelf waves trapped at the shelf. Fortunato et al. (2002) dedicated a full article to discuss these phenomena, by using a finite element model (ADCIRC). Their study pointed out the Tagus Plateau's responsibility as the trapped wave trigger. Recently, Marta-Almeida and Dubert (2006) applied the ROMS model to the same region in order to show the structure of eight principal tide harmonics (M2, S2, N2, K2, K1, O1, P1 and Q1) over the northern Portuguese shelf. This study reinforced the strong topographic effect of the Tagus Plateau in the reshaping of the diurnal solution (intensification of surface elevation and current magnitude, as well as the modulation of their phase velocity).

The originality of the present work was the simulation of a polychromatic tidal spectrum to obtain a regional tide solution. Eight principal constituents, essential to reproduce the regional tide behaviour, were assembled and forced at the open boundaries. This option allows non-linear harmonic interactions in the resulting solution, as expected in nature. Other authors frequently adopt a monochromatic methodology in short period model runs to reduce numerical costs and avoid uncontrolled constituent interactions. The present model outputted an absolute tidal solution and its evaluation was performed by harmonic analysis. Higher accuracy was achieved by adding the gravitational tidal gradient force into HYCOM momentum equations and by improving the bathymetric information over the region. Self-attraction/loading (SAL) terms were not included, based on the principle that they are negligible near coastal regions and that the utility

Please cite this article as: Quaresma, L.S., Pichon, A., Modelling the barotropic tide along the West-Iberian margin, J. Mar. Syst. (2011), doi:10.1016/j.jmarsys.2011.09.016

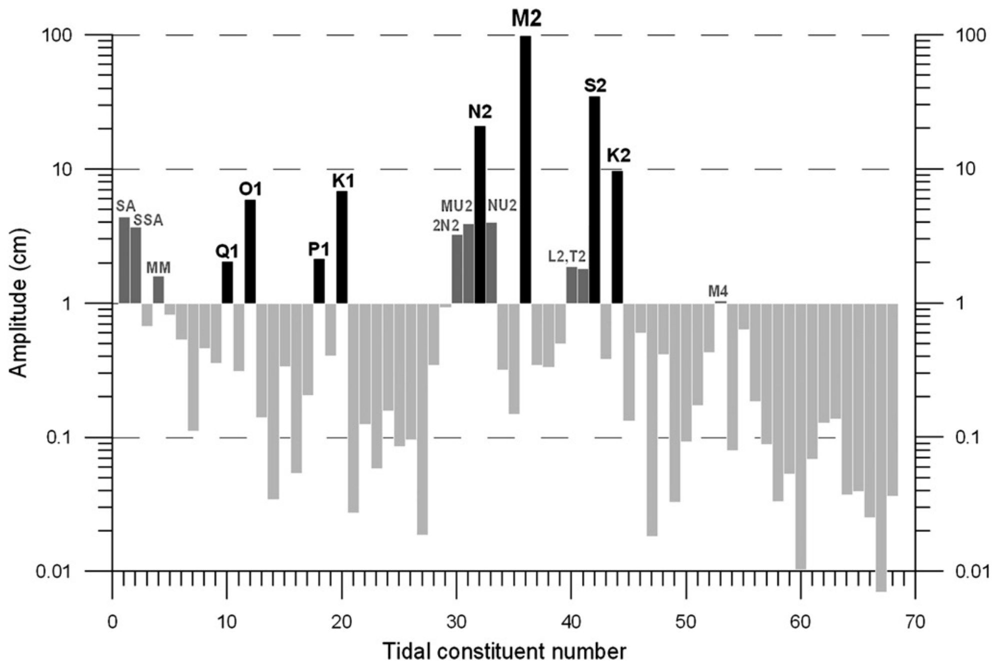

Fig. 2. Tidal constituents at Cascais tide gauge (Portugal). The amplitude was obtained by harmonic analysis of 4 years record. The length of the used time-series allows the extraction of 68 constituents. The y-axis divides the constituents with amplitudes higher than 1 cm from all the others. Notice that the eighth modelled constituents are not the most energetic. Other semi-diurnal harmonics (2N2, MU2, NU2, L2 and T2) have the same order of magnitude as Q1 and P1. Radiational harmonics are also present with relevant energy (SA, SSA and MM).

of adopting them is questionable (Ray, 1998). Finally, an effort was made to validate both sea-surface height and tidal current velocity solutions for each constituent. Accurate barotropic tidal ellipse simulations enabled better estimations of the internal tide generation forcing term, as done by Pichon and Correard (2006).

In Section 2, *in situ* observation datasets are presented. The numerical model is briefly introduced, focusing on momentum and continuity equations. The viscosity parameterization in the model is also considered. A new bathymetry is proposed and two different global tide solutions are discussed.

Table 1
Tide-gauge datasets location and record lengths. FR1 stands for SHOM, ES for PUERTOS DEL ESTADO and PT for HIDROGRAFICO. Tide-gauge technology is present in System column. The dataset from Casablanca tide-gauge was taken from SHOM's database.

Site		Position (WGS-84)		System	Record length (years)	Period
St Jean-de-luz (Socoa)	FR1	43° 23′ 42.0″ N	1° 40′ 54.0″ W	Radar	3	2007–2009
Santander	ES	43° 27′ 45.0″ N	3° 47′ 22.0″ W	Ultrasonic	7	1993–2000
Gijón	ES	43° 33′ 33.0″ N	5° 41′ 50.0″ W	Ultrasonic	4	1996–2000
Coruña	ES	43° 21′ 31.0″ N	8° 23′ 17.0″ W	Ultrasonic	6	1993–1999
Leixões	PT	41° 11′ 07.8″ N	8° 42′ 14.0″ W	Float gauge	3.5	2005–2008
Peniche	PT	39° 21′ 13.5″ N	9° 21′ 28.2″ W	Pressure	2	2007–2008
Cascais	PT	38° 41′ 35.4″ N	9° 24′ 55.4″ W	Float gauge	3	2004–2006
Sines	PT	37° 56′ 53.4″ N	8° 53′ 16.2″ W	Float gauge	3	2006–2008
Lagos	PT	37° 05′ 56.0″ N	8° 40′ 06.0″ W	Float gauge	3	2000–2002
Huelva	ES	37° 07′ 56.0″ N	6° 50′ 02.0″ W	Ultrasonic	3	1997–2000
Casablanca	FR1	33° 36′ 46.0″ N	7° 36′ 19.8″ W	Float gauge	0.5	2005

Model results are validated in Section 3 by tide-gauge records and current profile datasets. The barotropic structure of the tide is illustrated and analysed in Section 4. A general description is made for diurnal and semi-diurnal constituents, using the K1 and M2 harmonics as representatives of each sub and super-inertial forcing group. A specific discussion is dedicated to the small-scale shelf variability observed along the West-Iberian margin (Section 5). In Section 6 the barotropic forcing term is calculated over the study region and the main internal tide generation “hotspots” are identified.

2. Materials and methods

2.1. Data analysis

Several sea-level records and mid-shelf current profiles were made available for the present study (see Tables 1 and 2). They were used to validate model results and to help its parameterization. Data are the property of the following institutions: HIDROGRAFICO (Portuguese Hydrographic Office and Marine National Laboratory, PT), SHOM (French Hydrographic Office, FR1), IFREMER (French Marine National Laboratory, FR2) and PUERTOS DEL ESTADO (Spanish National Harbours Office, ES). Tide gauges were selected by location criteria. They are spaced along the domain and reflect, as much as possible, the offshore tide solution. The adopted model spatial resolution (1-arc minute) restrained the desirable representation of coastal

Table 2
ADCP current profile dataset locations, record lengths and depth. FR2 stands for IFREMER and PT for HIDROGRAFICO. ADCP working frequency is present in System column.

Project		Position (WGS-84)		System	Record length (days)	Depth (m)
ASPEX	FR2	44° 00′ N	001° 33′ W	ADCP 300 kHz	47	70
HERMIONE	PT	39° 48′ N	009° 12′ W	ADCP 300 kHz	46	80
MITIC	PT	38° 52′ N	009° 55′ W	ADCP 190 kHz	6	120
SIRIA	PT	37° 02′ N	007° 34′ W	ADCP 300 kHz	42	75

Please cite this article as: Quaresma, L.S., Pichon, A., Modelling the barotropic tide along the West-Iberian margin, J. Mar. Syst. (2011), doi:10.1016/j.jmarsys.2011.09.016

inlets. This constraint advised the discard of tide gauges placed inside estuaries and inside the Galician Rias. Nodal corrections were applied to amplitude and phase estimations. No correction was made for atmospheric effects.

Tide-gauge data was re-sampled hourly and submitted to classical harmonic analysis, using the available open source tool T_TIDE (Pawlowicz et al., 2002). This option allows other authors to repeat the present analysis and perform equivalent evaluations. Different years and record lengths were used, based on data availability and data quality. These requisites ensure the absence of large holes (invalid data) in the employed time series, enabling coherent harmonic analysis. Exception is made to PUERTOS DEL ESTADO data, where their own harmonic constants were used to validate present model results.

Four Acoustic Doppler Current Profiler (ADCP) records were validated and reprocessed to extract the barotropic tidal current. These datasets were obtained at depths of near 100 m, over different mid-shelf regions (Fig. 1). The ADCPs profiled the water column velocities from bottom to surface, enabling a vertical data integration to obtain the barotropic component of the observed current. These time series (Table 2) were submitted to similar harmonic analysis in order to calculate current ellipses for each tidal constituent.

2.2. Numerical model

The *HYbrid Coordinate Ocean Model* (HYCOM) is a hydrostatic primitive equations, free surface, ocean general circulation model (Bleck, 2002) that evolved from the *Miami Isopycnic-Coordinate Ocean Model*, MICOM (Bleck and Boudra, 1981; Bleck and Smith, 1990). The present work used the new HYCOM barotropic/baroclinic time-splitting scheme, recently modified to resolve external gravity waves over wet-and-dry regions (Morel et al., 2008). The model was also customized to force tidal solutions (sea-level and current velocity) as boundary conditions at the open frontiers. Gravitational tidal gradient force was added to HYCOM's momentum equations.

The model was used in 2D isopycnical single-layer configuration (pure barotropic mode), suitable for long-period gravity waves studies. This option has a smaller numerical cost and enables multiple one-year runs in a short period of time. By imposing the polychromatic tidal spectrum as the boundary condition, HYCOM radiates the correspondent waves by resolving both momentum (1) and continuity (2) equations, in the following adiabatic isopycnic forms. The single-layer nonlinear momentum equations (Bleck and Smith, 1990) are:

$$\begin{aligned}\frac{\partial u}{\partial t}+\frac{\partial}{\partial x}\frac{U^2}{2}-(\zeta+f)v&=-\frac{\partial M}{\partial x}+\frac{1}{H}[g\Delta\tau_{bx}+\nabla\cdot(\upsilon H\nabla u)]\\ \frac{\partial v}{\partial t}+\frac{\partial}{\partial y}\frac{U^2}{2}-(\zeta+f)u&=-\frac{\partial M}{\partial y}+\frac{1}{H}[g\Delta\tau_{by}+\nabla\cdot(\upsilon H\nabla v)]\end{aligned}\tag{1}$$

where u, v are the horizontal components of the velocity vector U, ζ is the relative vorticity, f the Coriolis parameter, $M=g\eta$ the Montgomery potential (g gravity, H the mean depth at rest and η the sea-surface elevation), $\Delta\tau_b$ the bottom stress gradient and υ is an horizontal turbulent viscosity coefficient. The general continuity equation, in single-layer configurations, is

$$\frac{\partial\eta}{\partial t}+\nabla\cdot((H+\eta)\cdot U)=0\tag{2}$$

The bottom stress is formulated by a quadratic function of the barotropic current, parameterized by a drag coefficient, $\tau_b=-C_D|\,U\,|\,U$. For the present study, the momentum diffusion term is configured with a simple Smagorinsky frictional harmonic parameterization, where υ is defined as the maximum value of the following relation:

$$\upsilon=\max\left\{U_2dx;\quad \lambda_2\left[\left(\frac{\partial u}{\partial x}-\frac{\partial v}{\partial y}\right)^2+\left(\frac{\partial u}{\partial y}+\frac{\partial v}{\partial x}\right)^2\right]^{1/2}dx^2\right\}\tag{3}$$

where λ_2 is an eddy viscosity coefficient and U_2 is a diffusivity parameter. Spatial resolution was set to 1 arc-minute ARAWAKA-C grid ($dx=dy$ ~1.8 km).

2.2.1. Friction parameterization

Shallow water tides can physically create residual currents (tidal rectification), arising from the asymmetry between the flooding and ebbing phases (over very shallow water regions) or from local vorticity generation (especially near coastline and sloping topography). In nature, tidal rectification residual currents are usually one or two orders magnitude smaller than the forcing tidal flow velocities (Robinson, 1981). The use of discrete approximations to solve the momentum advection terms, in Eulerian equations, is also a source of artificial residual circulation. The resulting numerical diffusion is function of the grid resolution and the velocity shear. To minimize this effect, viscosity coefficients (3) were introduced to parameterize **turbulent friction** U_2 controls the numerical diffusion introduced by the unresolved scales within a constant grid resolution; λ_2 limits the uncontrolled turbulent diffusion added by strong velocity shears (verified over steep topography and rough coastlines). However, strong coefficients will falsely reduce the linear tidal velocity magnitude. This parameterization

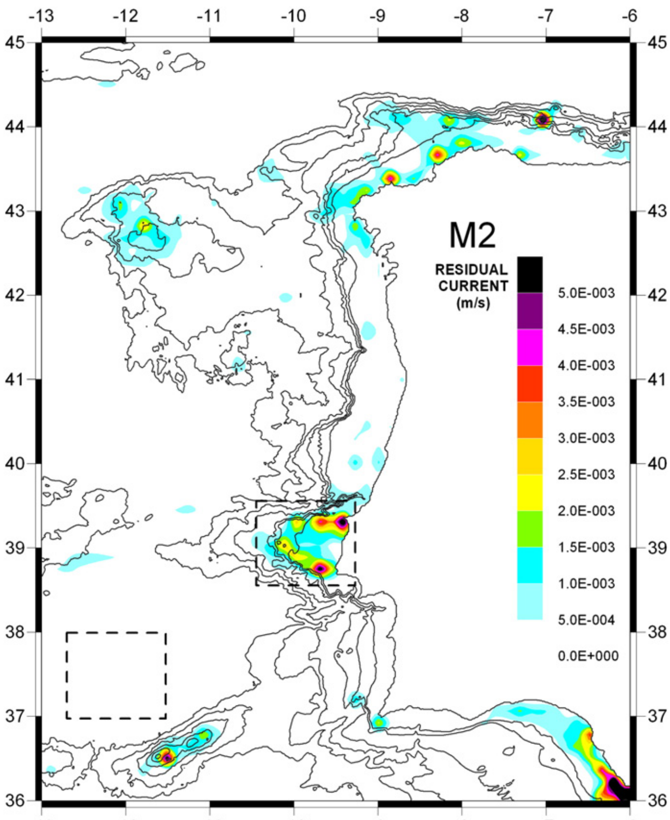

Fig. 3. M2 residual current extracted from harmonic analysis. Model parameterization: lateral friction enabled; $C_D=2.5\times10^{-3}$; $\lambda_2=0.2$ and $U_2=0.04\ \mathrm{m.s^{-1}}$. Two control areas are represented: 1. Offshore, where bottom topography is deep and flat, the numerical diffusion was reduced to values lower than $5\times10^{-4}\ \mathrm{m.s^{-1}}$; inshore, over the Portuguese margin, the residual circulation arises at this region of strong slope and coastline roughness (reaching values $>5\times10^{-3}\ \mathrm{m.s^{-1}}$).

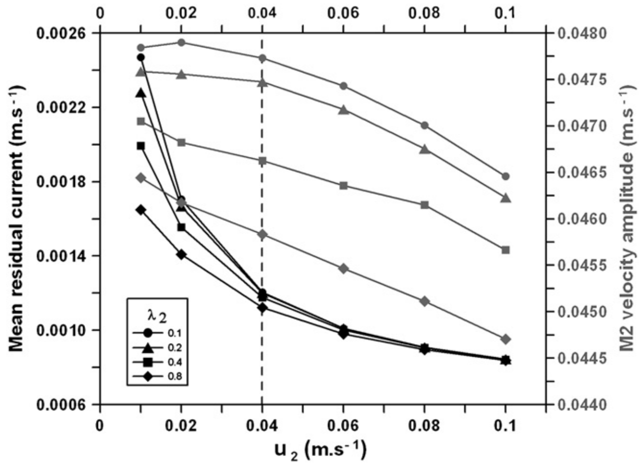

Fig. 4. Viscosity parameters evaluation. Several runs were performed with monochromatic tide (M2) and different viscosity parameterization. The residual current and M2 velocity amplitude was extracted from harmonic analysis and quantified at the control area 2, placed over the Portuguese shelf (see location at Fig. 3).

becomes then a compromise between an efficient numerical diffusion reduction and a realistic tide velocity simulation.

The adopted viscosity coefficients, λ_2 and U_2, were defined by optimal adjustment. Several monochromatic simulations were performed with different coefficient choices. The tidal current was extracted from each simulated solutions by harmonic analysis. A control sub-domain (see Fig. 3), covering the continental slope and shelf region, was chosen to quantify a mean coastal M2 velocity magnitude, as well as a mean residual current (non-harmonic circulation). The results were assembled with the variation range of the two viscosity coefficients (Fig. 4). Small λ_2 and U_2 values conduct to strong residual velocities and unvarying harmonic velocity magnitudes. On the other hand, strong λ_2 and U_2 values reduce the tidal velocity and converge the residual current to a minimum magnitude. In order to minimize the artificial residual flow and retain a steady tidal current magnitude the following parameter values were chosen: $\lambda_2 = 0.2$ and $U_2 = 0.04$ m.s^{-1}.

Boundary lateral friction was set to force a null tangential velocity at the coastline (no slip condition). Simulations with other boundary conditions reveal the intensification of artificial circulation along this frontier (not shown here). A standard drag coefficient of $C_D = 2.5 \times 10^{-3}$ was adopted to parameterize the bottom stress. In the present single layer configuration this parameter plays a small role, since water depth is high over most of the domain (Prandle, 1997). Simulations with other drag coefficient values (between 0.5×10^{-3} to 3.0×10^{-3}) gave no significant impact to the tidal solution (not shown here).

2.3. Bathymetry

The accuracy of regional tide models is often limited by bottom topography errors, normally manifested over the shelf and shallow regions. In recent years some global bathymetry datasets were made available, derived from both hydrographic soundings and the inversion of sea-surface satellite altimetry measurements. Over the study region, a common used bathymetry is the ETOPO1 global relief model (Amante and Eakins, 2009). However, this source reveals some inaccuracies over the Iberian shelf and misses topographic details along its continental slope. To overcome this problem, a new 1 arc-minute bathymetric Digital Terrain Model (DTM) of the West-Iberia domain was built from different bathymetry databases (called here after WIBM2009). Accurate data, detained by both Portuguese and French Hydrographic Offices (HIDROGRAFICO and SHOM) were complemented with ETOPO1 where no available hydrographic data existed.

WIBM2009 ensures a more realistic bathymetry over the Portuguese and Galicia region, where abrupt shelf discontinuities and complex coastline coexist in shallow-water regions. The domain extends from 32.0° to 46.0°N latitudes and from 16.0° to 1.0°W longitudes. It is horizontally referenced to the ellipsoid WGS-84 and vertically to the Portuguese hydrographic zero. For the present use, WIBM2009 was projected to MERCATOR coordinate system and vertically to the Mean Sea-Level by the use of MARMONDE MSL solution (Simon, 2007).

2.4. Tidal forcing

Tides are predominantly simulated in regional circulation numerical models by boundary conditions forcing. The sea-surface elevation and the corresponding 2D velocity components are imposed as tidal harmonics along the open limits. These ocean basin solutions are obtained from global ocean tide models, normally accurate in the deep-ocean but with significant errors near coastal and shallow regions. The present work explores the use of two recently revised and updated global tide solutions: TPXO7.2 and NEA2004 Tidal Atlas. Each results from different modelling approaches. TPXO7.2 is the most recent solution of the OTIS model (Egbert et al., 1994) that best fits the Laplace tidal equations to altimetry data from TOPEX/Poseidon plus Jason (since 2002 until present). The North-East Atlantic tidal atlas (NEA2004) results from a regional nesting of FES2004 (Lyard et al., 2006), carried out by the Toulouse Unstructured Grid Ocean model (T-UGOm) in a 2D barotropic, shallow water mode (Pairaud et al., 2008). FES2004 is also a global tide hydrodynamic model, improved by tide-gauge and altimetry data assimilation (TOPEX/Poseidon plus ERS-2).

The two global solutions were introduced, one at a time, as HYCOM's open boundary conditions. The performance of each simulation was evaluated by comparing harmonic analysis of the sea-surface height with the tide-gauge records network (Fig. 1). This accuracy assessment showed better semi-diurnal results when NEA2004 was applied and better diurnal solutions when TPXO7.2 was used. Exception was found in the K2 constituent. The adopted polychromatic solution, used as boundary conditions in the present HYCOM configuration, resulted from the assembling of N2, M2 and S2 constituents from NEA2004 and K2, Q1, O1, P1 and K1 from TPXO7.2. This choice allowed the best regional tide prediction and was made possible because, in the harmonic decomposition of the tide, the eight adopted constituents are independent from each other.

A further step was made to simulate the astronomical tide-raising forces acting regionally inside the study domain. The gravitational tidal gradient force, $\partial P/\partial x$ and $\partial P/\partial y$, was added to HYCOM barotropic momentum equations (1), as:

$$P = C_L g \sum_i \varphi_i a_i D_i \ \cos[q_i(t-t_0) + V_i(t_0) + b_i] \tag{4}$$

where C_L is the moon's reference potential (0.2687536×10^{-3} km), φ_i a Latitude coefficient, D_i the Doodson coefficient for each constituent (i) and a_i, b_i the respective nodal corrections parameters.

3. Model accuracy

The regional barotropic tide solution was obtained through one-year simulation, forced by polychromatic tidal spectrum (assembling four diurnal and four semi-diurnal constituents). The simulation started with an ocean at rest and the tide was introduced as boundary conditions with an exponential growth, completed after 10 semi-diurnal cycles. This option enabled the smooth settling of the tidal current inside the domain.

3.1. Sea surface height

Tidal sea-level amplitude and phase solutions were validated against harmonic analysis of tide gauge records, placed along the domain's coastline. La Coruña, Leixões, Peniche, Cascais, Sines and Lagos were chosen to represent the regional solution along the Portuguese and Galician West-coast (Section 4). Casablanca and Saint-Jean-de-Luz (Socoa) were chosen as representatives of the near open boundary tidal solution. All the other tide-gauges gave an overall model accuracy response. Model performance at the Gibraltar strait is not discussed here, since this is a complex domain where more careful work should be dedicated. However, this region was included in the model's domain since it modifies the tidal wave solution inside the gulf of Cadiz, which was validated by the Huelva tide-gauge.

Table 3
Accuracy evaluations of the model in the simulation of semi-diurnal tidal constituents. This estimation was made by the differences of the harmonics parameters (amplitude and phase) between tide-gauge records and model results (at the nearest point). The biggest differences were shaded. For each calculated value a confidence interval size was added (estimation error). In the model accuracy column the errors correspond to the sum of the previous two confidence intervals (tide-gauge plus model).

Harmonics		Tide gauge				Model				Model Accuracy					
name	period (hours)	amplitude		phase		amplitude		phase		amplitude			phase		
		(cm)	error (cm)	(°)	error (°)	(cm)	error (cm)	(°)	error (°)	(cm)	%	error (cm)	(°)	(min)	error (°)
SAINT JEAN–DE LUZ															
N2	12,658	28,12	0,36	73,31	0,76	28,11	< 0,01	70,47	0,01	0,00	0,01	0,37	2,84	5,99	0,77
M2	12,421	132,04	0,41	94,03	0,17	132,56	< 0,01	92,17	0,00	−0,52	−0,40	0,42	1,86	3,85	0,17
S2	12,000	45,96	0,43	126,34	0,51	44,81	< 0,01	124,14	0,01	1,15	2,50	0,44	2,20	4,40	0,52
K2	11,967	12,88	0,47	126,14	2,27	13,23	< 0,01	120,10	0,02	−0,35	−2,72	0,48	6,04	12,05	2,29
SANTANDER															
N2	12,658	28,20	–	76,25	–	27,55	<0,01	70,66	0,01	0,65	2,29	–	5,59	11,79	–
M2	12,421	134,29	–	95,43	–	129,97	<0,01	92,22	0,00	4,32	3,22	–	3,21	6,65	–
S2	12,000	46,56	–	128,71	–	43,91	<0,01	123,89	0,01	2,65	5,69	–	4,82	9,64	–
K2	11,967	13,08	–	126,89	–	12,96	<0,01	119,92	0,02	0,12	0,94	–	6,97	13,90	–
GIJON															
N2	12,658	27,52	–	71,45	–	26,98	<0,01	70,17	0,01	0,54	1,97	–	1,28	2,70	–
M2	12,421	131,08	–	91,20	–	127,29	<0,01	91,59	0,00	3,79	2,89	–	−0,39	−0,81	–
S2	12,000	45,83	–	123,43	–	43,02	<0,01	122,90	0,01	2,81	6,14	–	0,53	1,06	–
K2	11,967	13,11	–	121,41	–	12,68	<0,01	119,01	0,02	0,43	3,30	–	2,40	4,79	–
CORUNHA–2															
N2	12,658	25,42	–	67,73	–	25,08	<0,01	66,14	0,01	0,34	1,34	–	1,59	3,35	–
M2	12,421	120,18	–	86,68	–	118,03	<0,01	87,05	0,00	2,15	1,79	–	−0,37	−0,77	–
S2	12,000	42,19	–	117,97	–	39,98	<0,01	117,34	0,01	2,21	5,24	–	0,63	1,26	–
K2	11,967	11,81	–	115,67	–	11,70	<0,01	113,58	0,02	0,11	0,94	–	2,09	4,17	–
LEIXOES															
N2	12,658	22,26	0,16	58,55	0,40	22,55	<0,01	55,64	0,01	−0,28	−1,28	0,17	2,91	6,14	0,41
M2	12,421	104,65	0,17	76,42	0,09	105,03	<0,01	75,21	0,00	−0,37	−0,36	0,18	1,21	2,50	0,09
S2	12,000	36,44	0,16	104,66	0,25	35,76	<0,01	103,17	0,01	0,67	1,85	0,17	1,49	2,98	0,26
K2	11,967	10,23	0,11	101,69	0,65	10,34	<0,01	100,61	0,02	−0,11	−1,08	0,12	1,08	2,15	0,67
PENICHE															
N2	12,658	21,94	0,15	51,57	0,44	22,13	0,01	51,30	0,01	−0,18	−0,83	0,16	0,27	0,57	0,45
M2	12,421	102,95	0,16	69,62	0,09	102,89	0,01	70,21	0,00	0,06	0,06	0,17	−0,59	−1,22	0,09
S2	12,000	35,77	0,14	96,99	0,27	35,17	0,01	97,15	0,01	0,60	1,68	0,15	−0,16	−0,32	0,28
K2	11,967	9,93	0,12	93,83	0,59	10,11	0,01	94,99	0,01	−0,18	−1,77	0,13	−1,16	−2,31	0,60
CASCAIS															
N2	12,658	21,20	0,13	46,95	0,34	21,36	0,01	46,90	0,01	−0,16	−0,75	0,14	0,05	0,11	0,35
M2	12,421	99,18	0,14	64,11	0,08	99,12	0,01	65,22	0,00	0,06	0,06	0,15	−1,11	−2,30	0,08
S2	12,000	34,91	0,13	90,71	0,22	34,08	0,01	90,54	0,00	0,83	2,38	0,14	0,17	0,34	0,22
K2	11,967	9,73	0,10	86,90	0,54	9,73	0,01	89,54	0,01	0,00	−0,01	0,11	−2,64	−5,27	0,55
SINES															
N2	12,658	21,33	0,17	46,58	0,52	21,53	<0,01	45,73	0,01	−0,20	−0,94	0,18	0,85	1,79	0,53
M2	12,421	99,21	0,15	63,61	0,10	99,88	<0,01	63,90	0,00	−0,67	−0,68	0,16	−0,29	−0,60	0,10
S2	12,000	34,90	0,18	90,15	0,28	34,34	<0,01	89,85	0,00	0,56	1,60	0,19	0,30	0,60	0,28
K2	11,967	9,52	0,13	86,91	0,79	9,79	<0,01	88,07	0,01	−0,27	−2,81	0,14	−1,16	−2,31	0,80
LAGOS															
N2	12,658	21,11	0,15	41,21	0,38	21,65	<0,01	41,57	0,00	−0,54	−2,54	0,16	−0,36	−0,76	0,38
M2	12,421	99,09	0,13	57,68	0,09	100,50	<0,01	59,16	0,00	−1,42	−1,43	0,14	−1,48	−3,06	0,09
S2	12,000	35,68	0,14	83,04	0,21	34,87	<0,01	84,49	0,00	0,82	2,29	0,15	−1,45	−2,90	0,21
K2	11,967	9,88	0,11	79,47	0,62	9,85	<0,01	82,60	0,01	0,03	0,27	0,12	−3,13	−6,24	0,63
HUELVA–5															
N2	12,658	22,51	–	41,83	–	22,33	<0,01	40,06	0,01	0,18	0,80	–	1,77	3,73	–
M2	12,421	104,97	–	57,99	–	103,58	<0,01	57,58	0,00	1,39	1,32	–	0,41	0,85	–
S2	12,000	38,47	–	85,16	–	35,88	<0,01	83,00	0,00	2,59	6,72	–	2,16	4,32	–
K2	11,967	10,76	–	83,01	–	10,10	<0,01	80,40	0,01	0,66	6,09	–	2,61	5,21	–
CASABLANCA															
N2	12,658	20,86	1,11	37,92	3,24	22,12	<0,01	37,74	0,00	1,26	6,02	1,12	−0,18	−0,38	3,24
M2	12,421	98,99	1,08	55,86	0,73	102,43	<0,01	54,84	0,00	3,44	3,47	1,09	−1,02	−2,11	0,73
S2	12,000	35,39	1,27	80,84	1,94	35,50	<0,01	79,48	0,00	0,11	0,30	1,28	−1,36	−2,72	1,94
K2	11,967	9,75	1,67	76,52	9,14	9,94	<0,01	78,25	0,01	0,19	1,91	1,68	1,73	3,45	9,15

Please cite this article as: Quaresma, L.S., Pichon, A., Modelling the barotropic tide along the West-Iberian margin, J. Mar. Syst. (2011), doi:10.1016/j.jmarsys.2011.09.016

The selected gauges were compared with their nearest grid point in the model. The eight tidal constituents were evaluated in amplitude and phase, expressed in Table 3 for semi-diurnal harmonics and Table 4 for diurnal. Confidence intervals were added to the harmonic parameters estimation (amplitude and phase), function of each record lengths and time-series noise (from Pawlowicz et al., 2002). The model accuracy was expressed by the differences between the simulated and the observed tide, at each tide-gauge location. It is important to point out that the interpretation of these differences should take into account the related confidence intervals.

Table 4
Accuracy evaluations of the model in the simulation of diurnal tidal constituents. This estimation was made by the differences of the harmonics parameters (amplitude and phase) between tide-gauge records and model results (at the nearest point). The biggest differences were shaded. For each calculated value a confidence interval size was added (estimation error). In the model accuracy column the errors correspond to the sum of the previous two confidence intervals (tide-gauge plus model).

Harmonics		**Tide gauge**				**Model**				**Model Accuracy**					
name	period (hours)	amplitude		phase		amplitude		phase		amplitude			phase		
		(cm)	error (cm)	(°)	error (°)	(cm)	error (cm)	(°)	error (°)	(cm)	%	error (cm)	(°)	(min)	error (°)
SAINT JEAN–DE LUZ															
Q1	26,867	2,27	0,11	267,27	2,99	2,36	< 0,01	269,19	0,07	−0,09	−3,97	0,12	−1,92	−8,60	3,06
O1	25,820	7,02	0,11	318,97	0,95	7,40	< 0,01	314,81	0,02	−0,38	−5,34	0,12	4,16	17,90	0,97
P1	24,067	1,93	0,12	54,84	2,78	1,69	< 0,01	59,77	0,11	0,24	12,32	0,13	−4,93	−19,78	2,89
K1	23,935	6,19	0,11	69,49	1,13	5,73	< 0,01	67,97	0,03	0,46	7,43	0,12	1,52	6,06	1,16
SANTANDER															
Q1	26,867	2,24	–	277,08	–	2,28	<0,01	268,99	0,07	−0,04	−1,76	–	8,09	36,23	–
O1	25,820	7,15	–	324,02	–	7,10	<0,01	316,69	0,02	0,05	0,66	–	7,33	31,54	–
P1	24,067	2,04	–	59,06	–	1,82	<0,01	62,42	0,11	0,22	10,71	–	−3,36	−13,48	–
K1	23,935	6,60	–	71,49	–	6,16	<0,01	69,86	0,03	0,44	6,70	–	1,63	6,50	–
GIJON															
Q1	26,867	2,10	–	280,00	–	2,21	<0,01	268,56	0,08	−0,11	−5,11	–	11,44	51,23	–
O1	25,820	7,03	–	323,96	–	6,83	<0,01	318,46	0,02	0,20	2,86	–	5,50	23,67	–
P1	24,067	2,24	–	59,22	–	1,93	<0,01	64,51	0,10	0,31	13,82	–	−5,29	−21,22	–
K1	23,935	6,83	–	70,69	–	6,52	<0,01	71,40	0,02	0,31	4,59	–	−0,71	−2,83	–
CORUNHA–2															
Q1	26,867	2,18	–	271,19	–	2,06	<0,01	266,21	0,07	0,12	5,53	–	4,98	22,30	–
O1	25,820	6,77	–	324,74	–	6,37	<0,01	319,84	0,02	0,40	5,84	–	4,90	21,09	–
P1	24,067	2,38	–	60,77	–	2,12	<0,01	64,36	0,08	0,26	11,12	–	−3,59	−14,40	–
K1	23,935	7,67	–	73,21	–	7,18	<0,01	70,95	0,02	0,49	6,39	–	2,26	9,02	–
LEIXOES															
Q1	26,867	1,95	0,11	274,73	3,18	1,96	<0,01	262,93	0,07	−0,01	−0,47	0,12	11,80	52,84	3,25
O1	25,820	6,18	0,11	318,15	1,03	6,10	<0,01	316,98	0,02	0,08	1,27	0,12	1,17	5,03	1,05
P1	24,067	2,08	0,14	49,85	3,97	1,99	<0,01	56,58	0,09	0,08	3,98	0,15	−6,73	−27,00	4,06
K1	23,935	6,86	0,12	60,71	0,98	6,83	<0,01	62,36	0,02	0,02	0,36	0,13	−1,65	−6,58	1,00
PENICHE															
Q1	26,867	1,84	0,08	269,35	3,16	1,94	<0,01	257,45	0,07	−0,10	−5,40	0,09	11,90	53,29	3,23
O1	25,820	6,21	0,10	314,47	0,91	6,29	<0,01	314,44	0,02	−0,07	−1,20	0,11	0,03	0,13	0,93
P1	24,067	2,35	0,11	47,23	2,66	2,18	<0,01	57,53	0,08	0,17	7,06	0,12	−10,30	−41,32	2,74
K1	23,935	7,49	0,09	55,56	0,76	7,42	<0,01	62,92	0,02	0,08	1,01	0,10	−7,36	−29,36	0,78
CASCAIS															
Q1	26,867	2,06	0,06	262,30	1,71	1,87	<0,01	258,33	0,08	0,19	9,22	0,07	3,97	17,78	1,79
O1	25,820	5,93	0,06	314,84	0,61	5,93	<0,01	312,95	0,02	−0,01	−0,11	0,07	1,89	8,13	0,63
P1	24,067	2,16	0,08	44,03	2,07	1,97	<0,01	52,93	0,08	0,20	9,06	0,09	−8,90	−35,70	2,15
K1	23,935	6,93	0,06	54,13	0,51	6,75	<0,01	58,44	0,02	0,18	2,55	0,07	−4,31	−17,19	0,53
SINES															
Q1	26,867	1,95	0,06	265,81	1,85	1,89	<0,01	257,60	0,08	0,06	3,09	0,07	8,21	36,76	1,93
O1	25,820	6,05	0,07	314,39	0,54	6,02	<0,01	311,51	0,02	0,03	0,42	0,08	2,88	12,39	0,56
P1	24,067	2,19	0,07	45,08	1,81	1,96	<0,01	51,98	0,08	0,23	10,28	0,08	−6,90	−27,68	1,89
K1	23,935	6,85	0,07	55,14	0,52	6,75	<0,01	57,57	0,02	0,10	1,47	0,08	−2,43	−9,69	0,54
LAGOS															
Q1	26,867	1,96	0,07	252,21	2,34	1,84	<0,01	255,29	0,08	0,12	6,12	0,08	−3,08	−13,79	2,42
O1	25,820	5,93	0,08	309,56	0,78	5,95	<0,01	308,11	0,02	−0,01	−0,21	0,09	1,45	6,24	0,80
P1	24,067	2,24	0,10	40,56	2,23	1,89	<0,01	47,55	0,08	0,35	15,73	0,11	−6,99	−28,04	2,31
K1	23,935	6,71	0,08	48,92	0,71	6,50	<0,01	53,26	0,02	0,21	3,14	0,09	−4,34	−17,31	0,73
HUELVA–5															
Q1	26,867	1,83	–	265,12	–	1,86	<0,01	256,17	0,11	−0,03	−1,90	–	8,95	40,08	–
O1	25,820	6,12	–	311,52	–	6,12	<0,01	305,52	0,03	0,00	−0,02	–	6,00	25,82	–
P1	24,067	2,51	–	42,28	–	1,73	<0,01	43,61	0,11	0,78	31,20	–	−1,33	−5,33	–
K1	23,935	6,81	–	50,38	–	5,98	<0,01	49,66	0,04	0,83	12,15	–	0,72	2,87	–
CASABLANCA															
Q1	26,867	1,70	0,28	253,43	9,03	1,95	<0,01	252,92	0,07	0,25	14,94	0,29	−0,51	−2,28	9,10
O1	25,820	5,83	0,33	309,93	2,55	6,05	<0,01	305,34	0,02	0,22	3,79	0,34	−4,59	−19,75	2,57
P1	24,067	2,04	0,23	38,72	7,24	1,83	<0,01	48,53	0,09	−0,21	−10,38	0,24	9,81	39,35	7,33
K1	23,935	6,76	0,26	48,15	2,16	6,30	<0,01	54,41	0,02	−0,46	−6,82	0,27	6,26	24,97	2,18

Please cite this article as: Quaresma, L.S., Pichon, A., Modelling the barotropic tide along the West-Iberian margin, J. Mar. Syst. (2011), doi:10.1016/j.jmarsys.2011.09.016

The model revealed a very good performance, especially in the semi-diurnal constituents. Generally, each semi-diurnal harmonic was reproduced with amplitude errors lower than 1 cm (corresponding to an amplitude percentage lower than 3%) and phase mismatch shorter than 5 min (equivalent to less than 2.5°). Exception must be pointed out to the S2 constituent, with a slightly higher amplitude error over the Spanish coast, ~2.5 cm (equivalent to 6%). The fact that both Casablanca and Saint Jean-de-Luz evidenced lower S2 mismatch reflects a probable discrepancy in the adopted harmonic analysis methods (between the one used in the present work and the method used by Puertos del Estado) or a sensitive result to less accurate bathymetry data detained by WIBM2009 over the Northern Spanish continental margin (Section 2.3).

The model was less accurate in the simulation of the diurnal constituents. Amplitudes were reproduced with errors lower than 0.5 cm (corresponding to amplitude percentage lower than ~10%). However, phase discrepancies exceeded 30 min in some cases (corresponding to phase differences > 7°). These mismatches were higher near the open boundaries and reflect tide solutions inaccuracies transposed from the adopted Global models (Section 2.4). Nevertheless, the obtained accuracy was globally superior to previous literature results. This gave credit to the bathymetry improvement and to the polychromatic tidal forcing option.

3.2. Tidal currents

Four shallow water current profile measurements were used to validate the barotropic tidal velocities simulated by the model (Table 2). *In situ* and numerical time-series were evaluated by harmonic analysis. The resulting current velocity ellipses were compared for the major tidal constituents (Figs. 5, 6 and 7). The short ADCP record lengths (under 40 days) restricted this evaluation to the following semi-diurnal harmonics: M2, S2 and N2. The diurnal tidal ellipses are very small, of the order of a few millimetres per second. These values are near the threshold precision of the ADCP measurement and smaller than the adopted accuracy of the model (1 $cm.s^{-1}$). Exception was made to the MITIC record, where the diurnal velocity is magnified over the Tagus Plateau. However, the short record length and the high noise level disabled a precise evaluation of the K1 ellipse. For these reasons, diurnal ellipses were not evaluated.

The M2 current velocity was reproduced highly accurate over the shelf, generally matching the semi-major and semi-minor axis magnitude, orientation, phase and sense of rotation of the ellipses (Fig. 6). The small differences in the shape of each ellipse can be attributed to missing topographic detail within the 1-arc minute model resolution, as discussed next.

The HERMIONE simulated M2 ellipse differed only in the semi-minor axis magnitude and consequently shows higher eccentricity than the *in situ* observation. This is a direct consequence of the adopted model resolution, which transforms the narrow Nazaré canyon head into a deep channel that funnels the local tidal circulation.

The MITIC simulation reproduced the increase of the M2 current velocity magnitude, as well as the clockwise rotation sense, induced by the Tagus plateau configuration. However, a small difference exists in the ellipse orientation and phase. These two mismatches are linked and put in evidence a similar lack in topographic detail. This deduction comes from the existing correlation between the ellipse orientation, β, and the velocity phase, G, by $\beta = G + atan\ (i_p/r_p)$, where i_p and r_p are the trigonometric coefficients obtained by harmonic analysis.

ASPEX and SIRIA simulations highlighted the effective performance of the model in the reproduction of M2 tidal flow. Both model and observed ellipses match, with axis length error <5%, orientation error <5° and phase error <10° (Fig. 5).

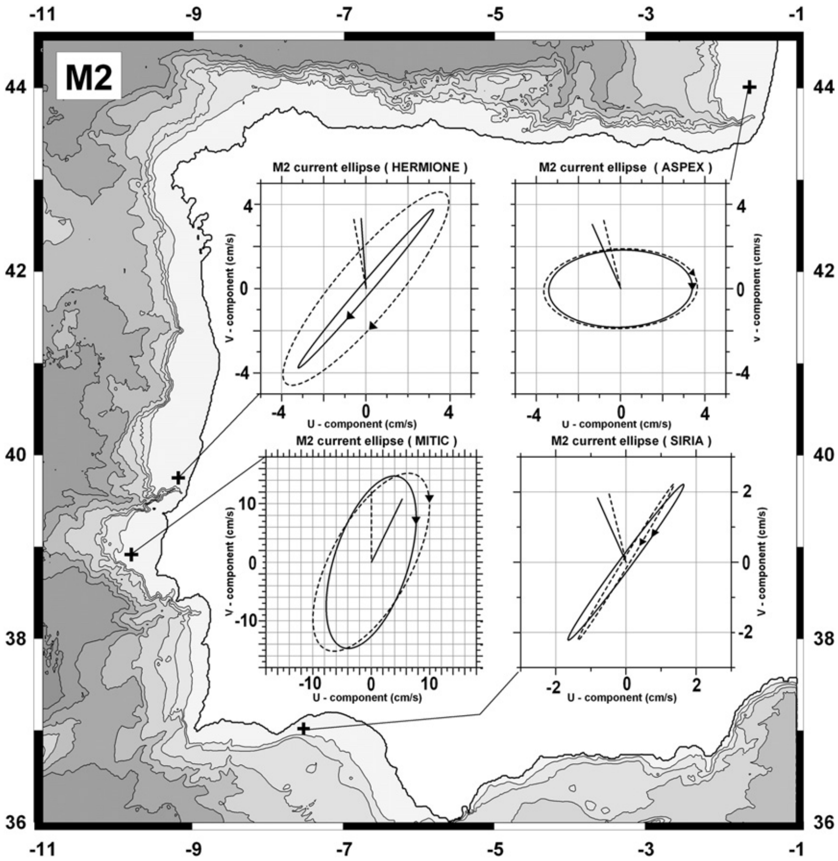

Fig. 5. Validation of the M2 tidal current simulated by the model. The tidal ellipses were obtained from ADCP datasets (dashed line) are compared with model results (solid line). The velocity phase is represented by the vector orientation (in polar coordinates) and the sense of rotation by the arrow.

Please cite this article as: Quaresma, L.S., Pichon, A., Modelling the barotropic tide along the West-Iberian margin, J. Mar. Syst. (2011), doi:10.1016/j.jmarsys.2011.09.016

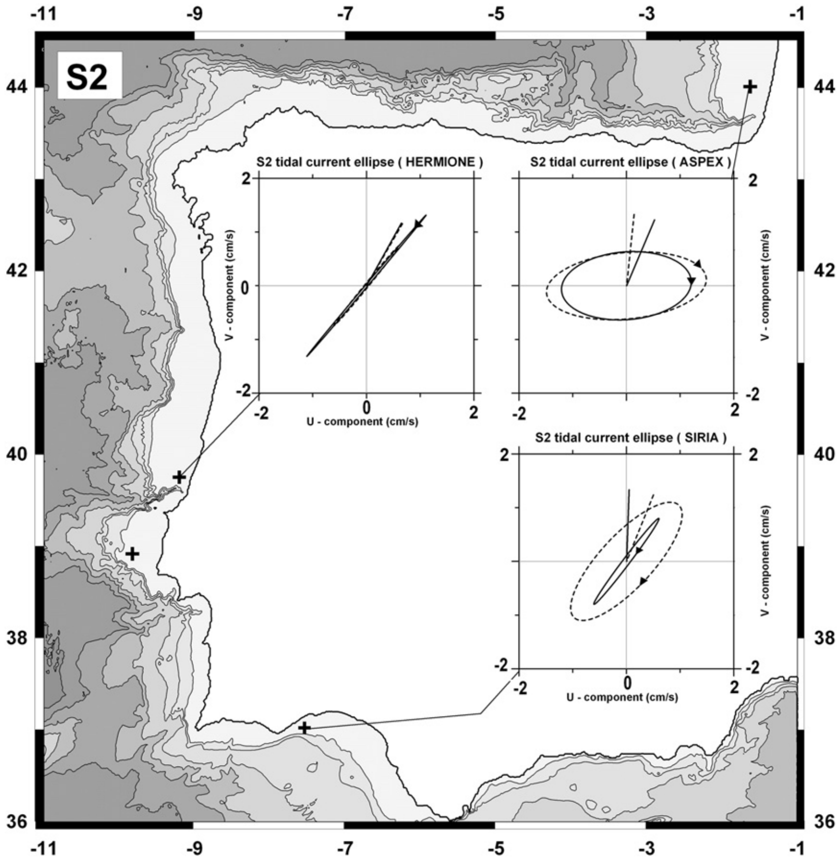

Fig. 6. Validation of the S2 tidal current simulated by the model. The tidal ellipses were obtained from ADCP datasets (dashed line) are compared with model results (solid line). The velocity phase is represented by the vector orientation (in polar coordinates) and the sense of rotation by the arrow. The short MITIC's time-series (~6 days) disables the estimation of the S2 constituent.

Model results also showed a fair reproduction of S2 and N2 tidal current velocity constituents (Figs. 6 and 7). Here, the model performance was difficult to evaluate since these velocities are very small (~1 cm.s^{-1}). The critical parameter is the ellipse's eccentricity, which is very sensitive to small-scale topographic details (hidden within the present model resolution).

4. Results

The accuracy of the model reveals a successful simulation of the barotropic tide, along the West-Iberian continental margin. The harmonic analysis of one-years simulation was assembled to construct tidal maps around the domain. The solution is hereafter evaluated by spatial analyses of the sea-surface height and barotropic tidal flow.

The tide shows a dual behaviour, distinct between semidiurnal and diurnal harmonics. This contrast is a function of the local inertial period $T_f = 2\pi/f$, that varies from ~17 h (45° N) to ~20.5 h (36° N) and divides the polychromatic tidal spectrum into a super-inertial (semi-diurnal constituents) and a sub-inertial group (diurnal constituents). N2, M2, S2 and K2 exhibit similar sea-surface amplitude and flow variability, differing from each other primarily in magnitude and phase values. In an analogous way, Q1, O1, P1 and K1 share the same intra-group behaviour, with different magnitude and phase values. From this, M2 and K1 were chosen to illustrate the distinct super-inertial and sub-inertial spatial structures. A zoom was made over the West-Iberian margin, from 36° to 45° N and from 6° to 13° W (study region).

4.1. Semidiurnal tide

Along the West-Iberian coast, the M2 is the most energetic tidal constituent, with sea surface amplitude (η ~1.0 m) and phase increasing from south to north (Fig. 8). Across-shelf, the amplitude decreases offshore with a mean gradient of ~0.027 cm.km^{-1}. Co-tidal lines are almost perpendicular to the coast, skirting regularly the continental margin, with a mean phase velocity of C_{M2} ~245 m.s^{-1} (calculated from numerical solution, between Cape of Sagres, 37° N, and Cape of Finisterra, 43° N). Offshore, the M2 velocity component perpendicular to the coast is almost inexistent and the ellipses are extremely eccentric, aligned tangentially to the West-Iberian margin (Fig. 10). These characteristics suggest a semi-diurnal tidal wave trapped as a Kelvin mode around the narrow West-Iberian shelf. This foremost tidal constituent is followed, with the same behaviour and spatial structure, by S2 (η ~ 0.35 m), N2 (η ~0.22 m) and K2 (η ~0.10 m).

The shelf width is determinant in the tidal wave amplitude and current velocity magnitude (Battisti and Clarke, 1982). For example, the M2 amplitude is smaller in the southern region (η <1 m), revealing locally the almost absent shelf. On the other hand, M2 is amplified along the wider northern Portuguese margin (η >1 m), especially over the Tagus plateau (η ~1.03 m) where the shelf reaches its maximum width (65 km).

The Bay of Biscay confines the tidal wave, forcing the amplification of the semi-diurnal constituents towards the French Armorican shelf. This semi-enclosed sea effect generates a strong amplitude gradient along the North-Iberian margin and especially at the Galician shelf (varying from η ~1.05 m at Leixões to η ~1.30 m at Gijon). A similar effect, in smaller proportions, is observed inside the Gulf of Cadiz (η ~1.05 m).

Over the slope and shelf, where the tidal phase velocity is not in balance with the varying depth, the Kelvin semi-geostrophic equilibrium breaks apart and the cross-shelf velocity component appears. This gives rise to rotary tidal currents in cyclonic sense. The ellipse eccentricity decreases as function of the shelf slope (Fig. 9).

Please cite this article as: Quaresma, L.S., Pichon, A., Modelling the barotropic tide along the West-Iberian margin, J. Mar. Syst. (2011), doi:10.1016/j.jmarsys.2011.09.016

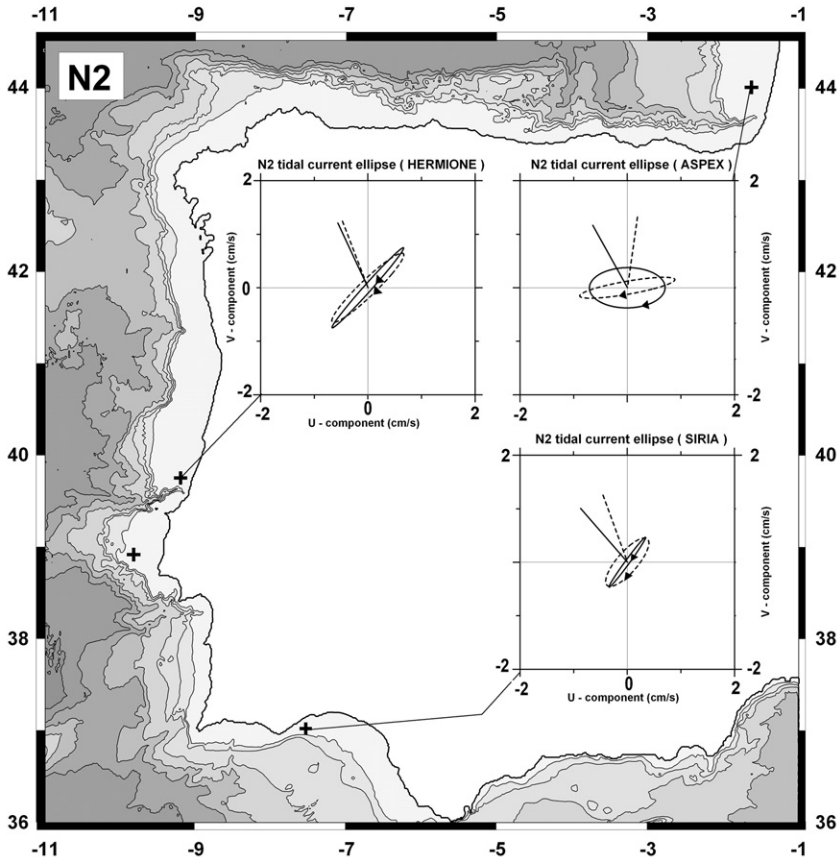

Fig. 7. Validation of the N2 tidal current simulated by the model. The tidal ellipses were obtained from ADCP datasets (dashed line) are compared with model results (solid line). The velocity phase is represented by the vector orientation (in polar coordinates) and the sense of rotation by the arrow. The short MITIC's time-series (~6 days) disables the estimation of the S2 constituent.

Along-shelf, the semi-diurnal velocities show higher spatial variability than sea-surface amplitudes. The current is magnified (Fig. 10) and changes the rotation sense to anti-cyclonic (Fig. 9), over the major shelf-width anomalies (as submarine canyons and promontories). The same behaviour is observed around important Capes as Finisterra and Sagres, as well as over the nearby seamounts (Gorringe and Galicia banks). This effect seems to be linked to the fluid vorticity production over the strong along-shelf slopes that surround these topographic features.

4.2. Diurnal tide

The principal diurnal constituents are less energetic than the semi-diurnal. Nevertheless, they contribute significantly to the modulation of the tide along the domain (mainly forced by O1 and K1). The amplitude ratio between the semi-diurnal and diurnal group is smaller here than in nearby coastal regions, like in the Bay of Biscay (LeCann, 1990) or in the Gulf of Cadiz. The diurnal tidal amplitude grows from south to north, with maximums located at the Galician shelf and over the Tagus plateau (reaching $\eta = 7.4$ cm for K1). Its phase speed is locally lower than for the semi-diurnal tide (C_{K1} ~ 198 m.s^{-1}). Another important difference is the distortion of the diurnal cotidal lines, especially over the Portuguese shelf (Fig. 12). This fact results from the settling of continental shelf waves, trapped along the northern Portuguese coast. Their patterns are visible in K1 amplitudes (Fig. 12) and in current velocity phases (Fig. 15). This process is discussed in Section 5.

Diurnal tidal velocities are almost inexistent offshore (Fig. 13). They become measurable over the shelf and, like for the semi-diurnal constituents, are magnified over the major shelf width anomalies, capes and seamounts (Fig. 14). The diurnal ellipses are anti-cyclonic, as consequence of the sub-inertial forcing. The Q1, O1, P1 current velocities evidence similar spatial distribution as K1, different in magnitude but following the same ratio as presented in Fig. 2.

5. Analysis

Model results highlight complex tidal structures along the West-Iberian margin (Figs. 9–16). The large-scale tidal wave (propagating mainly in a Kelvin mode) runs along a narrow continental shelf, where the non-uniform depth gives rise to a wide set of possible coastal trapped modes (Huthnance, 1975). These modes are discrete solutions of the momentum and continuity equations, obtained in the frequency/wave number space [ω, k]. The trapping condition is defined by Eq. (5) and is translated by an offshore decay of the wave amplitude,

$$\omega/f < \sqrt{1 + gHk^2 f^{-2}} \quad (5)$$

For tidal forcing modes, the frequencies are fixed (harmonic constituents) and the wave number solutions, k, (or wavelengths by $\lambda = 2\pi/k$) are obtained as eigenvalues of the corresponding wave dispersion relationships (cross-shelf profile dependent).

The wave trapping is naturally ruled by the inertial frequency, f. This physical limit splits the full set of possible wave modes in two distinct domains: 1. Sub-inertial modes governed by the potential-vorticity conservation restoring force (continental shelf waves) and 2. Super-inertial modes governed mainly by gravity (edge waves). The Kelvin mode makes the exception, coexisting in both frequency domains ($0 < \omega < \infty$) and simultaneously verifying the

Please cite this article as: Quaresma, L.S., Pichon, A., Modelling the barotropic tide along the West-Iberian margin, J. Mar. Syst. (2011), doi:10.1016/j.jmarsys.2011.09.016

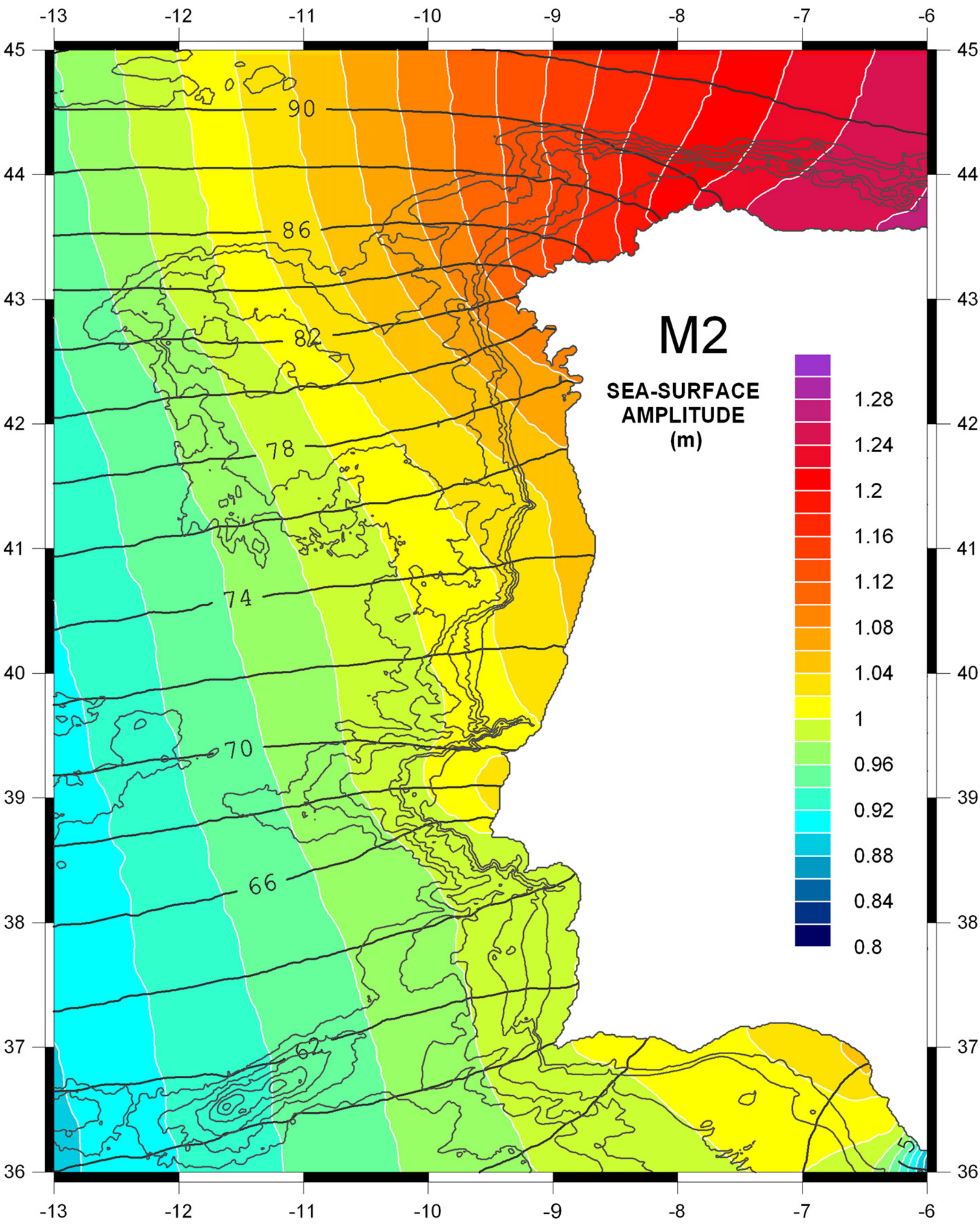

Fig. 8. M2 sea-surface amplitude map. Amplitude (m) is represented by the colour contour and phase (degrees referenced to GMT) by black line contour. Isobaths of 200 m, 500 m, 1000 m, 2000 m, 3000 m and 4000 m were added to help interpretation.

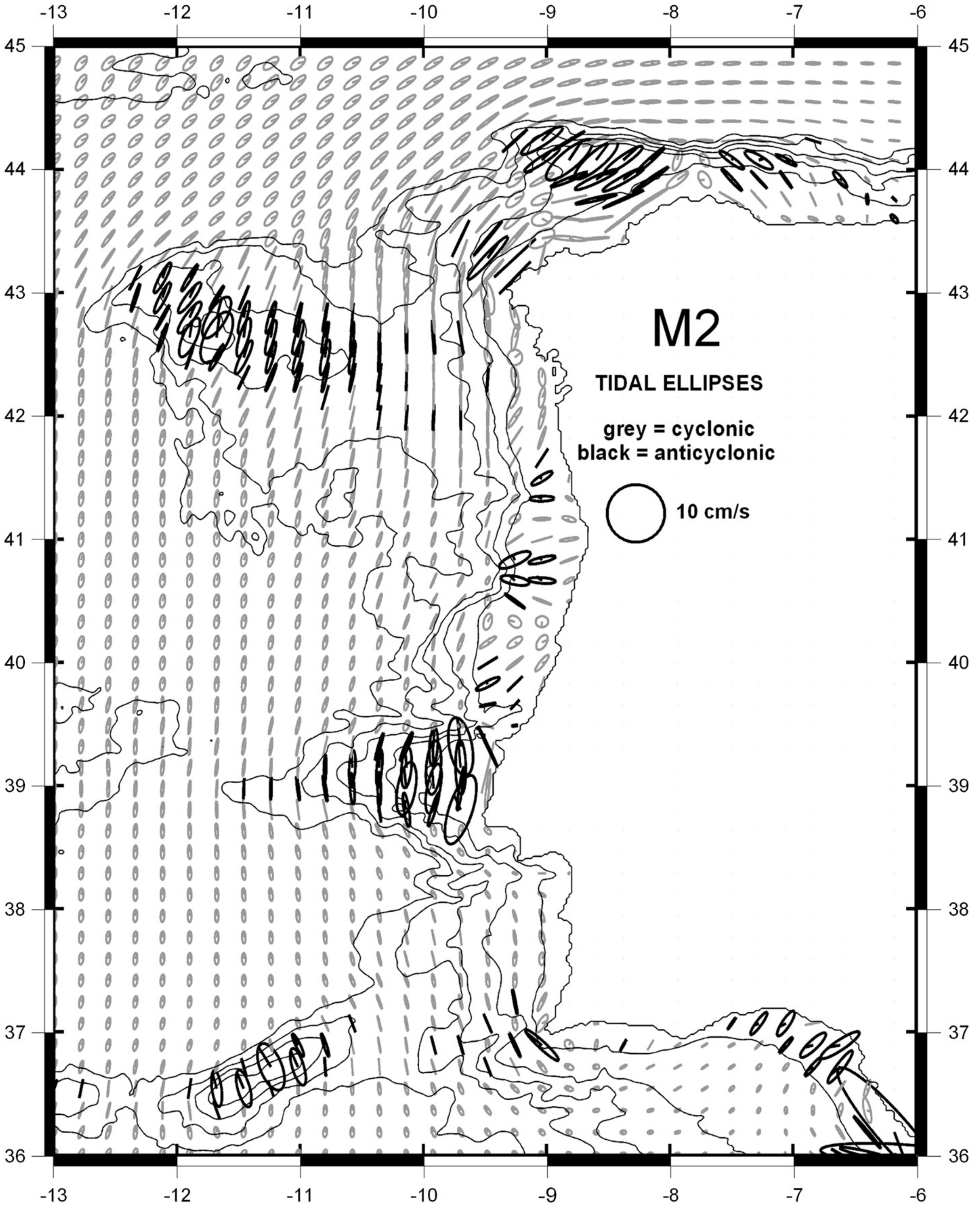

Fig. 9. M2 tidal ellipses map. The grey ellipses represent cyclonic rotation and the bold ellipses anti-cyclonic. The polar axis, traced inside each ellipse, represents the velocity phase and translates the M2 velocity vector at the same instance. Isobaths of 200 m, 500 m, 1000 m, 2000 m, 3000 m and 4000 m were added to help interpretation.

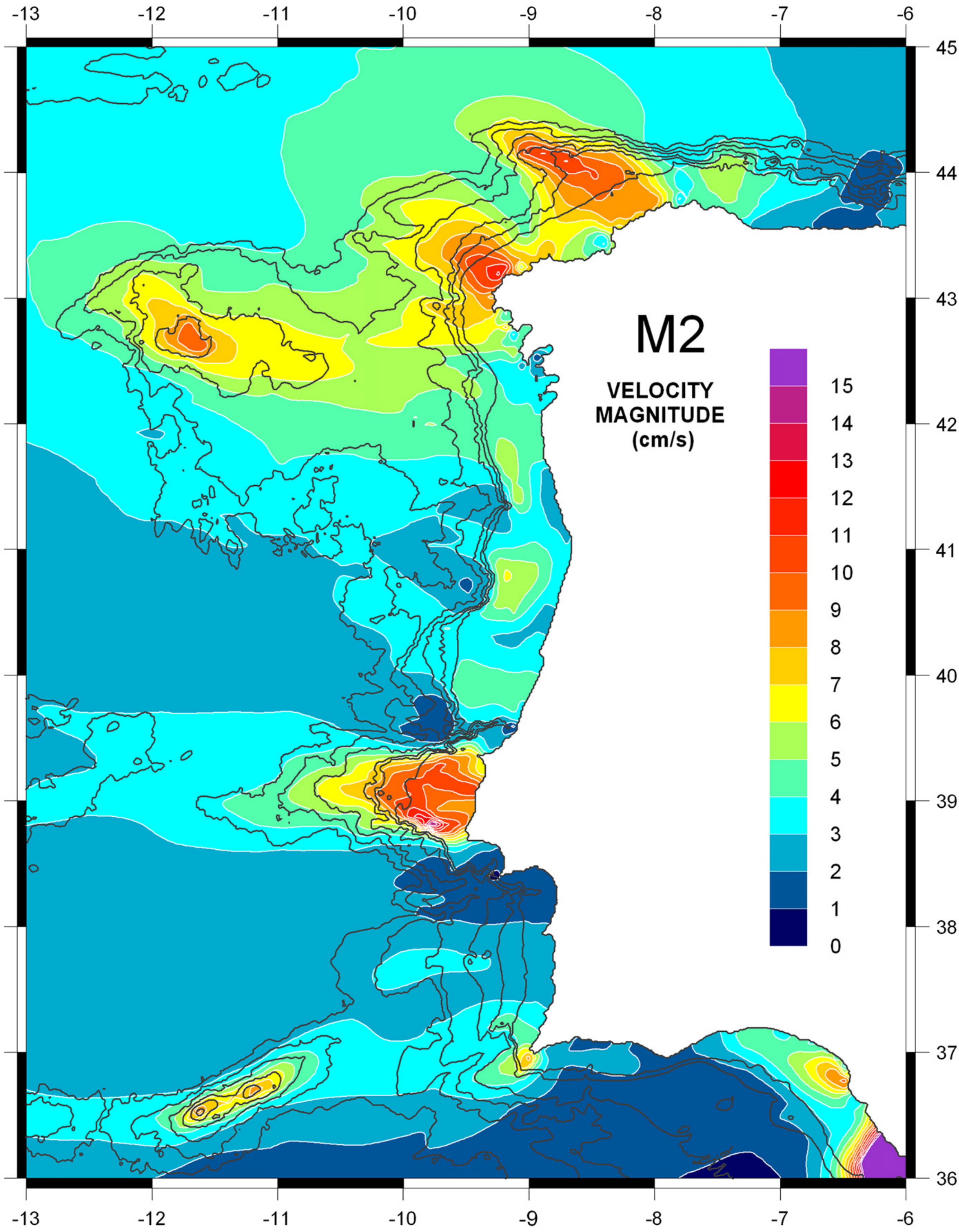

Fig. 10. M2 barotropic current velocity map. The maximum M2 velocities (cm.s^{-1}) are illustrated by the tidal ellipse semi-major axis magnitude. Isobaths of 200 m, 500 m, 1000 m, 2000 m, 3000 m and 4000 m were added to help interpretation.

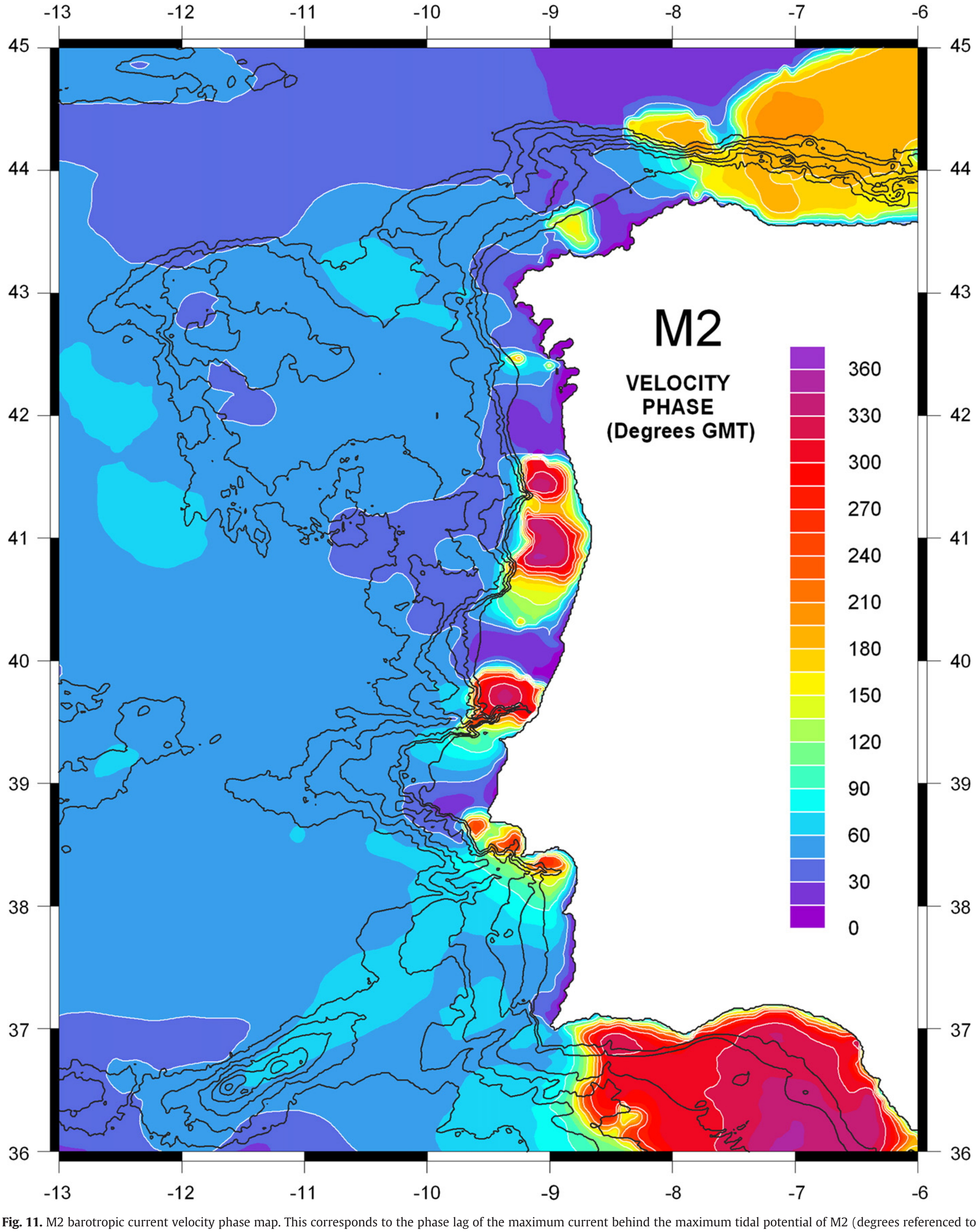

Fig. 11. M2 barotropic current velocity phase map. This corresponds to the phase lag of the maximum current behind the maximum tidal potential of M2 (degrees referenced to GMT). Isobaths of 200 m, 500 m, 1000 m, 2000 m, 3000 m and 4000 m were added to help interpretation.

Please cite this article as: Quaresma, L.S., Pichon, A., Modelling the barotropic tide along the West-Iberian margin, J. Mar. Syst. (2011), doi:10.1016/j.jmarsys.2011.09.016

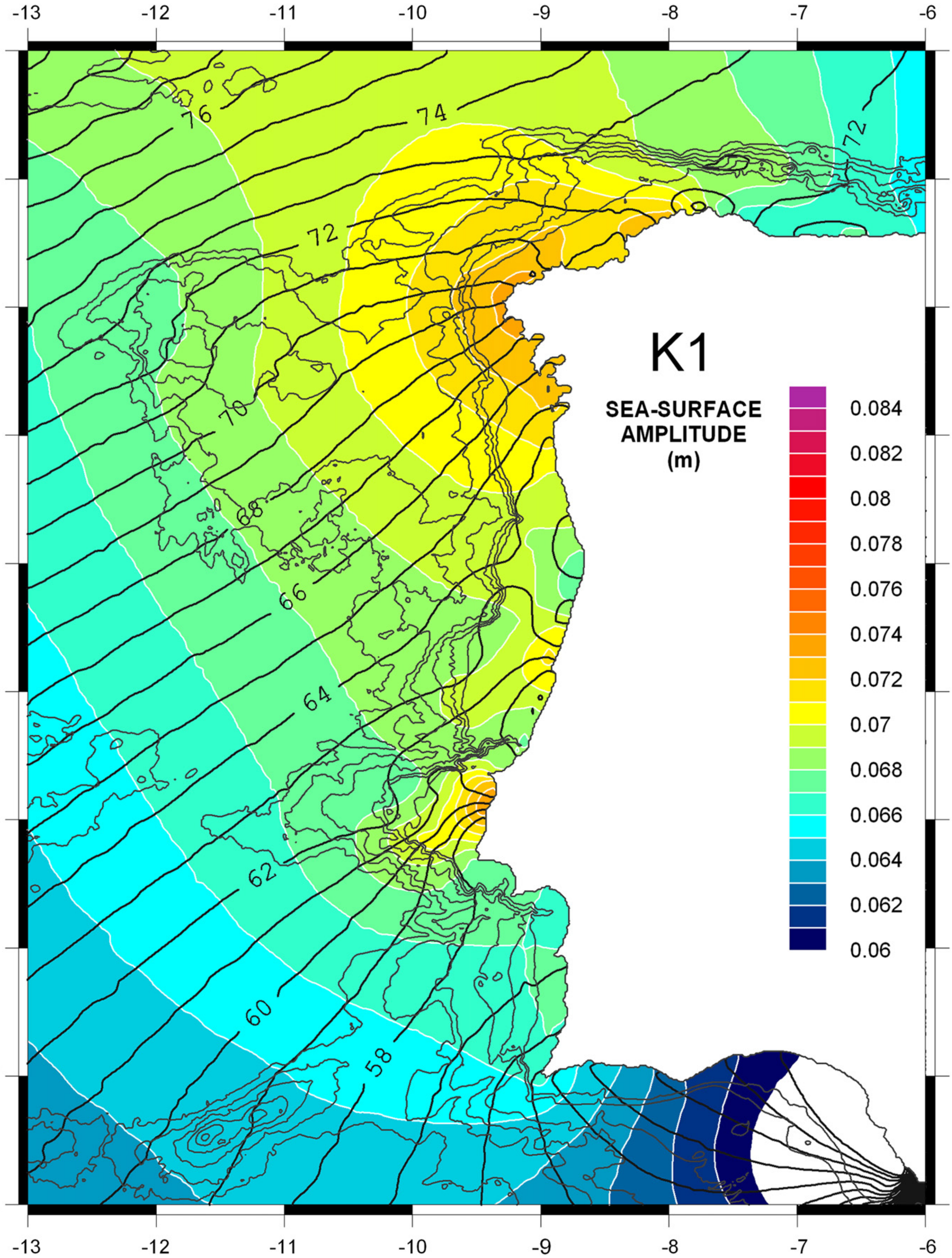

Fig. 12. K1 sea-surface amplitude chart. Amplitude (m) is represented by the colour contour and phase (degrees referenced to GMT) by black line contour. Isobaths of 200 m, 500 m, 1000 m, 2000 m, 3000 m and 4000 m were added to help interpretation.

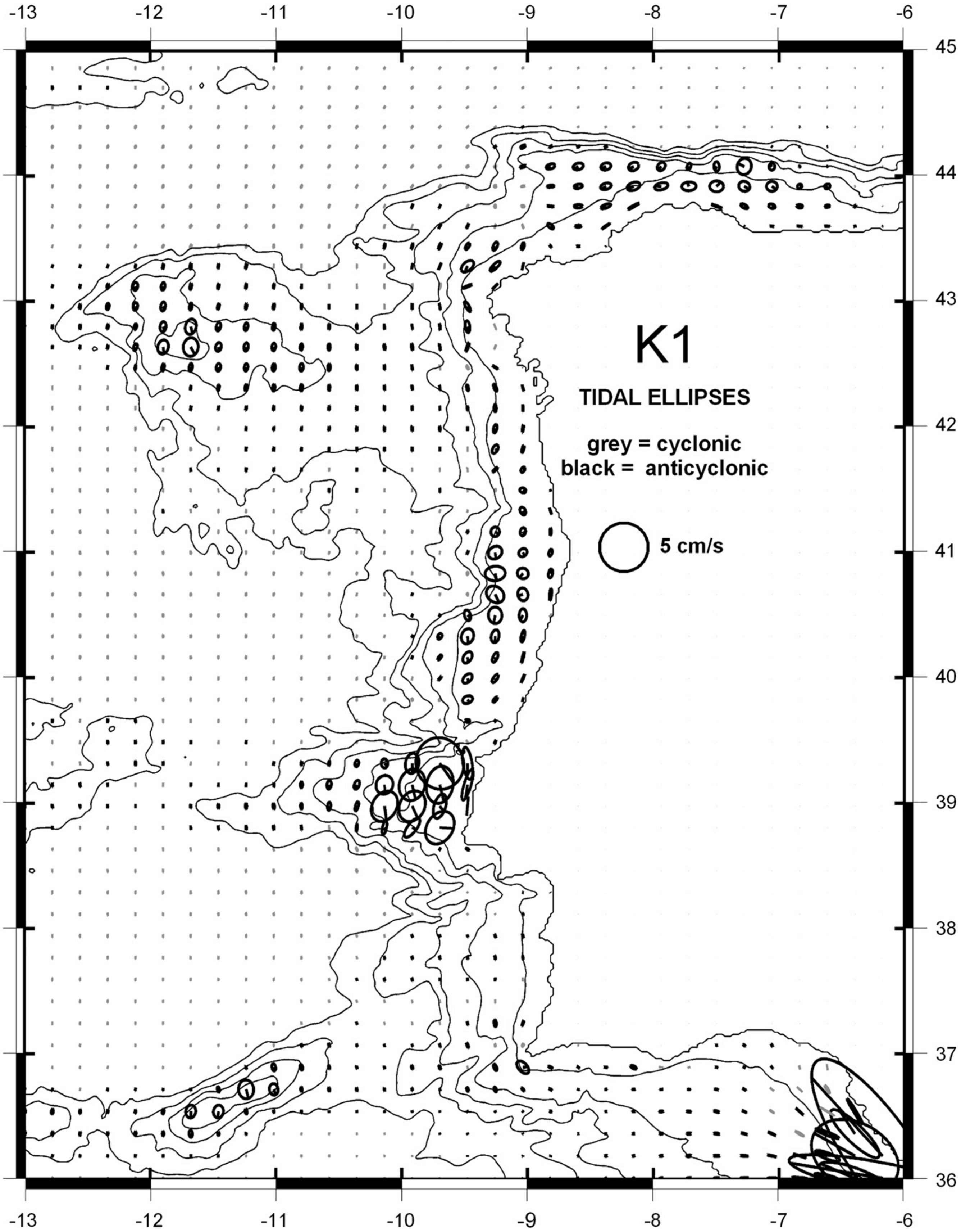

Fig. 13. K1 tidal ellipses map. The grey ellipses represent cyclonic rotation and the bold ellipses anti-cyclonic. The polar axis, traced inside each ellipse, represents the velocity phase and translates the M2 velocity vector at the same instance. Isobaths of 200 m, 500 m, 1000 m, 2000 m, 3000 m and 4000 m were added to help interpretation.

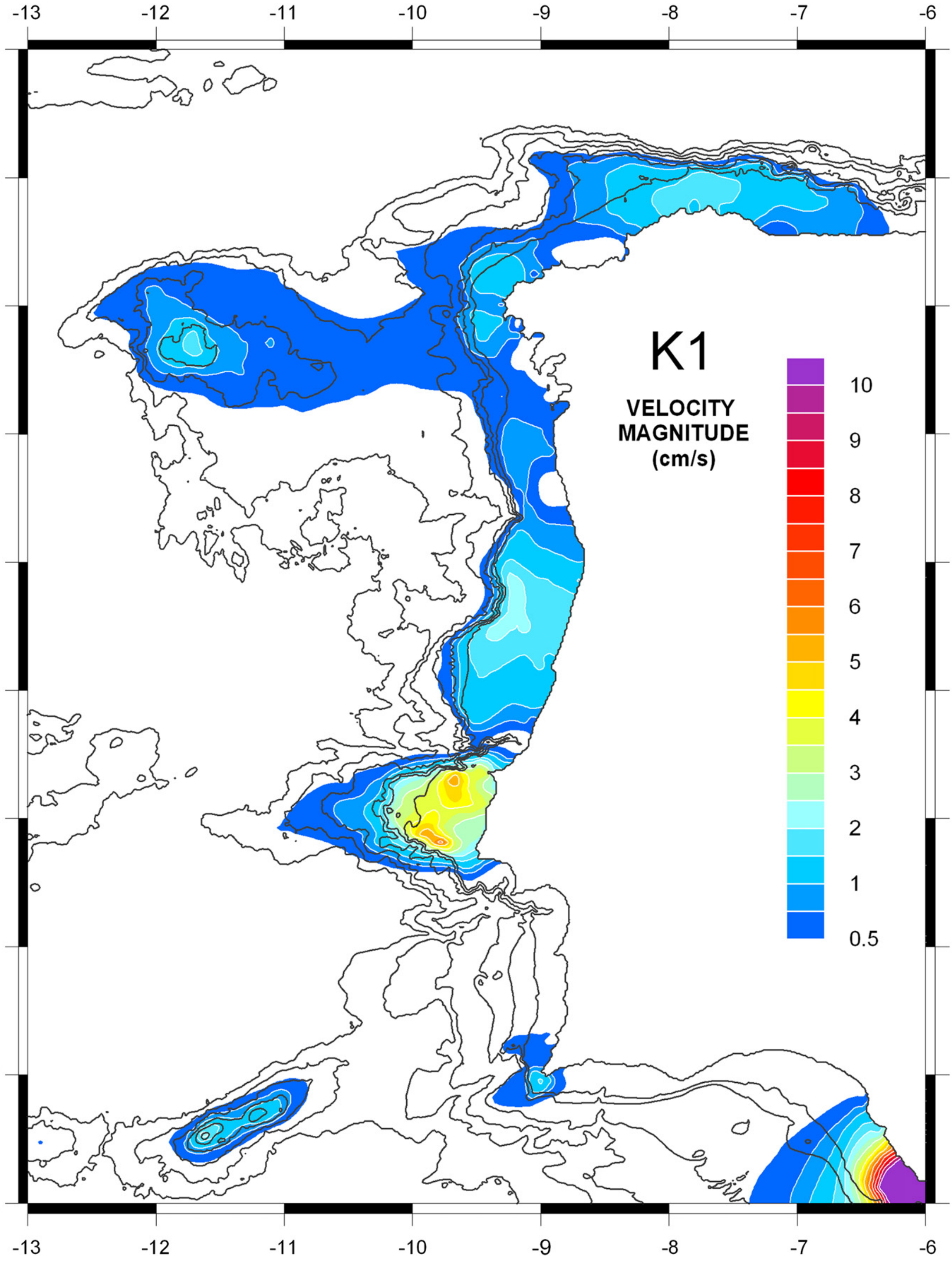

Fig. 14. K1 barotropic current velocity map. The maximum M2 velocities (cm.s^{-1}) are illustrated by the tidal ellipse semi-major axis magnitude. Isobaths of 200 m, 500 m, 1000 m, 2000 m, 3000 m and 4000 m were added to help interpretation.

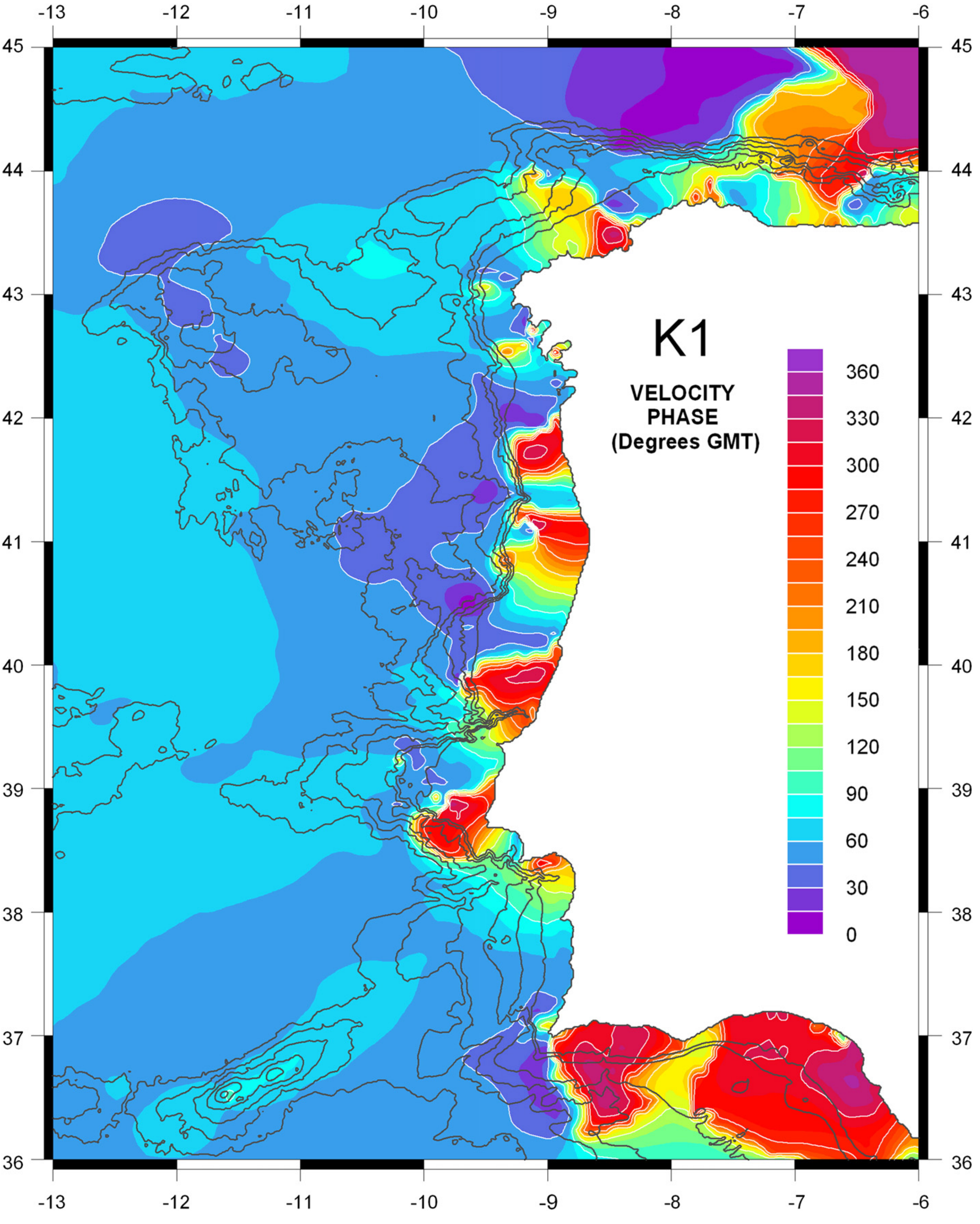

Fig. 15. K1 barotropic current velocity phase map. This corresponds to the phase lag of the maximum current behind the maximum tidal potential of M2 (degrees referenced to GMT). Isobaths of 200 m, 500 m, 1000 m, 2000 m, 3000 m and 4000 m were added to help interpretation.

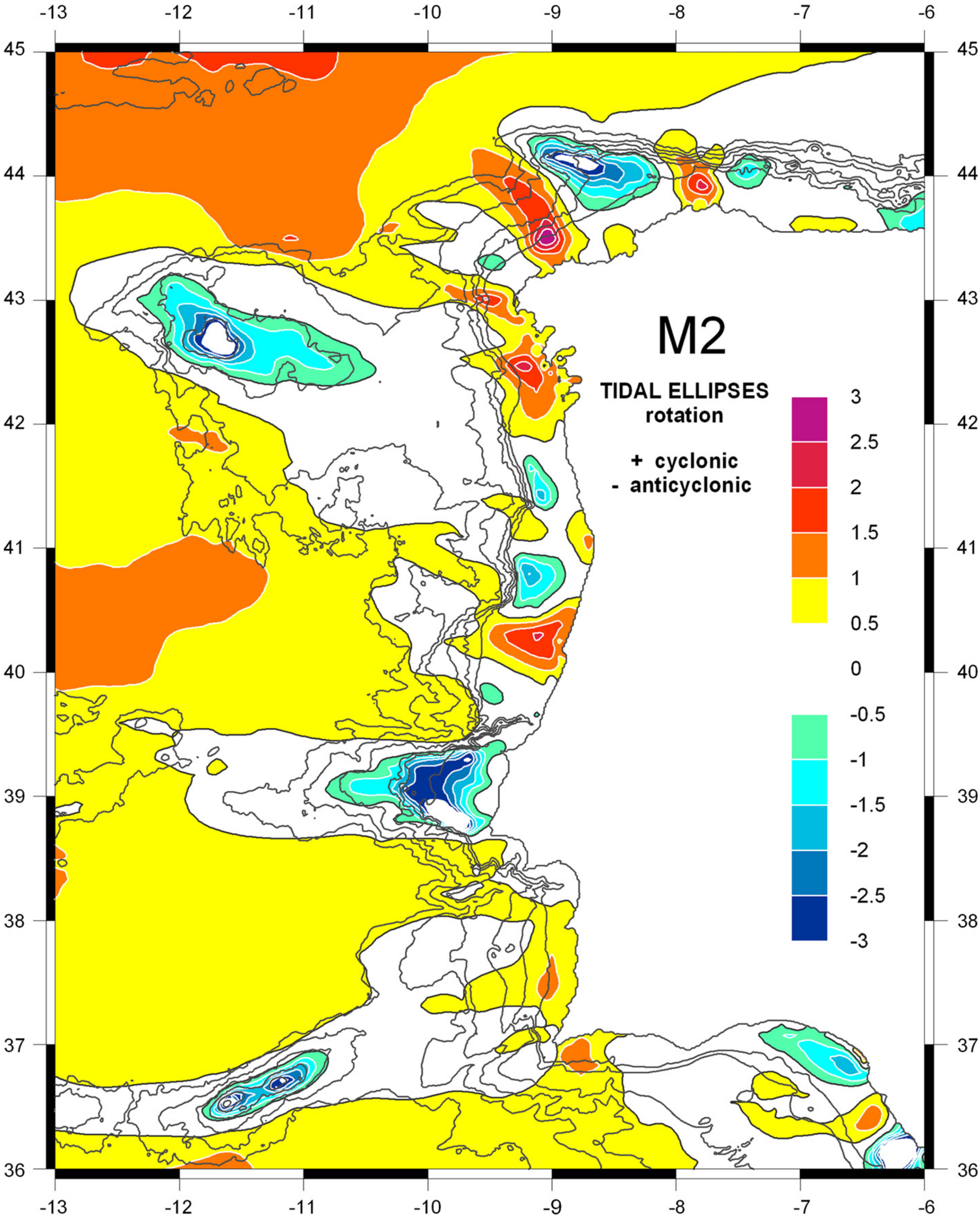

Fig. 16. M2 tidal ellipses rotation sense map. The tidal ellipse semi-minor axis sign illustrates rotation sense: positive = counter-clockwise (cyclonic); negative = clockwise (anti-cyclonic). Notice that negative values over the main topographic features are saturated in colour-scale. Isobaths of 200 m, 500 m, 1000 m, 2000 m, 3000 m and 4000 m were added to help interpretation.

trapping condition. This fundamental solution is obtained by imposing a flat ocean bottom, bounded by a straight wall. As a result, the dispersion relationship, $\omega^2 = gHk^2$ (6), is independent of f and the wave gets a linear solution in the space [ω, k], simply function of a constant depth.

Over the continental margin, the shallowing depth unbalances the Kelvin wave velocity and other modes appear, function of the forcing frequency, with wavelengths dependent of the cross-shelf profile. These modes are discussed in the next sections for each frequency domain.

5.1. Diurnal continental shelf waves

Sub-inertial trapped waves are observed along sloping margins with small offshore wave numbers, progressing along-shelf in a cyclonic sense around the deep-sea (Robinson, 1964). Continental Shelf Waves (CSW) usually calls the respective barotropic solution. Over the study region, diurnal tides are sub-inertial forcing frequencies ($\omega < f$) and can be source of these discrete sub-inertial trapped modes. This scenario is real for latitudes higher than 30° N, where f equals the diurnal tidal frequency and increases its value towards the North.

Model results suggested the presence of diurnal CSW, trapped along the West-Iberian margin, from the Tagus Plateau (39º N) towards the North. This suggestion was based on the small-scale spatial variability of the diurnal sea-surface amplitudes (large wave number structures) confined along the Portuguese northern shelf (Fig. 12). The same variability was shown in the current velocity magnitude (Fig. 14) and current velocity phase (Fig. 15). The generation seems to be linked to the abrupt coastal bathymetry features since they represent important obstacles to the tidal wave propagation. Fortunato et al. (2002) studied numerically this hypothesis and pointed out the topographic interception of the Tagus Plateau as the trigger of the observed CSW. These authors noticed also the importance of the shelf width and slope strength in the growing amplitude of the trapped wave mode.

To test the previous deductions and to validate present model results, simple analytical approach (Larsen, 1969) was applied to calculate the CSW long-shore wave number, k, and to verify it's trapping condition. The northern Portuguese margin was simplified into a step shelf of constant depth ($h_1 = 200$ m) bounded by a straight coastline and a flat abyssal plain ($h_2 = 4000$ m). The shelf width was set to vary from $L = 30$ km to $L = 50$ km. The analytical dispersion relationship turns into:

$$\frac{\omega}{f} = -\frac{h_2 - h_1}{h_1 + h_2 \coth(kL)} \tag{7}$$

The local scaled K1 frequency is [ω/f]~0.78 and the horizontal scale length, L, limited by the shelf width (verified by Fig. 15). Applying Eq. (7) to these shelf characteristics, the CSW long-shore wave number varies from $k = -3.54 \times 10^{-5}$ rad.m^{-1} ($L = 30$ km) to $k = -2.12 \times 10^{-5}$ rad.m^{-1} ($L = 50$ km). This means that equivalent wavelengths vary from $\lambda = 170$ km ($L = 30$ km) to $\lambda = 230$ km ($L = 50$ km). The observed wavelengths were taken from the numerical solution, ranging from 100 to 200 km. These lengths were estimated from the spatial scales presented in the phase of the diurnal tidal currents simulated over the northern Portuguese shelf (Fig. 15). Both analytical and numerical values are of the same order, confirming the proper simulations of CSW. The negative sign of k reflects right bounded wave propagation. The wide wavelength interval shows how sensitive the CSW solution is to the shelf width, along irregular continental margins. The differences between the analytical and numerical estimations show that the step shelf approach is not enough to accurately characterise the observed CSW structures. Other approaches, like the use of exponential shelf profiles, can be explored to obtain better results (Buchwald and Adams, 1968; Fortunato et al., 2002).

The trapping condition was verified since the scaled frequency is always smaller than the unit ($\omega < f$) and the right hand side of Eq. (5) ranges from 1 to ∞ .

The model highlighted different CSW amplitudes, extending from the Tagus Plateau to the Galician shelf. This behaviour seems to be related to other existent topographic features along this margin, as submarine valleys (negative shelf width anomalies) and promontories (positive shelf width anomalies). This issue should be addressed in a future work, in order to understand how the varying 2D topography modulates locally the sub-inertial trapped waves modes.

5.2. Semidiurnal waves shelf variability

The cotidal charts of the semi-diurnal constituents suggested a large-scale tidal wave propagating in Kelvin mode, along the West-Iberian margin (Fig. 8). However, tidal velocity maps showed small-scale structures over the continental margin with wavelengths of about 100 km (Figs. 10 and 11). These structures seem trapped by shelf-width anomalies, creating the impression of a “wave-like” configuration (Fig. 16).

In nature, besides the fundamental Kelvin mode, other coastal super-inertial modes exist: edge waves and modified Poincaré waves. Edge waves are topographic trapped modes with large wave number (small-scale oscillations). Poincaré waves are free modes with small wave number, modified by topography (large-scale waves). The trapping condition Eq. (5) splits these coastal wave modes in distinct [ω, k] domains (Huthnance, 1975). For an imposed super-inertial frequency there is a continuum of Poincaré waves solutions and a discrete sequence of unique edge-wave modes. The number of possible existing edge-wave modes is function of the wave frequency. For the same frequency, the Kelvin mode arises at higher wave number and consequently becomes the smaller wavelength trapped at the coast. This statement sets aside the hypothesis of small-scale semi-diurnal trapped waves simulated over the West-Iberian margin.

Rosenfeld and Beardsley (1987) encountered a similar behaviour when analysing tidal velocity observations along the Californian shelf. They proposed a bumpy coastline as an inductor of velocity differences over short distances (<100 km). Similar to the present simulation, the resulting effect was more visible in the velocity field than in the sea-surface amplitude. The spatial variability acquired a wavelength of the same order of magnitude as the distance between coastline bumps.

Several shelf width anomalies, like submarine canyons and shelf spurs are evenly spaced along the West-Iberian margin. The along-shelf distance between these features vary from 40 to 100 km. The small-scale velocity structures, observed in the ellipse magnitude (Fig. 10), phase (Fig. 11) and rotation sense (Fig. 16) exhibit similar wavelengths. These deductions suggest that the “wave-like” configuration do not result from trapped wave mode, but is consequence of along-shelf wave modulation by evenly spaced bathymetry features.

6. Barotropic forcing term

One of the present work's main objectives was the improvement of the barotropic tide regional simulation, to be used in future numerical modelling of the subsequent baroclinic modes, when water-column stratification is introduced. Internal tides are generated by small-scale horizontal pressure gradients created by alternate barotropic tidal flow over steep topography. This mechanism can be scaled locally by the respective forcing term, function of the current velocity magnitude and bathymetry slope:

$$\frac{1}{H} U \cdot \nabla H \quad or \quad \left[\frac{U_n \cos(\omega_n t - \phi_{Un})}{H} \frac{\partial H}{\partial x} + \frac{V_n \cos(\omega_n t - \phi_{Vn})}{H} \frac{\partial H}{\partial y} \right] \tag{8}$$

Please cite this article as: Quaresma, L.S., Pichon, A., Modelling the barotropic tide along the West-Iberian margin, J. Mar. Syst. (2011), doi:10.1016/j.jmarsys.2011.09.016

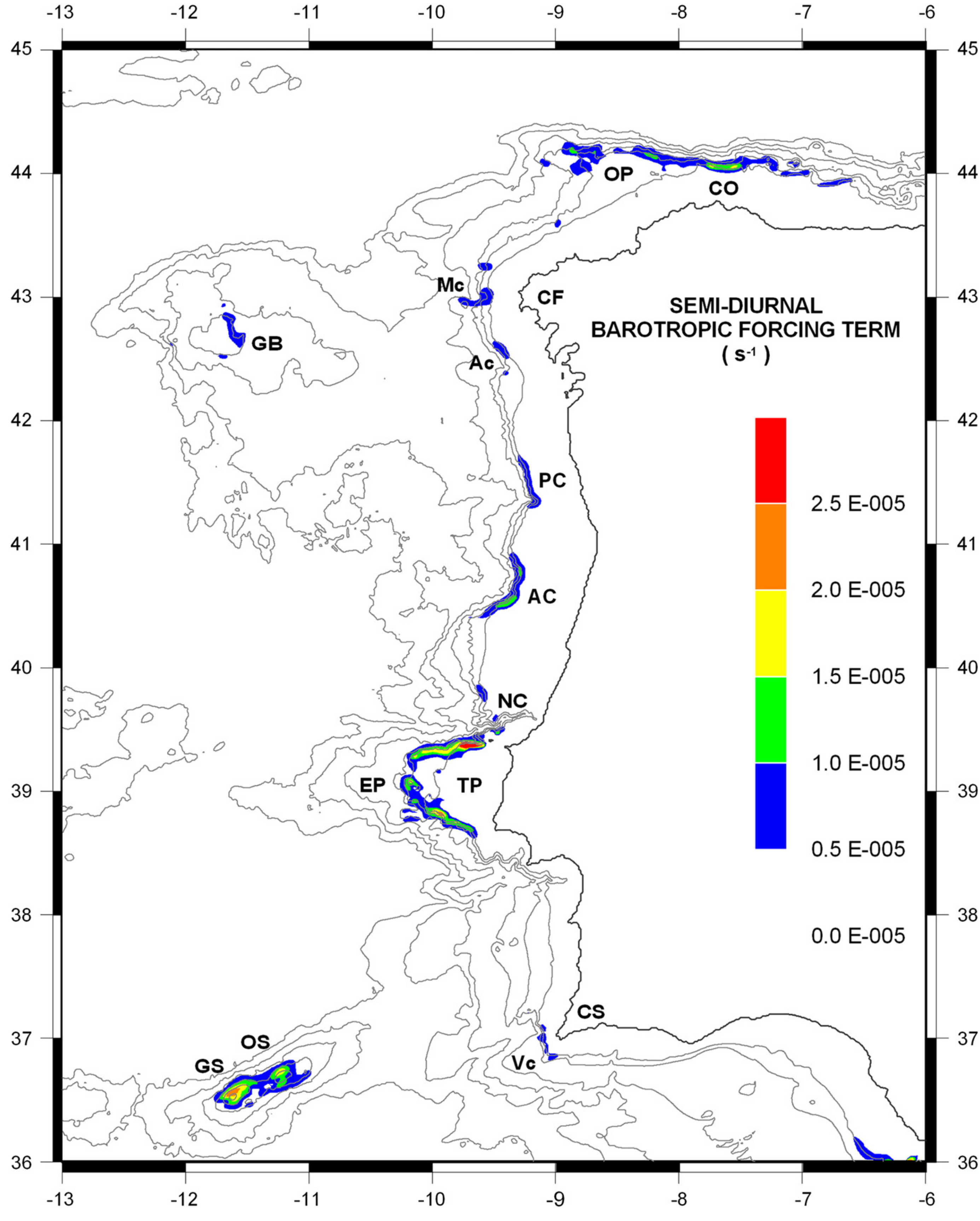

Fig. 17. Semi-diurnal barotropic forcing term map (s^{-1}). Isobaths of 200 m, 500 m, 1000 m, 2000 m, 3000 m and 4000 m were added to help interpretation. Internal tide generation "hotspots" are pointed out by the following symbols: TP (Tagus Plateau); EC (Estremadura promontory); OP (Ortegal promontory); NC (Nazaré canyon); AV (Aveiro canyon); PC (Porto canyon); Ac (Arosa canyon); Mc (Murgia Canyon); Vc (S. Vicente canyon); GB (Galician banks); CO (cape of Ortegal); CF (cape of Finisterra); CS (cape of Sagres) and the Gorringe banks are presented by GS (Gettysburg seamount) and OS (Ormonde seamount).

Please cite this article as: Quaresma, L.S., Pichon, A., Modelling the barotropic tide along the West-Iberian margin, J. Mar. Syst. (2011), doi:10.1016/j.jmarsys.2011.09.016

Barotropic velocity was decomposed in orthogonal component magnitudes (U, V) and by tidal constituents (n). The forcing term only accounted for super-inertial constituents, since internal waves are limited in frequency by [$N<\omega_n<f$], where N represents the buoyancy frequency. Semi-diurnal polychromatic simulations (M2, S2, N2 and K2) were performed in order to calculate the barotropic forcing term set up by the tide along the West-Iberian margin. As expected, maxima values were found along the shelf-break of the major topographic reliefs faces (Fig. 17). These locations constitute internal tide generation "hotspots", where the barotropic tide transfers energy to higher order vertical modes (baroclinic tide).

Most of the identified "hotspots" were already pointed separately in literature. The northern continental slope of the Galician margin reveals several maximal values, primarily at the promontory of Ortegal (Azevedo et al., 2006; Pichon and Correard, 2006) reaching $2.0\times10^{-5}\ s^{-1}$. Around the cape of Finisterra, other areas evidence important forcing term values, like the edges of the submarine canyons of Murgia and Arosa. Offshore, Galicia banks are also known sources of internal tide generation.

Along the northern Portuguese shelf, two major submarine valleys (Porto and Aveiro) highlight an extensive shelf-break belt (200 to 500 m depth) where the forcing term is considerably high (reaching $1.5\times10^{-5}\ s^{-1}$). In the central region of the West-Iberian margin, two huge topographic features (Nazaré submarine Canyon and the Estremadura promontory) imprint the higher forcing values found ($\sim3.0\times10^{-5}\ s^{-1}$). Several "hotspots" are displaced around the Tagus Plateau shelf-break. This fact results from significant tidal velocity amplification (verified earlier) over very strong topographic slopes, as the northern and southern faces of the Estremadura promontory. The achieved barotropic forcing values are comparable to the ones estimated at French slope in Bay of Biscay and are higher than the values estimated at the faces of the promontory of Ortegal (Pichon and Correard, 2006). The Nazaré canyon rim reveals also measurable forcing values, already suggested by Quaresma et al. (2007). In the southern Portuguese margin, other "hotspots" were found offshore the cape of Sagres, where an important submarine canyon comprises strong slopes (S. Vicente canyon).

One very strong "hotspot" is revealed southwest of the Iberian margin (36.5° N/11.5° W). This corresponds to the Gorringe bank where the Gettysburg and Ormonde seamounts rise from the abyssal plain to depths of 25 m and 48 m respectively. Here, the M2 flow is blocked and velocities punctually exceed 10 $cm.s^{-1}$ in the middle of Atlantic Ocean.

The precedent evaluation highlights the main baroclinic tide generation spots at the West-Iberian margin. However, other smaller areas have been proposed in literature, based on satellite Syntactic Aperture Radar imagery (SAR) interpretation (Jeans and Sherwin, 2001; Sherwin et al., 2002; Small, 2002). The topographic slope, calculated in Eq. (8), is function of the adopted model grid resolution (1 arc-minute). This constraint filters the spatial distribution of the barotropic forcing term. Small-scale topographic slopes are not represented by the present model and can be also sources of internal tidal waves (observed in SAR images as internal solitary wave surface signatures).

7. Summary

A circulation numerical model was successfully applied to simulate the barotropic tide along the West-Iberian margin. A new DTM was constructed and validated by model results. The tidal residual current was suitably used as a proxy to tune the viscosity parameterization in the numerical model. Astronomical tide-raising forces, acting regionally, were taken into account by adding the gravitational tidal gradient force into HYCOM momentum equations.

Eight principal harmonics were accurately modelled together by forcing a polychromatic tidal spectrum at the open boundaries. The best semi-diurnal results were obtained when forcing the model with NEA2004 (K2 constituent was the exception) and the best diurnal by forcing TPXO7.2. The model was evaluated by a consistent set of *in situ* observations (11 Tide-gauges and 4 current profile time-series), spaced along the domain. The results attest an accuracy improvement from previous references.

Spatial analysis of the tide shows that its principal harmonics can be grouped in super and sub-inertial classes. Within each class, the regional tidal amplitude and velocity distribution exhibit similar behaviour. The model, in agreement with analytical analysis, reproduces diurnal continental shelf waves along the northern Portuguese shelf. Small-scale semi-diurnal variability is also present. These structures were evaluated and pointed out as being a result of tidal wave modulation by shelf width anomalies, imposed by coastal bathymetry features.

The barotropic forcing term was calculated along the West-Iberian margin and the main internal tide "hotspots" were revealed, namely over the major submarine canyons and promontories, as well as over nearby seamounts. The numerous hotspots and their significant forcing term values suggests strong internal tide activity along the West-Iberian margin, already observed by cited authors.

Acknowledgements

The present study is part of Luis Quaresma PhD work, taking place at the SHOM (French Service Hydrographique et Océanographique de la Marine), followed by UBO (French Université de Bretagne Occidentale) and HIDROGRAFICO (Portuguese Instituto Hidrográfico) and co-supported by FCT (Portuguese Fundação para a Ciência e Tecnologia). The authors would like to give special thanks to *Bernard Le Cann* for the important discussions on the subject. Also to HIDROGRAFICO, SHOM, PUERTOS DEL ESTADO and IFREMER for the available data access.

References

Amante, C., Eakins, B.W., 2009. ETOPO1 1 Arc-minute Global Relief Model: Procedures, Data Sources and Analysis. NOAA Technical Memorandum NESDIS NGDC, 19 pp.
Azevedo, A., Da Silva, J.C.B., New, A.L., 2006. On the generation and propagation of internal solitary waves in the southern bay of Biscay. Deep Sea Research 53 (6), 927–941.
Battisti, D.S., Clarke, A.J., 1982. A simple method for estimating barotropic tidal currents on continental margins with specific applications to the M2 tide off the Atlantic and Pacific coasts of the United States. Journal of Physical Oceanography 12, 8–16.
Bleck, R., 2002. An oceanic general circulation model framed in hybrid isopycnic-cartesian coordinates. Ocean Modelling 4, 55–88.
Bleck, R., Boudra, D.B., 1981. Initial testing of a numerical ocean circulation model using a hybrid (quasi-isopycnic) vertical coordinate. Journal of Physical Oceanography 11, 755–770.
Bleck, R., Smith, L., 1990. A wind-driven isopycnic coordinate model of the north and equatorial Atlantic Ocean. 1.Model development and supporting experiments. Journal of Geophysical Research 95C, 3273–3285.
Buchwald, V.T., Adams, J.K., 1968. The propagation of continental shelf waves. Proceedings of the Royal Society A 305, 235–250.
Da Silva, J.C., Ermakov, S.A., Robinson, I.S., Jeans, D.R., Kijashko, S.V., 1998. Role of surface films in ERS SAR signatures of internal waves on the shelf, 1, short-period internal waves. Journal of Geophysical Research 103, 8009–8031.
Egbert, G., Bennett, A., Foreman, M., 1994. TOPEX/ POSEIDON tides estimated using a global inverse model. Journal of Geophysical Research 99, 24821–24852.
Fanjul, E., Gómez, B., Sánchez-Arévalo, I., 1997. A description of the tides in the Eastern North Atlantic. Progress in Oceanography 40, 217–244.
Fortunato, A., Pinto, L., Oliveira, A., Ferreira, J., 2002. Tidally generated shelf waves off the western Iberian coast. Continental Shelf Research 22, 1935–1950.
Huthnance, J.M., 1975. On trapped waves over a continental shelf. Journal of Fluid Mechanics 69, 689–704.
Jeans, D.R.G., Sherwin, T.J., 2001. The variability of strongly non-linear solitary internal waves observed during an upwelling season on the Portuguese Shelf. Continental Shelf Research 21, 1855–1878.
Larsen, J.C., 1969. Long waves along a single-step topography in a semi-infinite uniformly rotating ocean. Journal of Marine Research 27, 1–6.
LeCann, B., 1990. Barotropic tidal dynamics of the Bay of Biscay shelf: observations, numerical modelling and physical interpretation. Continental Shelf Research 10 (8), 723–758.
Lyard, F., Lefevre, F., Letellier, T., Francis, O., 2006. Modelling the global ocean tides: modern insights from FES2004. Ocean Dynamics 56, 394–415.
Marta-Almeida, M., Dubert, J., 2006. The structure of tides in the western Iberian region. Continental Shelf Research 26, 385–400.

Morel, Y., Baraille, R., Pichon, A., 2008. Time splitting and linear stability of the slow part of the barotropic component. Ocean Modelling 23 (3–4), 73–81.
Pairaud, I.L., Lyard, F., Auclair, F., Letellier, T., Marsaleix, P., 2008. Dynamics of the semi-diurnal and quarter-diurnal internal tides in the Bay of Biscay. Part 1: Barotropic tides. Continental Shelf Research 28, 1294–1315.
Pawlowicz, R., Beardsley, B., Lentz, S., 2002. Classic tidal harmonic analysis including error estimates in MATLAB using T_TIDE. Computers and Geosciences 28, 929–937.
Pichon, A., Correard, S., 2006. Internal tides modeling in the bay of Biscay. Comparisons with observations. Scientia Marina 70S1, 68–88.
Prandle, D., 1997. The influence of bed friction and vertical eddy viscosity on tidal propagation. Continental Shelf Research 17, 1367–1374.
Quaresma, L.S., Vitorino, J., Oliveira, A., DaSilva, J., 2007. Evidence of sediment resuspension by nonlinear internal waves on the western Portuguese mid-shelf. Marine Geology 246, 123–143.
Ray, R.D., 1998. Ocean Self-Attraction and Loading in Numerical Tidal Models. Marine Geodesy 21, 181–192.
Robinson, A.R., 1964. Continental shelf waves and the response of sea level to weather systems. Journal of Geophysical Research 69, 367–368.
Robinson, I.S., 1981. Tidal vorticity and residual circulation. Deep Sea Research 28A (3), 195–212.
Rosenfeld, L.K., Beardsley, R.C., 1987. Barotropic semi-diurnal tidal currents off Northern California during the Coastal Ocean Dynamics Experiment (CODE). Journal of Geophysical Research 92, 1721–1732.
Sauvaget, P., David, E., Guedes Soares, C., 2000. Modelling tidal currents on the coast of Portugal. Coastal Engineering 40, 393–409.
Sherwin, T.J., Vlasenko, V.I., Stashchuk, N., Jeans, D.R.G., Jones, B., 2002. Along-slope generation as an explanation for unusually large internal tides. Deep-Sea Research I 49, 1787–1799.
Simon, B., 2007. La Marée Océanique Côtière. Inst. Oceanogr., Paris. 443 pp.
Small, J., 2002. Internal tide transformation across a continental slope off Cape Sines, Portugal. Journal of Marine Systems 32, 43–69.

Please cite this article as: Quaresma, L.S., Pichon, A., Modelling the barotropic tide along the West-Iberian margin, J. Mar. Syst. (2011), doi:10.1016/j.jmarsys.2011.09.016

PART II

Barotropic tide over idealized bathymetry shelf features

***CONTENTS*:**

Chapter I: 1D Kelvin wave distortion 46

1. The "smooth" shelf aproximation
2. Validating the Kelvin solution over flat bottom
3. Exploring the Kelvin wave distortion over slopping bottom

Chapter II: Building 2D academic simulations 57

1. Bathymetry construction
2. Numerical model linearization

Chapter III: Super-inertial tides over abrupt continental shelf features. . . . 61
Part I: Barotropic solution.
Quaresma L.S. & A. Pichon,
submitted to Journal of Physical Oceanography (2011)

1. **Introduction** 62

2. **Solution over regular shelves** 65

a. Theory
b. Cross-shelf profiles

3. **Solution over irregular shelves** 72

a. Numerical model
b. Idealized topography
c. Boundary conditions

4. **Results** 76

a. Sea-surface amplitude
b. Current velocity

5. **Analysis** 80

a. Fluid vorticity
b. Flow rotation
c. Tidal flow over promontories
d. Tidal flow over canyons
e. 2D Kelvin wave distortions

6. **Discussion** 90

***Appendix A*: Bottom friction** 95

1. Depth-average tidal flow
2. Tidal current profiles over the shelf
3. Bottom boundary layers

***Appendix B:* 1D barotropic tide solutions across regular margins** 105

Chapter I
1D Kelvin wave distortion

Laplace tidal equations (LTE) correspond to the momentum and continuity shallow water equations, for long barotropic wave motions in a thin fluid layer covering a rotating spherical globe (Part I). Over small regions of interest, such as continental shelves, the curvature of the Earth can be neglected (*f*-plane approximation) as well as the large-scale astronomic tidal forcing (η_e). The small tidal amplitude, relative to the continental shelf depth and its weak current velocity relative to the wave propagation speed, enables the linearization of the LTE, in the form:

$$\begin{cases} u_t - fv &= -g\eta_x + \tau_{bx}/\rho H \\ v_t + fu &= -g\eta_y + \tau_{by}/\rho H \\ \eta_t + H(u_x + v_y) &= 0 \end{cases} \qquad (1)$$

Here, the frictional stress is reduced to the bottom friction component, expressed in the form of a drag stress (τ_{bx} ,τ_{by}) applied to the vertically integrated flow. In the following developments of tidal flow governing equation the bottom stress is neglected, based on its secondary importance when compared to the other terms for shelf regions deeper than ~25m. This approximation is discussed later on (*Appendix A*), and is supported by the reviews of May (1979), Prandle (1997) and Ostendorf (1984). Without friction, the linear equation (1) can be developed in order to get a single equation for η. This is achieved in 3 steps. First, one should derive (1) with respect to time to get

$$\begin{cases} u_{tt} - fv_t &= -g\eta_{xt} \\ v_{tt} + fu_t &= -g\eta_{yt} \\ \eta_{tt} + (Hu_t)_x + (Hv_t)_y &= 0 \end{cases} \qquad (2)$$

Then, derive again the continuity equation in (2) with respect to time and replace here the terms v_{tt} , u_{tt} by their solutions in momentum equations from (2). Finally, rearrange the new continuity expression to formulate a general equation of the sea-surface vertical displacement along an arbitrary topography, as (Clark & Battisti, 1981):

$$\eta_{xxt} + \eta_{yyt} + \frac{H_x}{H}\left(f\eta_y + \eta_{xt}\right) + \frac{H_y}{H}\left(\eta_{yt} - f\eta_x\right) - \left(\frac{\partial^2}{\partial t^2} + f^2\right)\frac{\eta_t}{gH} \quad = \quad 0 \qquad (3)$$

1. The "smooth" shelf approximation

Solution of equation (3) can be found analytically, in the form of a plane wave $\eta\ exp\ \{i\ (\omega t\ -\ kx\ -\ ly)\}$, and can be studied under certain approximations. Over continental margins, the tide wave is commonly considered as propagating over a monotonous shelf profile ($H_y = 0$), bounded by a straight coastline (considered here as a north-south wall). This method is valid for "smooth" continental margins, where along-shelf topographic variations are usually smaller than the strong cross-shelf bathymetry gradients, imposed by continental slopes ($H_x >> H_y$). This approximation reduces (3) to the following form:

$$\eta_{xxt} + \eta_{yyt} + \frac{H_x}{H}\left(f\eta_y + \eta_{xt}\right) - \left(\frac{\partial^2}{\partial t^2} + f^2\right)\frac{\eta_t}{gH} \quad = \quad 0 \qquad (4)$$

Narrow continental margins ($<10^2$ km) represent small obstacles for Kelvin waves, whose typical length (given by the external Rossby deformation radius) is of the order of 2×10^3 km. Let us consider the along-shelf tide variability to the one associated with its propagating phase and replace it by a fixed wavenumber component, l. This parameter can then be taken as function of the near deep-ocean depth, given by $\omega/\sqrt{gH}$. Focusing on the cross-shelf solution of tidal harmonics, one can find the solutions of (4) in the form $\eta = [F(x) + i\ G(x)]\ exp\ \{i\ (\omega t\ -\ ly)\}$. Variations of η with respect to time and along-shelf direction allows to write

$$\begin{aligned} \eta_t &= i\omega\,\eta \quad , \ \eta_{tt} = -\omega^2\,\eta \\ \eta_y &= -i\,l\,\eta \quad , \ \eta_{yy} = -l^2\,\eta \end{aligned} \qquad (5)$$

Replacing time and along-shelf variation terms in (4) one will get a second order ordinary differential "smooth" shelf tidal elevation equation:

$$\eta_{xx} + \frac{H_x}{H}\eta_x + \left(\frac{\omega^2 - f^2}{gH} - \frac{H_x}{H}\frac{f}{\omega}l - l^2\right)\eta \quad = \quad 0 \qquad (6)$$

To solve this equation, one needs to reduce it to a system of first order equations, as

$$\begin{cases} \eta = \left[F(x) + iG(x)\right]\ e^{i(\omega t - ly)} \\ \eta_x = \left[F'(x) + iG'(x)\right]\ e^{i(\omega t - ly)} \\ \eta_{xx} = \left[F''(x) + iG''(x)\right] e^{i(\omega t - ly)} \end{cases} \qquad (7)$$

The solution for *F(x)* and *G(x)* can then be calculated using an iterative numerical method, like the Runga-Kutta of fourth order, when the following two initial value conditions are define: 1) Sea-surface amplitude (A) and phase (Φ) at the coastline; 2) null condition for the cross-shelf velocity component at this border (u = 0 at x = 0). Notice from (7) that the initial value of F(x) and G(x) differs by

$$F(x_0) = A\,cos\,\Phi \quad , \quad G(x_0) = A\,sin\,\Phi \qquad (8)$$

From the linear momentum equations (1), without friction, where u and u_t are set to be null at the border, one can express $F'(x = 0)$ and $G'(x = 0)$ as function of $F(x = 0)$ and $G(x = 0)$ by

$$F'(x=0) = \frac{f}{\omega} l F(x=0) \quad , \quad G'(x=0) = \frac{f}{\omega} l\, G(x=0) \qquad (9)$$

The cross-shelf curve solutions of *F(x), G(x), F'(x), G'(x)* are obtained once the iterative method has been applied over the entire profile, function of the terms present in the "smooth" shelf tidal elevation equation as

$$\begin{cases} F''(x) + \dfrac{H_x}{H} F'(x) + \left(\dfrac{\omega^2 - f^2}{gH} - \dfrac{H_x}{H}\dfrac{f}{\omega} l - l^2 \right) F(x) & = & 0 \\ G''(x) + \dfrac{H_x}{H} G'(x) + \left(\dfrac{\omega^2 - f^2}{gH} - \dfrac{H_x}{H}\dfrac{f}{\omega} l - l^2 \right) G(x) & = & 0 \end{cases} \qquad (10)$$

These auxiliary variables can now be converted to trace the sea-surface height and phase cross-shelf profiles following the relation

$$\eta = \sqrt{F(x)^2 + G(x)^2} \quad , \quad \Phi = atan^2\left(\frac{G(x)}{F(x)} \right) \qquad (11)$$

Similar equations can also be obtained for both cross-shelf and along-shelf velocity components. This is obtained starting from (2) and replacing here the terms v_t , u_t by their solutions in momentum equations from (1). Finally, by rearranging the new momentum expressions, where time and along-shore variations are replaced by the harmonic terms defined earlier, we get

$$\begin{aligned} u &= \frac{g}{\omega^2 - f^2} \; (i\omega\eta_x - ilf\eta) \\ v &= \frac{g}{\omega^2 - f^2} \; (\omega l\eta - f\eta_x) \end{aligned} \qquad (12)$$

Using the same $F'(x)$, $G'(x)$, $F(x)$ and $G(x)$ functions this yields,

$$
\begin{aligned}
u &= \frac{g}{\omega^2 - f^2}\left[(-\omega G'(x) + f\,l\,G(x)) + j(-\omega F'(x) - f\,l\,F(x))\right] e^{j(\omega t - l y)} \\
v &= \frac{g}{\omega^2 - f^2}\left[(\ \omega\,l\,F(x) - f\,F'(x)) + j(\ \omega\,l\,G(x) - f\,G'(x))\right] e^{j(\omega t - l y)}
\end{aligned}
\qquad (13)
$$

Which gives the magnitude and phase profiles for each velocity component

$$
\begin{aligned}
u &= \frac{g}{\omega^2 - f^2}\sqrt{[-\omega G'(x) + f\,l\,G(x)]^2 + [\omega F'(x) - f\,l\,F(x)]^2} \\
v &= \frac{g}{\omega^2 - f^2}\sqrt{[\omega\,l\,F(x) - f\,F'(x)]^2 + [\omega\,l\,G(x) - f\,G'(x)]^2}
\end{aligned}
\qquad (14)
$$

$$
\Phi_u = \frac{[\omega F'(x) - f\,l\,F(x)]^2}{[-\omega G'(x) + f\,l\,G(x)]^2} \quad , \quad \Phi_v = \frac{[\omega\,l\,G(x) - f\,G'(x)]^2}{[\omega\,l\,F(x) - f\,F'(x)]^2} \qquad (15)
$$

This method enables, in one iterative run, the estimation of both sea-surface elevation and tidal velocity cross-shelf sections, as a function of the same auxiliary functions (*F(x), G(x), F'(x), G'(x)*). These solutions, known as Bassel curves, depend on the difference between tidal and Coriolis frequencies (whose resulting sign is opposite for sub-inertial and super-inertial harmonics) and are shaped by the cross-shelf bathymetry gradient (H_x). This method was explored and validated by Jézéquel and Mazé (2001). Notice that the resulting solutions are very sensitive to the chosen along-shelf wavenumber (in order to get convergent solutions) and to the spatial resolution discretization. For typical smooth continental shelves and slopes this last parameter should be of $O(10^2\ \text{m})$.

2. Validating the Kelvin solution over flat bottom

The pure Kelvin wave solution (see Part I, *Chapter II. b*),

$$\eta = \eta_0\ e^{(-f x/C)} \cos(ly - \omega t) \qquad (16)$$

$$v = \eta_0 \sqrt{g/H}\ e^{(-f x/C)} \cos(ly - \omega t) \qquad (17)$$

with phase velocity $C = \omega / l = \pm(gH)^{1/2}$, is a solution of equation (6) when flat ocean bottom, bounded by a straight wall, is forced to the previous method. As mentioned earlier, the wave solution is reduced to a boundary condition problem where one can force a tide sea-surface amplitude and tide phase at the coast, as well as a null cross-shelf velocity component at this border ($u = 0$ at $x = 0$).

The iterative method, formulated above to solve (6) and (12), is now tested using the straightforward analytical solution (16) and (17). Consider a 4000 m depth flat ocean, located at 40ºN ($f = 0.935\text{x}10^{-04}\ \text{s}^{-1}$), limited by a north-south vertical wall (coast) placed to the right (Figure 1).

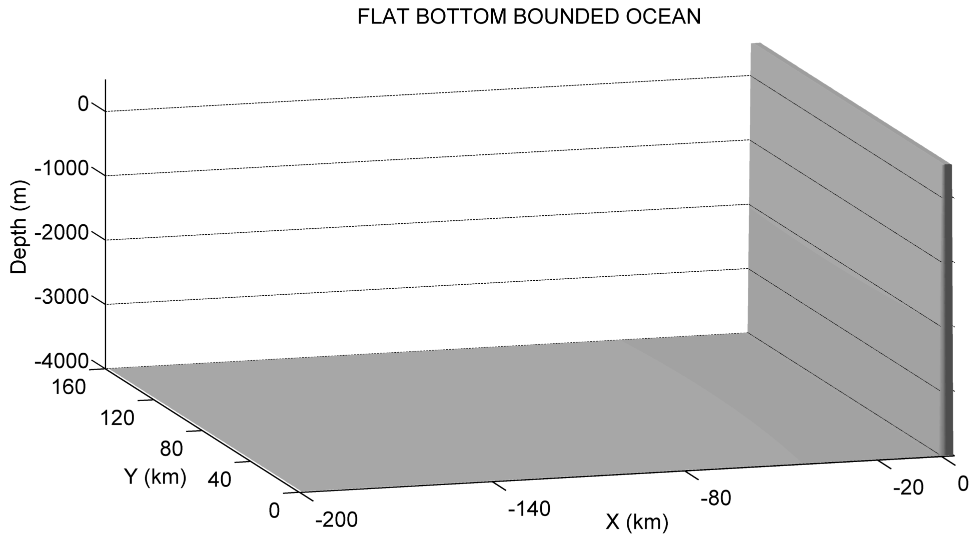

Figure 1. Flat ocean bottom configuration, bounded by a straigth wall (coast) to the right of the domain.

Let us now force a monochromatic M2 tide ($\omega = 1.4\ \text{x}10^{-4}\ \text{s}^{-1}$), with 1 m amplitude at the coast ($C = 198\ \text{m.s}^{-1}$) and calculate from the iterative method the respective tide wave configuration across this plain margin, from coastline to 200 km offshore. The resulting solution (Figure 2) can then be validated by applying in parallel the straightforward equations (16) and (17). Both methods give identical results: η (x = 200 km) ~0.91 m and v (x = 200 km) ~0.045 m.s^{-1}. This simple test enables us to employ here after the same method to solve the one-dimensional Kelvin wave solution across regular continental margins, which will be introduced in different configurations. Notice that the wavenumber l is fixed, in balance with the 4000 m ocean depth, $l = \omega/(gH)^{1/2}$, and for that distorted Kelvin wave solutions are expected.

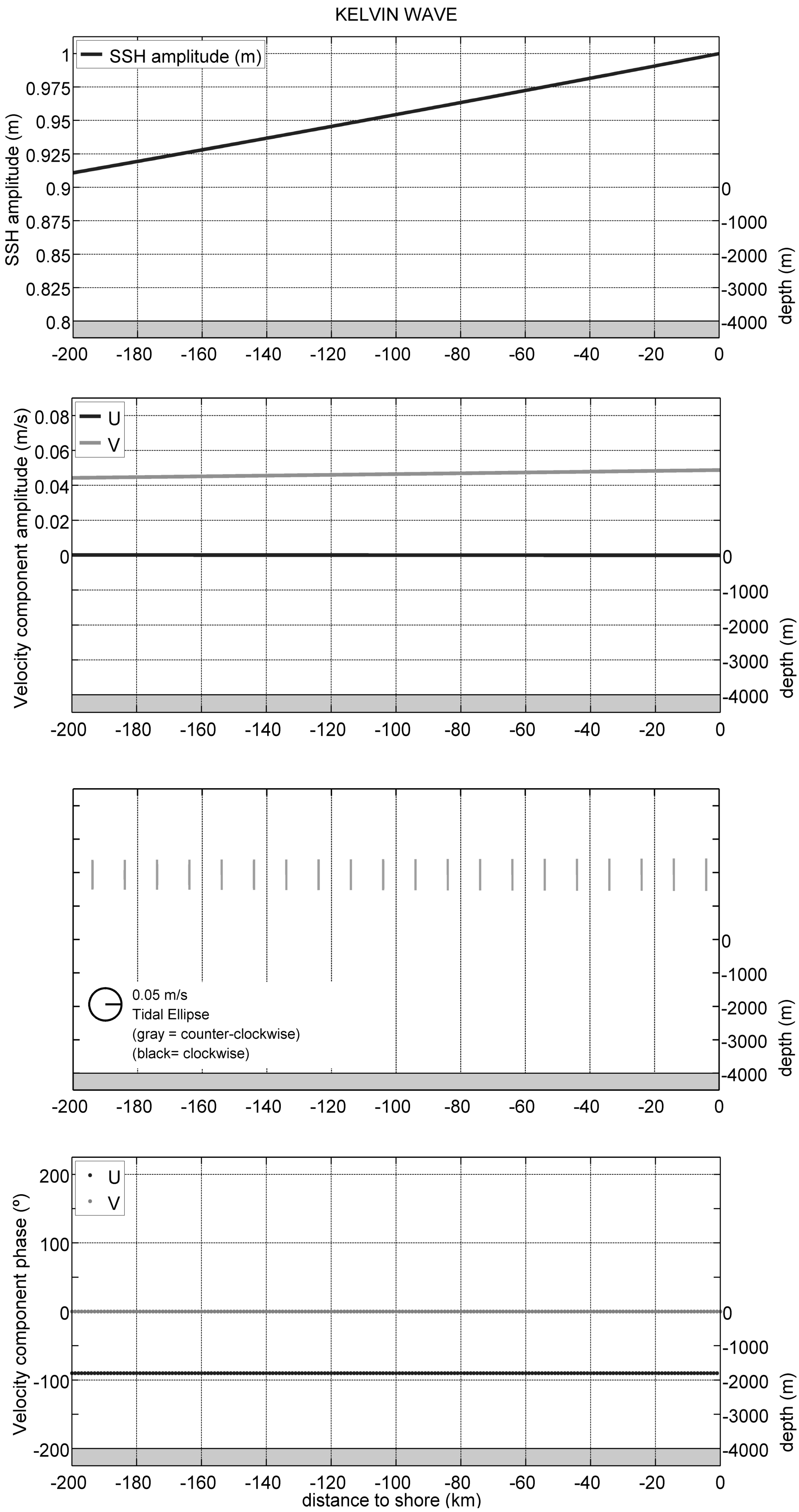

Figure 2. **Kelvin wave** solution over **4000m flat ocean**, bounded at the right of the domain (**1m wave amplitude** is imposed at the coastline, x = 0)

3. Exploring the Kelvin wave distortion over slopping bottom

As seen before, away from the boundaries, tides propagate as free waves governed by gravity and inertia. When bounded by a fixed wall, they become bounded Kelvin waves (Figure 2). This solution, also called semi-geostropic equilibrium, is expressed by the governing equation (18), where terms in brackets disappear at the boundary, $u(0) = 0$.

$$\begin{cases} [u_t] - f v = -g\eta_x \\ v_t + [f u] = -g\eta_y \\ \eta_t + (Hv)_y + [(Hu)_x] = 0 \end{cases} \quad (18)$$

In the northern hemisphere these modes propagate right bounded, and one can approximate its phase velocity as a function of the deep-ocean depth, $C_0 = (gH)^{1/2}$, if the shelf width is much smaller than the external Rossby length. This assumption allows the along-shelf tidal wavenumber to be approximated to $l = \omega / C$. However, shallow water shelves, whose width varies from kilometres to few hundred kilometres, usually follow real continental margins. Over these shallow regions, C is unbalanced by the driving l and consequently the Kelvin's semi-geostrophic (18) equilibrium breaks apart. This gives rise to a cross-shelf velocity component (x-direction) that increases with the distance from the coastline. The Kelvin wave distortion is set up by the coefficients [1] and [2] that compose the "smooth" shelf tide formulation (6) and their impact is verified next by computing the solution across different idealized continental margins (most of these figures are placed in *Appendix* A).

$$\eta_{xx} + [1]\,\eta_x + [2]\,\eta = 0 \quad (*6)$$

Let us start to reduce (6) by restricting it to the Kelvin wave solution. The flat bottom condition gives $H_x = 0$ and this equation becomes

$$\eta_{xx} + \left[-\frac{f^2}{C^2} + \frac{\omega^2}{C^2} - l^2 \right] \eta = 0 \quad (19)$$

In our simulation (Figure 2), the imposed wavenumber l^2 is in equilibrium with the wave phase velocity estimated by $C^2 = gH$ and for that one can replace it by $\omega^2/C^2 = l^2$, reducing (19) to

$$\eta_{xx} + \left[-\frac{f^2}{C^2} \right] \eta = 0 \quad (20)$$

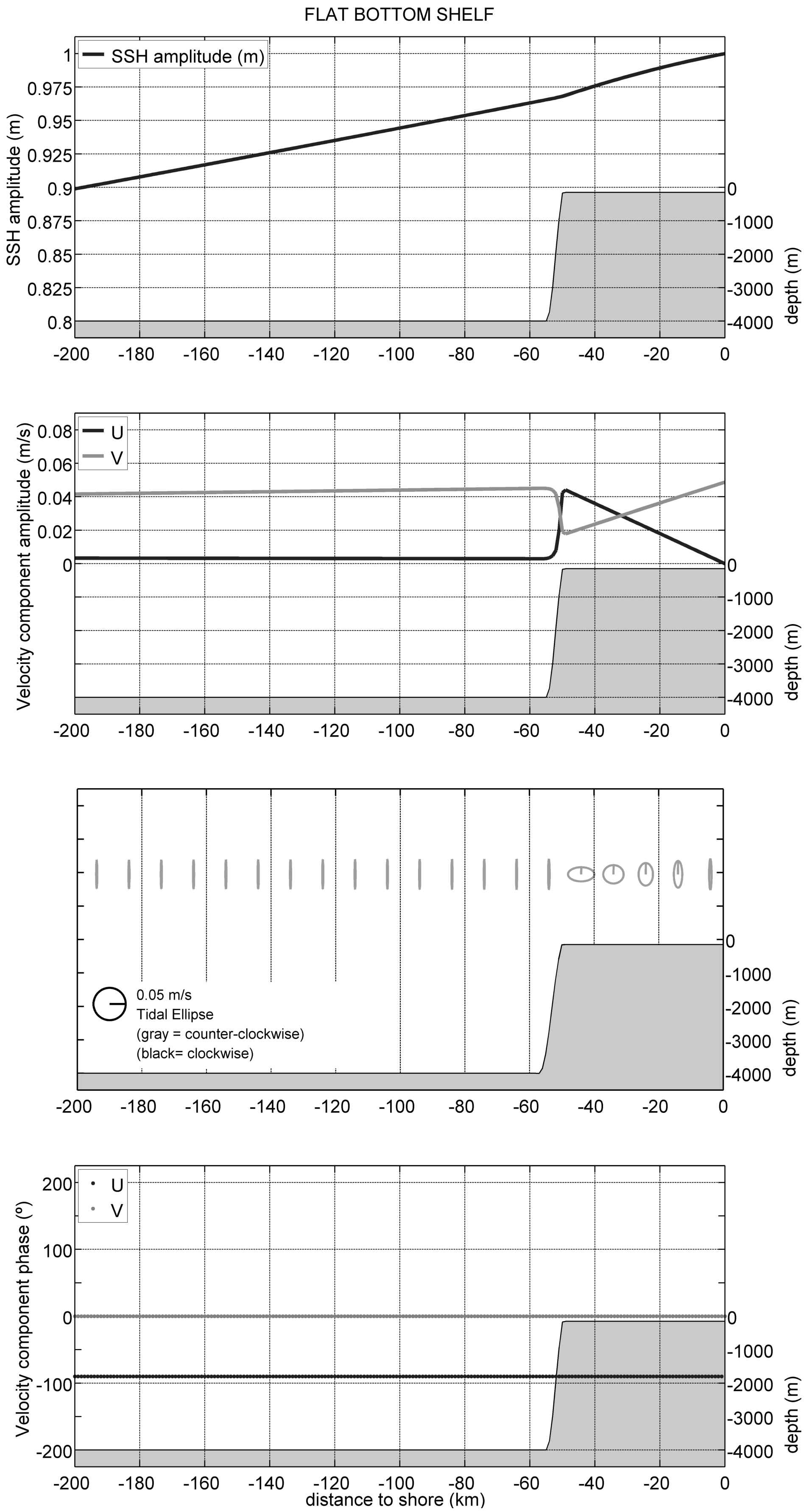

Figure 3. M_2 super-inertial harmonic (1m amplitude at the coast) cross-shelf solution, over a **150 m depth** flat bottom shelf of **50 km length**.

In (20) one can identify the Kelvin's exponential decay factor $-f^2/C^2$, which sets the behaviour of the Kelvin's sea-surface structure. The exponential rate with which η varies along x is determined by the value of the coefficient (2) in equation (6) and a negative sign gives an offshore decrease.

When a step continental margin is considered, very distinct solution is obtained (Figure 3). Note that the imposed shelf is flat and that the continental slope is reduced to a minimum length to avoid abrupt bottom transitions, which causes the numerical method to diverge (the spatial resolution is set here to 100 m). The solution shows a quasi-linear growth of the component u over the shelf and an equivalent decrease of the orthogonal velocity component v. In fact, this behaviour results primarily from the unbalanced wavenumber l (fixed by deep-ocean Kelvin's phase velocity) and ω/C established over the shallow shelf (where the wave phase velocity becomes significantly smaller). This means that coefficient [2] in (6) will not be reduced to (20) and its higher absolute value will increase the sea-surface slope over the shelf, in exponential form determined by [2], since $H_x = 0$ and the equation gets the form (19). Consequently, η_x is no longer in balance with $-fv$ and an orthogonal velocity component must naturally appear to equilibrate the pressure gradients in (18).

If the shelf depth is kept constant ($H = const$) and the **shelf width** enlarged, the linear decrease of the component v will make it disappear at a certain distance from the coastline, while u will continue to increase exponentially. When the component v becomes null, u cannot balance the along-shelf slope η_y, forcing the re-appearance of the along-shelf velocity component v, this time with an opposite sign to compensate the exponential grow of [fu], since $-g\eta_y$ is kept constant by the fixed l, from (18). Consequently, tidal ellipses invert their rotation sense in the outer-shelf shelf region (Figure 4, in *Appendix B*). This mechanism is the major reason to observe super-inertial counter-clockwise tidal ellipse rotation in narrow "smooth" shelves and clockwise rotation in wider shelves (for the northern hemisphere). Nevertheless this balancing process depends on the shelf configuration:

1. **Coastline wall.** Near the coast, the tidal ellipse direction is parallel to the border since the solution is forced with a null cross-shelf velocity component at this limit ($u = 0$ at $x = 0$).

2. **SSA amplitude.** The sea-surface amplitude (SSA) imposed as boundary condition, $\eta(x = 0)$, controls the tidal current magnitude over the shelf without changing the ellipse inversion structure (see differences between Figure 4 and Figure 5, in *Appendix B*). This result out-comes directly from continuity equation (18).

3. **Shelf depth.** The tidal velocity magnitude is also function of the depth of the shelf, increasing for shallower shelves (see differences between Figure 4 and Figure 6, in *Appendix* B). Its impact is especially observed in the outer region since near the coast the magnitude is a function of the SSA condition. Moreover, this parameter defines the distance from the coast where the along-shelf component disappears and change sign when moving toward the shelf-break (i.e. Figure 4 and 5 share the same inversion *x*-position in clear contrast to Figure 6, in *Appendix B*).

4. **Slopping shelves.** If a slopping bottom replaces the flat shelf, the quasi-linear variation of each velocity component becomes visibly exponential, resulting from the activation of the coefficient [1] in equation (6) since $H_x \neq 0$. Consequently, stronger distortion of the tidal ellipses will occur without changing the ellipse inversion *x*-position (see differences between Figure 3 above, and Figure 7 in *Appendix B*). For wider sloping shelves (keeping the same slope value, H_x) the inverted ellipses will increase in magnitude toward the shelf break (see differences between Figure 7 and Figure 8, in *Appendix* B).

5. **Shelf-break depth.** If one fixes the coastline depth to reproduce real littoral regions (5-20m), the shelf-break depth will define the cross-shelf bathymetry gradient (H_x) of the idealized shelf. By increasing outer-shelf depth, one will increase H_x and consequently H, and vice versa. This combined effect (H_x, H) intensify tidal distortion and reinforce ellipses inversion in shallower shelves (where H_x and H are smaller), bringing the transition region closer to the coast (see differences between Figure 8 and Figure 9, in *Appendix B*). As can be expected, stronger slopes make the shelf-break deeper than and tidal distortion will be attenuated.

6. **Continental slope**. The continental slope width is of only secondary importance in the cross-shelf profile curve, simply dictating the transition between the

distorted solution over shelf and the deep-ocean Kelvin wave (see differences between Figure 7 and Figure 10, in *Appendix B*).

7. **Tidal wavelength.** The chosen tidal alongshore wavenumber, $l = C / \omega$, determines the driving wave mode. For Kelvin waves, the phase velocity is identical for rotating or non-rotating reference frames: $C = (gH)^{1/2}$. All the solutions calculated before show the semi-geostrophic equilibrium established offshore, as a result of the balance between the phase velocity and the imposed wavelength ($\lambda = 2\pi / l$). If another value for l is chosen, the solution will be modified. For example, one can adopt a wavenumber representing a shallow water Poincaré wave, whose phase velocity in rotating frame is:

$$C = \sqrt{\frac{gH}{1 - f^2/\omega^2}} \qquad (21)$$

   As free propagating modes, Poincaré tide waves will intercept the coastline with any possible angle and consequently be reflected with the same angle relative to the perpendicular direction to coastline. This angle will reduce the alongshelf wavenumber l, which implies shorter wavelengths that magnifies the tidal currents over the shelf and increases ellipses distortion (see differences between Figure 10 and Figure 11, in *Appendix B*). This solution is discussed by Das & Middleton (1997) and Jézéquel & Mazé (2001).

From the previous analysis, continental margins can be split in narrow and wide shelves, based on the super-inertial cross-shelf current velocity structure. Considering sloping bottom shelves (most common in nature) with 200m-depth shelf break (usually used as a reference shelf limit), one can verify that “smooth” shelves straighter than 80 km show invariant counter-clockwise tidal ellipses (Figure 12, in *Appendix B*), while clockwise rotation dominate wider shelf cross-sections (Figure 13, in *Appendix B*). Battisti & Clark (1982) obtained similar results, when validating model simulations from the narrow west-shelf and wider east-shelf of the United States of America. These two continental margins share a right bounded tide wave and differ on the observed tidal ellipses rotation sense, with anti-clockwise rotation over the narrow shelf (10-30 km) and clockwise rotation over the wider shelf (larger then 100km).

Chapter II

Building 2D academic simulations

2. Numerical model linearization

The present work adopts a finite-difference method to solve the linear Laplace primitive equations (2) under a regular staggered mesh grid (type Arakawa-C). A free-surface shallow water model (Bleck & Smith 1990, BS1990) is used in a linearized form. The model employs an explicit time-splitting scheme to separate the fast barotropic gravity waves from the slower modes (internal tidal waves in the presence of stratified water columns). This method requires the splitting of the prognostic variables into their barotropic (i.e. depth-independent) and baroclinic components. A vertically integrated component (denoted by an over-bar) is removed from the velocity profile (u, v) to obtain a baroclinic profile (denoted by a prime), as $u = \bar{u} + u'$, $v = \bar{v} + v'$ and $\bar{u'} = 0$, $\bar{v'} = 0$. The pressure field $p = p'(1+\tilde{\eta})$ is also decomposed into a barotropic component depth-independent, $\tilde{\eta}$, and a baroclinic pressure field component p', whose bottom value is $p'_b = \langle\rho\rangle g H$, and $\langle\rho\rangle$ is a reference density averaged in space and time. The barotropic time step becomes:

$$\begin{cases} \dfrac{\partial \bar{u}}{\partial t} - f\,\bar{v} = -\alpha_0 \dfrac{\partial(p'_b\,\tilde{\eta})}{\partial x} + \dfrac{\partial \bar{u}^*}{\partial t} \\ \dfrac{\partial \bar{v}}{\partial t} - f\,\bar{u} = -\alpha_0 \dfrac{\partial(p'_b\,\tilde{\eta})}{\partial y} + \dfrac{\partial \bar{v}^*}{\partial t} \\ \dfrac{\partial(p'_b\,\tilde{\eta})}{\partial t} + \nabla(\bar{V}\cdot\, p'_b) = 0 \end{cases} \qquad (22)$$

where α_0 is the mean specific volume, $\alpha_0 = 1/\langle\rho\rangle$ and $\partial(\bar{u}^*,\bar{v}^*)/\partial t$ relates to all the depth-integrated non-linear terms (inertial, viscosity and bottom stress friction) transposed from the baroclinic time-step to the barotropic one. In the present work, BS1990 is configured with a single isopycnal layer (reducing the velocity solution to the barotropic contribution) and is linearized by neglecting $\partial(\bar{u}^*,\bar{v}^*)/\partial t$ in the barotropic momentum equations. The one-layer configuration sets $p = p'_b(1+\tilde{\eta})$ and $\tilde{\eta} = \eta/H$, where η is the sea-surface displacement. The barotropic pressure gradient results therefore from the time-dependent pressure $(p'_b\tilde{\eta})$ and

$$\begin{cases} \dfrac{\partial(p'_b\,\eta)}{\partial x} = g\dfrac{\partial \eta}{\partial x} \\ \dfrac{\partial(p'_b\,\eta)}{\partial y} = g\dfrac{\partial \eta}{\partial y} \end{cases} \qquad (23)$$

References

Battisti, D. S. & A. J. **Clark**, **1982**: Estimation of nearshore tidal currents on nonsmooth continental shelves, *Journal of Geophysical Research*, vol. 87, 7873-7878.

Bleck, R., & L. **Smith**, **1990**: A Wind-Driven Isopycnic Coordinate Model of the North and Equatorial Atlantic Ocean - 1. Model Development and Supporting Experiments, *Journal of Geophysical Research*, 95, 3273–3285

Clarke, A. J., & D. S. **Battisti**, 1981: The effect of continental shelves on tides, *Deep Sea Research,* 28, 665–682.

Das, P., & J. **Middleton**, **1997**: Obliquely Incident Poincaré waves on a sloping continental shelf, Journal of Physical Oceanography 27, 1274-1285.

Jézéquel, N., & R. **Mazé**, **2001**: A barotropic model of the linear semidiurnal tide over a continental slope, *Deep-Sea Research*, 48, 1375–1399.

May, P. W., 1979: Analysis and Interpretation of tidal currents in the coastal boundary layer. *Phd thesis, MIT-Woods Hole Oceanographic Institution*.

Prandle, D., 1997: The influence of bed friction and vertical eddy viscosity on tidal propagation. *Continental Shelf Research*, 17, 1367–1374.

Chapter III

Super-inertial tides over abrupt continental shelf features. Part I: Barotropic solution*

LUIS S. QUARESMA
Instituto Hidrográfico - Marinha, Lisboa, Portugal.

ANNICK PICHON
Service Hydrographique et Océanographique de la Marine, Brest, France.

* *Article submitted to Journal of Physical Oceanography in December 2011*

Abstract

[1] Two-dimensional barotropic tide solutions are obtained and discussed over irregular continental shelves, where abrupt geomorphic features impose strong along-shelf slopes. A finite-difference numerical model, under idealized bathymetry configurations, super-inertial monochromatic boundary conditions, solves the bounded solution of linear Laplace tidal equations, over small regions of interest (f-plane). Solutions are obtained for submarine canyon and promontory features, simplified here to opposite sinusoidal shelf width anomalies along narrow continental margins. Each geomorphic structure sets up important distortion of the tidal flow. The impact is strong enough to reverse the rotation sense, magnitude and eccentricity of the tidal current ellipses. This behaviour is justified by fluid vorticity dynamics under the principle of angular momentum conservation.

[2] Key words: barotropic tide, Kelvin wave distortion, fluid vorticity, submarine canyons and promontories.

1. Introduction

[3] Semi-diurnal tides propagate offshore as free waves governed by gravity and inertia (Poincaré waves). At mid-latitude regions these super-inertial waves ($\omega > f$, ω = tidal frequency, f = Coriolis parameter) are deflect by coastlines and spread as Kelvin and/or Poincaré modes (Mysak & Howe, 1978). The partial distribution of the scattered energy depends on the shape and roughness of continental margins. Narrow shelves seem to trap tidal energy mainly into Kelvin mode (Howe & Mysak, 1973) while wider shelves reflect shallow water Poincaré waves that can constructively interfere to increase tidal amplitude near the shelf-break region (Middleton & Bode 1987). Munk et al. (1970) and Le Cann (1990) verified this behaviour by assembling different modes, in distinct partial contributions, to match the observed tidal solution.

[4] In nature, these flat bottom analytical modes are distorted by topography (Miles, 1972). Several authors developed one-dimensional analytical solutions of Laplace tidal equations to reproduce the basic cross-shelf tide structure (reviewed by Clark, 1991). Their work share the same "smooth" shelf assumption, in the sense that continental margins are usually straight and their depth varies primarily in the cross-shelf direction (perpendicular to coastline). Quaresma (2012) examined this smooth shelf tidal solutions and show that over right bounded narrow shelves (< 10^2 km), the offshore decrease of tidal amplitude and the counter-clockwise rotation of very eccentric tidal ellipses, aligned parallel to coastlines (as distorted Kelvin waves). On the other hand, wider shelves (> 10^2 km) show less eccentric tidal ellipses rotating clockwise. Here, ellipse orientation changes offshore from parallel to perpendicular to the coastline with a semi-minor/semi-major axis ratio of f/ω (as Poincaré waves).

[5] Fandry & Jacket (1987) expanded the 1D "smooth" shelf approach to include moderate corrections due to linear along-shore topographic variations. Their results indicate that tidal solutions can be very sensitive to this parameter, especially if topographic gradients are related with local widening or narrowing of the shelf (observed earlier by Holloway 1983 and after by Lentz et al., 2001).

[6] Submarine canyons and/or promontories often shape irregular continental margins. These geomorphic features represent abrupt shelf width anomalies and impose strong along-shore bathymetry gradients. Several observation reports and published works notice the distortion of tide waves over these regions, where amplitude increases over promontories and reduces over submarine canyons. Moreover, tidal currents become stronger and reverse their rotation direction. Quaresma & Pichon (2011) show this behaviour in semi-diurnal tides over several geomorphic features, of different size and shape, located along the narrow west-Iberian margin. Both negative (submarine canyons and valleys) and positive (promontories and spurs) shelf width anomalies hold stronger clockwise, less eccentric tidal ellipses, in contrast to weaker, counter-clockwise, eccentric ellipses aligned along regular shelf lengths (Figure 1). High-frequency radar surface-current observations (Wang et al., 2009), in complement with numerical simulations (Carter, 2010) reveal analogous topographic impacts around the Monterey submarine canyon head (west-California coast) and over the Sur promontory (Rosenfeld et al., 2009). Similar behaviour is observed across the west coast of Vancouver Island near the Juan de Fuca Canyon, (Foreman & Walters, 1990) and over the Gaoping canyon at the Taiwan margin (Chiou et al., 2011).

[7] The "smooth" shelf simplification of the Laplace tidal equation cannot be applied to the previous coastal regions and a different approach is developed in the present work to reproduce and understand the observed tidal behaviour. Two-dimensional tide solutions are obtained by solving the linear Laplace tidal equations (section 2) with a finite-difference numerical model (section 3). Regular "narrow" continental margins ($< 10^2$ km), invariant along-shelf, are reshaped in the middle of the domain by single shelf width anomalies (reproducing the submarine canyon and the promontory features). This option enables the use of 1D "smooth" shelf tidal solutions as boundary conditions, at the same time as the 2D modified solutions are computed by the model in the interior of the domain. Results express the impact of opposite shelf width anomalies in both tidal amplitude and flow (section 4). Fluid vorticity diagnostic shows that the modified velocity solution outcomes directly from angular momentum conservation in the course of water column stretching and squeezing, when advected across strong along-shelf bathymetry slopes (section 5). Schematic diagrams, summarizing the different barotropic solution obatained for the promontory and submarine canyon configuration, are discussed in section 6.

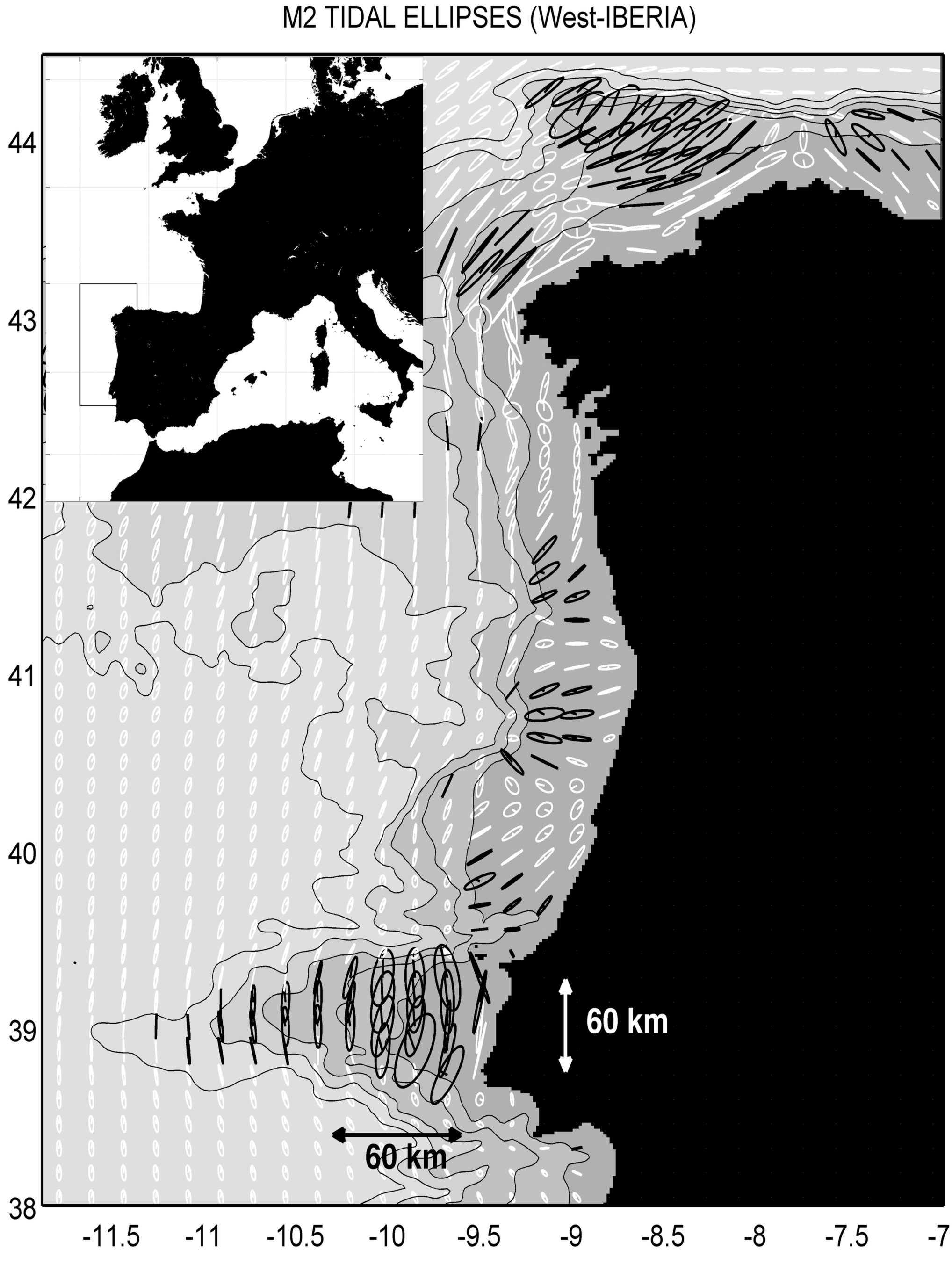

Figure 1: M2 tidal ellipses along the West-Iberian margin (Quaresma & Pichon 2011). The white ellipses represent counter-clockwise rotation and the black ellipses clockwise rotation. The polar axis, traced inside each ellipse, represents the velocity phase and expresses the M2 velocity vector at a certain instance. Isobaths of 200 m, 500 m, 1000 m, 2000 m, 3000 m and 4000 m were added to help interpretation.

2. Solutions over quasi-straight shelves

a. Theory

[8] The Laplace tidal equations (LTE) have been used as the basic formulation of the dynamical theory of barotropic tides. When vertical integrated and using the hydrostatic relation, to replace pressure by free surface elevations, η, these equations take the form (under the *f*-plane approximation),

$$\begin{cases} u_t + u u_x + v u_y - f v & = & -g(\eta-\eta_e)_x + \tau_{bx}/\rho H \\ v_t + u v_x + v v_y + f u & = & -g(\eta-\eta_e)_y + \tau_{by}/\rho H \\ \eta_t + \left[(H+\eta)u\right]_x + \left[(H+\eta)v\right]_y & = & 0 \end{cases} \qquad (1)$$

where the x and y subscripts represent the cross-shelf and along-shelf directions and t the time derivate. The symbols u, v, f, g, η, ρ and H stand respectively for the x and y velocity components, inertial frequency, gravity, sea-surface elevation, water density and mean depth. The astronomic tidal forcing is included in equations by an equivalent sea-surface vertical displacement, η_e, and seabed friction is expressed by a bottom drag related-stress (τ_{bx},τ_{by}). The subscripts specify the derivative with respect to the x, y directions and time, t.

[9] Over small regions of interest, such as continental shelves, the tidal forcing term can be neglected and tides are usually treated as freely propagating waves (Defant, 1960). On the other hand, small tidal amplitudes (relative to the continental shelf depth) and weak current velocities (relative to phase speed) enable the LTE linearization. Non-linear tidal effects are subject of several precedent works (Robinson, 1981; Garreau & Mazé, 1992; Maas & Zimmerman, 1987). Prandle (1997) evaluates the impact of bottom shear stress in the vertical structure of tidal velocity profiles. Single-point analytical solutions show that for weak super-inertial tidal velocities (< $0.1 m.s^{-1}$), over mid-latitude shelves (*30-50ºN*) deeper than *25m*, bottom (and internal) friction is only of secondary importance. Under these circumstances, one can neglect bottom friction and use depth integrated (2-D) frictionless models to accurately predict tidal flow. Moreover, May (1979) shows that the vertical structure of tidal ellipticity (including the sense of rotation) is feebly modified by bottom friction, which small impact is restricted to bottom boundary layers, rarely thicker than 10 m high for velocity magnitudes <

$0.1 m.s^{-1}$. The previous assumptions, discussed by Quaresma (2012), enable the LTE simplification in the form:

$$\begin{cases} u_t - f v = -g\eta_x \\ v_t + f u = -g\eta_y \\ \eta_t + (Hu)_x + (Hv)_y = 0 \end{cases} \qquad (2)$$

[10] Equations (2) can now be derived with respect to time to eliminate all variables in favour of η, to formulate a general equation of the sea-surface height along an arbitrary topography (Clarke & Battisti, 1981):

$$\eta_{xxt} + \eta_{yyt} + \frac{H_x}{H}\left(f\eta_y + \eta_{xt}\right) + \frac{H_y}{H}\left(\eta_{yt} - f\eta_x\right) - \left(\frac{\partial^2}{\partial t^2} + f^2\right)\frac{\eta_t}{gH} = 0 \qquad (3)$$

[11] Equation (3) can be solved analytically by reducing the number of variables under certain approximations. The tidal solution over continental margins is commonly computed by taking into consideration a monotonous shelf profile, along a straight coastline ($H_y = 0$). This method is valid for "smooth" continental margins, where along-shelf topographic variations are usually weaker than the strong cross-shelf bathymetry gradients imposed by continental slopes ($H_x >> H_y$). This approximation reduces (3) to the following form:

$$\eta_{xxt} + \eta_{yyt} + \frac{H_x}{H}\left(f\eta_y + \eta_{xt}\right) - \left(\frac{\partial^2}{\partial t^2} + f^2\right)\frac{\eta_t}{gH} = 0 \qquad (4)$$

[12] Narrow continental margins (< 10^2 km) represent small obstacles to the Kelvin wave dispersion (wavelength of the order of 2×10^3 *km*), which propagation can be approximated by a constant alongshore wavenumber, l. Assuming a monochromatic tidal wave M2 frequency, ω, this parameter becomes then function of the near deep-ocean depth by $\omega / \sqrt{gH}$. Focused on the cross-shelf solution of tidal harmonics, one can find the roots of (4) in the waveform taking $\eta(x)e^{i(\omega t - ly)}$, where alongshore dependency is fixed by deep-ocean Kelvin wave propagation. Time dependency $\partial / \partial t$ is replaced by $i\omega$ and conversely $\partial^2 / \partial t^2$ by $-\omega^2$. Similarly, $\partial / \partial y$ can be replaced by $-il$ and $\partial^2 / \partial y^2$ by $-l^2$:

$$\eta_{xx} + \frac{H_x}{H}\eta_x + \left(\frac{\omega^2 - f^2}{gH} - \frac{H_x}{H}\frac{f}{\omega}l - l^2\right)\eta = 0 \qquad (5)$$

[13] Finally, by rearranging the equations (2), where time and alongshore variations are replaced by the harmonic terms define earlier, a general equation system for the cross-shelf tidal current velocity profiles is formulated by (Das, 1997):

$$
\begin{aligned}
u &= \frac{g}{\omega^2 - f^2}\,(i\omega\eta_x - ilf\eta) \\
v &= \frac{g}{\omega^2 - f^2}\,(\omega l\eta - f\eta_x)
\end{aligned}
\qquad (6)
$$

b. Cross-shelf profiles

[14] Equations (5) and (6) can be solved to obtain both sea-surface height and tidal currents across regular continental shelves. As an initial value problem, one can impose the tidal amplitude at the coast η (x = 0), a null cross-shelf velocity component at this border, $u_{x=0} = 0$ and solve it with an explicit iterative method as the common fourth-order Runge–Kutta (Jézéquel & Mazé, 2001). This method is applied next to obtain the semi-diurnal tide solution (ω = 1.4 × 10^{-4} s^{-1}; $l_{H = 4000m}$ = 7.0 × 10^{-5} m^{-1}; $\eta_{M2}(x_0)$ = 1 m) across right bounded narrow continental margin profiles located in an f-plane fixed at 40ºN (f_0 = 9.35 × 10^{-5} s^{-1}). These parameter values are selected to reproduce the semi-diurnal lunar tide harmonic (M_2) observed in Figure 1. Two different shelf width solutions (20 and 80 km) are computed in order to be used as boundary conditions in section 3. The adopted continental margin width (Figure 2) represent less than 5% of the Rossby radius (C_0 / f) for a Kelvin wave propagating with phase speed (C_0) function of an abyssal plain depth of H_3 = 4000m. By taking this narrow continental margin case, and disregarding bottom friction, one can set the tidal *wavenumber* to $l = \omega / (gH_3)^{1/2}$.

$$
\begin{cases}
H(x) = H_1 - m x, \quad m = \dfrac{H_2 - H_1}{W_1}, & W_1 < x < 0 \\[2ex]
H(x) = H_2 - (H_2 - H_3)\sin^2 \dfrac{\pi}{2}\left(\dfrac{x - W_1}{W_2}\right), & W_1 + W_2 < x < W_1 \\[2ex]
H(x) = -4000\,m, & 450km < x < W_2
\end{cases}
\qquad (7)
$$

[15] The idealized continental margins are right bounded by a straight coastline of constant depth (H_1 = 15m) that closes the domain at x_0 (Figure 2). Their shelf extends offshore, across W_1, to the shelf-break (H_2) with a constant slope, m = 3.25 × 10^{-3}. A continental slope extends, across W_3, to the abyssal plain (H_3), shaped by a sinusoidal function (7). Both profiles (one narrower than the other) are built with the same functions and different parameters (see Figure 2 and Table 1).

Table 1. Cross-shelf bathymetry sections used as northern and southern boundary configurations at the 2D submarine canyon and promontory simulations. Dimension widths are in the x-direction.

	Wider Profile (WP)	*Narrower Profile (NP)*
coastline depth	$H_1 =$ 15 m	
abyssal plain depth	$H_3 =$ 4000 m	
continental slope width	$W_2 =$ 60 km	
shelf-break depth	$H_2 = 275$ m	$H'_2 = 80$ m
shelf-width	$W_1 = 80$ km	$W'_1 = 20$ km

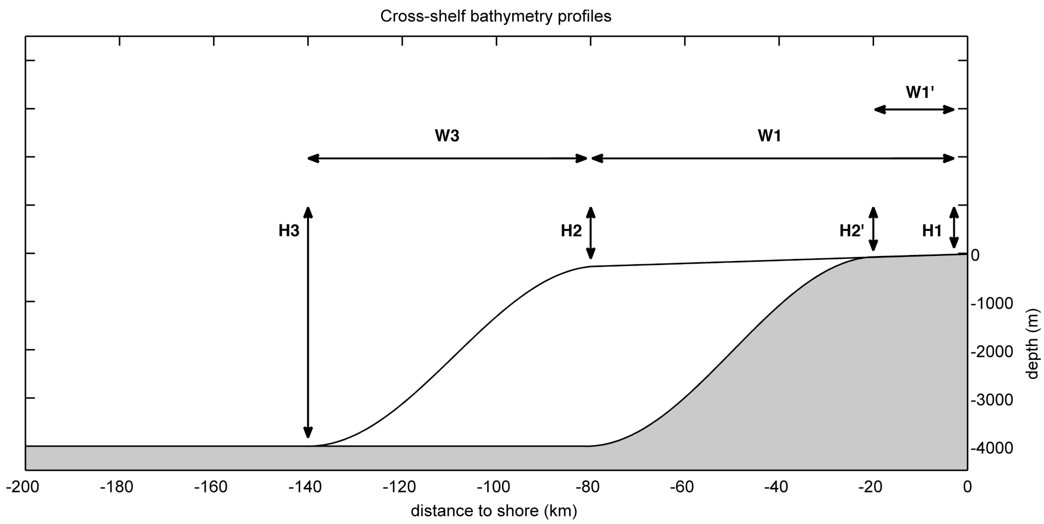

Figure 2. Cross-shelf bathymetry section used as northern and southern boundary of the promontory (area) and canyon configuration (line). The same profiles represent the promontory (line) and canyon (area) cross-shelf sections at $y = 0$. H_1 = depth at the coast; H_2 = depth at the shelf-break; H_3 = depth at the ocean plain; W_1 = shelf-width; W_2 = continental-slope width. See Tables 1 and 2 for detailed values.

[16] Cross-shelf profiles are obtained from (5) and are presented in Figure 3 for the narrower shelf profile (NP) and in Figure 4 for the wider shelf profile (WP). The NP solution reveals the main Kelvin wave behaviour, with maximum sea-surface amplitude (SSA) at the coast and an offshore decay. Over the continental shelf, where the Kelvin wave semi-geostrophic balance breaks apart, the SSA slope increases and the cross-shelf velocity component, u, appears. This behaviour is followed by an equivalent decrease of the along-shelf velocity component, v. The tidal flow acquires counter-clockwise rotation, as a distorted Kelvin wave. Out of the shelf, the wave solution regains the semi-geostrophic equilibrium, where tide wavelength and phase speed mach the imposed *wavenumber*. This balance recovers the Kelvin wave solution, with the cross-shore velocity component decaying drastically and the alongshore v-component becoming predominant. Offshore, both SSA and v decrease exponentially (characteristic of the Kelvin mode).

[17] The wider shelf profile (WP) also shows the main Kelvin wave-distorted behaviour (Figure 3). However, its larger shelf reduces the offshore SSA once it reproduces the same SSA slope as NP. This fact results from the same η_{M2} imposed at x_0 and should be interpreted in the opposite direction: A similar Kelvin wave propagating along these two different profiles, will be amplified by the wider shelf and consequently will increase its amplitude at the coast. The larger shelf also enables the re-orientation of the tidal ellipses to become perpendicular to coast. Both NP and WP profiles show similar ellipses magnitude and eccentricity since these parameters are function of the slope value of the plain shelf ($m = 3.25 \times 10^{-3}$), identical for NP and WP. If one changes the previous profiles configuration (namely the depth at the coast and the cross-shelf topography gradients) it is possible to verify that near the coast the alongshore velocity component is function of the local depth and that tidal ellipse eccentricity is function of the topography gradient.

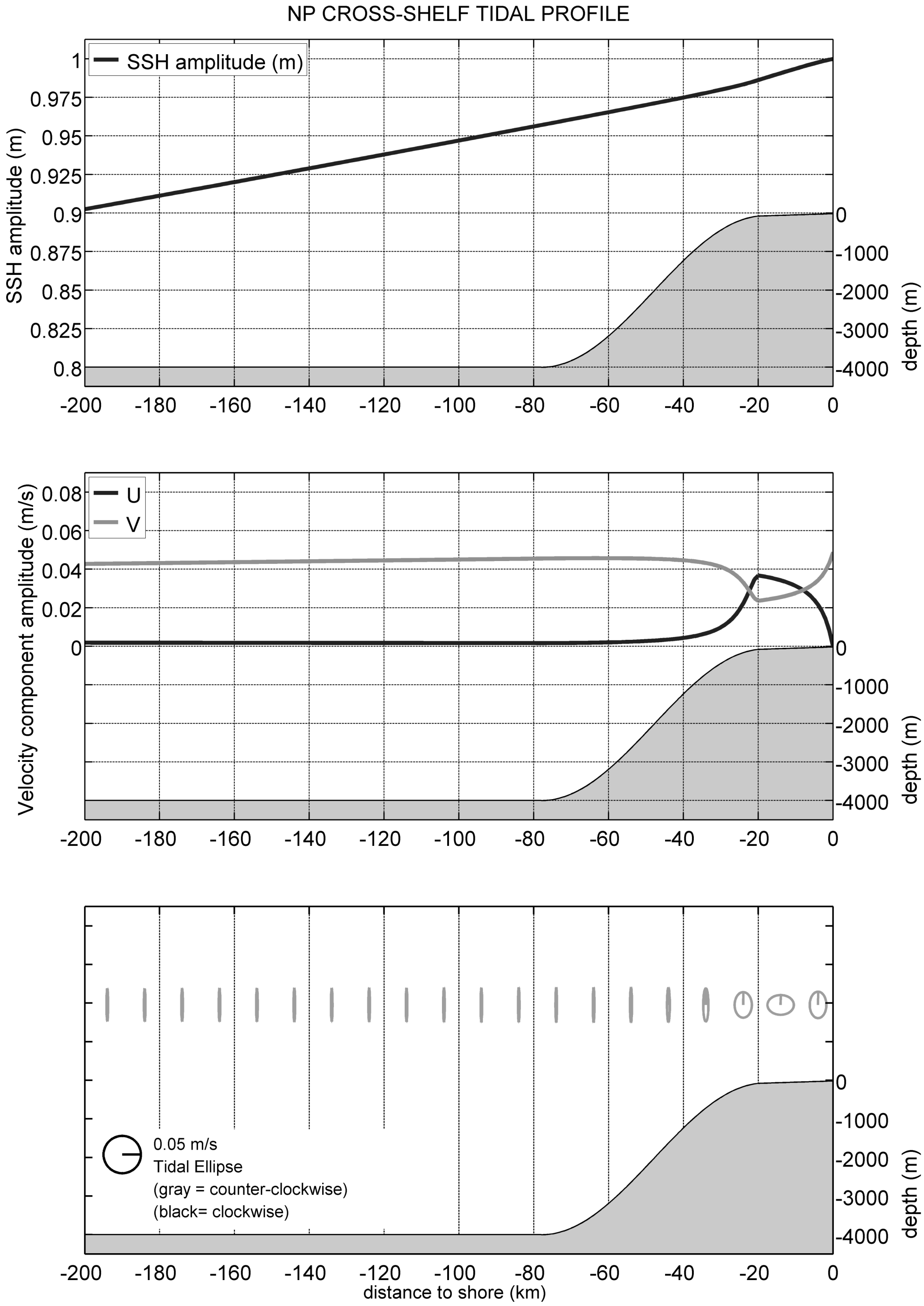

Figure 3. The “smooth-shelf” tide solution over 20 km shelf width continental margin. This cross-shelf profile (NP) corresponds to northern and southern limits of the 2D promontory configuration and also to the principal submarine canyon’s cross-shelf profile. This tidal solution is imposed as northern and southern boundary conditions in the 2D promontory model configuration.

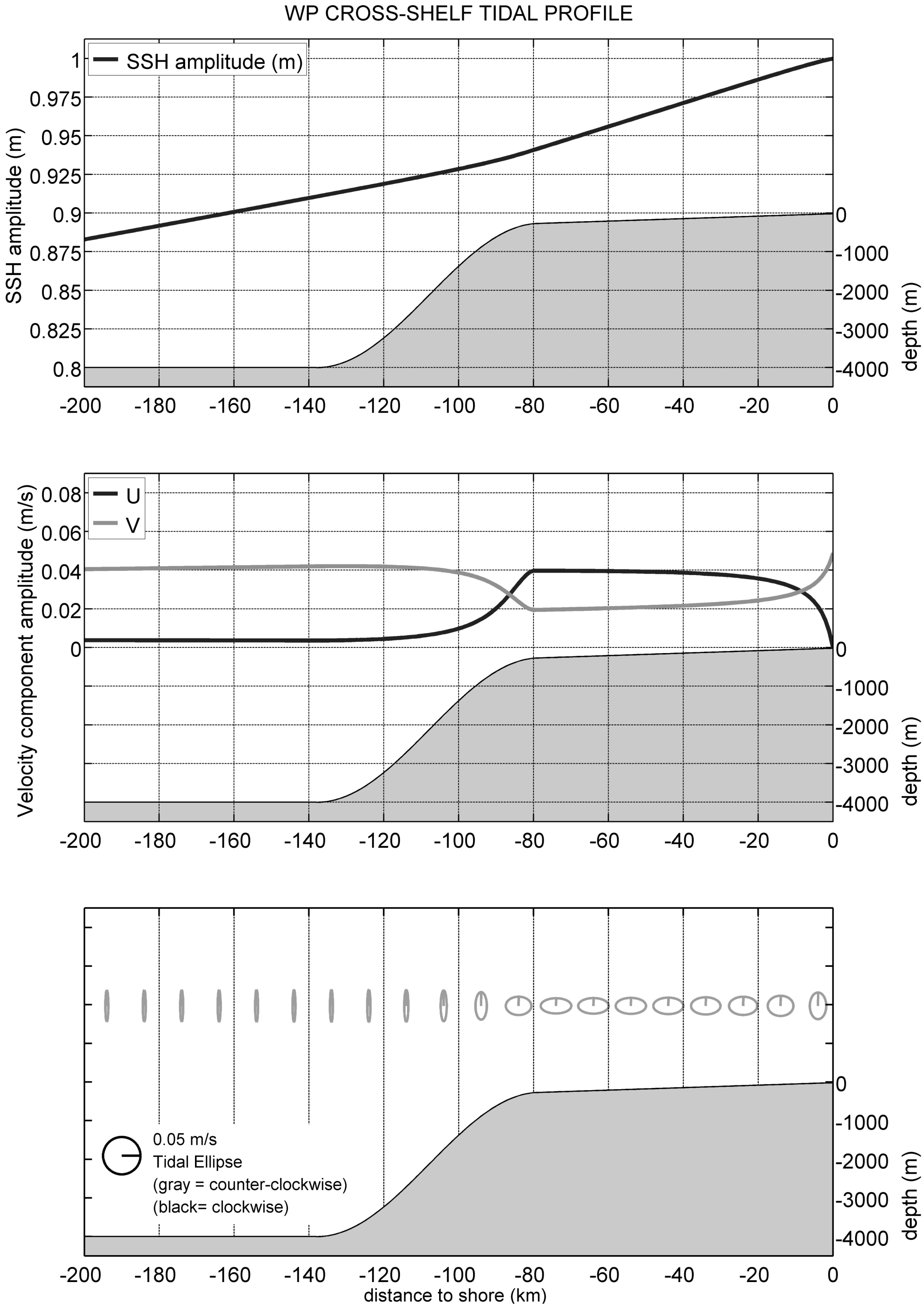

Figure 4. The “smooth-shelf” tide solution over 80 km shelf width continental margin. This cross-shelf profile (WP) corresponds to northern and southern limits of the 2D canyon configuration and also to the principal promontory’s cross-shelf profile. This tidal solution is imposed as northern and southern boundary conditions in the 2D canyon model configuration.

3. Solution over irregular shelves

[18] When geomorphic shelf features, such as submarine canyons and promontories, impose significant along-shelf bathymetry gradients, the previous 1D solution cannot by applied and the complete two-dimensional elliptic Laplace tidal equation (3) must be solved (boundary value problem). The 2D coastal bounded tidal solution is thus a partial differential equation problem, solved here over idealized abrupt features (section 3.b) by a finite difference primitive equation model (section 3.a) forced by 1D analytical solutions (section 3.c).

a. Numerical Model

[19] The linear Laplace tidal primitive equations (2) are solved by a finite-difference, free-surface shallow water model (Bleck & Smith 1990) under a regular staggered mesh grid (type Arakawa-C). The model employs an explicit time-splitting scheme to separate the fast barotropic gravity waves prognostic from the slower baroclinic modes in both mass and momentum conservation equations (Morel et al., 2008). In the present work, BS1990 is configured with a single isopycnal layer. Advection and viscosity terms (bottom and turbulent frictions) are neglected from the momentum equations (1). The shallow water equations from BS1990 are then linearized to become strictly equivalent to (2) and the model to be reduced to its barotropic time-step. Monochromatic 1D tidal solutions are computed from CB1981 using a similar iterative method as used by JM2001 and used as boundary conditions at the three open boundaries of the numerical model (where the tide wave propagation is approximated by a constant along-shore wavenumber, l). No sponge layers are used.

b. Idealized Topography

[20] Two-dimensional irregular continental margins are simulated in the present study by single shelf width anomalies, shaped symmetrically along regular narrow shelves. Two distinct bathymetry configurations are built aiming the evaluation of the impact of a positive (promontory) and a negative (canyon) anomaly on the barotropic tide solution. Each topographic configuration is built in three steps. Firstly, a XY-plane grid ($450 \times 540km$) of constant depth $H_3 = 4000\ m$ is created with *one* arc-minute resolution ($dx = dy \sim 1.8\ km$). Secondly, a narrow continental margin, assembling a plain shelf and a sinusoidal slope, is added to the eastern border. The shelf width varies in the two configurations (*20* and *80 km*) in order to be reshaped by opposite topographic features: a narrower margin with a cross-section profile NP configures the promontory topography, while a wider margin with the cross-section profile WP configures the submarine canyon (Figure 2). Finally, each regular margin is reshaped in the middle of the domain by either positive or negative shelf width anomalies (Table 2) to feature respectively a promontory and submarine canyon (Figure 5). The cross-shelf anomaly length is set to $W_3 = 60km$ (*x-direction*) and the along-shelf to $L_1 = 60km$ (*y-direction*).

Table 2. Geomorphic shelf-features configuration set by distinct shelf width modulation. Dimension widths are in the x-direction and length in the y-direction.

	Canyon	Promontory
Anomaly width (x-direction)	W_2 = - 60 km	W_2' = +60 km
Anomaly length (y-direction)	L_1 = 60 km	
Cross-shelf profile of the configuration limits	Wider shelf (WP)	Narrower shelf (NP)
Cross-shelf profile of the feature's principal x-axis (*y=0*)	Narrower shelf (NP)	Wider shelf (WP)

[21] The topographic modulation set in Table 2 reproduces the abrupt shelf widening (promontory) and narrowing (canyon), as along-shelf variations of the distance between the coastline and the shelf-break (W_{cs}) by a sinusoidal function (8).

$$\begin{cases} W_{cs}(y) = W_1\,, & -270km < y < -L_1/2 \\ W_{cs}(y) = W_1 + W_2 \sin^2\left(\dfrac{\pi}{2} + \dfrac{y\pi}{L_1}\right), & -L_1/2 < y < L_1/2 \\ W_{cs}(y) = W_1\,, & L_1/2 < y < 270km \end{cases} \qquad (8)$$

[22] The continental slope width W_3 is invariant along both configurations. From this, promontory and submarine canyon feature rises from each NP and WP continental margin (Figure 6), sharing similar cross-shelf ($\partial H/\partial x$) and along-shelf slopes (H_y). It should be noted that this option sets the NP cross-shelf profile common to the submarine canyon cross-section ($y = 0$) and to the northern and southern limits of the promontory configuration. Similarly, the WP cross-shelf profile becomes common to promontory cross-section ($y = 0$) and to the northern and southern limits of the submarine configuration (Figure 2).

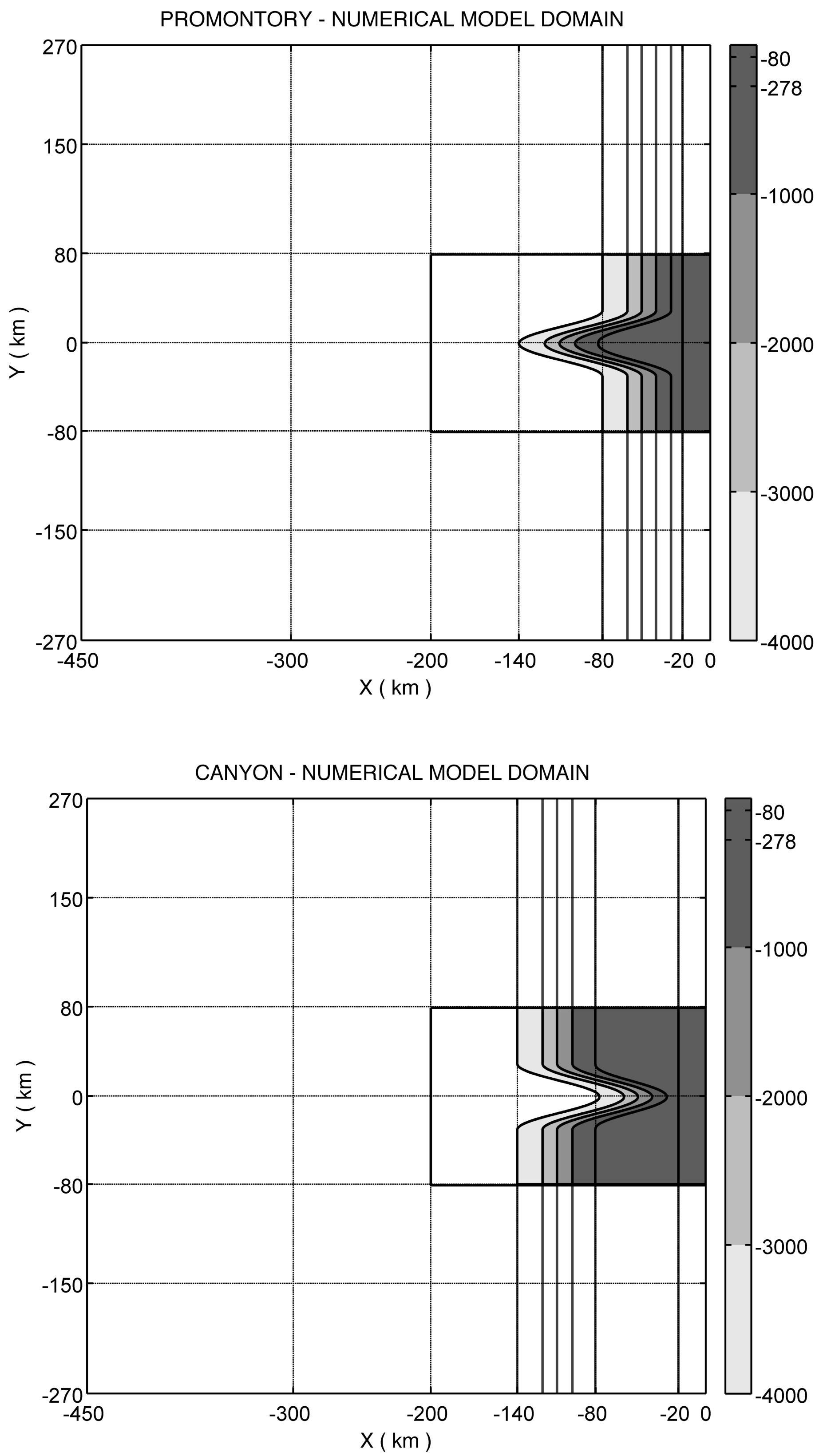

Figure 5. The numerical model domain, and the sub-domain of analysis (shaded here and represent in 3D in Figure 6), for: a) promontory and b) submarine canyon configuration. The abrupt geomorphic features are shaped symmetrically in the middle of each domain, away from open borders where "smooth" shelf boundary conditions are forced.

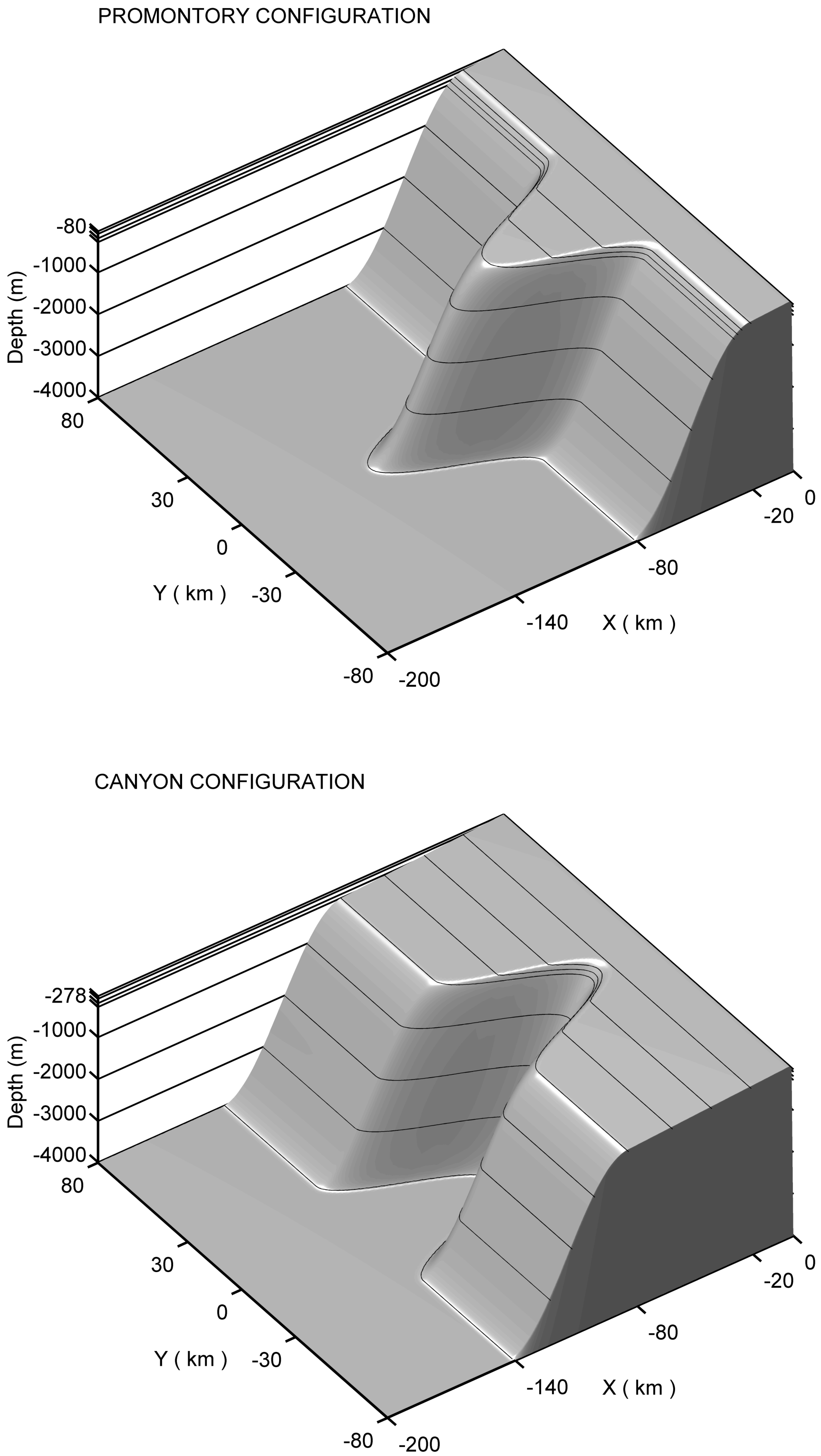

Figure 6. Idealized geomorphic shelf features: a) promontory and b) submarine canyon. Here, a zoom is made focusing the sub-domain of analysis (represented here after in the following figures). The outer shelf-break depth is indicated for each feature in the z-axis. Regular spaced isobaths help the interpretation of the bathymetry slopes. Notice that the present topography configuration give rise to bottom slopes, $m^2 = (\partial H/\partial x)^2 + (\partial H/\partial y)^2$, stronger at the faces of the promontory and canyon ($m_{max} > 0.3$) then over the invariant continental margin slope ($y < -L_1/2$ and $y > L_1/2$) where the unique x-direction slope is $m_{max} < 0.15$.

c. Boundary Conditions

[23] Figure 5 shows that each topographic feature, where $H_y \neq 0$, is shaped at a small region in the middle of the numerical XY-plane, away from each open limit where the smooth-shelf approximation is assured ($H_y = 0$). It is important to remember here that the numerical model solves the linear Laplace tidal equation system (3) and therefore no diffusion is expected in the numerical solution. On the other hand, tidal excursion (U/ω) is very small when compared to the distance between the topographic obstacles and the open boundaries. Previous assumptions let us suppose that the tidal solutions near the open boundaries are predominantly function of the local cross-shelf bathymetry section. This hypothesis enables the use of the precedent 1D solutions (section 2.b) as the northern and southern boundary conditions (SSA, meridional velocity component amplitude, $\boldsymbol{v}$, and respective phases function of y and l) to be forced in the 2D numerical model. The narrower shelf solution *NP* (Figure 3) sets the northern and southern boundaries of the promontory configuration; the wider shelf profile WP sets the northern and southern boundaries of the submarine canyon configuration (Figure 4).

[24] The offshore boundary condition imposed at x = -450km is also calculated by a similar 1D "smooth" shelf approach. The analytical model is applied at each consecutive cross-shelf section (y = const), from south to north. The solution values of SSA, longitudinal velocity component amplitude, **u**, and respective phases (function of y and l), calculated at x = -450km for each cross-section from -270km < y < 270km compose the offshore boundary condition of the 2D numerical model. For both bathymetry configurations, this approximation is validated by similar model results, obtained under different XY-plane domain extensions (from 450km to 900km, not shown here). At the coast, the cross-shelf velocity component is set to null ($u_{x=0,\,y} = 0$).

4. Results

[25] The simulation starts with an ocean at rest forced by monochromatic M2 tide at the open boundaries, with an exponential growth. This ramp-up state enables a smooth settling of the tidal current solution and lasts for 5 semi-diurnal cycles, after which the wave amplitude reaches its predefined value at the north and south coastlines (*1m*). The solution in the interior of the domain is driven by the boundary conditions and after this ramp-up phase it is in equilibrium with the adopted wavenumber. The 2D tidal solution is here after represented and discussed for the sub-domain of study (Figure 5) and result from harmonic analysis of the SSH and velocity time-series. In the outer parts of the domain, the solution converges to the boundary conditions, as these are imposed without any sponge layer.

a. Sea-Surface Amplitude

[26] Submarine promontories extend the continental margin offshore, expressing positive anomalies to the shelf-width. At the coast, the promontory slows down the long gravity waves and decreases their amplitude compared to the referenced 1D solution (Figure 7). Both impacts can be interpreted by the 1D solution, as a direct result of the widening of the shelf width imposed by this configuration (section 2.b).

[27] The positive shelf width anomaly modifies the sea-surface amplitude (SSA) solution mainly across-shelf (Figure 7). This can be verified comparing the SSA gradients (η_x, η_y) across section $y = 0km$ ($\eta_x \sim 0.08m/140km$) and along sections $x = -80km$ and $x = -20km$ ($\eta_y < 0.02m/80km$). Thus the present SSA modulation reinforces the across-shelf pressure gradient ($-gp_x$), especially at high tide and low tide phases when the Kelvin's cross-shelf SSH gradients are also maximum ($|\eta_x| = max.$).

[28] Submarine canyons constrict the continental margin onshore, expressing negative anomalies to the shelf-width. The corresponding tidal solution shows important modulation of the SSA over the surrounding region of the obstacle. The SSA is reduced around the canyon (Figure 7), where its deeper cross-shelf section accelerates the Kelvin wave. Both impacts can be interpreted by the 1D solution, as a direct result of the narrower longitudinal cross-feature section, which is identical to the NP boundary profile imposed in the promontory configuration (section 2.b).

[29] Contrary to the promontory configuration, the canyon distorts the SSA solution in both along-shelf and across-shelf directions. This can be verified comparing the respective gradient, across section $y = 0km$ ($\eta_x \sim 0.06m/140km$) and along sections $x = -20km$ ($\eta_y \sim 0.04m/80km$). Equivalent gradients show that at high tide and low tide phases, when $|\eta_x| = max.$, important along-shelf pressure gradients ($-gp_y$) will also be present alongside cross-shelf ($-gp_x$). Both gradients introduce significant SSA anomaly that increases regionally the distortion of the Kelvin wave solution.

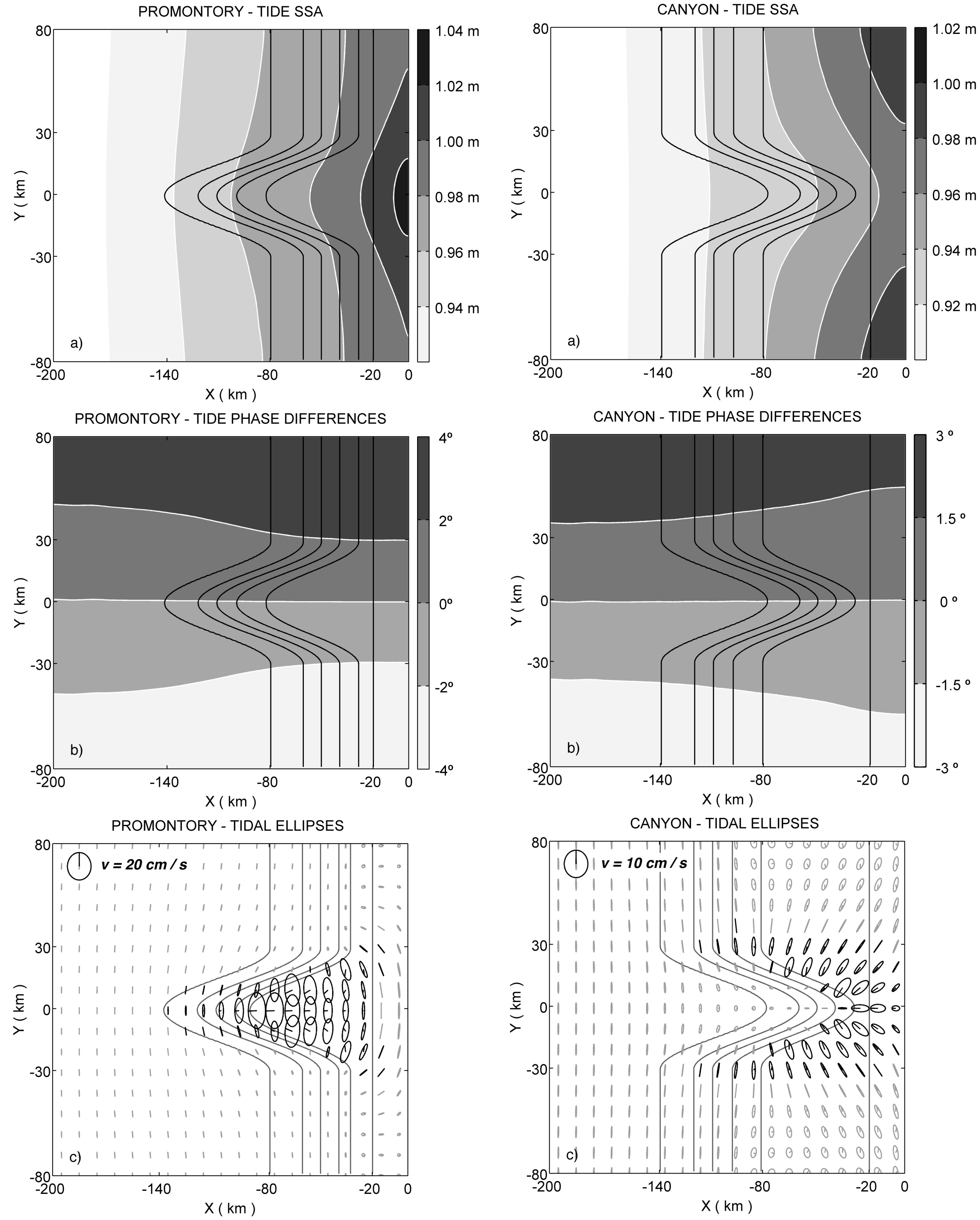

Figure 7. The barotropic solution for M2 super-inertial tide over positive (promontory) and negative (canyon) shelf width anomalies. The topographies are represented by the following isobaths contours: 80, 278, 1000, 2000, 3000 and 4000m. The tide wave a) SSA and b) Sea-surface Phase differences relative to $y = 0$ (both represented by contour levels) are calculated by harmonic analysis of the sea surface height solution. c) Tidal velocity ellipses are represented in gray for counterclockwise rotation and the black clockwise. Their axis indicates velocity current vectors at mid-flood tide phase.

[30] The symmetric structure of each geomorphic feature is expressed in the solution's symmetry. Although the major SSA modulations can be interpreted by the varying 1D cross-shelf profiles, an additional distortion can be observed along-shelf (Figures 7). This distortion is observed around sections $y = -30km$ *and* $y = 30km$, where SSA anomalies exceed the canyon's length (L_1), with a smooth transition between each cross-shelf NP and WP profiles.

b. Current Velocity

[31] As seen above, canyons and promontories impose distinct sea-surface modulation of the tide. The resulting SSA anomalies distort the Kelvin's pressure gradient field and consequently distinct tidal flow solutions are expected over each obstacle. This statement is verified by harmonic analysis of the current velocity time-series, when tidal ellipses are traced.

[32] The velocity solution obtained over the promontory reveal the main Kelvin wave driving mechanism, reinforced over its plateau by the stronger cross-shelf SSA gradient (Figure 7). As expected, the higher velocity magnitudes are established at high tide and low tide, in phase with the driving Kelvin wave (see Figure 8 in section 5.c). The across-shelf pressure gradients drive the water column to climb the promontory slopes, and by continuity its current velocity increases over this shallow water region. However, in clear disagreement with Kelvin's solution, tidal ellipses reduce their eccentricity and reverse their rotation to clockwise (Figure 7), in opposite sense to the 1D solution attained over invariant narrow shelves (section 2.b).

[33] The velocity solution obtained over the canyon configuration does not mach the Kelvin wave solution (Figure 7). Tidal ellipses are amplified and reoriented perpendicular to the canyon isobaths. In addition, ellipses reduce their eccentricity and reverse their rotation sense to clockwise, in opposite sense to the 1D solution attained over invariant narrow shelves (section 2.b). This solution reveals a convergent tidal flow, entering the canyon during the ebb-tide phase, and a divergent flow coming out of it during flood tide (see Figure 11 in section 5.d). This water ventilation mechanism is 90º out-of-phase (in time) between the maximum pressure gradient fields (verified at high and low-tide) and the stronger convergent/divergent tidal flows (verified at mid-ebb and mid-flood phases).

[34] Both idealized configurations yield important tidal current modulation, forcing the flow to cross the strong bathymetry gradients (isobaths) imposed by each topographic feature. By continuity balance the flow accelerates over the shallow regions and fluid vorticity is created by the consequent stretching and squeezing of the water column. Over abrupt topographic obstacles, the latter process is at the origin of reverse rotation sense of velocity (discussed in the next section).

[35] The previous solutions also highlight the stronger amplification of the tidal currents by the promontory when compared to the canyon configuration (Figures 7). This can be explained by fluid continuity under a Kelvin wave flow, whose ellipses are aligned parallel to the continental slope. As it can be verified by the 1D solutions (Figure 3 and 4), the tidal flow ($\vec{U} \times H$) is larger offshore than onshore. In consequence, promontories represent abrupt obstacles to this volume transport, increasing significantly the fluid velocity over the blocking shallower region. On the contrary, submarine canyons represent obstacles to smaller tidal flows verified over the shelf, resulting in weaker fluid constriction. These differences are also observed in Quaresma & Pichon (2011), where stronger tidal currents are observed over the wider West-Iberian promontories ("Estremadura"; "Finisterra" and "Ortegal"), relative to nearby submarine canyons ("Nazaré", "Aveiro" and "Porto").

5. Analysis

[36] To interpret the previous results, and in particular the reversing of the rotation sense of the tidal ellipses over the abrupt shelf features, a specific analysis is addressed to fluid vorticity, throughout the super-inertial tidal cycle. As the tidal flow crosses the strong along-slope bathymetry gradients, imposed by each topographic obstacle, relative vorticity ($\zeta = u_y - v_x$) will be produced under the principle of angular momentum conservation in frictionless flows, and will modify the 2D linear solution. Four consecutive SSH tidal instants are considered for the present analysis (taking T_{M2} as the M2 tidal harmonic period): high tide (t_0), mid-ebb tide ($t = t_0 + 1/4T_{M2}$), low tide ($t = t_0 + 1/2T_{M2}$) and mid-flood tide ($t = t_0 + 3/4T_{M2}$).

a. Fluid Vorticity

[37] By forcing a semi-diurnal tide at mid-latitude regions, one imposes a super-inertial periodic oscillation. This factor decreases largely the magnitude of the inertial terms in

(2) and the velocity acceleration becomes mainly function of the 2D pressure gradient fields. Yet, when these gradients decrease in magnitude during the tidal cycle (at mid-ebb and mid-flood phase) the angular momentum detained by the fluid will determine the tidal velocity solution. A fluid vorticity term appears in the linear *f*-plane Laplace tidal system under the momentum equations (2), by cross-differentiating them and subtracting. A time derivative of the fluid relative vorticity is obtained as function of its divergence,

$$\zeta_t = -f_0(u_x + v_y) \qquad (9)$$

[38] This relationship shows that if the flow is divergent, i.e. $(u_x + v_y) > 0$, the fluid vorticity decreases, and vice versa. Similar mechanisms can also be expressed in terms of the vertical stretching of the water column. For that, one can replace the horizontal divergence in (9) by expand the derivative of the products in the continuity equation in (2), taking $h = H + \eta$ to obtain,

$$\zeta_t = f_0\left(\frac{u}{h}h_x + \frac{v}{h}h_y + \frac{1}{h}\eta_t\right) \qquad (10)$$

[39] Equation (10) can be rearranged using the total derivative Dh/Dt to get the following PV conservation expression to express the fluid vorticity production when the water column is squeezed in time and/or in space

$$\zeta_t = \frac{f_0}{h}\frac{Dh}{Dt} \qquad (11)$$

[40] When the flow is forced to climb or descend strong topographic slopes, like the ones imposed by the present submarine canyons and promontories, a relative vorticity production takes place as the result of the consequent water column squeezing ($Dh/Dt < 0$, negative vorticity) or stretching ($Dh/Dt > 0$, positive vorticity). This relative vorticity time variation can be assumed as driven mainly by the stretching/squeezing of the water column since the ratio $F = \eta_t / U \cdot \nabla h$ (from equation 10) has a maximum value close to $F = 7.5 \times 10^{-4}$ for a M2 tide wave of one meter amplitude at coast ($U_{max} \sim 0.2 \mathrm{m.s^{-1}}$; $\nabla h_{max} \sim 0.3$), for the both topography configurations described above. A Rossby number, $R = \zeta / f_0$, estimated from results presented in the following section gives $R{\sim}10^{-1}$, which verifies the validity of linearity assumption, in equations (9-11).

b. Flow rotation

[40] Under the present barotropic linear solution and considering the small tidal excursion, the previous ζ production mechanism is restricted to a small area, delimiting each abrupt topographic slope. The surface integral of ζ, along the *x* and *y* directions is for each time instant (*i*),

$$Q_i = \iint (u_y - v_x)\ dx\,dy \qquad (12)$$

[41] While the vorticity production inside these restricted regions can be quantified for small time intervals by

$$\Delta Q_i = \iint f_0 \left(\frac{u}{h} h_x + \frac{v}{h} h_y + \frac{1}{h} \eta_t \right) \Delta t\ dx\,dy \qquad (13)$$

[42] The linear solution implies that these two parameters must be balanced during a complete tidal cycle, where for each time instant, $Q_{i+1} = Q_i + \Delta Q_i$. They are quantified next as diagnostic variables of the flow rotation, demonstrating the mechanism behind tidal ellipse reversing and transient vortex generation in the 2D solutions.

c. Tidal flow over promontories

[43] Fluid vorticity and vorticity production, represented in Figure 8 and Figure 9 at four consecutive SSH tidal instants, shows its concentration over the abrupt along-shelf slopes imposed by the promontory. Taking in consideration these results, the small tidal excursion and the linear momentum formulation, one can define two independent areas delimiting each along-shelf slope, named hereafter south-face (-30km < y < 0km, -100km < x < 0km) and north-face (0km < y < 30km, -100km < x < 0km), where vorticity should be produced and destroyed in a balanced cycle.

[44] Let us start by following the trajectory of the water column, over the south-face, during a semi-tidal cycle: At high tide, when the Kelvin wave solution imposes a maximum northward flow (positive cross-shelf pressure gradient), the water is forced to climb the promontory from the south-face (Figure 8.a). During this period (starting from mid-flood and extending to mid-ebb phases), the water column is continuously squeezed here and thus gains negative vorticity (Figure 9.a), forcing the tidal flow to rotate shoreward (to the right of the current). This anomalous circulation superimposes the northward Kelvin's wave current, becoming dominant at mid-ebb phase (Figure 8.b) when the cross-shelf SSH gradient is absent. At this instant the circulation is being driven by fluid vorticity (Figure 10). From this stage forward, the tidal flow will respond to the increasing Kelvin's SSH cross-shelf gradient and for that rotates southward (Figure 8.c). The water is now forced to descend from the promontory by the south-face and the consequent water column stretching will produce positive vorticity (Figure 9.c), which will reduce the amount of negative vorticity detained previously by the tidal flow, over this southern area (Figure 10). At low tide the fluid vorticity reaches a minimum and the tidal current flows straight to the south.

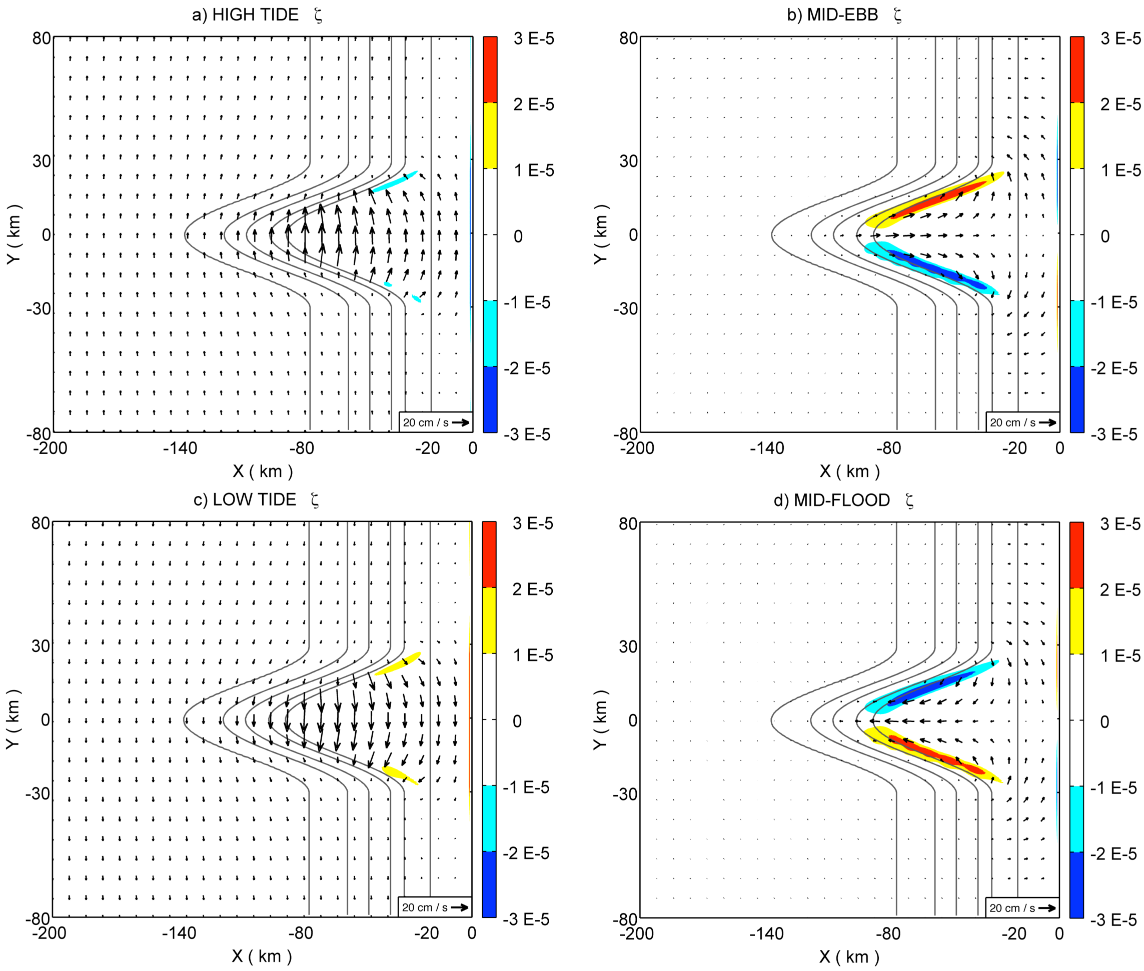

Figure 8. Tidal flow (vectors) and instantaneous fluid vorticity (filled contours, s^{-1}) over a promontory bathymetry configuration at four consecutive tidal instants.

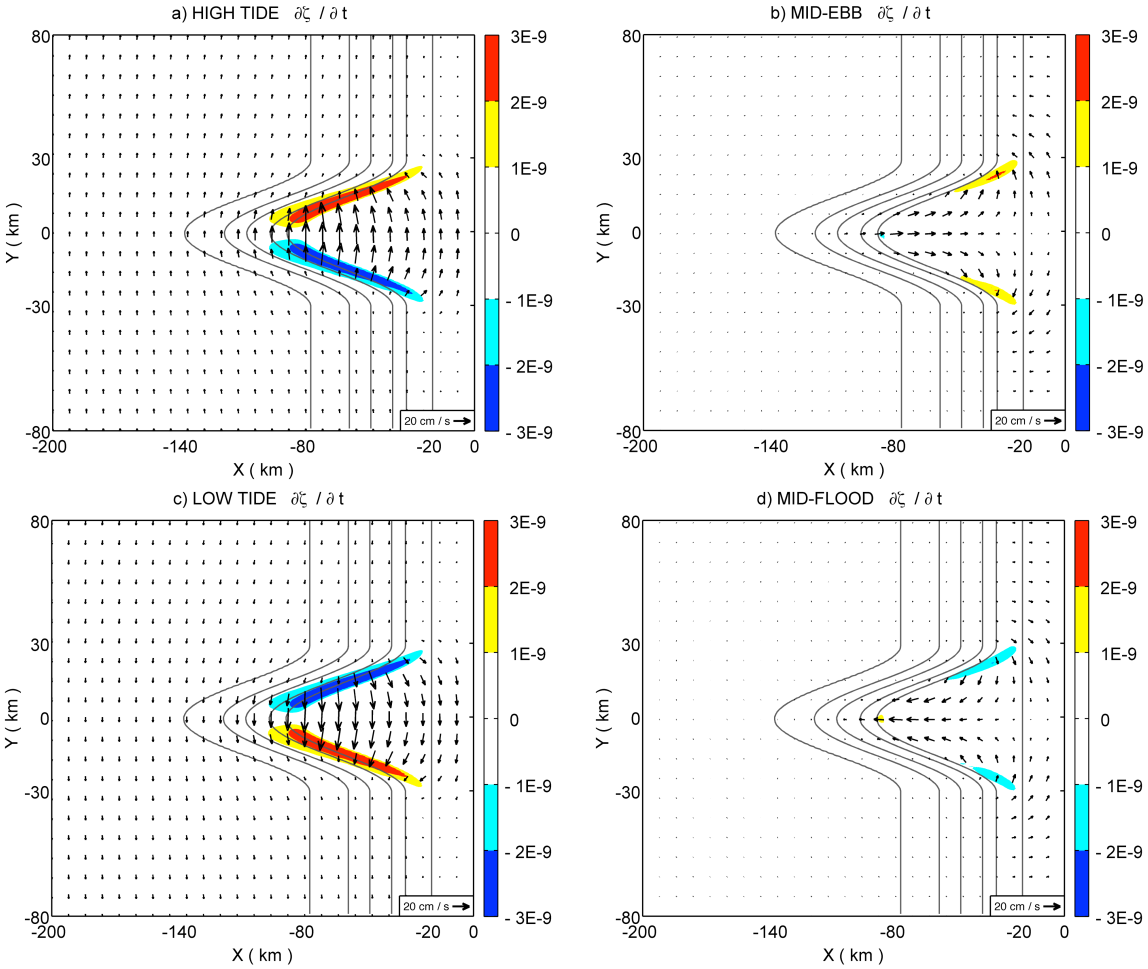

Figure 9. Tidal flow (vectors) and instantaneous fluid vorticity production (filled contours, s^{-2}) over a promontory bathymetry configuration at four consecutive tidal instants.

[45] During the second half tidal cycle, the circulation over the promontory is determined by the tidal flow climbing from the north-face. For this reason one should look now for the vorticity balance occurring over this slope (Figure 10). At low tide, when the Kelvin wave solution imposes a maximum southward flow (negative cross-shelf pressure gradient), the water is forced to climb the promontory from the north-face (Figure 8.c). During this period (starting from mid-ebb and extending to mid-flood phases), the water column is continuously squeezed here and thus gains negative vorticity (Figure 9.c), forcing the tidal flow to rotate offshore (to the right of the current). This anomalous circulation superimposes the southward Kelvin's wave current, becoming dominant at mid-flood phase (Figure 8.d) when the cross-shelf SSH gradient is absent. At this instant the circulation is being driven again by fluid vorticity (Figure 10). From this stage forward, the tidal flow will respond to the increasing Kelvin's SSH cross-shelf gradient and for that rotates northward (Figure 8.a). The water is now forced to descend from the promontory by the north-face and the consequent water column stretching will produce positive vorticity (Figure 9.a) that will reduce the amount of negative vorticity detained previously by the tidal flow, over this northern area (Figure 10). At high tide the fluid vorticity reaches again a minimum and the tidal current flows straight to the north, closing the cycle. This sequence of vorticity production and destruction justifies the clockwise rotation of the tidal ellipses over the promontory, as summarized in Figure 16.

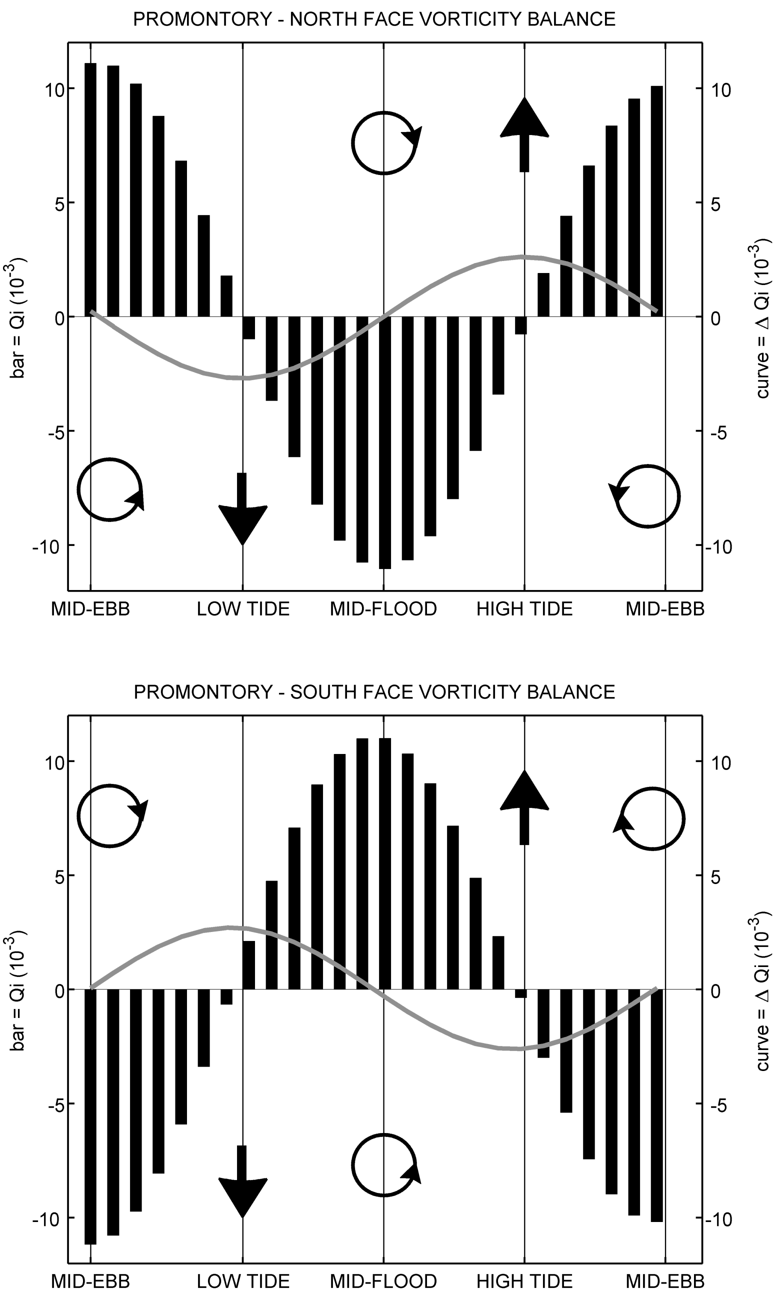

Figure 10. Budget cycle of surface integrated fluid vorticity Q_i (bars, $m^2.s^{-1}$) *vs* vorticity production ΔQ_i (grey curve, $m^2.s^{-1}$), integrated every half an hour, over the promontory's southern slope and northern slope. Q_i is calculated by (12) and ΔQ_i by (13). Schematic vectors are added to help the interpretation of the flow behaviour, over the promontory's plateau, in the 2D solution.

d. Tidal flow over canyons

[46] Similar to the promontory solution, the canyon shows an amplification of the tidal velocities over the surrounding shelf region, as well as tidal ellipse reversing (Figure 7). However, this similar behaviour results form distinct modulation of the tidal current vectors. The concave configuration of the submarine canyon (Figure 6) approaches the two opposite along-shelf slopes into the same vorticity production area. On the other hand, the tidal flow that crosses these isobaths is driven by an already distorted Kelvin wave solution, where an important meridional SSA gradient modulates the 2D solution (section 4). Consequently, the tidal flow converges strongly into the canyon during the ebb tide (Figure 11.b) and diverges out of it during the flood tide (Figure 11.d). During these periods, the cross slope flow is thus in phase along both northern and southern faces of the canyon. In other words, water columns are advected up-slope, or down-slope, at the same tidal instants and thus fluid vorticity is generated with equal signs. As a result, single transient eddies become visible during high tide (Figure 11.a) and low tide phases (Figure 11.c), when the Kelvin's cross-shelf pressure gradients are stronger.

[47] To understand how this vorticity dynamics is added to the Kelvin wave flow and drives a different tidal current solution, let us now follow the water column over the canyon during a complete tidal period. Contrary to the promontory, the present configuration shows single vortex structures trapped over the canyon head, whose length-scale is of the order of the tidal excursion. For this, a single area centred at the canyon head is chosen to close the region of vorticity production (-30km < y < 30km, -100km < x < 0km), where Q_i (equation 9) and ΔQ_i (equation 10) are quantified and balanced in Figure 13. Again, it is important to remember that the solution is obtained under linear equations and consequently no vorticity advection is present due to *tidal rectification process*.

[48] At high tide, when the SSA anomaly is stronger, the 2D wave solution shows the settling of a transient clockwise eddy (Figure 11a). The water circles around the canyon rim, which creates an opposite tidal flow between inshore and offshore tidal circulation. The meridional pressure gradient induced by the distorted Kelvin wave amplitude (Figure 7), forces the current vectors to rotate into the canyon axis. Consequently, water column stretching produces positive vorticity (Figure 12.b) that reduces the negative vorticity anomaly (Figure 11.a). This process inhibits the associated clockwise circulation until it almost disappears at mid-ebb phase (Figure 11.b). At this stage the flow converges directly into the canyon and produces positive vorticity by crossing isobaths (Figure 12.b). As a result, the fluid starts to gain counter-clockwise circulation until an eddy becomes visible at low tide (Figure 11.c).

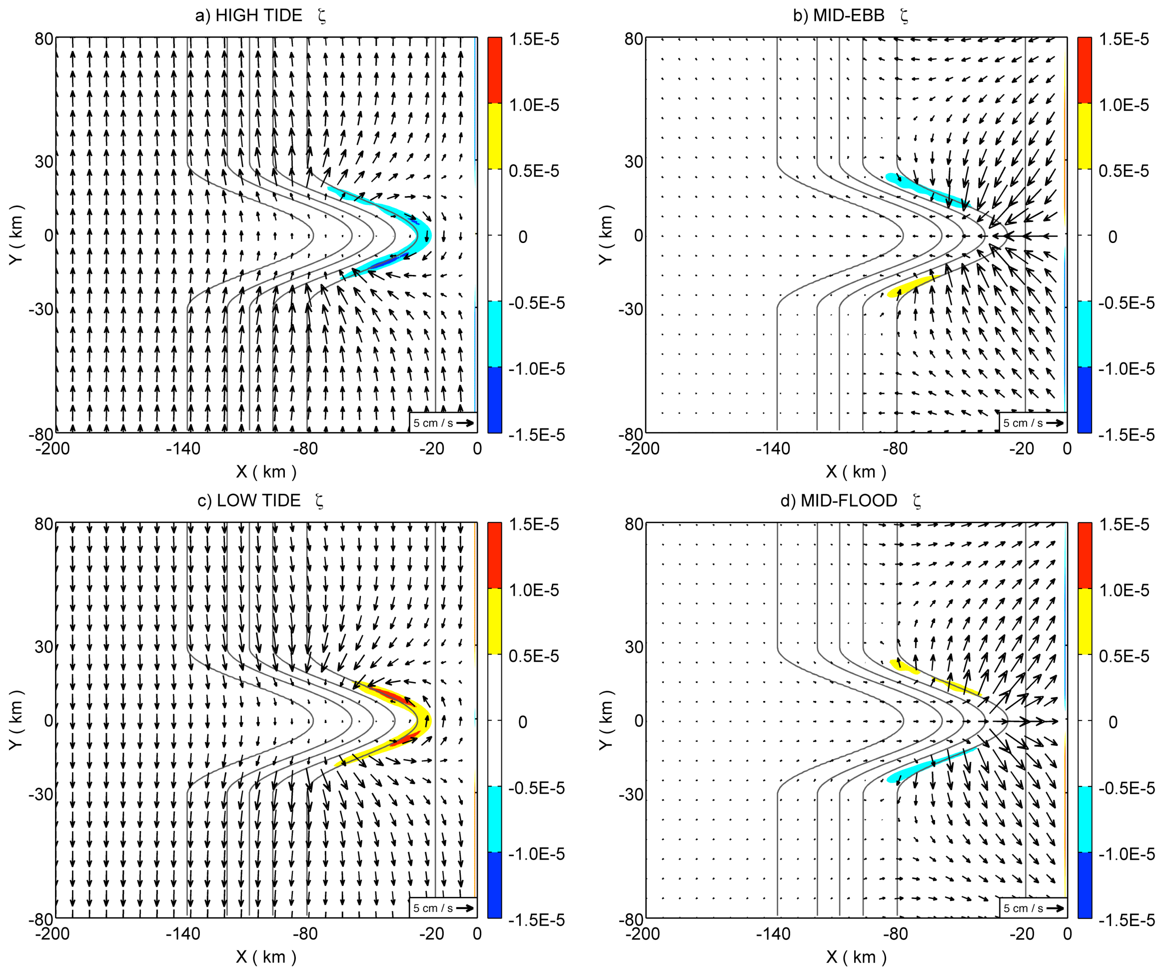

Figure 11. Tidal flow (vectors) and instantaneous fluid vorticity (filled contours, s^{-1}) over a submarine canyon bathymetry configuration at four consecutive tidal instants.

[49] At low tide, the meridional pressure gradient induced by the distorted Kelvin wave amplitude (Figure 7) forces the current vectors to rotate out from the canyon (toward the shelf). Consequently, water column squeezing inhibits the cyclone circulation by negative vorticity production (Figure 12.d). At mid-flood phase the water diverges directly from the canyon axis (Figure 11.d) and the fluid starts to gain counter-clockwise circulation by negative vorticity production (Figure 13), until an eddy becomes visible at high tide (Figure 11.a).

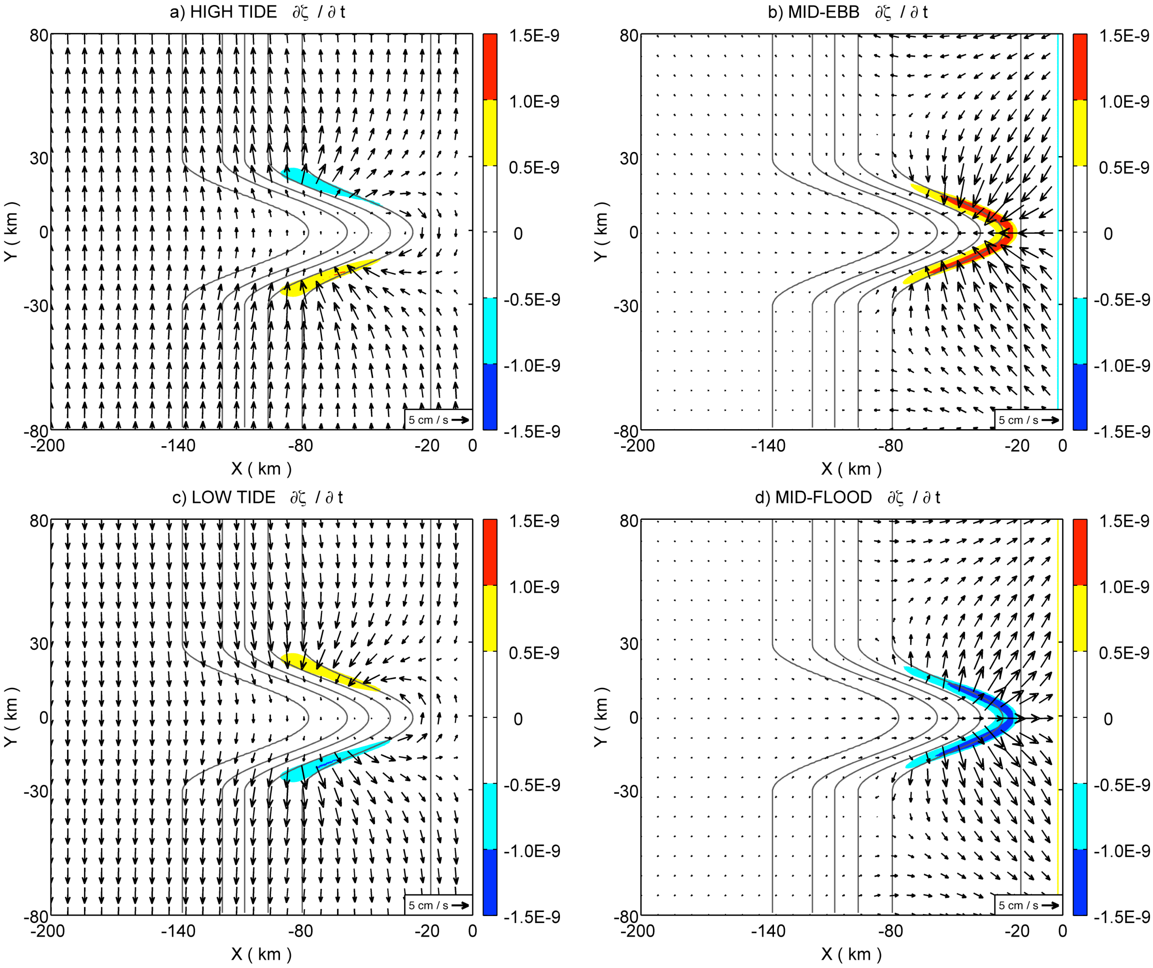

Figure 12. Tidal flow (vectors) and instantaneous fluid vorticity production (filled contours, s^{-2}) over a submarine canyon bathymetry configuration at four consecutive tidal instants.

[50] The previous analysis shows how the SSA anomaly, setup around the canyon, is driving a cyclic production of positive and negative vorticity that generates transient eddy circulation, over this topographic feature. These structures force in the inner-shelf (near canyon head) northward (low-tide) and southward (high-tide) currents that superimpose the Kelvin wave flow. This additional circulation reverses the tidal ellipses around the canyon and seems to reinforce the tidal current in its outer bounds (Figure 11). The vorticity production mechanism is summarized in Figure 16.

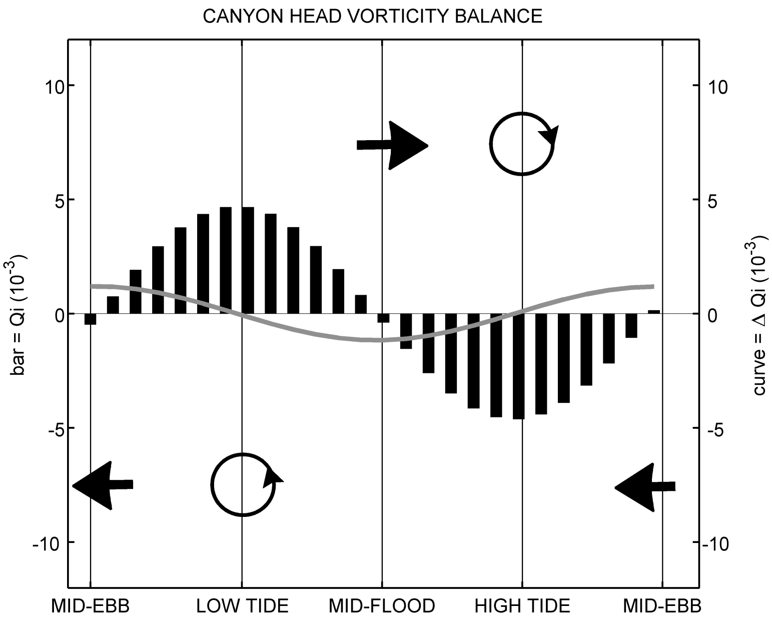

Figure 13. Budget cycle of surface integrated fluid vorticity Q_i (bars, $m^2.s^{-1}$) *vs* vorticity production ΔQ_i (grey curve, $m^2.s^{-1}$), integrated every half an hour, over the canyon-head slope. Q_i is calculated by (12) and ΔQ_i by (13). Schematic vectors are added to help the interpretation of the flow behaviour, over the promontory's plateau, in the 2D solution.

e. Kelvin wave distortions

[51] The sea-surface solutions, obtained over each topographic feature, show different distortions of the driving tidal wave, propagating as a Kelvin mode. The promontory extends the narrower shelf offshore, where the Kelvin wave solution is well established and sets the dominant driving mechanism. For this reason the maximum tidal velocities are obtained at high tide and low tide, when the Kelvin's cross-shelf SSH gradients are also maximum (semi-geostrophic balance).

[52] On the contrary, the submarine canyon cuts in the continental shelf, where the semi-geostrophic balance of the Kelvin wave breaks apart and tidal flow is clearly ageostrophic (concept normaly used to classify flows driven by pressure gradients unbalanced with the Coriolis force). This condition becomes then dominant over the wider shelf WP, with larger and less eccentric ellipses (Figure 7). As a clear exhibition of this state, the canyon solution shows one quarter of period out-of-phase between the maximum tidal velocities and the maximum along-shelf pressure gradients. Moreover, as expected from time derivatives, the solution shows one quarter of period out-of-phase between the maximum vorticity values and the maximum vorticity production (verified also in Figures 10 and 13). If one sets this behaviour in a process chain, along the tidal cycle, will get a half cycle period out-of-phase between the forcing pressure gradients and the consequent eddy circulations.

6. Discussion

[53] Abrupt topographic features, as submarine canyons and promontories, modify drastically the tide solution along narrow continental margins. These shelf width anomalies amplify the tidal velocity and reverse the rotation of super-inertial tidal ellipses. The evaluation performed in the present paper show that this behaviour is due to strong bathymetry gradients imposed by these geomorphic obstacles on the path of the tidal flow (along-shelf direction). Both canyon and promontory configurations distort the tidal SSA, which pressure gradients force the tidal flow to cross tight isobaths. Consequently, fluid vorticity is produced under the principle of angular momentum conservation in frictionless flows, which evaluation shows here its impact on the 2D solution of super-inertial linear tides.

[54] Submarine promontories represent positive anomalies of the shelf-width. That is, they extend these shallow water regions offshore into the deep-ocean region, where the Kelvin mode dominates along narrow continental margins. These structures become then an obstacle to the offshore tidal flow, whose velocity is strongly amplified by fluid constriction (fluid continuity). Maximum velocities are verified during high tide and low tide, in phase with the driving Kelvin mode. The convex shape of the promontory disconnects its north and south faces (along-shelf slopes). Consequently, vorticity production is limited to a small area, delimited over each slope by the small tide excursion. The vorticity production cycle forces the tidal current vectors to rotate clockwise, in opposite sense from the expected one-dimensional solutions (under the “smooth” approximation)

[55] On the contrary, submarine canyons stand for negative shelf width anomalies, forming deep gaps in these shallow water regions. These reliefs become then an obstacle to the tidal flow circulation over the shelves (smaller than offshore). This fact limits the amplification of the tidal current but does not inhibit the vorticity production. Indeed, canyons concentrate the vorticity production in a delimited canyon head region, where the concave configuration connects the two opposite along-shelf slopes (north and south faces). The tidal currents are driven here by an ageostrophic forcing cycle imposed by a very distorted Kelvin wave SSA. Consequently, the maximum velocities are shifted by one quarter of the tidal period, forcing the tidal flow to converge into the canyon during the ebb tide and to diverge out of it during the flood tide. As a result, production of positive and negative vorticity occurs in phase around the canyon head. This mechanism generates transient vortex circulations, observed during high tide and low tide with opposite rotation senses (Figure 16).

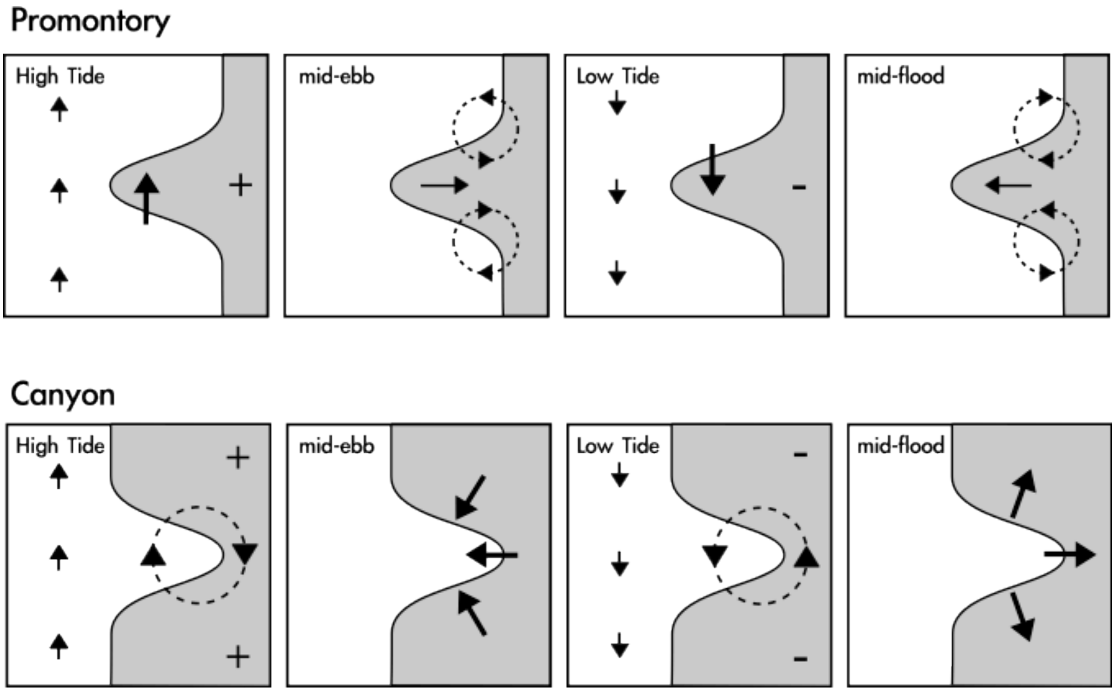

Figure 16. Schematic diagram of the 2D barotropic tidal current solution over two distinct abrupt continental shelf features: a) Promontory; b) Submarine Canyon. Vectors indicate the direction and magnitude of the tidal velocity current. Dashed circles indicate transient vortex circulation and the respective arrows the rotation sense. Signs over the shelf indicate pressure gradient anomalies.

[56] An interesting result from the present tide wave distortions is the fact that both solutions show mass transport from deep-ocean and the shelf, and vice-versa, inverting the character of the Kelvin wave mode over regular continental margins. These results corroborate the idea that irregular margins, namely shaped by submarine canyons and promontories, affect the ocean-margin circulation and are focus regions of enhanced wave energy, mixing, suspended sediment and shelf-sea export (Huthnance, 1995).

[57] Finally, a word should be addressed to the transposition of the present tidal solutions to real irregular continental margins. The barotropic mode dominates the tidal velocity profile in weakly stratified water columns, as for example during winter seasons over shallow continental margins (*0-150m* depth). Such conditions are common to mostly narrow shelf regions surrounding submarine canyons and promontories (exceptions must be considered near river mouths). When upper ocean stratification is present, baroclinic modes rise and modify the current vertical profile. Nevertheless, the depth-integrated velocity should reproduce the present barotropic solution if nonlinear effects are neglected and the amount of energy dissipated from the surface tide to the internal tide is small, ~10% (Wunsch, 1975). Baroclinic tidal solutions are subject of a complementary work (Quaresma & Pichon, Part II), which discuss the generation and scattering of internal tidal modes over the same idealized bathymetry features.

References

Bleck, R., and L. Smith, 1990: A Wind-Driven Isopycnic Coordinate Model of the North and Equatorial Atlantic Ocean 1. Model Development and Supporting Experiments. *Journal of Geophysical Research*, 95, 3273–3285

Carter, G. S., 2010: Barotropic and baroclinic **M**2 tides in the Monterey bay region. *Journal of Physical Oceanography*, 40, 1766-1783.

Chiou, M. D., S. Jan, J. Wang, R. C. Lien, H. Chien, 2011: Sources of baroclinic tidal energy in the Gaoping Submarine Canyon off southwestern Taiwan. *Journal of Geophysical Research*, 116, C12016.

Clarke, A. J., 1991: The dynamics of barotropic tides over the continental shelf and slope (review). *Tidal Hydrodynamics,* B. B. Parker, Ed., John Wiley, 79–108.

Clarke, A. J., and D. S. Battisti, 1981: The effect of continental shelves on tides. *Deep Sea Research Part A. Oceanographic Research Papers*, 28, 665–682,

Das, P. and J. H. Middleton, 1997**:** Obliquely Incident Poincaré Waves on a Sloping Continental Shelf. *Journal of Physical Oceanography*, 27, 1274-1285.

Defant, A., 1960: *Physical Oceanography*. Volume 2, 598 pp. London, Pergamon Press.

Fandry, C. B., and D. R. Jacket, 1987: Tides on continental shelves with longshore topographic variations. *Continental Shelf Research*, 7, 519–534.

Foreman, M. G. G., and R. A. Walters, 1990: A finite - element tidal model for the southwest coast of Vancouver Island A Finite-Element Tidal Model for the Southwest Coast of Vancouver Island. *Atmosphere-Ocean*, 28, 261–287.

Garreau, P., and R. Mazé, 1992: Tidal Rectification and Mass Transport over a Shelf Break: A Barotropic Frictionless Model. *Journal of Physical Oceanography*, 22, 719–731.

Holloway P. E., 1983. Tides on the Australian North-West Shelf. *Australian Journal of Marine and Freshwater Research*, 34, 213-230.

Howe, M. S., and L. A. Mysak, 1973: Scattering of Poincaré waves by an irregular coastline. *Journal of Fluid Mechanics*, 57, 111–128.

Huthnance, J. M., 1995: Circulation, exchange and water masses at the ocean margin: the role of physical processes at the shelf edge. *Prog. Oceanog.*, 35, 353-431.

Jézéquel, N., and R. Maze, 2001: A barotropic model of the linear semidiurnal tide over a continental slope. *Deep-Sea Research*, 48, 1375–1399.

Le Cann, B., 1990: Barotropic tidal dynamics of the Bay of Biscay shelf: observations, numerical modelling and physical interpretation. *Continental Shelf Research*, 10, 723–758.

Lentz, S., M. Carr, and T. H. Herbers, 2001: Barotropic Tides on the North Carolina Shelf *. *Journal of Physical Oceanography*, 31, 1843–1859.

Maas, L. R. M., and J. T. F. Zimmerman, 1987: On the Exact Shape of the Horizontal Profile of a Topographic Rectified Tidal Flow. *Geophys. Astrophys. Fluid Dynamics*, 38, 105–129.

May, P. W., 1979. Analysis and Interpretation of tidal currents in the coastal boundary layer. *Phd thesis, MIT-Woods Hole Oceanographic Institution.*

Middleton, J. H., and L. Bode, 1987: Poincaré waves obliquely incident to a continental shelf. *Continental Shelf Research*, 7, 177–190.

Miles, J. W., 1972: Kelvin waves on oceanic boundaries. *Journal of Fluid Mechanics*, 55, 113–127.

Morel, Y., R. Baraille, A. Pichon, 2008. Time splitting and linear stability of the slow part of the barotropic component. *Ocean Modell*. 23 (3–4), 73–81.

Munk, W., Snodgrass, F., Wimbush, M., 1970. Tides offshore: transition from California coastal to deep-sea waters. *Geophys. Fluid Dyn*. 1, 161–235.

Mysak, L. A., and M. S. Howe, 1978: Scattering of Poincaré waves by an irregular coastline . *Journal of Fluid Mechanics*, 80, 337–363.

Prandle, D., 1997: The influence of bed friction and vertical eddy viscosity on tidal propagation. *Continental Shelf Research*, 17, 1367–1374.

Quaresma, L. S., Pichon, A., 2011: Modelling the barotropic tide along the West-Iberian margin, *J. Mar. Syst.,* doi:10.1016/j.jmarsys.2011.09.016

Quaresma, L. S., 2012: Super-inertial tides over irregular narrow shelves, *phd thesis, Université de Bretagne Ocidentale*.

Robinson, I. S., 1981: Tidal vorticity and residual circulation. *Deep-Sea Research*, 28, 195–212.

Rosenfeld, L., I. Shulman, M. Cook, J. Paduan, L. Shulman, 2009: Methodology for a regional tidal model evaluation, with application to central California. *Deep-Sea Research*, 56, 199–218.

Wang, X., Y. Chao, D. Changming, J. Farrara, Z. Li, J. C. McWilliams, J. D. Paduan, L.K. Rosenfeld, 2009: Modeling tides in Monterey Bay, California. *Deep-Sea Research II*, 56, 219–231.

Wunsh, C., 1975: Internal tides in the ocean. *Reviews of Geophysics and Space Physics*, 13, 1, 167-182.

Appendix A

Bottom friction

In the original Laplace Tidal Equations (LTE), friction was entirely neglected as it generates non-linear solutions, difficult to handle at that time. Similar approach is adopted in chapter III by the linearization of the governing momentum equations. Nevertheless, frictional forces are an important element in fluid motion. Tidal velocity profile observations show important distortion near the seabed, where the bottom stress component should be considered (τ_{bx} ,τ_{by}). Bottom roughness and fluid viscosity modify the velocity profiles within the bottom boundary layer (BBL). Its shape depends on the vertical distribution of the turbulent momentum transfer coefficient, usually parameterized in momentum equations by an eddy viscosity term, associated with fluid viscosity, ν. A short literature review is presented below in order to support the adopted approach and show that it is still valid for super-inertial barotropic tide waves over continental shelves.

The effect of a depth varying eddy viscosity and the choice of this coefficient value on barotropic tide solutions has been study by Sverdrup (1926), Butman (1975), May (1979) and Prandle (1982a, 1982b, 1997). In the deep ocean, the total depth greatly exceeds the BBL thickness and bottom friction can be simply neglected. However, in the coastal shelf regions, where the BBL height compares to the water depth, bottom stress become determinant for the flow dynamic, as we will see next.

1. Depth-average tidal flow

Prandle (1997) computed single-point analytical solutions from the horizontal momentum equations in order to evaluate the influence of bottom friction (and vertical eddy viscosity) on the vertical current structure. LTE equations are simplified to solve velocity profiles excited by surface gradient forces, $g\nabla\eta$, associated a single tidal constituents, of frequency ω.

$$\frac{\partial R}{\partial t} + R \cdot \nabla R + j R f + g\nabla\eta = \frac{\partial}{\partial z} \cdot E \frac{\partial}{\partial z} R \qquad (1)$$

Where $R = U + j\,V$ represents the velocity vector composed by each orthogonal x and y

components, f is the Coriolis frequency and E is the vertical eddy viscosity coefficient. Assuming zero stress at the surface and a quadratic bed friction law, expressed in terms of depth-average velocity, the vertical integration of (1) yields

$$R\,(\pm i\omega + jf + C_D|R|/H) = -g\nabla\eta \quad (2)$$

where i represents the imaginary axis in the frequency domain. Analytical solutions of equation (2) are provided by Prandle (1982a) and discussed by Prandle (1997) as functions of latitude (set by the value of f) and of the water depth, H. In general, this work concludes that diurnal currents are more sensitive to friction than semi-diurnal ones of the same magnitude (a direct result from balancing the values of the terms within brackets in equation 2). Let us focus here on the super-inertial tidal solutions, with a forcing frequency $\omega = 1.4\text{x}10^{-4}\ \text{s}^{-1}$ (corresponding to the M2 tidal constituent), a mean current velocity R = 0.32 m.s^{-1} and a bottom drag coefficient C_D = 0.0025. Figure 1 expresses the depth-averaged tidal ellipse modelling when bottom friction is imposed to the solution. Contours represent changes relative to no-friction solution, which ellipse as 360º for phase and direction, 0 for eccentricity (which corresponds to a perfect circle) and a unit amplitude value (1m).

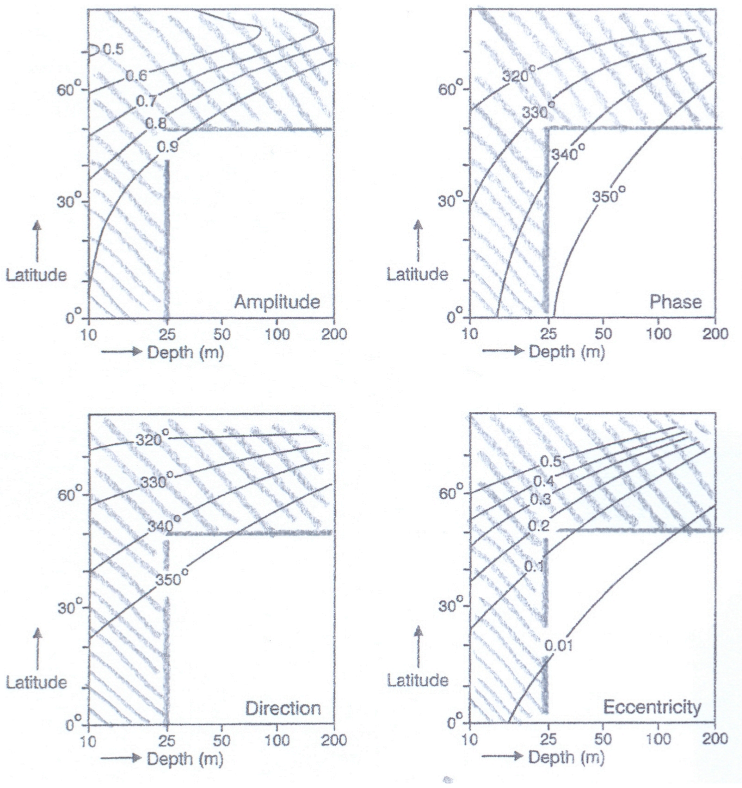

Figure 1: Modeling of depth-averaged tidal ellipse parameters due to bed friction. Contours show changes relative to deep-water values (where bed friction should represent no effect of τ_b). *From Prandle (1997)*

From Figure 1 (where regions not considered in the present study are shadowed), let us evaluate the influence of bottom friction on the depth-averaged tidal ellipse, at mid-latitude continental margins (from 30ºN to 50ºN) and from 25-200 meters depth. Both amplitude (less than 10%) and eccentricity (from 0-0.1) are barely changed, while orientation and phase can vary to about 20º (corresponding to 40 minutes difference at 50ºN and 25 m depth). At 40ºN, where the present work focuses its analysis, the previous variation ranges are reduced to one half.

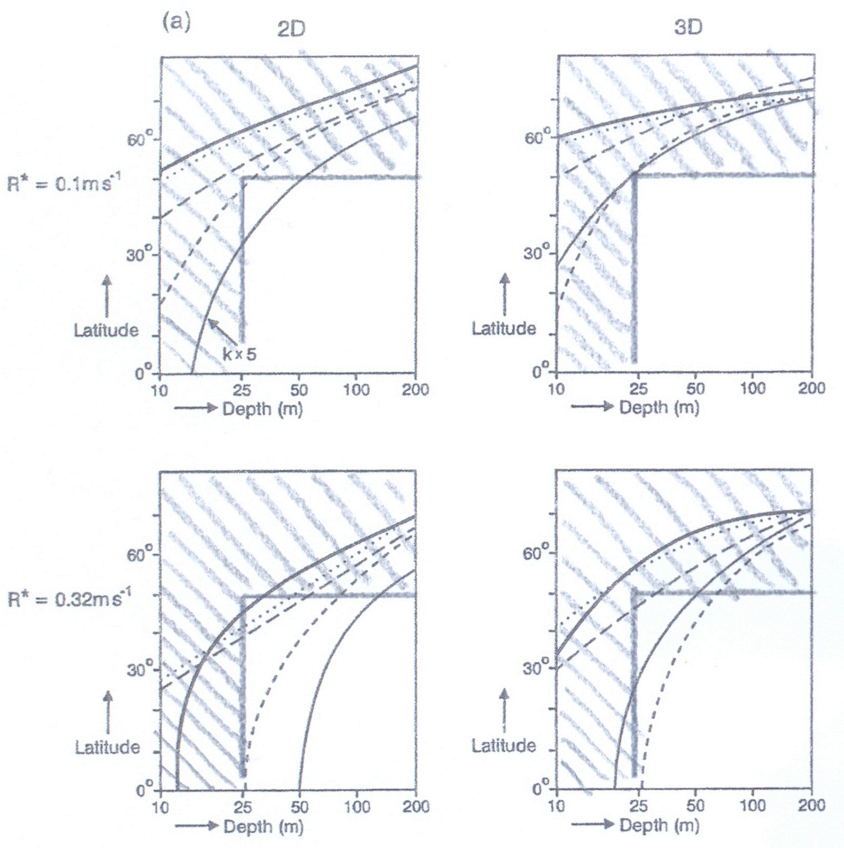

Figure 2. Modelling the impact of friction in a depth-averaged tidal ellipse of reference (calculated without friction). In the upper graphics the averaged tidal current magnitude is set to 0.1m.s^{-1} and in the bottom set to 0.32m.s^{-1}. At the left the resulting tidal ellipses are modeled by the 2D model (just bottom friction, C_D = 0.0025), while at the right they are modeled by the 3D model (bottom friction, C_D = 0.0025 + vertical eddy viscosity, MY2.5). Contours show, __ (bold) ellipse amplitude difference of 0.1 m.s^{-1}, -- phase difference of 10°,— — direction difference of 10°, ... eccentricity difference 0.1. The thin line (__) represents ellipse amplitude difference of 0.1 m.s^{-1} when C_D = 0.0025x5. *From Prandle (1997)*

Prandle (1997) obtained similar solutions when the previous 2-D (depth-integrated) analytical model or a 3D numerical model, which incorporates a vertical eddy viscosity parameterization (Mellor and Yamada, 1974). The adopted vertical average current velocity value (R^*) was varied from 0.1 to 1 $m.s^{-1}$, and 3D model results were vertically averaged to compare to 2D model outputs. Let us focus on the structure of depth-averaged tidal ellipse for velocity magnitudes of 0.1 and 0.32 $m.s^{-1}$, and for mid-latitude continental margins (Figure 2).

From Figure 2, one can see that for low barotropic tidal velocities (< 0.1 $m.s^{-1}$) both 2D and 3D model results are almost insensible to bottom friction stress and share nearly identical solutions. However, for stronger velocities (0.32 $m.s^{-1}$) the differences between model's depth integrated solutions can become significant (especially for region shallower than 50m).

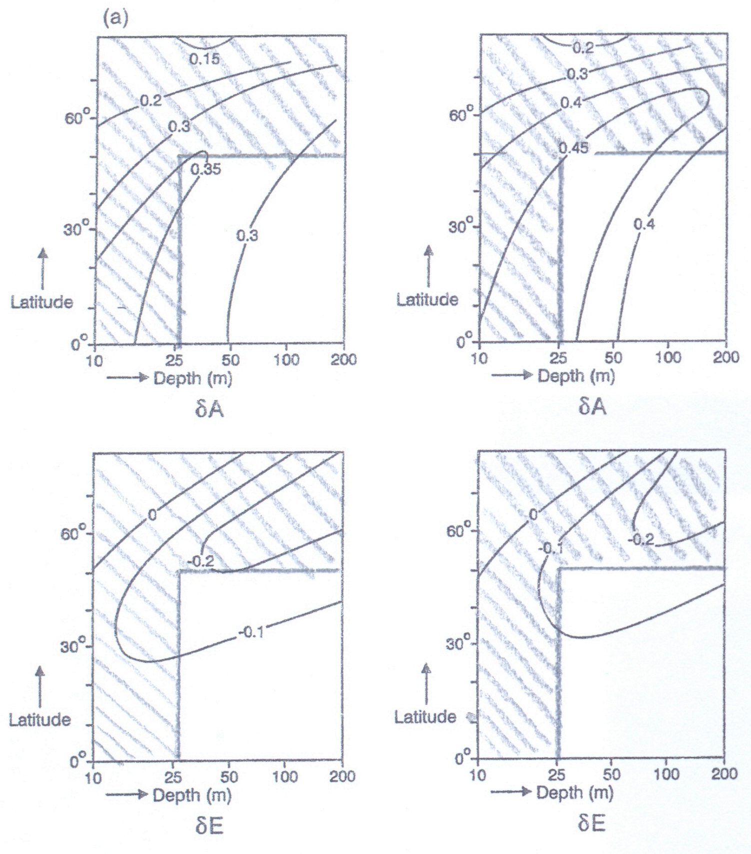

Figure 3: Surface to bed differences for ellipse amplitude (∂A) and eccentricity (∂E). At the left results from 2D-expanded analytical solutions and at the right from 3D numerical model MY-2.5. *From Prandle (1997)*

The same model, with an extended development of the 2D analytical solution, was used to study velocity behaviour at different vertical levels (see Prandle 1997 for details), and to estimate the impact of different eddy viscosity parameterization on the ellipse solutions. The two models were used to solve the tidal ellipse near bottom and surface boundary layers. The 2D-expanded analytical solutions are associated with a constant eddy viscosity value, while the Mellor and Yamada 3D numerical model enables a time and vertical variations of this parameter. Figure 3 shows the differences in amplitude and eccentricity between these two layers. At the same latitude, and depth ranges, from previous analysis, this last evaluation shows that velocity amplitude differences do not vary more than 10% between each model and eccentricity is unaffected by the vertical eddy viscosity choice.

The previous analysis also indicates that for tidal propagation simulations, when current velocities are of the order of 0.1 $m.s^{-1}$ in depths greater than 25m, bottom and internal friction are of secondary importance and hence 2-D (depth averaged) models are adequate to model super-inertial tides along mid-latitude (30-50ºN) shelves. On the contrary, higher latitudes or shallower regions require the use of fully 3D models, variations of the vertical velocity profiles and vertical eddy viscosity are determinant to achieve accurate simulations.

Although Prandle's analysis (Figure 3) focused on the impact of vertical eddy parameterization, another evidence should be pointed. The magnitude differences registered between the bottom and top layers show that the vertical profile of the tidal flow is not monotonous. Moreover, if depth-average velocities are more a less resilient to the vertical shape of this profile it means that the variations in the bottom and/or upper part are restricted to thin boundary layers that occupy small portion of the water column depth, notably in deep waters (as we will see next).

b. Tidal current profiles over the shelf

May (1979) also studied the effect of bottom friction and eddy viscosity on the vertical profile of tidal flows over the shelf. By the use of simple formulation and *in situ* data observations, May noticed that bottom friction can considerably attenuate tidal current velocity magnitudes but feebly modifies the vertical structure of tidal ellipticity and rotation sense. This work was based on LTE analytical solutions, where a simplified linear stress coefficient (τ) was parameterized by a constant eddy viscosity term ($K_v \sim 2.0 \times 10^{-5}\ m^2.s^{-1}$):

$$\tau = K_v \frac{\partial \mathbf{u}}{\partial z}$$

The observed mean vertical profiles of the tidal ellipticity and ellipse orientation (calculated for two different stratification seasons) and the correspondent analytical solutions obtained by May (1979) are shown in Figure 4, where physical variables are reduced to the following dimensional quantities:

$$\gamma = \frac{r}{fH} \quad and \quad \Delta = \frac{1}{H}\sqrt{\frac{2}{f}K_v}$$

where r is a damping coefficient (r ~ C_D |**u**|) introduced by Butman (1975) to approximate the non-linear bottom boundary condition. C_D is a bottom drag coefficient and H the water column depth from surface to bottom (f the coriolis frequency). Δ is the ratio of the Ekman layer depth to H, and was chosen by May (1979) to match the observed thickness of bottom frictional influence in his shallow water velocity profiles. The values of dimensionless bottom stress (γ) used by May (1979) can be compared to typical bottom drag coefficients ($C_D \sim \gamma f H$ / |**u**|) when tidal current velocity range from 20 cm/s to 2 cm/s, in 20 m depth water column, at mid-latitude regions (~40ºN). The results are expressed in Table 1 and show that he has covered a wide range of possible drag coefficients values.

Table 1: The values of dimensional bottom stress (γ) used by May (1979) can be reported to typical bottom drag coefficients (C_D) when tidal current velocity range from 20 cm/s to 2 cm/s, in 20 m depth water column, at mid-latitude regions (~40ºN).

f	γ	|**u**| = 0.2 m.s^{-1}	|**u**| = 0.02 m.s^{-1}
1.0 x 10^{-4} s^{-1} (~40ºN)	0.5	C_D = 7.0 x 10^{-3}	C_D = 7.0 x 10^{-2}
	0.2	C_D = 2.8 x 10^{-3}	C_D = 2.8 x 10^{-2}

This simple model reproduces the main features of May’s observations and shows that ellipticity and ellipses orientation are kept mostly constant despite the different bottom drag values used. Exception is found near the bottom, where ellipticity values can change sharply and even invert its rotation).

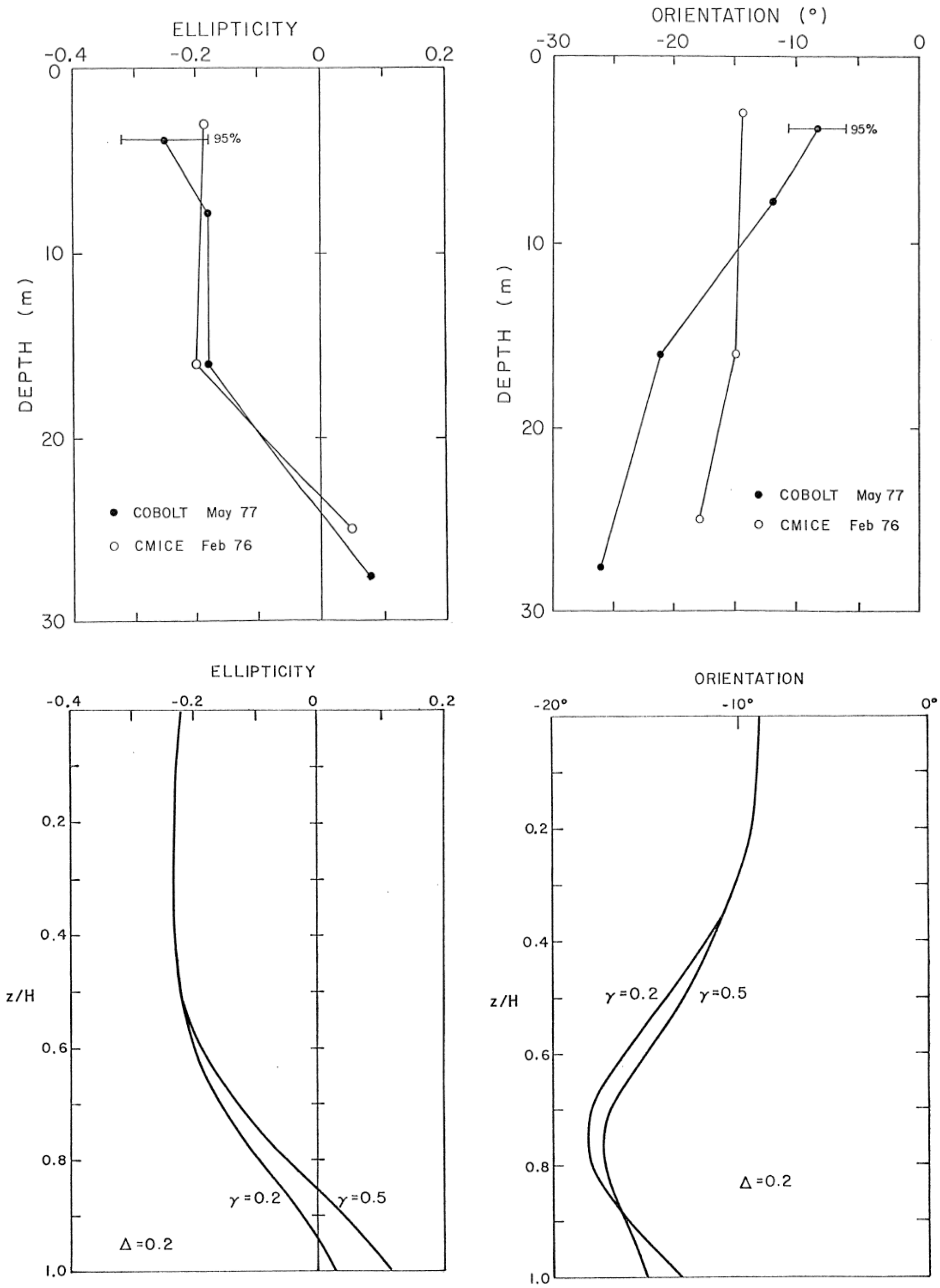

Figure 4. Observation and Theoretical vertical velocity profiles of semi-diurnal ellipticity and ellipse orientation calculated by May (1979) to water depth varying from 20 to 30 m. *From May (1979)*

c. Bottom boundary layers

In the previous section, observations and model results show that the key element that defines the importance of bottom frictional effects on tidal flows (as well as in all other fluids) is the vertical development of bottom boundary layers (BBL) relative to the water column height. This process is subject of numerous scientific works and was reviewed by Grant and Madsen (1986). The water motion over the seabed is driven by a number of mechanisms, including sea-surface slopes, atmospheric pressure gradients, density differences, tides and wind. Each driven flow will develop its own boundary layer characteristics, whose vertical scale is mainly a function of the forcing period of each mechanism. Nevertheless, the combination of different mechanisms sets a complex boundary layer structure, where smaller BBL forced by high frequency processes are embedded in larger BBL forced by low frequency. These are regions of strong turbulent mixing of mass, momentum and heat that play an important role in momentum balances.

Let us consider a single tide wave propagating over shallow water regions, along the *x*-direction. In the immediate vicinity above its bottom boundary layers, the linearized momentum equation is reduced to

$$\frac{\partial \tilde{u}}{\partial t} = -\frac{1}{\rho}\frac{\partial \tilde{p}}{\partial x} + \frac{1}{\rho}\frac{\partial \tau}{\partial z}$$

Assuming a sinusoidal time variation of the flow outside the boundary layer, an equivalent potential flow, $\tilde{u} = |u|\sin(\omega t)$, can replace the pressure gradient force in the equation,

$$\frac{\partial(\tilde{u} - \tilde{u}_\infty)}{\partial t} = \frac{1}{\rho}\frac{\partial \tau}{\partial z}$$

Which for oscillatory flows of frequency ω (harmonic motions, ∂/∂t = $i\omega$) the equation becomes,

$$i\omega(\tilde{u} - \tilde{u}_\infty) = \frac{\partial \tau / \rho}{\partial z}$$

This relationship shows that the bottom shear stress varies within a cycle oscillatory period. The important variables that determine the nature of the flow inside this domain are:

1. the velocity amplitude outside the BBL: $|\mathbf{u}|$
2. the particle excursion amplitude during the oscillation, a_b (tidal excursion): $|\mathbf{u}|\ /\omega$
3. the roughness of the "wall" (z_0), which characterizes the size of the irregularities on the surface of the boundary.
4. Fluid viscosity, ν, which is especially determinant for low Reynolds numbers (ratio of inertial to frictional terms).

The variables $|\mathbf{u}|$, a_b, z_0 and ν can be combined into independent dimensionless parameters as the Boundary layer Reynolds number, $Re_b = |\mathbf{u}|\ a_b\ /\ \nu$, and amplitude/ roughness ratio a_b / z_0 . These two parameters determine the main structure of the BBL, as its thickness δ_w and turbulence regime. Jonhsson (1980) finds wave boundary layers to be turbulent for Re > 10^5, which is common to most wave boundary layer flows observed on continental shelves. For these turbulent regimes the BBL thickness is $\delta_w = u_{*w}\ /\ \omega$, in which u_{*w} represents the friction velocity for the wave boundary layer flow. It is defined by $u_{*w} = |\mathbf{u}|\ (f_w\ /2)^{1/2}$ and f_w is the wave friction factor. Several expressions have been developed for f_w based on laboratory experiments (Jonsson 1966; Kamphuis, 1975) or in theoretical work (Grant 1977; Trowbridge & Madsen 1984). Ostendorf (1984) estimated friction factor values for tidal flows over bed forms and validated them against laboratory and field observations. He get the value $f_w = 0.00248$ which is fairly bounded by similar parameter estimations from different methods over plane bottoms ($f_w = 0.00171$) and bed forms bottoms ($f_w = 0.00203$).

The previous theory and numbers enable the estimation of theoretical bottom boundary layers height when considering a specific tidal flow. For semi-diurnal barotropic currents (ω = 1.4 x 10^{-4} s^{-1}) of magnitude $|\mathbf{u}| = 0.05$ $m.s^{-1}$ over plane bottoms ($f_w = 0.00171$), the linear friction velocity is $u_{*w} = 0.0015$ $m.s^{-1}$ and the correspondent BBL height is $\delta_w = 10.41$m. For 50m water depths this BBL corresponds to 20% of the water column and for 20m water depths 50%. If the magnitude is reduced to 0.02 $m.s^{-1}$ over a bed forms bottom ($f_w = 0.00248$), $u_{*w} = 7.0$ x 10^{-4} $m.s^{-1}$ and $\delta_w = 5.03$ m. This simple calculus shows that the frictionless approach becomes inappropriate for shallow regions such as the above one and is critical for the former one.

References

Butman, P. W., 1975. On the dynamics of shallow water current in Massachusetts Bay and on the New England continental shelf. *Phd thesis, MIT-Woods Hole Oceanographic Institution.*

Grant, W. & S. **Madsen**, 1986: The continental-shelf bottom boundary layer. *Annu. Rev. Fluid Mech.*, 18, 265-305.

Jonsson, I. G. 1966. Wave boundary layers and friction factors. Prec. Coastal Eng. Conf., lOth, 127-48.

Jonson, I. G., 1980: A new approach to oscillatory rough turbulent boundary layers. *Ocean Engineering*, 7, 109-52.

Grant, W. D. 1977: Bottom friction under waves in the presence of a weak current: Its relationship to coastal sediment transport. ScD thesis. Mass. Inst. Technol., Cambridge

Kamphuis, J. W. 1975: Friction factor under oscillatory waves. J. Waterways, Harbors Coastal Eng. Div., ASCE 101 (WW2), 135-44.

May, P. W., 1979. Analysis and Interpretation of tidal currents in the coastal boundary layer. *Phd thesis, MIT-Woods Hole Oceanographic Institution.*

Mellor, G. L. and **Yamada**, T. 1974: A hierarchy of turbulence closure models for planetary boundary layers. *Journal of Atmospheric Science*, 31, 1791–1806.

Ostendorf, W. B., 1984: Linearized Tidal Friction In Uniform Channels. *Journal of Hydraulic Engineering,* Vol. 110, No. 7, July, 1984.

Prandle, D., 1982a: The vertical structure of tidal currents and other oscillatory flows. *Continental Shelf Research*, 1, 191–207.

Prandle, D. 1982b: The vertical structure of tidal currents. *Geophysical and Astrophysical Fluid Dynamics*, 22, 29–49.

Prandle, D., 1997: The influence of bed friction and vertical eddy viscosity on tidal propagation. *Continental Shelf Research*, 17, 1367–1374.

Trowbridge, J., **Madsen**, O. S. 1984b. Turbulent wave boundary layers. 1. Model formulation and first-order solution. *J. Geophys. Res.* 89(C5), 7989-97.

Appendix B

1D barotropic tide solutions across regular margins

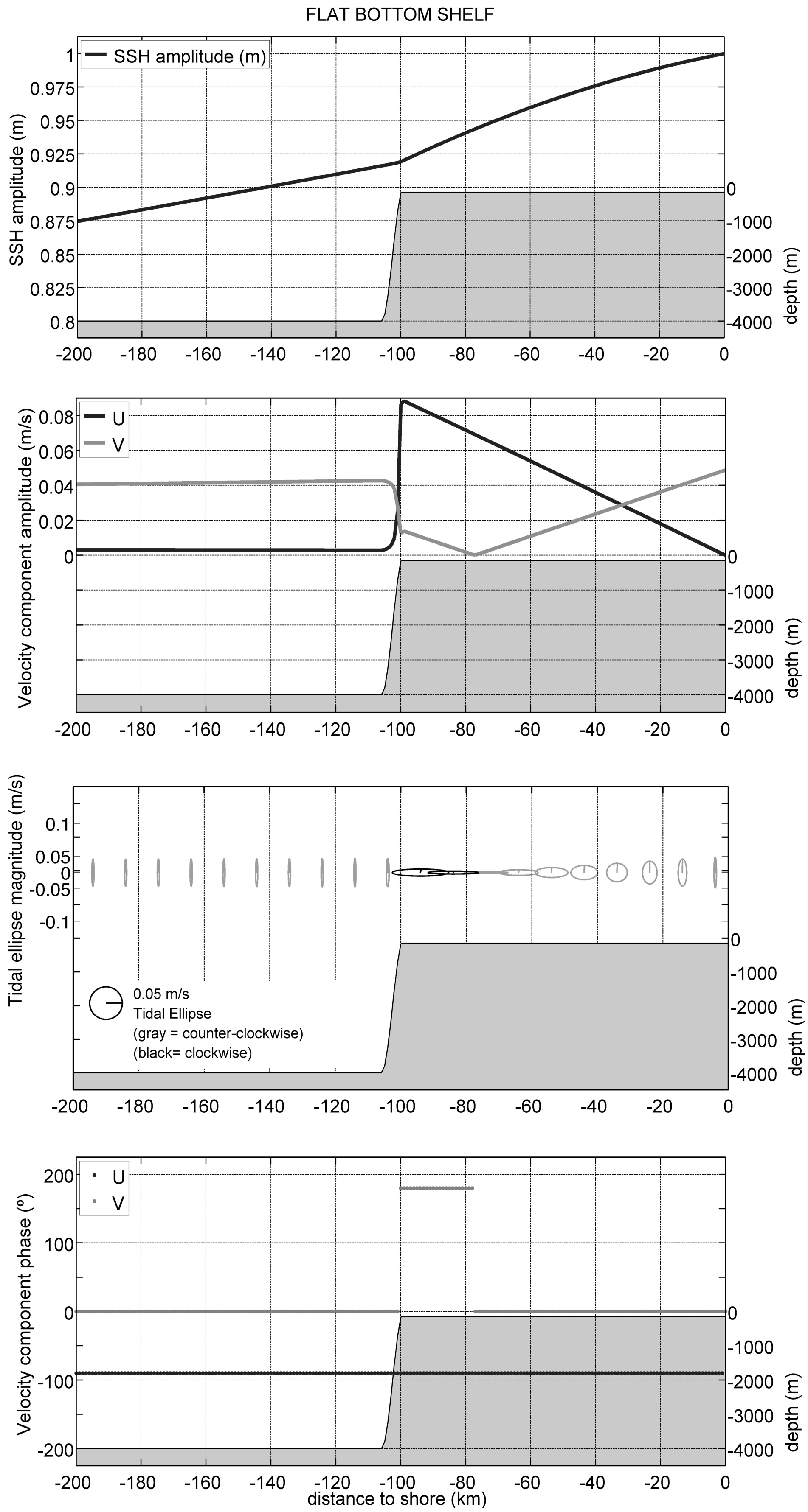

Figure 4. M_2 super-inertial harmonic (1m amplitude at the coast) cross-shelf solution, over a **150m depth** flat bottom shelf of **100 km length**.

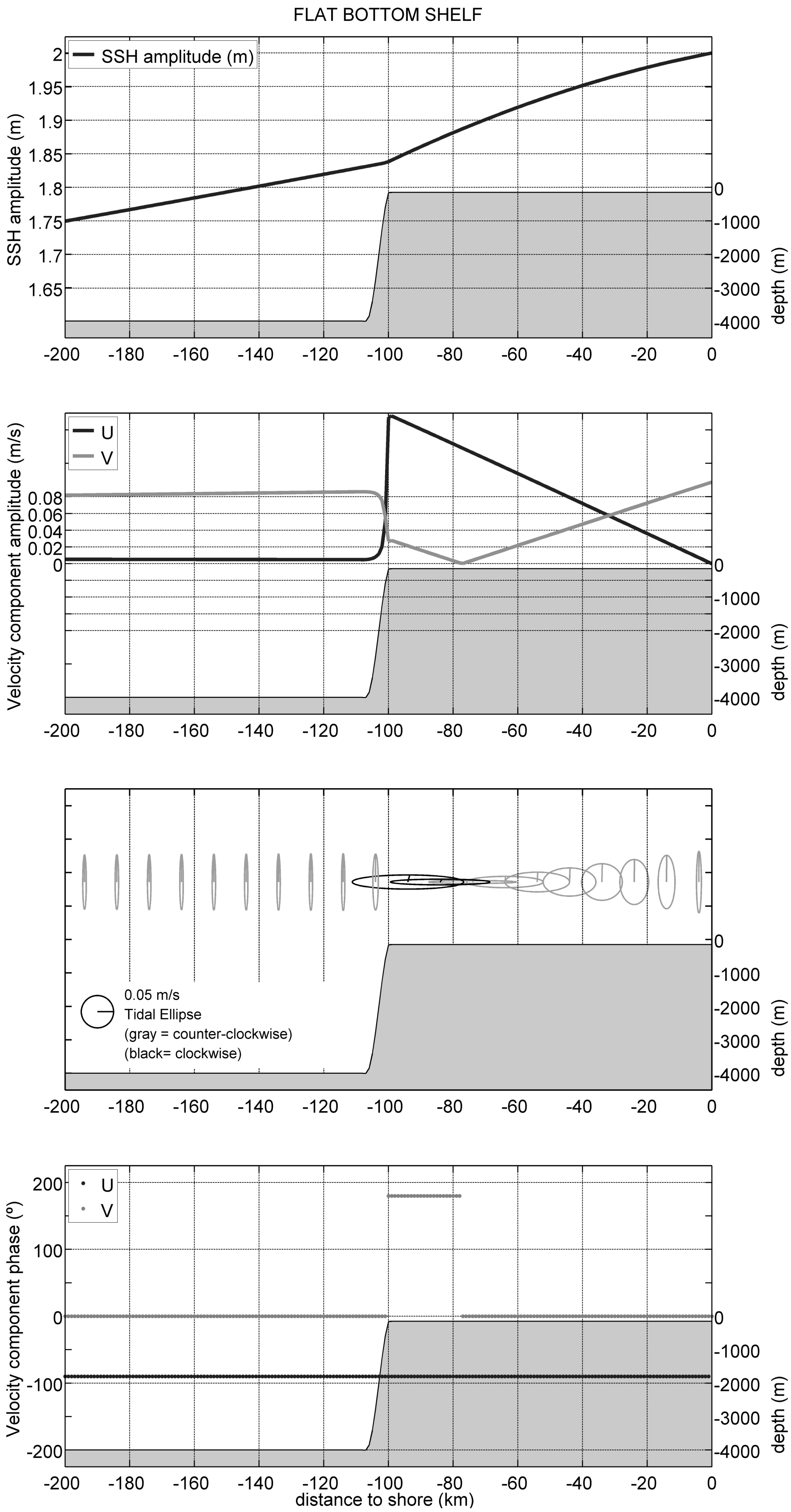

Figure 5. M_2 super-inertial harmonic (**2m amplitude at the coast**) cross-shelf solution, over a 150m depth flat bottom shelf of 100 km wide.

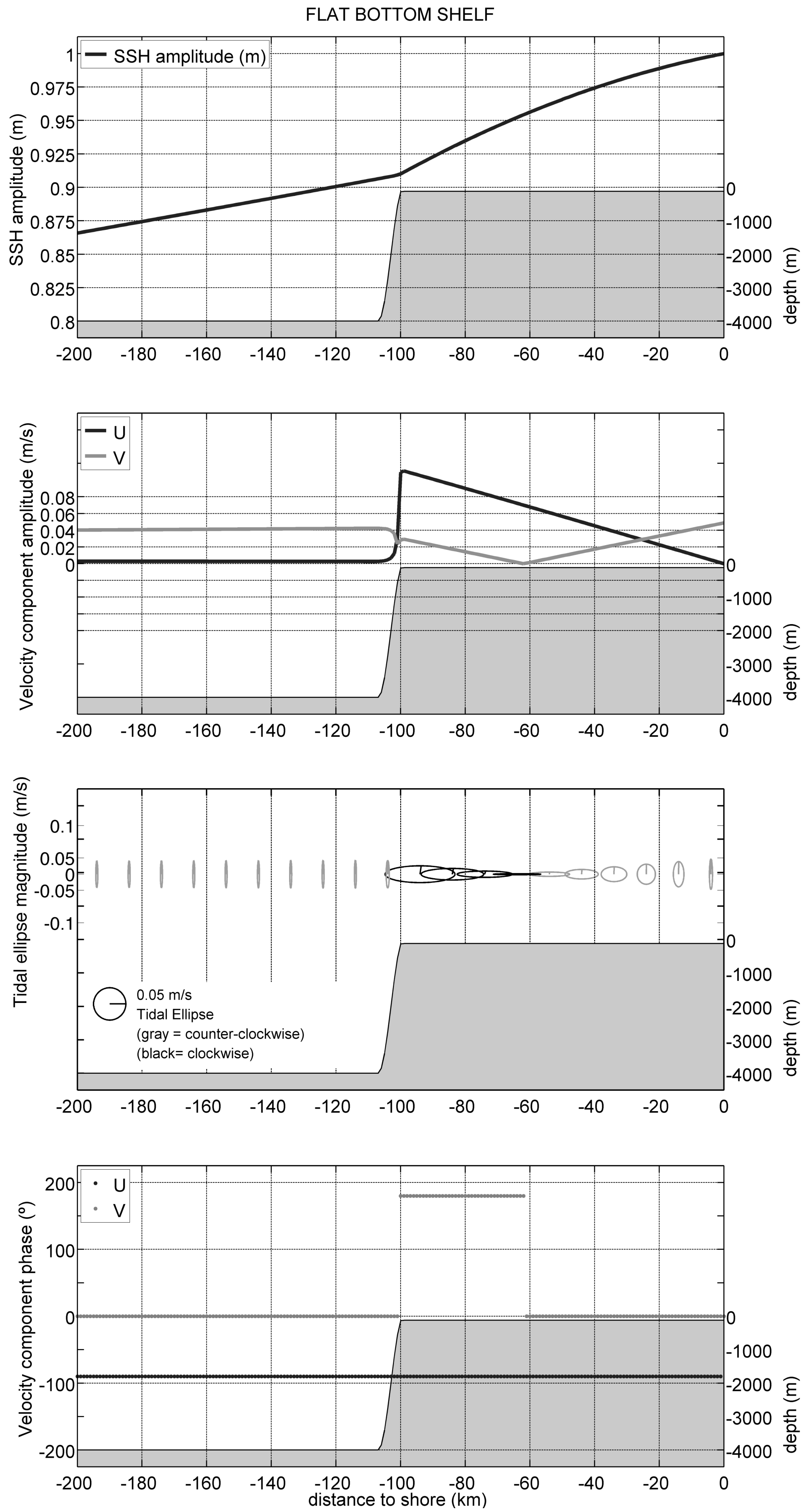

Figure 6. M_2 super-inertial harmonic (1m amplitude at the coast) cross-shelf solution, over a **120m depth** flat bottom shelf of 100 km length.

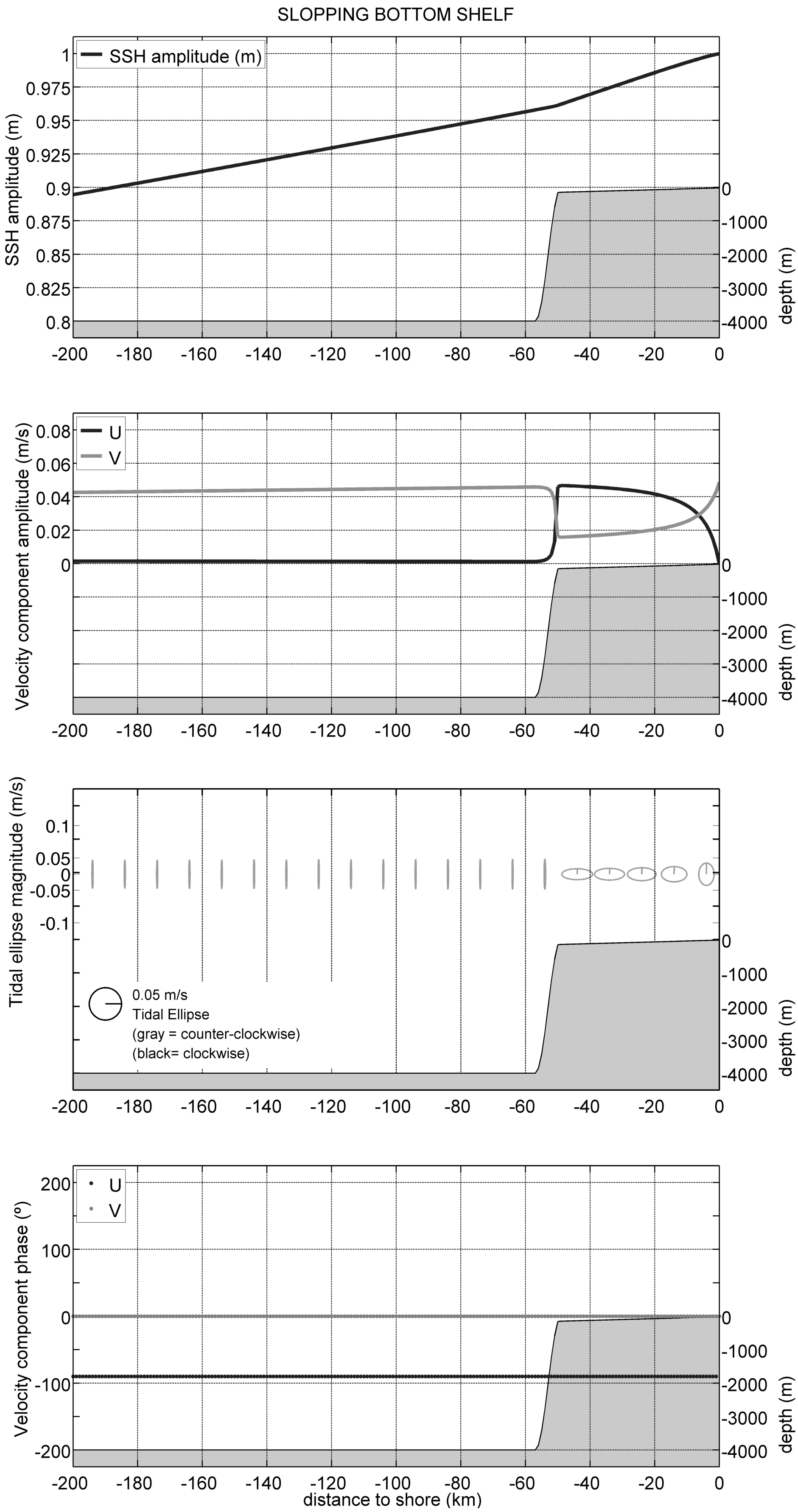

Figure 7. M_2 super-inertial harmonic (1m amplitude at the coast) cross-shelf solution, over a **slopping bottom** shelf (15-150m slope, m = 0.0027) of 50 km length.

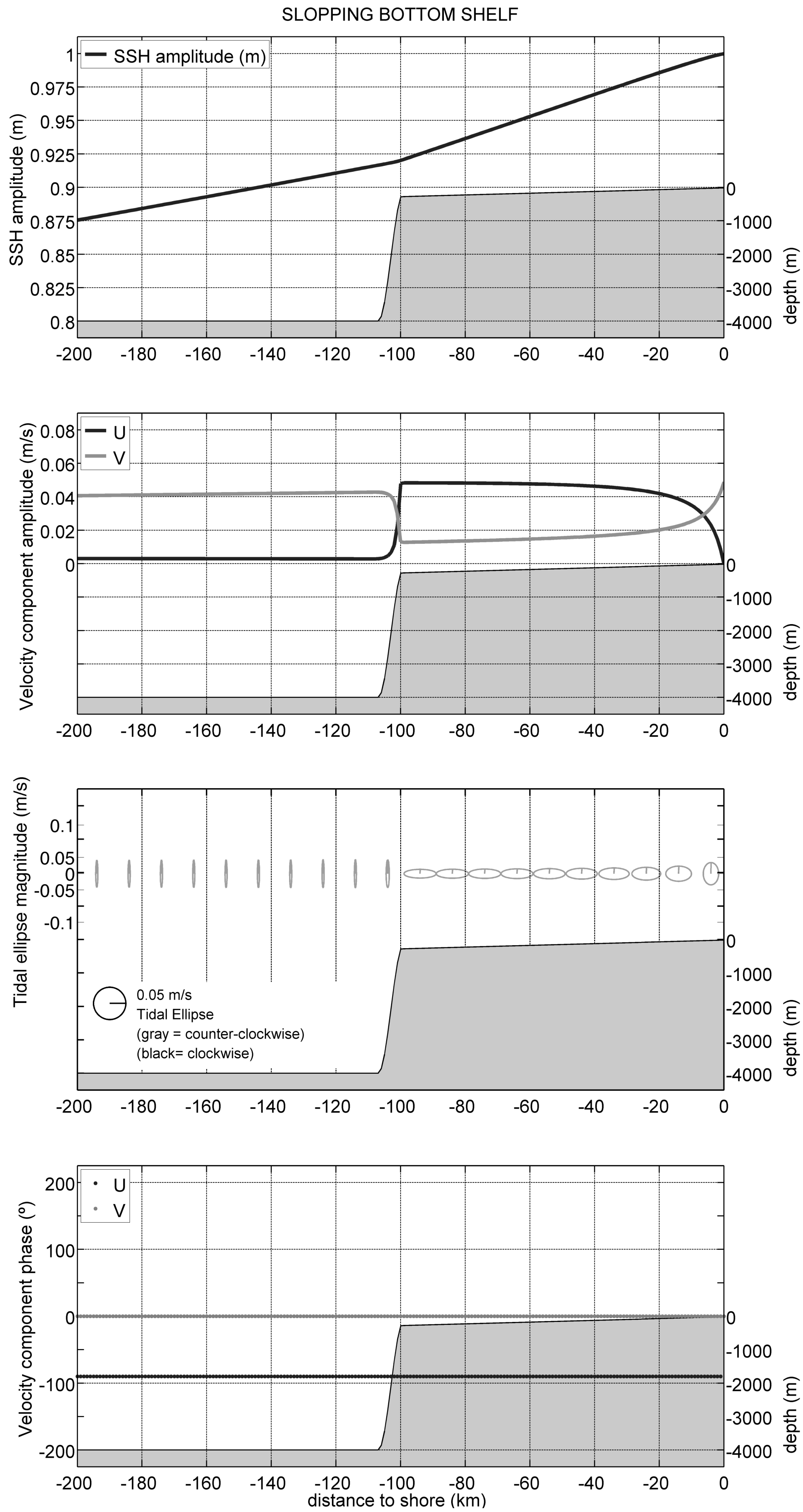

Figure 8. M_2 super-inertial harmonic (1m amplitude at the coast) cross-shelf solution, over a **sloping bottom** shelf (15-280m, m = 0.0027) of **100 km length**.

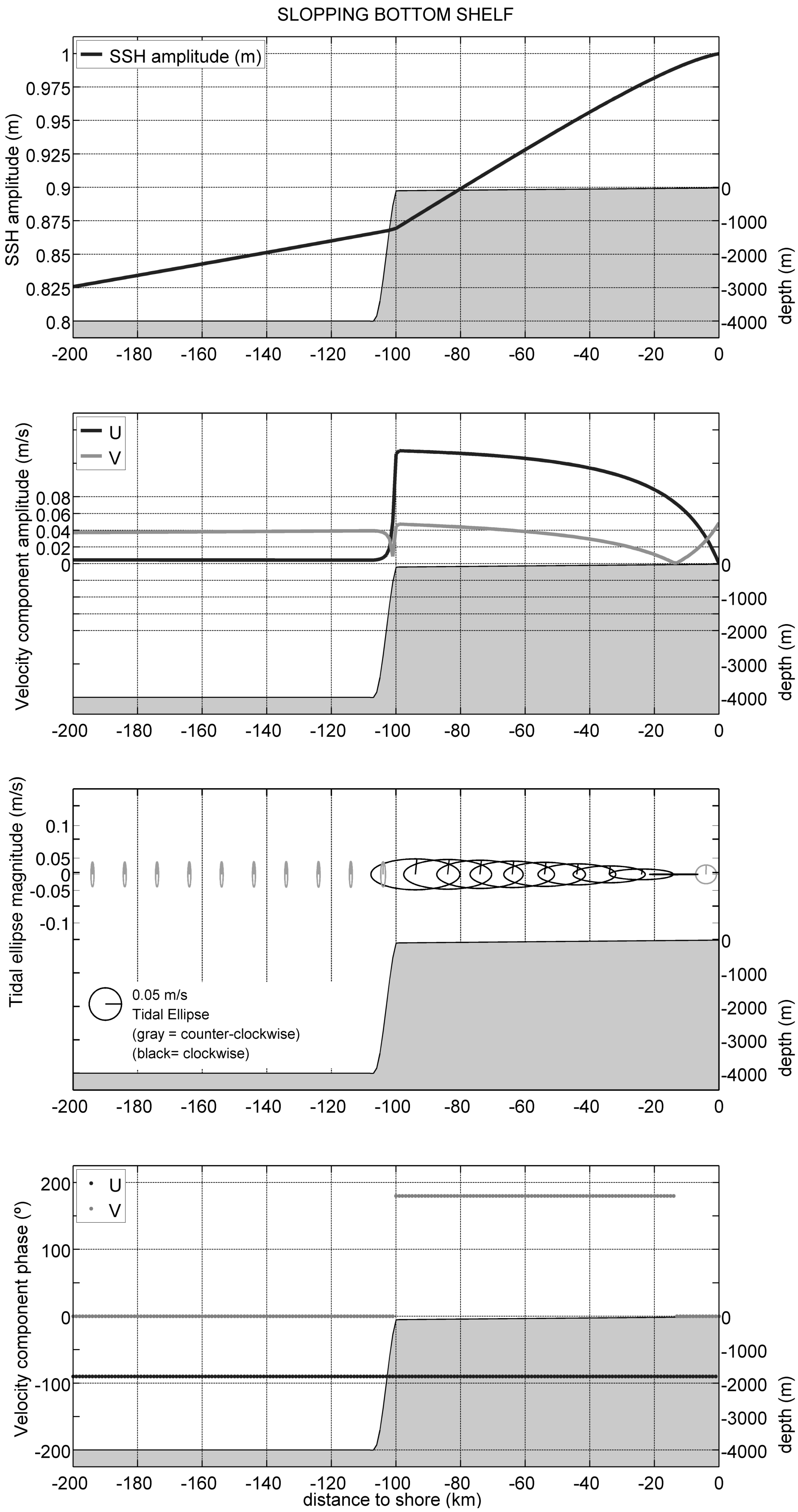

Figure 9. M_2 super-inertial harmonic (1m amplitude at the coast) cross-shelf solution, over a **sloping bottom** shelf (15-120m, m = 0.001) of **100 km length**.

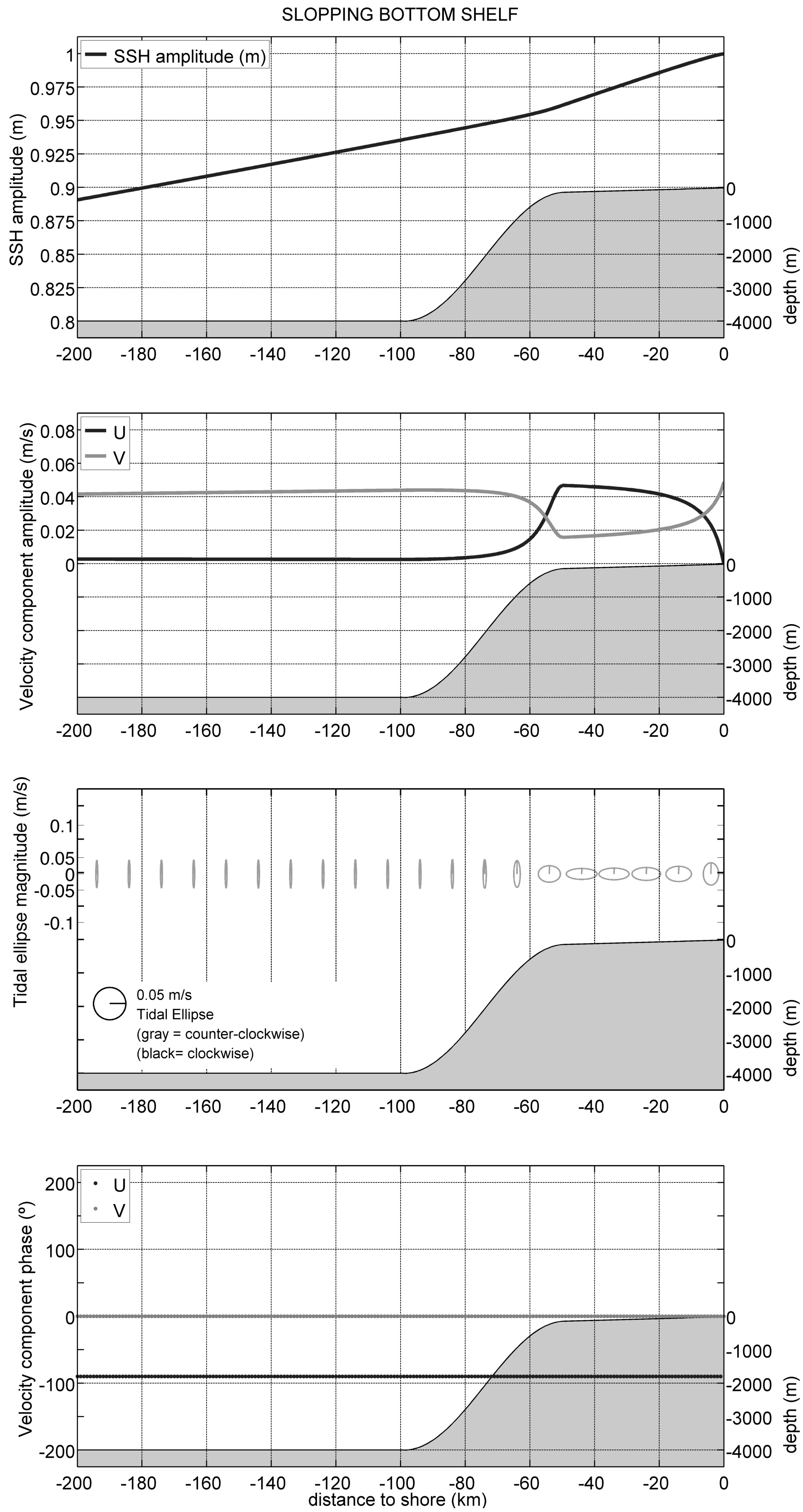

Figure 10. M_2 super-inertial harmonic (1m amplitude at the coast) cross-shelf solution, over a **sloping bottom** shelf (15-150m, m = 0.0027) of **50 km length** and a **50 Km continental slope.**

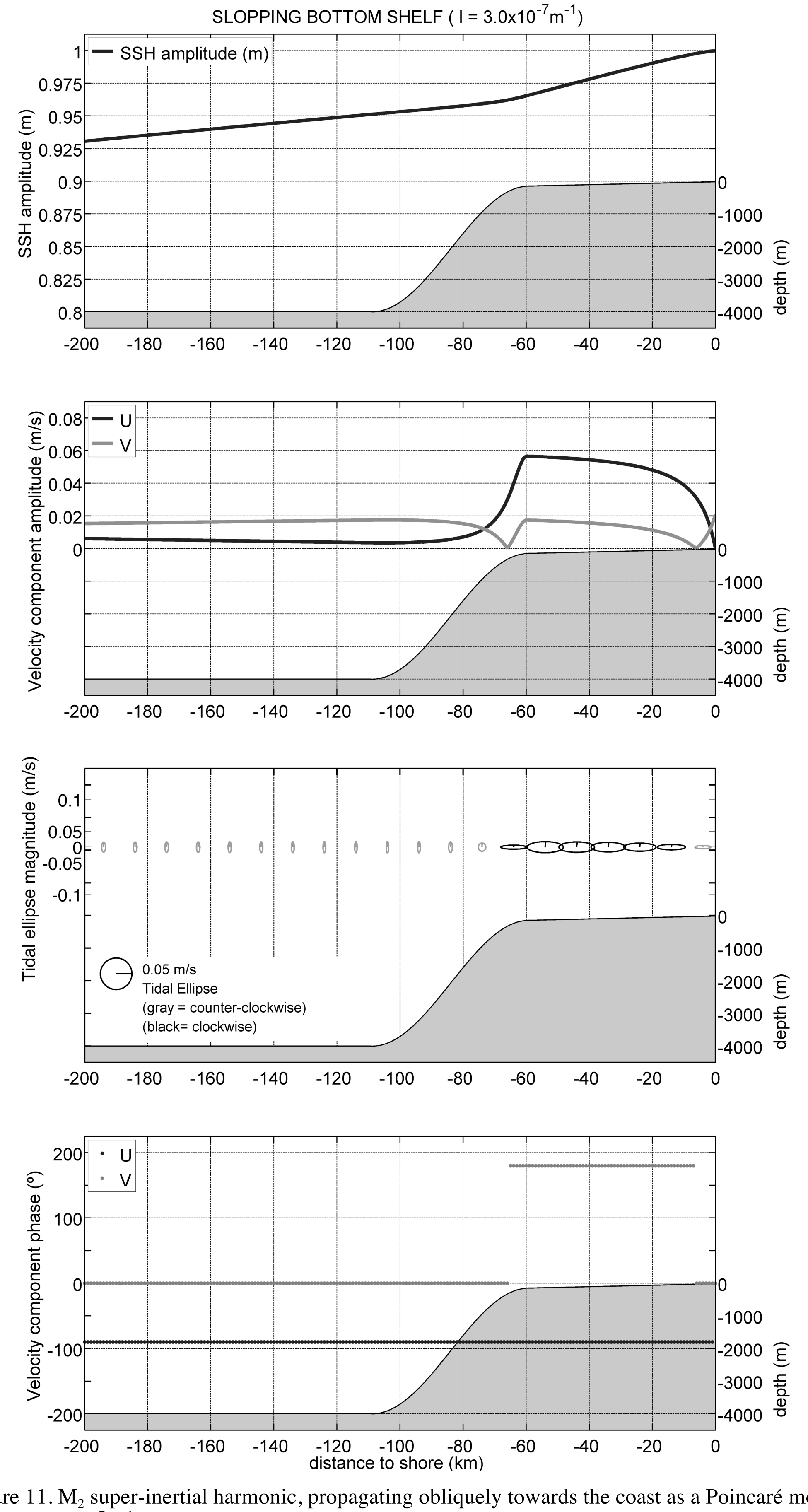

Figure 11. M_2 super-inertial harmonic, propagating obliquely towards the coast as a Poincaré mode (l = 3.0x10^{-7}m^{-1}), over a **sloping bottom** shelf (15-150m, m = 0.0027) with **100 km length**.

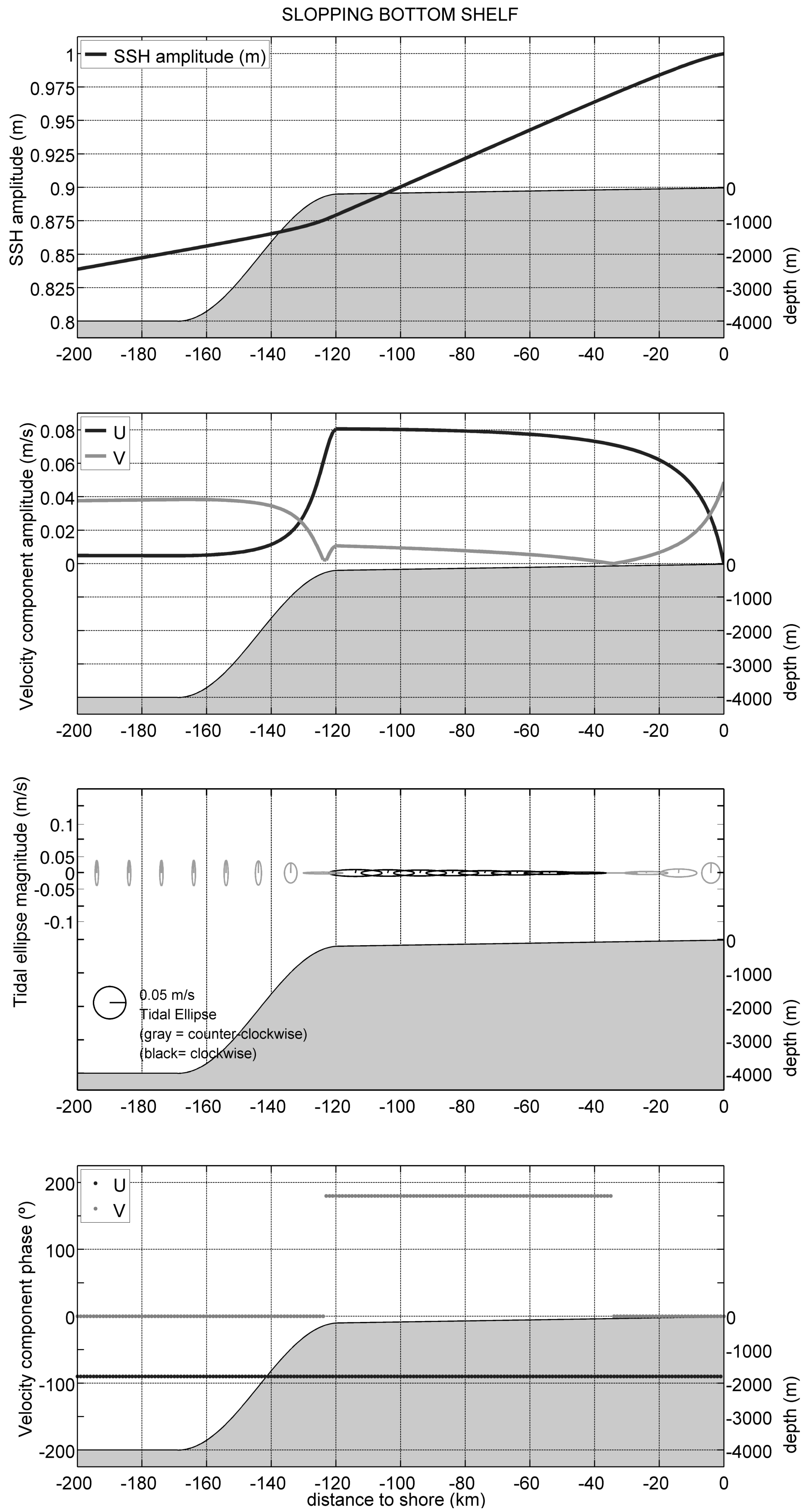

Figure 12. M_2 super-inertial harmonic (1m amplitude at the coast) cross-shelf solution, over a **sloping bottom** shelf (15-200m, m = 0.00154) with **120 km length**.

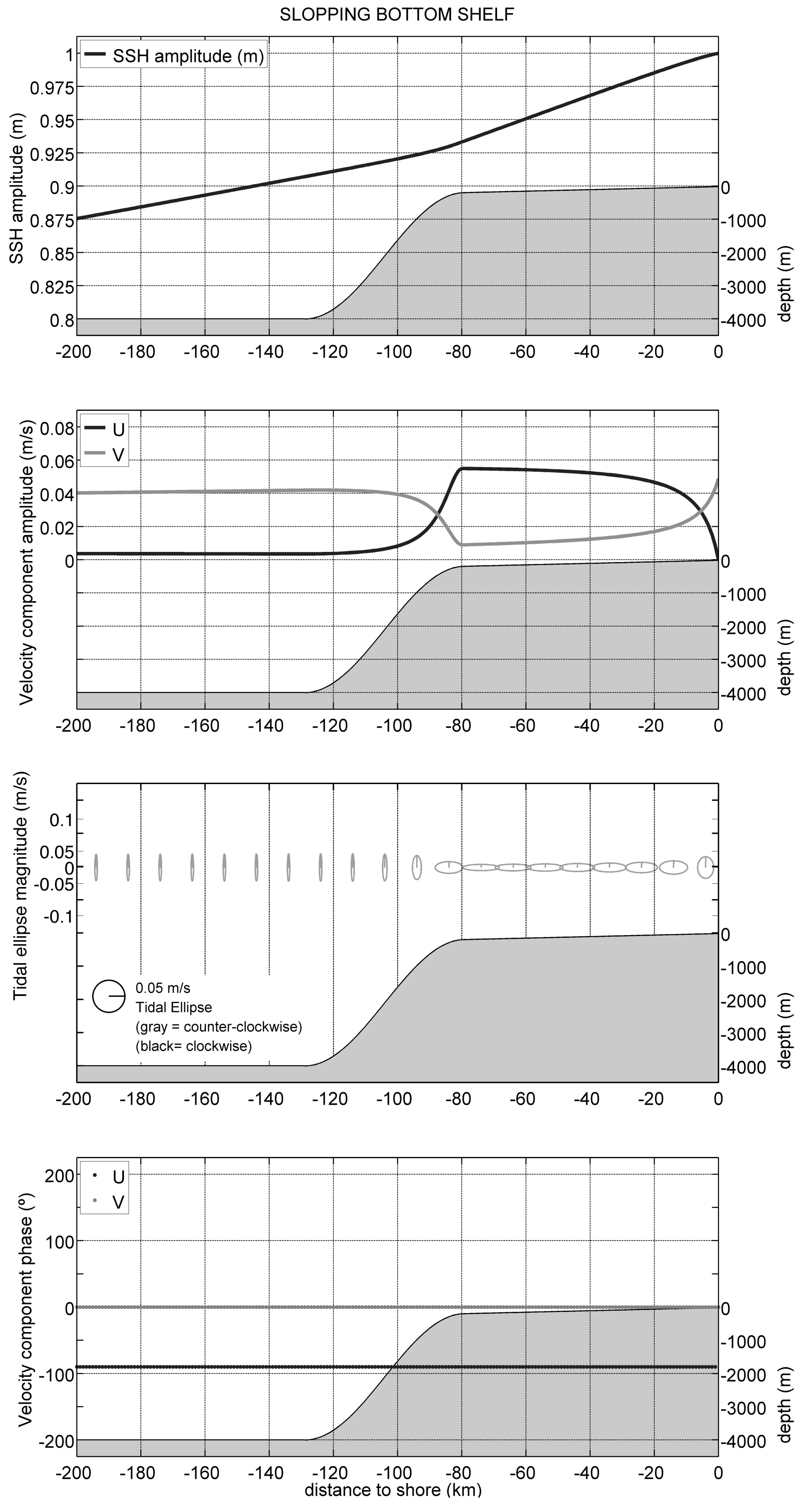

Figure 13. M_2 super-inertial harmonic (1m amplitude at the coast) cross-shelf solution, over a **sloping bottom** shelf (15-200m, m = 0.00231) with **80 km length**.

PART III

Baroclinic tide over idealized bathymetry shelf features

CONTENTS:

Chapter I: Internal tides 118

1. The linear approximation
2. The dispersion relation
3. Beam propagation
4. Interfacial propagation
5. Internal tide generation

Chapter II: Super-inertial tides over abrupt continental shelf features. . . 129
Part II: Internal waves.
Quaresma L.S. & A. Pichon, 2012.
submitted to Journal of Physical Oceanography (2012)

1. *Introduction* 130

2. *Linear internal tide approximation* 135

a. Internal tide generation
b. Barotropic forcing term

3. *Internal tide over irregular shelves* 141

a. Numerical model
b. Stratification
c. Idealized topography

4. *Interfacial internal tide* 143

a. Wavelength and wave patterns
b. Standing modes
c. Diamond patterns
d. Ring-like internal tide signatures
e. Progressive modes
f. Asymmetric interference

5. *Internal tidal beams* 154

a. Beam scattering
b. 3D bottom reflection

6. *Summary* 162

Appendix B: *Three-dimensional reflection* 165

Chapter I
Internal tides

Internal waves are ubiquitous in the stratified ocean. While atmospheric forcing defines the upper layer stratification, the superposition of water masses with different densities determines the deeper density profile. Two major mechanisms are responsible for the generation of internal waves. One is the movement of air masses over the sea-surface creating pressure gradient variations, which induce upper ocean disturbances that can propagate as inertial gravity internal waves. This process is not discussed in the present work. Another process, on which we will focus next, is the gravitational pull induced by the moon and sun that forces the seawater to flow in a permanent cycle over the irregular bottom of the ocean. Here, the barotropic tide is dissipated into baroclinic modes that oscillate with the same forcing frequency (internal tides) or with higher harmonic modes. The horizontal barotropic flow, associated with surface tide, acquires vertical velocity component whenever crossing irregular topography, such as continental margins and deep ocean reliefs. These vertical movements are produced cyclically, with the same tidal frequency, and become wavemakers of internal waves that propagate away from this origin. The internal waveforms and dispersion mechanisms are function of the ocean stratification and the seabed configuration, as we will see next.

1. The linear approximation

In the previous chapter, the linear Laplace tidal equations were used to analyze the barotropic solution of the surface tide. Here, similar shallow water equations are the starting point to develop the basic internal wave equations, which we must now consider to deal with non-homogenous fluid. The fluid stratification is usually characterize by a buoyancy frequency, N, defined as

$$N^2 = -\frac{g}{\rho}\frac{d\rho}{dz} \qquad (1)$$

Let us consider an internal wave as a small perturbation of an homogenous stratified ocean at rest, where both pressure and density fields can then be expressed as,

$$p = p_0(z) + p'(x, y, z, t) \quad , \quad \rho = \rho_0(z) + \rho'(x, y, z, t) \qquad (2)$$

where p_0 and ρ_0 represent the pressure and density values in hydrostatic equilibrium, defined by $dp_0/dz = -\rho_0 g$. The nonlinear inviscid equation of motion for the internal ocean perturbations (in a rotating framework) may then be formulated as (Baines 1982):

$$\begin{cases} (\rho_0+\rho')\dfrac{D\mathbf{u}}{Dt} + (\rho_0+\rho')(f\times\mathbf{u}) = -g\rho_0\hat{z} - g\rho'\hat{z} - \nabla(p_0+p') + F \\ \dfrac{\partial}{\partial t}(\rho_0+\rho') + \nabla\cdot(\rho_0+\rho')\mathbf{u} = 0 \\ \dfrac{D}{Dt}(\rho_0+\rho') = 0 \end{cases} \tag{3}$$

where $\mathbf{u}(u, v, w)$ is the fluid velocity vector in the Cartesian coordinate system x, y, z (eastward, northward, upward) and D/Dt is the Lagrangian derivative, f the Coriolis frequency, $\hat{\mathbf{z}}$ the unit vector in the upward direction and F represents unspecified forcing such as friction. In (3) the product of unknown variables enables nonlinear wave interactions solutions that are responsible for the generation of new tidal harmonics (not discussed here). When scaled (L = wavelength; T = wave period) one can neglect them if the ratio of each nonlinear term $[U^2/L]$ and the time derivative $[U/T]$ is small. This ratio can be expressed by $[U/C]$, which means that the approximation can be done if the horizontal velocity $[U]$ of the water flow is much smaller than its driving wave speed $[C]$. Under this assumption, nonlinear terms can then be neglected from the above governing equations.

Restarting from an ocean at rest, where the distribution of density and pressure are in hydrostatic equilibrium, the linear momentum equations for small perturbations in pressure (p') and density (ρ') are expressed (in the absence of friction) by,

$$\frac{\partial u}{\partial t} - f v = -\frac{1}{\rho_0}\frac{\partial p'}{\partial x} \tag{4}$$

$$\frac{\partial v}{\partial t} + f u = -\frac{1}{\rho_0}\frac{\partial p'}{\partial y} \tag{5}$$

$$\frac{\partial w}{\partial t} = -\frac{1}{\rho_0}\frac{\partial p'}{\partial z} + b \tag{6}$$

$$\frac{\partial u}{\partial x} + \frac{\partial v}{\partial y} + \frac{\partial w}{\partial z} = 0 \tag{7}$$

where b denotes the buoyancy force associated with the density perturbation, ρ', by

$b = -g\ \rho' / \rho_0$. Similarly, the mass conservation equation, under linear approximation, becomes:

$$\frac{\partial \rho'}{\partial t} - w\frac{N^2 \rho_0}{g} = 0 \qquad (8)$$

2. The dispersion relation

The previous governing equations (4-8), namely the horizontal and vertical momentum equations and continuity equations, can be combined to formulate an equation expressing the advection of the pressure anomaly, p'. This is made by eliminating u and v, when taking the time derivative of the continuity equation (7), and using the horizontal momentum equations (4) and (5),

$$\frac{\partial^2 w}{\partial z \partial t} + f\left(\frac{\partial v}{\partial x} - \frac{\partial u}{\partial y}\right) = \frac{1}{\rho_0}\left(\frac{\partial^2 p'}{\partial x^2} + \frac{\partial^2 p'}{\partial y^2}\right) \qquad (9)$$

Equation (6) can also be derived in order to time and associated with (8) to get,

$$\frac{\partial^2 w}{\partial t^2} + N^2 w = -\frac{1}{\rho_0}\frac{\partial^2 p'}{\partial z \partial t} \qquad (10)$$

While, $\partial/\partial y$ of (4) and $\partial/\partial x$ of (5) can be combined to obtain:

$$\frac{\partial}{\partial t}\left(\frac{\partial v}{\partial x} - \frac{\partial u}{\partial y}\right) = -\frac{\partial w}{\partial z} \qquad (11)$$

The last three equations can be used to derive an equation for the vertical velocity component associated to small pressure perturbation adjustments in a continuously stratified incompressible fluid, where the effect of rotation is taken in consideration. This is done by eliminating p' in favor to w, from (10) by subtracting the second derivatives in x and y of (10) and replacing the resulting terms ($\partial^2 p'/\partial x^2 + \partial^2 p'/\partial y^2$) in by the equivalent in (9), to obtain:

$$\frac{\partial^2}{\partial t^2}\left[\frac{\partial^2}{\partial x^2} + \frac{\partial^2}{\partial y^2} + \frac{\partial^2}{\partial z^2}\right] w + f^2 \frac{\partial^2 w}{\partial z^2} + N^2\left(\frac{\partial^2}{\partial x^2} + \frac{\partial^2}{\partial y^2}\right) w = 0 \qquad (12)$$

3. Beam propagation

By taking an ocean with constant buoyancy frequency N, one can find solutions of (12) in the form of a propagating plane wave as,

$$w = w_0 \exp\left\{ i\,(kx + ly + mz - \omega t)\right\} \quad (13)$$

where w_0 is the amplitude of the vertical velocity fluctuation, ω the wave frequency and **k** = (k, l, m) the wavenumber vector. Equation (10) then yields,

$$-\omega^2\left[-k^2 - l^2 - m^2\right] w \ - \ f^2 m^2 w \ + \ N^2\left(-k^2 - l^2\right) w \ = \ 0 \quad (14)$$

And the dispersion relation of beam propagating internal is thus

$$\omega^2 = \frac{f^2 m^2 \ + \ (k^2 + l^2) N^2}{(k^2 + l^2 + m^2)} \quad (15)$$

Taking the representation of the wavenumbers in polar coordinates (Figure 1) one can write (15) in a concise form,

$$\omega^2 = f^2 \sin^2 \beta \ + \ N^2 \cos^2 \beta \quad (16)$$

where β is the angle that the wavenumber vector makes with the horizontal plane, β is given by

$$tan^2\,\beta = \frac{N^2 - \omega^2}{\omega^2 - f^2} \quad (17)$$

This is the dispersion relation for any internal wave in a rotating framework, linking the forcing frequency ω to the restoring forces (buoyancy and Coriolis force) expressed by their respective frequency (N and f). Another important information given by this expression is that the propagating angle of the internal wave depends only on the forcing frequency and not on the wavenumber magnitude. Consequently, the group velocity phase vector is perpendicular to the wave vector by

$$\vec{c}_g = \left(\frac{\partial \omega}{\partial k}, \frac{\partial \omega}{\partial m} \right) \quad , \quad \vec{c}_g \cdot \vec{k} = 0 \quad , \quad \vec{c}_g \perp \vec{k} \quad (18)$$

The group velocity vector thus makes the same angle θ but this time with the vertical plane. Which implies that N and f must bound the internal wave frequency, $N < \omega < f$.

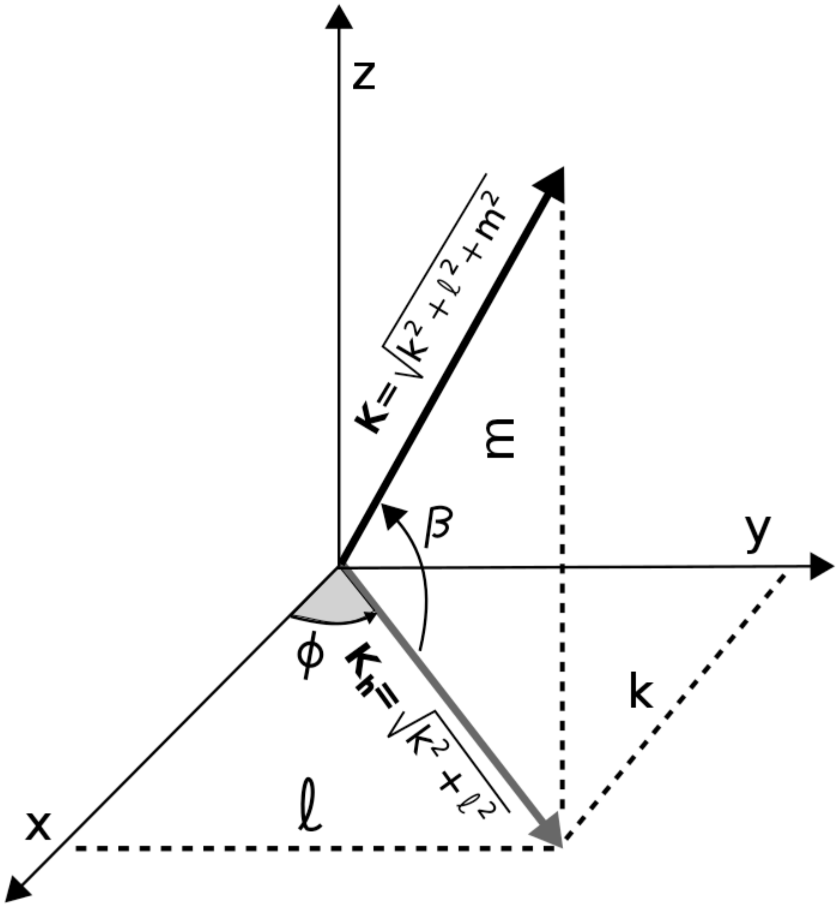

$$k = \mathbf{K}\cos\beta\cos\phi \quad , \quad l = \mathbf{K}\cos\beta\sin\phi \quad , \quad m = \mathbf{K}\sin\beta$$

Figure 1. Internal tide wave-number decomposition in 3D Cartesian domains (polar coordinate representation).

For a constant stratified medium in an f-plane approach, the steepness c (slope) of the group velocity vector (19) is only function of the forcing frequency. However, in the same vertical plane, c as the two possible signs since the energy beams (making angle θ with the horizontal) can propagate in both x and $-x$ directions, as well as z and $-z$ directions. The structure of a propagating perturbation, originate at a vibrating source, exhibits the so-called Saint Andrews cross (Figure 2).

$$c^2 = tan^2\,\theta = \frac{\omega^2 - f^2}{N^2 - \omega^2} \qquad (19)$$

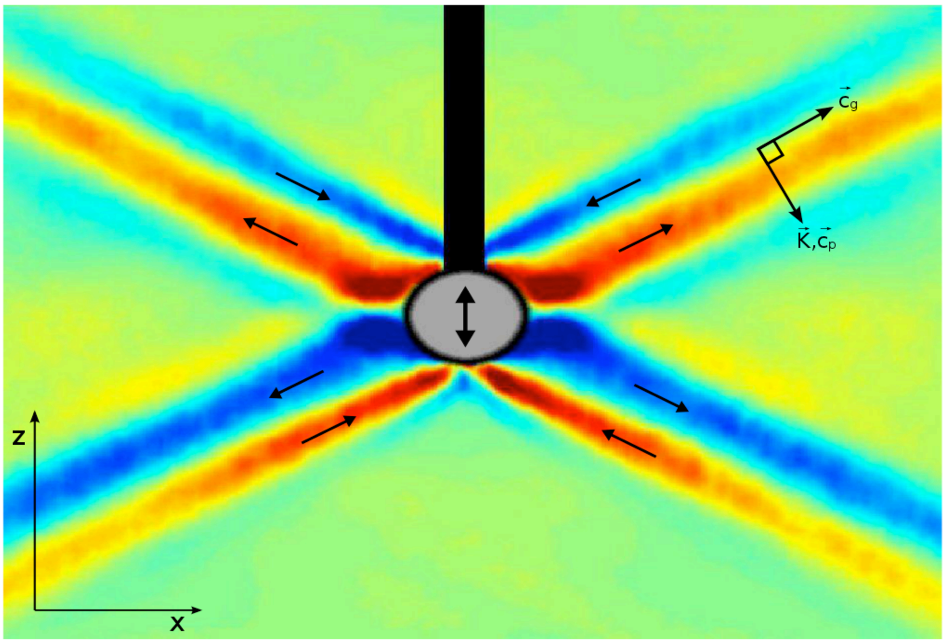

Figure. Waves generated in a stratified fluid of uniform buoncy frequency, *N*, tracing a "Saint-Andrews" cross. At the centre a vibrating source (oscilating periodically with vertical component) introduces vertical perturbations in the fluid's density structure that radiates along four distincted energy beams. The vector wavenumber, **K**, phase velocity, ***Cp***, and group velocity, ***Cg***, are traced over each internal tidal beam. The respective angles with the horizontal and vertical directions are also represented. Isopycnals are displaced in each beam intercepting region. [FINISH FIGURE].

4. Interfacial propagation

The simplest case of a stratification profile is the superposition of two immiscible fluids of different density. Consider an upper layer at rest characterized by a thickness H_1 and density ρ_1 and topping a bottom layer with thickness $H_2 = H - H_1$, and density ρ_2. The hydrostatic approximation yields (when atmospheric pressure is neglected):

$$\begin{aligned} p_1 &= \rho_1 g\,(\eta_1 - z) \\ p_2 &= \rho_2 g\,(\eta_2 - z - h_1) + \rho_1 g\,(\eta_1 - \eta_2 + h_1) \end{aligned} \qquad (18)$$

where p_1, p_2 are the pressure considered respectively at a certain point located in the upper or bottom layer (distanced by z from the sea-surface) and η_1, η_2 the vertical displacement respectively of the sea-surface and interface. These equations allow the elimination of the pressure variable in (4) and (5) to obtain

$$\begin{aligned} u_{1t} - f v_1 + g\eta_{1x} &= 0 \\ v_{1t} + f u_1 + g\eta_{1y} &= 0 \\ u_{2t} - f v_2 + g\eta_{1x} + g'(\eta_2 - \eta_1)_x &= 0 \\ v_{2t} + f u_2 + g\eta_{1y} + g'(\eta_2 - \eta_1)_y &= 0 \end{aligned} \qquad (19)$$

Where $g' = (\rho_2 - \rho_1)\, g \,/\, \rho_2$ is a reduced gravity for a two-layers configuration. If these relations are replaced in the continuity equation we get,

$$\begin{aligned} H_1\,(u_{1x} + v_{1y}) + (\eta_1 - \eta_2)_t &= 0 \\ (H_2 u_2)_x + (H_2 v_2)_x + \eta_{2t} &= 0 \end{aligned} \qquad (20)$$

Equation (19) and (20) are the governing primitive equations for linear interfacial modes. Its solution, in the form of a plane wave,

$$w = w_0 \exp\left\{ i\,(\omega t - kx + ly) \right\} \qquad (21)$$

will give the dispersion relation, when taking a rigid lid and a flat bottom approximation

$$\omega^2 = f^2 + k^2 \left[g' \frac{H_1 (H - H_1)}{H} \right] \qquad (22)$$

and respective the phase velocity

$$C = \sqrt{\frac{g'}{H} \frac{H_1\,(H - H_1)}{1 - (f^2/\omega^2)}} \qquad (23)$$

5. Internal tide generation

The physical principle of the internal tide generation relies on the buoyancy force acting to restore the vertical positions of the ocean isopycnals, when moved vertically by the tidal flow against bottom slopes (Baines 1982). To formulate this mechanism let us consider a simplified configuration where the bottom is invariant along the y-direction, $z = h(x)$, and a rigid sea-surface, $z = 0$. The respective boundary condition is that the velocity component normal to these surfaces must vanish ($w\perp = 0$).

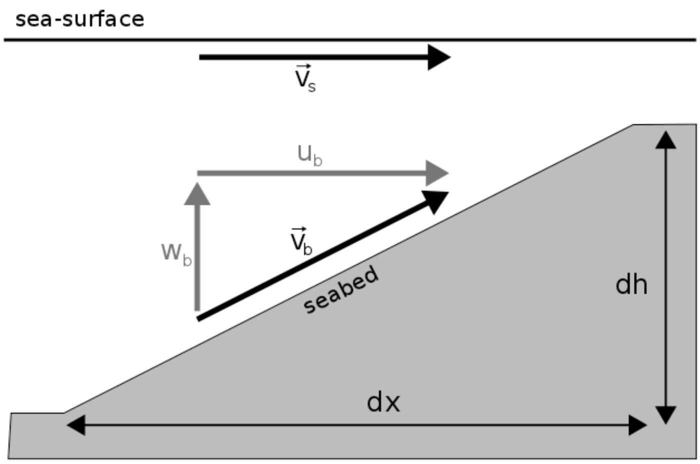

Figure 5. Simplified bottom configuration, invariant along y. The bottom vertical velocity component (v_b) can be expressed by the bathymetry gradient, as

$$\frac{\partial h}{\partial x} = -\frac{w_b}{u_b}$$

From Figure (5) it becomes evident that the vertical component of the barotropic tidal velocity varies from bottom (w_s) to surface (w_b) as:

$$\begin{cases} w_s = 0 & , \ z = 0 \\ w_b = -u\dfrac{\partial h}{\partial x} & , \ z = h(x) \end{cases} \qquad (24)$$

And one can express the vertical velocity component at any location of z and x by normalizing it with h / z :

$$w(x,z) = -u\frac{\partial h}{\partial x}\frac{z}{h} \qquad (25)$$

Taking the volume flux as $Q_x = u\,h$ one can rewrite (25) as,

$$w(x,z) = -\frac{Q_x}{h^2}\frac{\partial h}{\partial x}z \qquad (26)$$

The vertical velocity component will then vary within one tidal cycle ($2\pi / \omega$, ω = tide frequency) by,

$$w(x,z,t) = \frac{Q_x}{h^2}\frac{\partial h}{\partial x} z \cos \omega t \quad (27)$$

In addition to the momentum conservation relation, the fluid must also verify the mass conservation equation (8), which can be time derived to get a frequency dependent equation,

$$\omega \rho' + \frac{\rho_0 N^2}{g}\frac{\partial w}{\partial t} = 0 \quad (28)$$

The time derivative of (27) is replaced in (28) to obtain an equation for the buoyancy perturbation force, $-g\,\rho'/\rho_0$, which is generating force for the internal tide oscillation and for that usually called internal tide body force,

$$\frac{g\rho'}{\rho_0} = -\frac{N^2}{\omega}\frac{Q}{h^2} z\left(\frac{\partial h}{\partial x}\right)\sin \omega t \quad (29)$$

When this equation is used in the linear form of equation (3) the general formulation present by Baines (1973) is obtained, which expresses the physical basis of the internal tide generation,

$$\frac{\partial \mathbf{u}_i}{\partial t} + f \times \mathbf{u}_i + \frac{1}{\rho_0}\nabla p' + \frac{\rho g}{\rho_0}\hat{z} = -\frac{N^2}{\omega}\frac{Q}{h^2} z\left(\frac{\partial h}{\partial x}\right)\sin \omega t\ \hat{z} \quad (30)$$

For a two-dimensional varying topography the internal wave body force becomes,

$$\frac{g\rho'}{\rho_0} = -\frac{N^2}{\omega} z\left[\frac{u}{h}\left(\frac{\partial h}{\partial x}\right) + \frac{v}{h}\left(\frac{\partial h}{\partial y}\right)\right]\sin \omega t \quad (31)$$

Finally, one can identify in this body force formulation the three variables acting together to create internal unbalanced horizontal pressure gradients (disturbances): barotropic tidal flow, density stratification and bathymetry gradients. The term in brackets in equation (31) is the so-called barotropic forcing term (BFT), which is independent from the stratification profile but varies along the tidal cycle. The BFT is usually used as a diagnostic parameter to quantify the strength of the vertical velocity component induced by the tidal flow over bottom topography. This term is thus a proxy of the potential strength, location and phase of the energy dissipation from barotropic to baroclinic modes. And, becomes a coefficient that can be used for any stratification or configuration as

$$\frac{g\rho'}{\rho_0} = -\frac{N^2}{\omega} z \;\; BFT(x, y, t) \qquad (32)$$

In other words, baroclinic tides emanate from oceanic regions where the vertical velocity component, w, oscillates with frequency bounded by the local buoyancy and inertial frequencies. The internal tide generation potential is higher the stronger the perturbed vertical velocity component is but its magnitude depends also on the local stratification, forcing frequency and depth of the isopycnal interface (z).

References

Baines, P. G., 1982: On the internal tide generation models. *Deep Sea Research*, 29, 307-338.

Chapter II

Super-inertial tides over abrupt continental shelf features. Part II: Internal waves *

LUIS S. QUARESMA
Instituto Hidrográfico - Marinha, Lisboa, Portugal.

ANNICK PICHON
Service Hydrographique et Océanographique de la Marine, Brest, France.

* *Article submitted to Journal of Physical Oceanography in May 2012*

Abstract

[1] Three-dimensional internal tide solutions are obtained and discussed over irregular continental margins, where abrupt geomorphic features impose strong along-shelf bathymetry gradients. An isopycnal numerical model solves the structure of internal tide waves over idealized shelf features, namely a submarine canyon and a promontory. Monochromatic super-inertial tide is forced over small regional domains (*f*-plane) by boundary conditions calculated from a "smooth" shelf approach. Canyons and promontories are simplified as opposite shelf-width anomalies, along narrow continental margins. The barotropic tide, solved and discussed by Quaresma & Pichon (Part I), is extended here to take into account water column stratification. Different density structures are used to reproduce the seasonal upper-ocean interfacial mode (two-layers approach) and the permanent deep-ocean scattering of internal tide beams (continuous stratification). Two-dimensional wave interference and three-dimensional reflection solutions, function of the slopping topography and water column stratification, are shown to play a crucial role in the observed internal tide patterns, generally complex over such irregular continental margins.

[2] Key words: Internal tide, interference patterns, ray tracing, three dimensional bottom reflection, submarine canyons and promontories.

1. Introduction

[3] Oceanic internal waves are ubiquitous dynamic features. Two major forcing mechanisms take the inner ocean to oscillate: Atmospheric disturbances and tides. While atmospheric forcing processes seem to induce upper ocean disturbances that can propagate as oceanic internal gravity waves (inertial), the barotropic tide is dissipated over irregular topographies into baroclinic modes that oscillate with the same forcing frequency (internal tides) or with higher harmonic modes. Their waveforms and dispersion mechanisms become then function on the ocean stratification and seabed relief. When internal oscillations are excited with frequencies ranging from local buoyancy, N, to the inertial frequency, f, energy can propagate freely as interfacial modes (e.g. along seasonal thermoclines) or in the form of oblique beams through the continuous stratified ocean. The generation and propagation of internal tides (IT) is subject of numerous works since Rattray (1960) and Wunsch (1969).

[4] Abrupt topographic features, such as submarine canyons and submarine promontories set up important bathymetry gradients that generate internal tides, which propagate in the vicinity of continental margins. Baines (1983) was probably the first to explore the baroclinic solution inside a submarine canyon. By the use of a laboratory model of a narrow canyon, he succeeded to verify his previous two-dimensional (2D) internal tide generation model (Baines 1982). Petruncio (2002) extended this attempt to a numerical simulation of an idealized three-dimensional Monterrey canyon, discussing how its geometry affects the generation and propagation of internal tides. Results reveal the generation of energy beams, propagating inside this perpendicular-to-coast canyon, validated by earlier in situ observations (Petruncio et al., 1998). These two previous experiences (one in laboratory and the other numerical) were forced by monochromatic surface tides propagating perpendicularly into a continental shelf (i.e. along the deep canyon axis) in the form of Poincaré waves. This approach restricted the internal tide generation region primarily to the canyon head and foot, and consequently to a propagation along the deep-canyon axis, from offshore to the canyon head (Baines, 1983) and vice versa (Petruncio, 2002).

[5] Observation datasets show that internal waves inside submarines canyons are dominated by tidal frequencies (Kunze at al. 2002) but cannot reveal their generation point sources, as they become the result of multiple bottom reflections (Nash et al.

2004; Martini et al. 2007; Carter 2010) and constructively and destructively interferences (Rainville et al. 2010). Energy paths, estimated from coarse spatial sampling, show either up-canyon or down-canyon propagation directions, raising a number of questions on the origin of such energy (Kunze at al. 2002). Carter (2005) suggests, from observations, the existence of both local generation sites, leading to upward energy propagation, and remote sources (in the outer canyon rim) that seem to emanate energy offshore. In a different perspective, Jachec et al (2006) concluded that the main semidiurnal internal wave generation site in the vicinity of the Monterrey canyon is in fact a nearby submarine promontory (the Sur platform). More recently, Carter (2010) used an high-resolution numerical model to simulate the complex internal wave pattern observed in this region. Results show depth-integrated baroclinic energy fluxes, generated outside the canyon at multiple southern sources (e.g. Sur platform), propagating northward along the continental slope and steering the canyon mouth. This short overview expresses our poor comprehension of the physical processes behind the complex internal wave pattern observed worldwide near irregular continental margins.

[6] The previous internal tide behaviour problem starts on its forcing mechanism, which as itself a non-trivial solution over geomorphic shelf features such as submarine canyons and promontories (Quaresma and Pichon, here after Part I). Over narrow continental margins the barotropic tide propagates predominantly in Kelvin wave mode, driving the tidal flow along-shelf. Consequently, geomorphic shelf features, establishing along-shelf slopes, become inevitable obstacles to the tidal wave and will determine its propagation solution (Part I). Submarine canyon and promontories are identified as active IT generation sites by the interpretation of Synthetic Aperture Radar (SAR) images and from *in situ* observations. Figure 1 shows strong signatures of internal tide “solitons” propagating along the west-Iberian shelf, over the Estremadura plateau (an abrupt submarine promontory) and further north from the Nazaré submarine canyon, both geomorphic features located side by side in a configuration such as the Monterrey canyon and the Sur platform. Over such irregular continental margins, three-dimensional (3D) solutions are needed to interpret and predict the generation and propagation of the observed internal tide patterns.

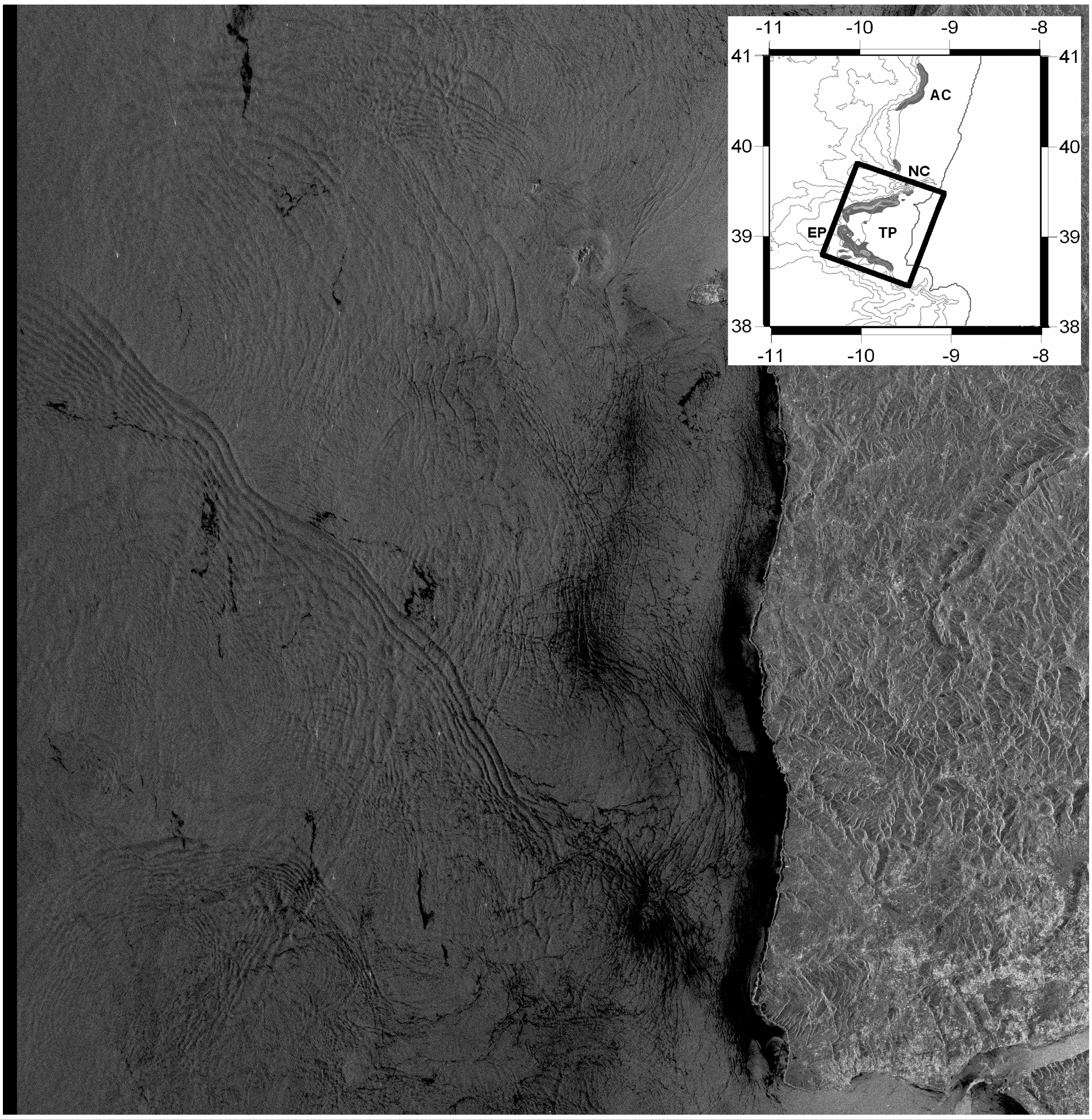

Figure 1a. ERS1-SAR image (08*AUG*1994, 11h 22min UTM), showing sea-surface manifestations of non-linear internal tides propagation over the promontory of Estremadura (EP), an abrupt geomorphic feature in the west-Iberian continental margin. The propagation directions are interpreted as southwest to northeast (stronger and numerous signatures) and from northeast to southwest (few weaker signatures). Multiple signatures propagating in other directions over layer this crossing over pattern. The image location is presented in the upper right corner, where its limits are traced over the semi-diurnal barotropic forcing term map, published by Quaresma & Pichon (2011) for the west-Iberian region (contour show strong BFT values). TP stands for Tagus Plateau, NC for Nazaré and AC for Aveiro submarine canyons.

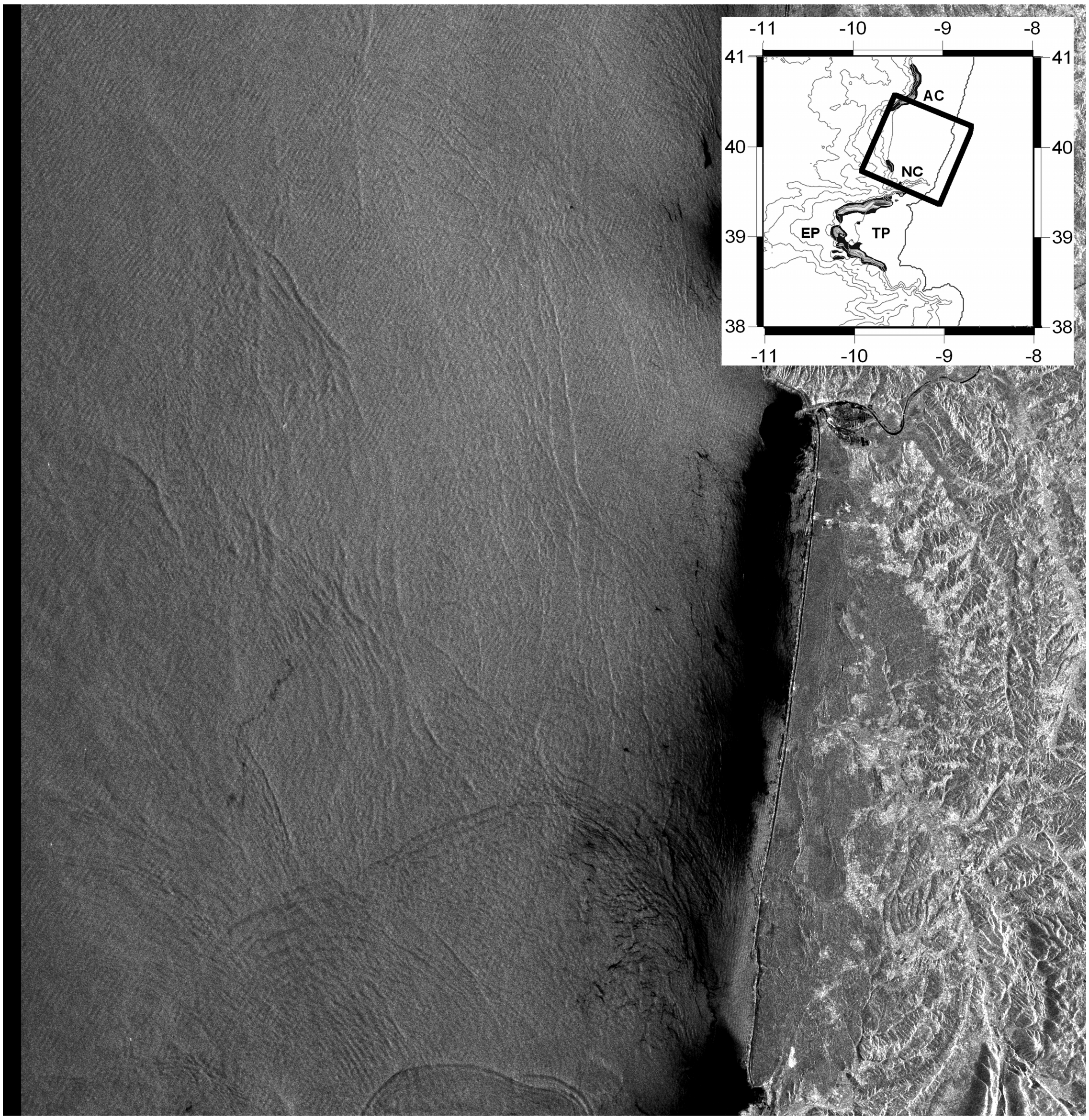

Figure 1b. ERS1-SAR image (19*SET*1993, 11h 21min UTM), showing sea-surface manifestations of non-linear internal tides propagation from the Nazaré submarine canyon (NC), an abrupt geomorphic feature in the west-Iberian continental margin. The propagation directions are interpreted as south to north (stronger signatures) and from offshore to the coast (dispersed signatures). Multiple signatures propagating in other directions over layer this crossing over pattern. The image location is presented in the upper right corner, where its limits are traced over the semi-diurnal barotropic forcing term map, published by Quaresma & Pichon (2011) for the west-Iberian region (contour show strong BFT values). TP stands for Tagus Plateau, NC for Nazaré and AC for Aveiro submarine canyons.

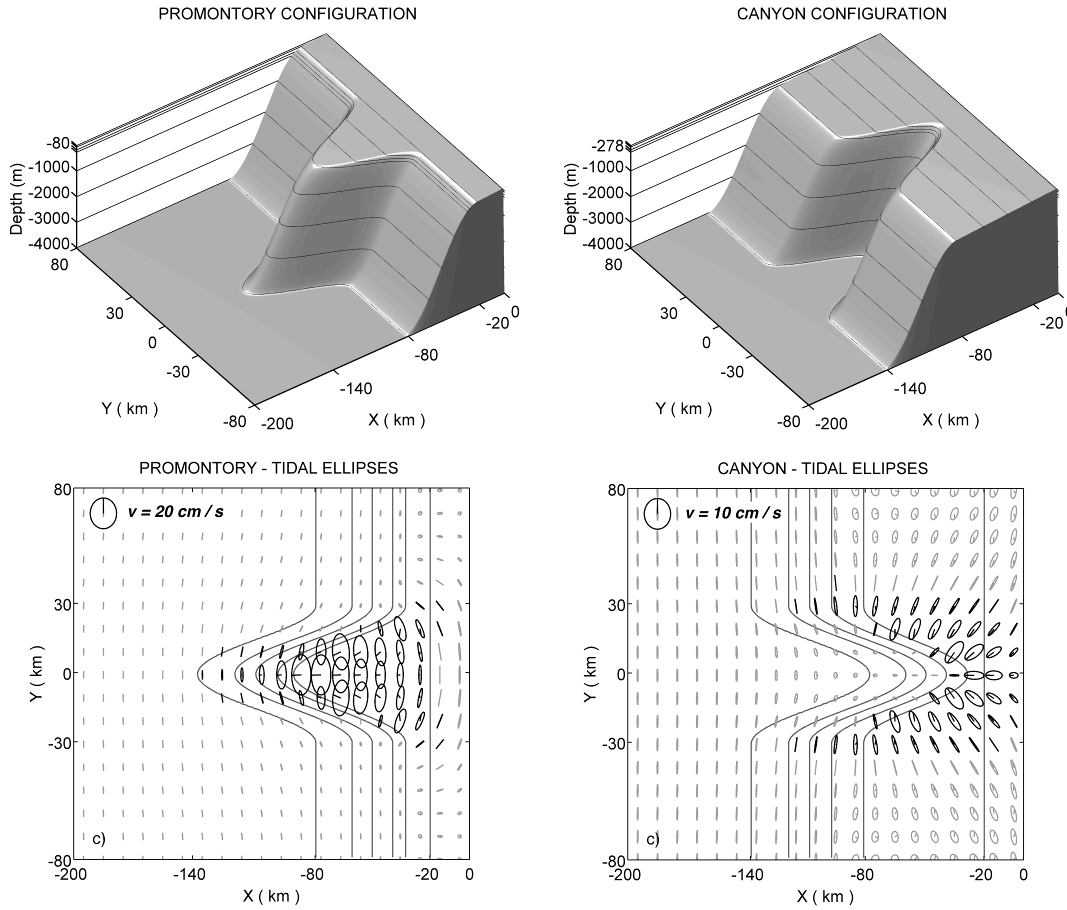

Figure 3. Barotropic solutions of tidal flow over two idealized geomorphic features, representing opposite shelf width anomalies: Promontory (left) and submarine canyon (right). Tidal velocity ellipses are represented in gray for counterclockwise rotation and in black for clockwise. Their axis indicates velocity current vectors at mid-flood tide phase. From Quaresma & Pichon (Part I)

[7] The present work pretends to introduce this along-shelf variability to the study of the internal tide scattering solution. In Quaresma & Pichon (Part I) the authors simplified the canyon and the promontory feature to idealized shelf width anomalies and solved the linear Laplace tidal equations bounded solution, over these bathymetries (Figure 3). Results show the distortion of the barotropic tidal flow over these features, highlighting the intensification of the tidal currents over the promontory and its diversion over the canyon configuration. The present paper (Part II) adds water column stratification to the precedent idealized bathymetry configurations in order to solve and discuss the local internal tide solution. Following the linear assumption of the governing equations, a barotropic forcing term is calculated from the two-dimensional surface tide solutions (Part I), to be used as a diagnostic parameter of the location, strength and phase of baroclinic modes generation (section 2). The same finite-difference numerical model is used here with different stratification configurations to solve the seasonal upper-ocean 2-layers internal tide and the internal tide beam scattering under constant buoyancy frequency (section 3). The interfacial mode shows complex wave patterns interpreted by 2D geometric interference in section 4, where discussion is made on the "diamond" pattern and "ring-like" tide features. In section 5, 3D ray tracing method interprets the continuous stratified solution. A final overview of the concerned dispersion mechanisms is summarized in section 5.

2. Linear internal tide approximation

[8] In the present study, linear wave theory is assumed to be sufficient to analyse and understand how internal tides (IT) are generated and dispersed over abrupt continental shelf features. It is thought that the barotropic tidal flow will originate internal waves in linear form. Both two and three-dimensional solutions become then the geometric result of the superposition of sinusoidal waves (Hydrostatic regime). Nonlinearity terms will promote the steepening of these waves, which non-hydrostatic condition becomes a dispersive mechanism (Gerkema, 1994). Although observations show the presence of non-linear features in the west-Iberian margin, one can suppose that, at their origin, a linear internal tide is generated over local bathymetry slopes when crossed by barotropic tidal flows. This approach becomes sufficient if tidal current velocities (U) are small compared with IT phase celerity ($U << C_0$). To verify this assumption let us take as reference the maximum barotropic tidal current velocities observed in the idealized promontory (~ 0.2 m.s^{-1}) and canyon (~ 0.1 m.s^{-1}) solutions (Figure 2). This velocity values can be compared with the internal wave celerity, C, when we considered an interfacial tide or a beam propagating internal tide (Figure 3). The respective dispersion linear equations, in rotating frameworks, are (1) for two-layers interface mode and (2) for each normal mode in a continuously stratified layer:

$$C_1 = \sqrt{\frac{g'}{H}\,\frac{h_1(H-h_1)}{1-f^2/\omega^2}} \quad (1)$$

$$C_{\omega,n} = \sqrt{\frac{C_n}{1-f^2/\omega^2}} \quad , \; C_n = \frac{NH}{n\pi} \quad , \; n = 1,2,3,\ldots \quad (2)$$

where H is the bottom depth, h_1 the upper-mixing layer thickness, $g' = g\ \Delta\rho / \rho_2$ is the reduced gravity, $\Delta\rho = \rho_2 - \rho_1$ the fluid density difference between the upper and the bottom layer (for the single interface mode), f is the inertial frequency and ω the tidal frequency. In equation (2), n represents the baroclinic mode number, H the depth of a flat bottom and N a constant buoyancy frequency. From linear internal wave approach, the dispersion relation of such waves is (3), which shows that internal tidal beam propagates obliquely, making an angle θ with the horizontal plane function of ω, f and N.

$$\omega^2 = f^2 \sin^2\theta + N^2 \cos^2\theta \quad (3)$$

[9] For both cases, one can estimate the respective wavelength, λ, given by $2\pi\ C / \omega$ (Figure 3). From Figure 3 one can verify that for the stratification profiles adopted in the present study, the linear assumption is satisfied. However, the wave phase and current velocity differences can be small (less than one order magnitude), especially for the interfacial tide solution over shallow regions. This fact shows that the present linear solutions can quickly change to nonlinear scenarios where a different approach must be applied (non-hydrostatic governing equations). In nature this feeble linear state generally becomes nonlinear when internal tidal currents get stronger by wave shoaling, wave-wave interference, wave-current interference or simply by variations in space or time of the local stratification. In this case the sinusoidal internal tide starts to be distorted to cnoidal form and if one take the non-hydrostatic dispersion they will be disintegrated in solitary waves (that eventually can break, giving rise to strong mixing).

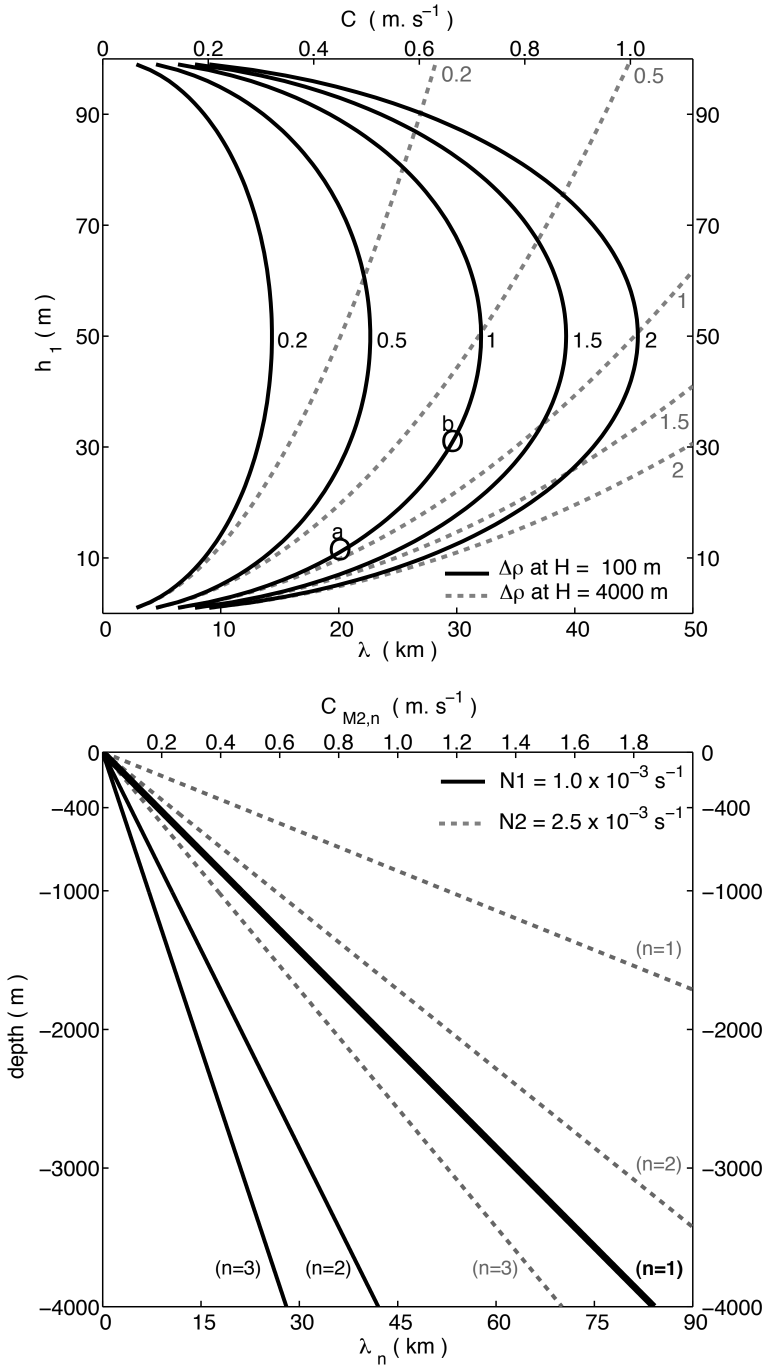

Figure 3. Wave phase celerity for: two-layer interfacial tides and Baroclinic modes propagating in continuously stratified layers: up) Interfacial mode velocity, C (and respective wavelength, λ) is represented by solid line when propagating over 100m depth shallow water regions and in gray slashed line when propagating over the 4000m abyssal plain. Each line represents a different $\Delta\rho$ (value indicated). h_1 is the upper layer thickness (meters). The present study adopts an interfacial surface ($\Delta\rho = 1$ kg.m^{-3}) placed at: a) 10m and b) 30 m depth. Notice that the solid line inverts when the interface is located at mid-depth (50 m); down) Baroclinic mode velocity, and wavelength, as function of water column depth, stratification N (two different buoyancy frequencies and the first 3 mode numbers are considered).

a) Internal tide generation

[9] The physical principle of the internal tide generation lies on the buoyancy force, acting to restore periodic vertical displacements of the ocean isopycnals, when pushed by the tidal flow against topographic slopes. This generation mechanism is called tide-topography interaction and was first recognized by Zeilon (1911, quoted by Wunsh 1975). Three variables (barotropic tidal flow, density gradients and bathymetry slopes) act to create internal unbalanced horizontal pressure gradients (disturbances) that will propagate away from the area of generation as progressive baroclinic oscillations (internal waves) dominated by lowest vertical modes (Wunsch, 1975, Mazé 1987). Taking the buoyancy perturbation $-g\,\rho'/\rho_0$ as the internal wave body force that gives rise to the internal tide oscillation, one can formulate its function as (Baines 1982)

$$\frac{g\rho'}{\rho_0} = -\frac{N^2}{\omega}\frac{Q}{H^2}z\left(\frac{\partial H}{\partial x}\right)\sin\omega t \qquad (4)$$

where ω is the tidal frequency, ρ_0 the density reference, ρ' the perturbation density, g the gravity, H the bottom depth, z the interface depth and N the buoyancy frequency, $N^2 = -\,g\,\rho^{-1}\,(d\rho\,/\,dz)$. From (4) one can separate the three acting variables and regroup them as

$$\frac{g\rho'}{\rho_0} = -\frac{N^2}{\omega}z\left[\frac{\mathrm{u}\sin(\omega t+\varphi_{\mathrm{u}})}{h}\left(\frac{\partial h}{\partial x}\right) + \frac{\mathrm{v}\sin(\omega t+\varphi_{\mathrm{v}})}{h}\left(\frac{\partial h}{\partial y}\right)\right] \qquad (5)$$

[10] The term in brackets (5), so-called barotropic forcing term (BFT), is independent of the stratification profile but varies along the tidal cycle (where u and v are the amplitudes and φ the phase of the east-west and north-south barotropic velocity components). The BFT is used next as a diagnostic parameter to quantify the strength of the vertical velocity component rising from the tidal flow crossing the bottom isobaths. This term becomes then a proxy of the potential, location and phase of the energy dissipation from barotropic to baroclinic modes.

b) Barotropic forcing term

[11] For the present study, the BFT is calculated from each tidal flow solution obtained by Quaresma & Pichon (Part I). Figure 4 and 5 show the BFT for the promontory and canyon configuration, at four consecutive SSH tidal instants (taking T_{M2} as the M2 tidal harmonic period): high tide (t_0), mid-ebb tide ($t = t_0 + 1/4T_{M2}$), low tide ($t = t_0 + 1/2T_{M2}$) and mid-flood tide ($t = t_0 + 3/4T_{M2}$). As expected, the higher values are located at the rim of each geomorphic feature, where stronger velocity components cross their along-shelf slopes. However, important differences are next pointed out for each shelf configuration.

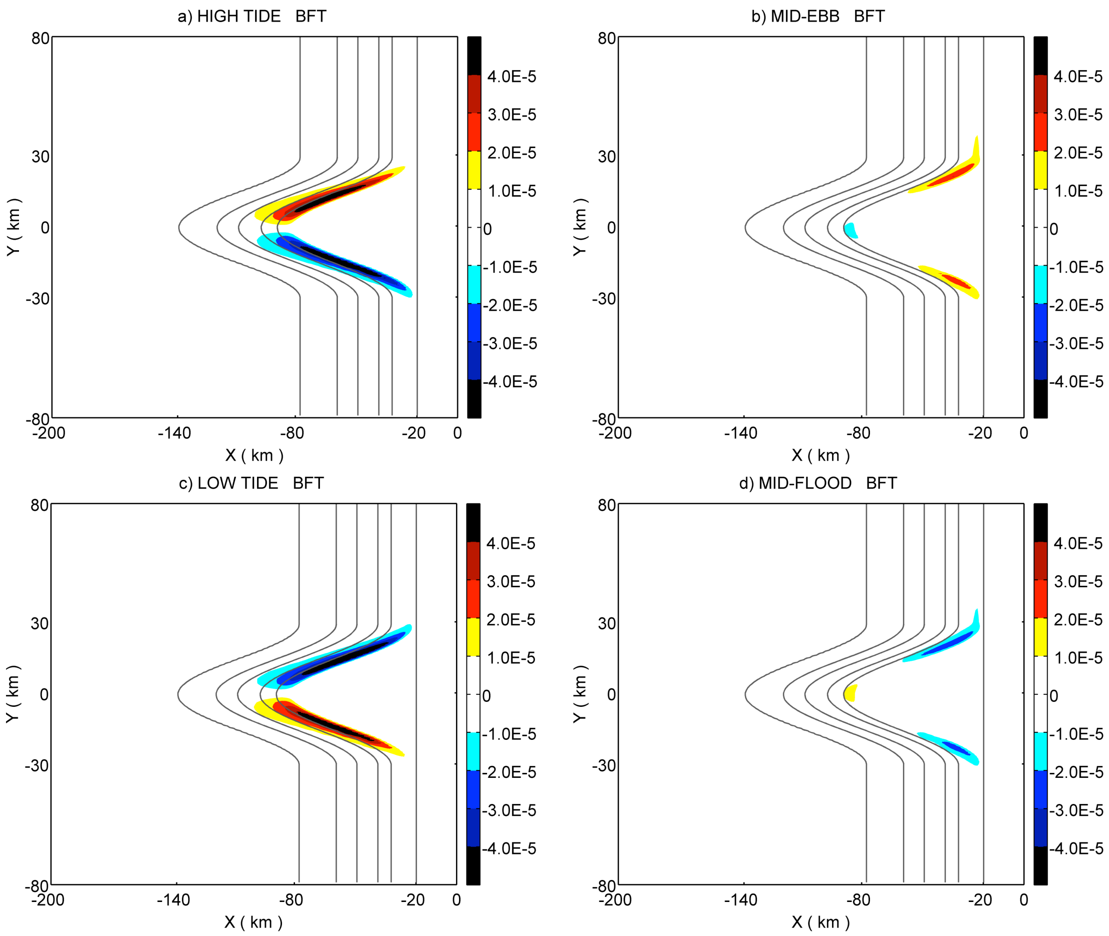

Figure 4. Barotropic forcing term (filled contours, s^{-1}) over a promontory bathymetry configuration at four consecutive tidal instants: a) High tide; b) mid-ebb tide; c) Low tide; d) mid-flood tide.

[12] The promontory evidences higher *BFT* values (Figure 4) as the result of stronger cross-slope current velocities, induced by the flow constriction of the offshore Kelvin wave (Figure 2). The maximum values are found at high tide and low tide, when Kelvin's cross-shelf pressure gradients are also stronger. The different *BFT* sign, verified at each side of the promontory, reveals the reverse phase of the tidal flow when climbing and falling over the two opposite along-shelf slopes. This implies the generation of baroclinic modes in opposite phase at each promontory's face.

[13] Contrary to the positive shelf width anomaly, the canyon configuration shows a smaller *BFT* strength (Figure 5), in the same proportion as the tidal currents crossing each obstacle isobaths (Figure 2). Here, the maximum flow, crossing the canyon's relief, is verified during mid-ebb and mid-flood phases as an ageostrophic response to the SSH anomaly (Part I). The concave bathymetry of the canyon puts in phase the tidal flow around the canyon head (at both northern and southern faces). In the outer canyon, when the distance between the northern and southern face increase to values that overcome the length of the tidal excursion order, the *BFT* reveals phase opposition. Over these offshore regions, the *BFT* solution resembles the promontory behaviour, with maximum values attained at high tide and low tide, in opposite phase between the opposed faces.

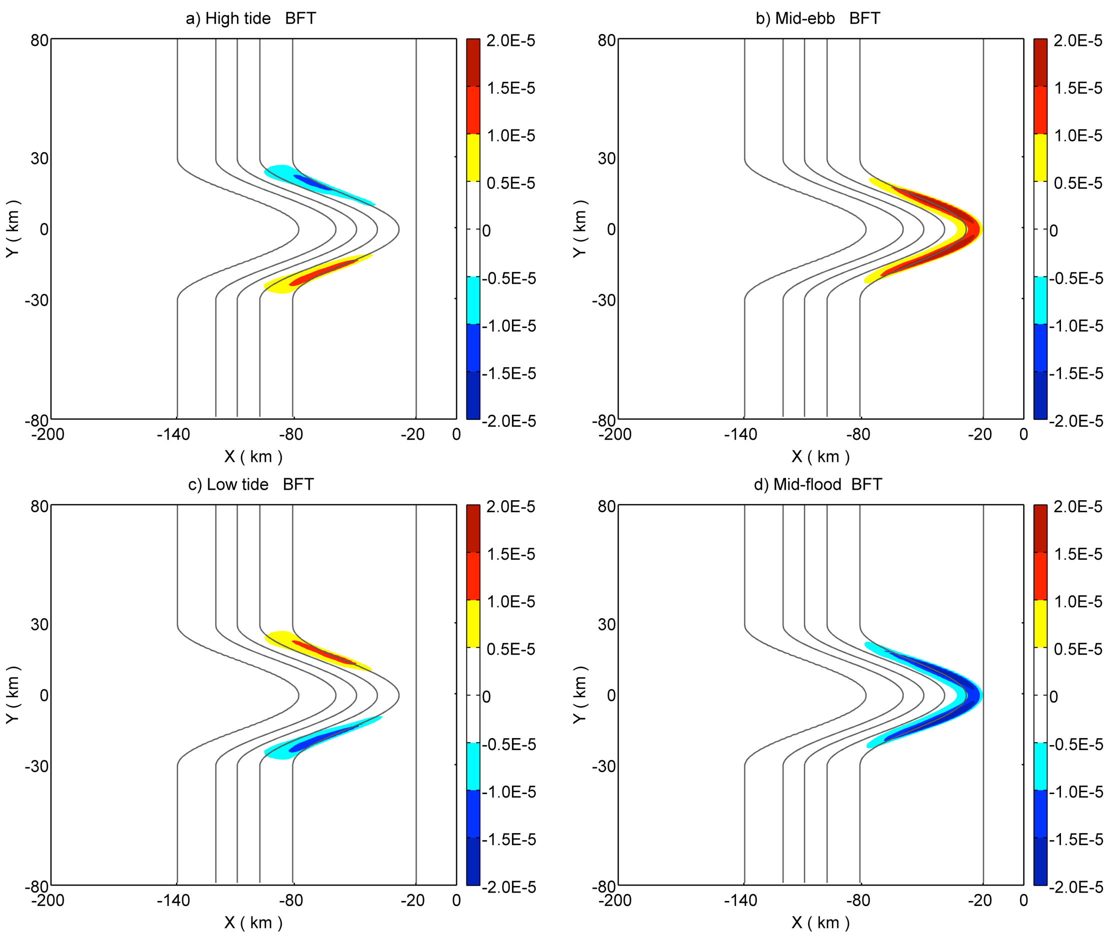

Figure 5. Barotropic forcing term (filled contours, s^{-1}) over a submarine canyon bathymetry configuration at four consecutive tidal instants: a) High tide; b) mid-ebb tide; c) Low tide; d) mid-flood tide.

3. Internal tide over irregular shelves

[14] When geomorphic shelf features, such as submarine canyons and promontories, impose significant along-shelf bathymetry gradients, internal tides are generated in different phases of the tidal cycle and probably scattered in multiple directions (from complex isobaths configurations). A finite difference primitive equation model solves here the 3D stratified tidal solution (section 3.a), forced by 1D "smooth" shelf analytical boundary conditions (Part I), different density profiles (section 3.b) and idealized bathymetries (section 3.c). Stratification is assumed to be homogenous in the horizontal.

a. Numerical model

[15] The governing equation of the fluid motion in a stratified rotating medium are solved by a finite-difference, hydrostatic, free-surface shallow water model (Bleck & Smith 1990) under a regular staggered mesh grid (type Arakawa-C). The model employs an explicit time-splitting scheme to separate the fast barotropic gravity waves prognostic from the slower baroclinic modes in both mass and momentum conservation equations (Morel et al., 2008). In the present work, different number isopycnal layers configure the vertical coordinated of the model. Advection and viscosity non-linear terms are parameterized, while bottom friction is neglected. Monochromatic 1D tidal solutions are computed from Part I and used as boundary conditions at the three open boundaries of the numerical model (where the tide wave propagation is approximated by a constant along-shore wavenumber, l). The model is initialized at rest and progressively forced in sponge layers at the open boundaries by monochromatic M2 tide ($\omega = 1.41 \times 10^{-4}$ s^{-1}; 1m amplitude at the coastline) propagating along shelf ($l = 7.0 \times 10^{-7}$ m^{-1}). The solution in the interior of the domain is driven by the boundary conditions and after the ramp-up phase it is in equilibrium with the adopted wavenumber, l.

b. Stratification

[16] Internal tides owe their existence to stratification, flow and topography interactions. If the BFT sets the generation potential strength, the density structure rules their form and propagation mechanism. Density gradients range from quasi-homogenous deep ocean waters to strong upper ocean pycnoclines (one order magnitude higher). For modelling proposes, the density structures are usually simplified to low number piecewise profiles (generally representing seasonal thermoclines) or to continuous stratified profiles of constant buoyancy frequency, N (expressing the weaker density gradients predominant from surface to the bottom of real oceans).

[17] Climatological profiles show the increasing buoyancy frequency from bottom to surface with maximum characterizing water masses transitions. For the present study two distinct density profiles are considered: 1) homogenous ocean covered by a thin upper mixed layer, in a two-layers configuration, where $\Delta\rho = 1$ kg.m^{-3}; 2) continuously stratified ocean with a buoyancy value of $N = 1\text{x}10^{-3}$ s^{-1}. The first configuration supports interfacial tidal waves propagating in baroclinic mode 1 (horizontal propagation), while the second configuration allows the energy to spread into numerous modes that compose internal tidal beams (3D propagation). Take γ as the bottom slope, given by $\gamma^2 = (\partial H/\partial x)^2 + (\partial H/\partial y)^2$, and c the internal tidal beam slope, given by $c = \tan\,\theta = (\omega^2 - f^2)^{1/2}\,(N^2 - \omega^2)^{-1/2}$. Tidal beams spread out from critical slopes ($\gamma/c = 1$), while interfacial internal waves radiate from regions of strong *BFT* values (Figure 6).

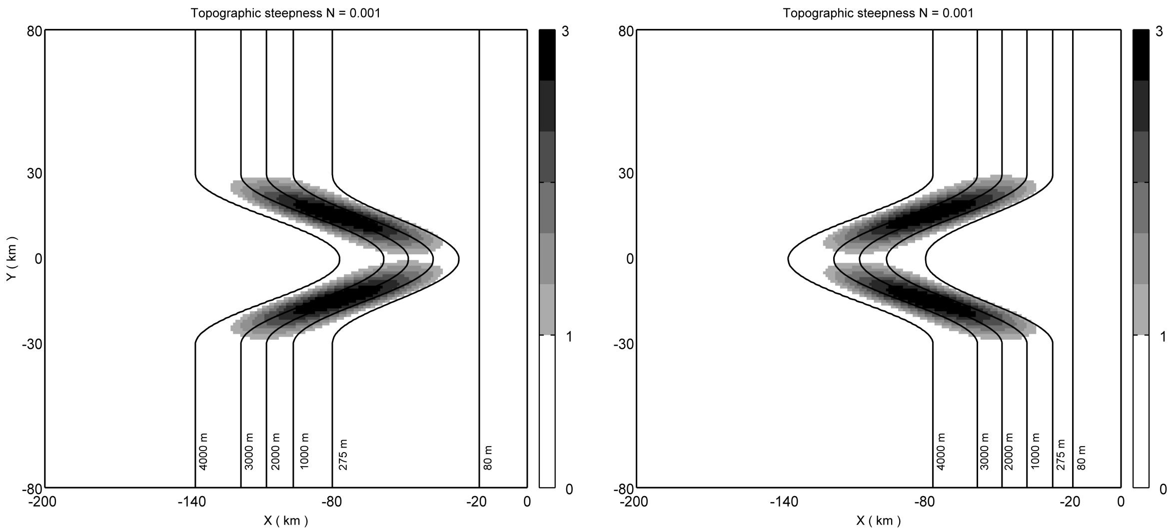

Figure 6. The topographic steepness γ/c for each bathymetry configuration under a constant stratification of buoyancy frequency N = 0.001 s^{-1}: $\gamma/c = 1$ (*critical*), $\gamma/c < 1$ (*subcritical*) and $\gamma/c > 1$ (*super-critical*). [

c. Idealized Topography

[18] Three-dimensional irregular continental margins are reproduced in the present study by single shelf-width anomalies, shaped symmetrically along regular narrow shelves. Two distinct bathymetry configurations are built aiming the evaluation of the impact of a positive (promontory) and a negative (canyon) anomaly on the baroclinic tidal wave solution. Each topographic configuration (Table 1) is built from XY-plane grid (450 x 540 km) with 1 arc-minute resolution (see Part I for details). The along-shelf slopes set up by submarine canyons and promontories become significant obstacles to the barotropic tidal stream (Part I). Strong velocity components crossing straight isobaths disturb upper-ocean density interfaces, which potential energy is radiated in the form of interfacial waves (section 4) or oblique beams (section 5). Over the 3D idealized topographies, and under continuous stratified configuration of $N = 1.0 \times 10^{-3}\ s^{-1}$ the critical slopes ($\gamma/c = 1$) trace uninterrupted belts around each feature, separating the sub-critical continental shelf and slope from the steep super-critical canyon and promontory walls (Figure 6).

4. Interfacial internal tide

[19] The interfacial internal tide solution is computed using a simple two-layers density structure (Figure 5). Two different configurations are defined to express the depth range of seasonal thermoclines, commonly observed during summer conditions over mid-latitude continental margins: a) The first reproduces a very shallow mixing-layer (10m depth) superimposed over a homogeneous ocean with1 kg.m^{-3} density anomaly ($\Delta\rho$); b) The second simulation sinks the previous density interface to 30m depths.

a. Wavelengths and wave patterns

[20] The linear two-layer approach shows a unique interfacial mode, generated above the shelf-breaks where the BFT presents stronger values, propagating in both perpendicular directions to the isobaths of origin (offshore and inshore). From equation (2), each adopted stratification profile gives rise to different interfacial tide wavelength: $\lambda_a \sim 20$km ($h_1 = 10$m) and $\lambda_b \sim 30$km ($h_1 = 30$m). And consequently to different phase velocities: $C \sim 0.45$m.s^{-1} ($h_1 = 10$m) and $C \sim 0.65$m.s^{-1} ($h_1 = 30$m). These solutions can be verified in Figure 3 and results in distinct IT wave pattern obtain over each abrupt shelf feature (Figure 7 and 8). Similar wavelengths, and consequent equal wave patterns, can be obtained under different stratification combinations (Figure 3). Figure 7.c and Figure 8.c show also the resulting baroclinic tidal current ellipses for the upper layers (where they are expected to be stronger if $h_1 < h_2$), which small magnitude (of the order of the barotropic currents) verifies the linear approximation assume earlier. The observed wave patterns are discussed next focusing the geometric interference solution under the linear approximation.

Figure 7. M2 interfacial tide solutions over positive shelf width anomaly (promontory). In the left hand side the pycnocline ($\Delta\rho$ = 1 kg.m^{-3}) is placed at 10m depth and in the right the same pycnocline is plunged to at 30m depth. a) pycnocline displacement from its equilibrium depth (η_1) at high tide phase. b) Internal tide amplitude calculated by harmonic analysis of $\eta_1(t)$; c) Upper-layer tidal velocity ellipses rotating clockwise. The geomorphic feature is represented by the following isobaths contours: 80, 278, 1000, 2000, 3000 and 4000m.

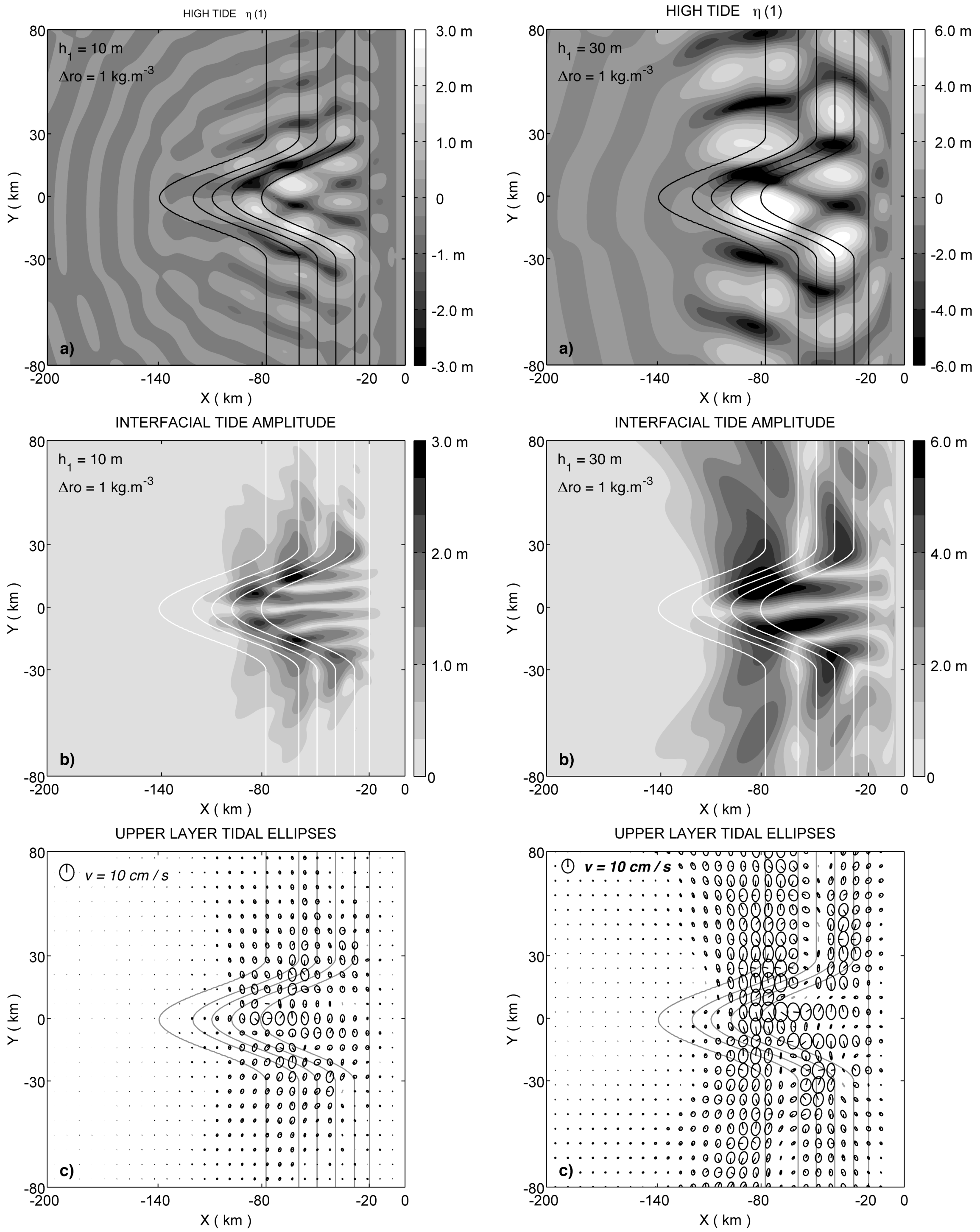

Figure 8. M2 interfacial tide solutions over negative shelf width anomaly (submarine canyon). In the left hand side the pycnocline ($\Delta\rho$ = 1 kg.m^{-3}) is placed at 10m depth and in the right the same pycnocline is plunged to 30m depth: a) pycnocline displacement from its equilibrium depth (η_1) at mid-ebb tide phase; b) Internal tide amplitude calculated by harmonic analysis of $\eta_1(t)$; c) Upper-layer tidal velocity ellipses rotating clockwise. The geomorphic feature is represented by the following isobaths contours: 80, 278, 1000, 2000, 3000 and 4000m.

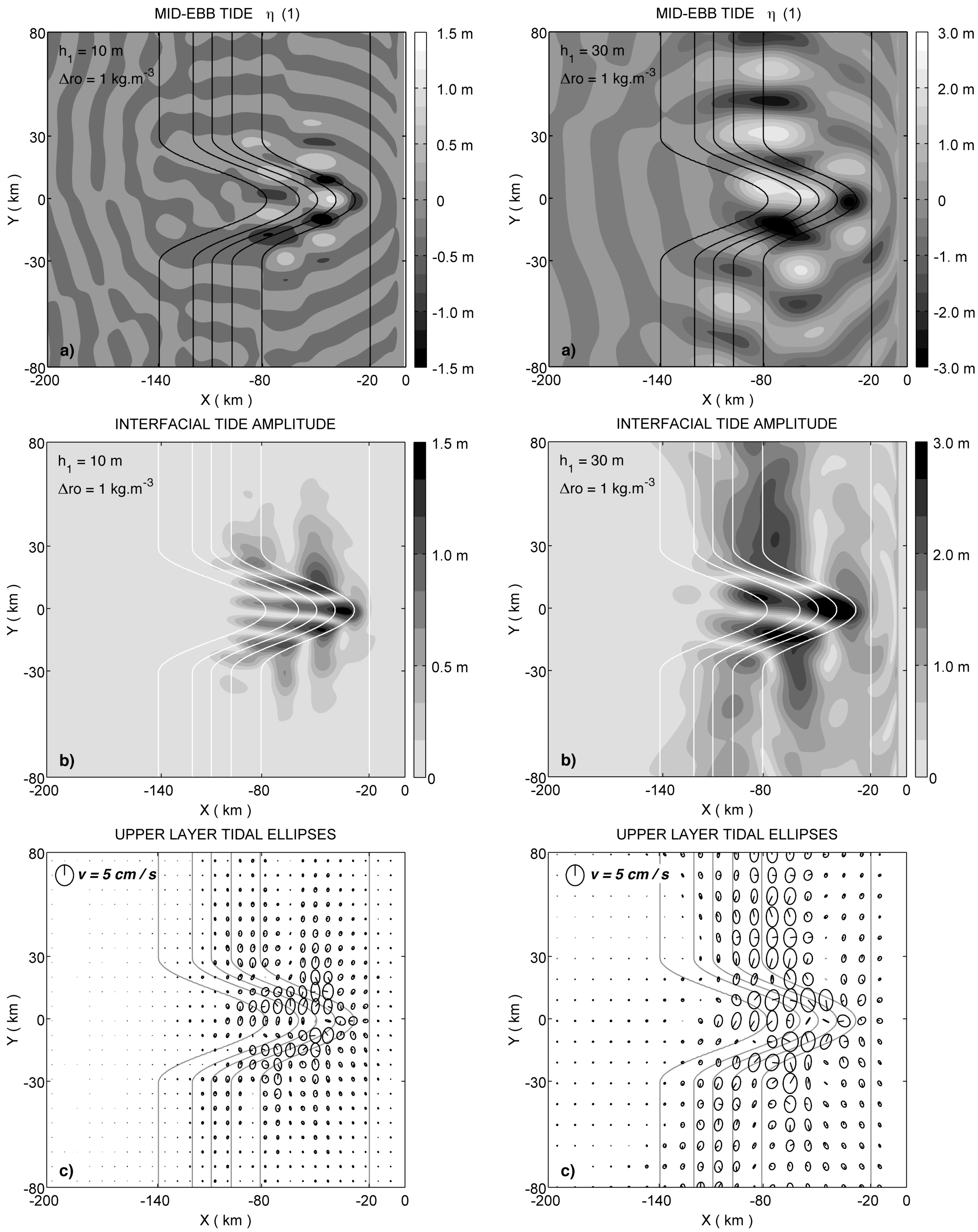

b. Standing modes

[21] Here the analysis focuses on the IT solution inside the topographic features, where results show standing wave modes in the along-shelf direction. In both topographic configurations, the density interface is vertically displaced above each generation rim in phase with the BFT sign (Figure 4 and 5). Its amplitude is proportional to the BFT value and consequently the promontory (Figure 7) gives rise to higher internal waves than the submarine canyon configuration (Figure 8).

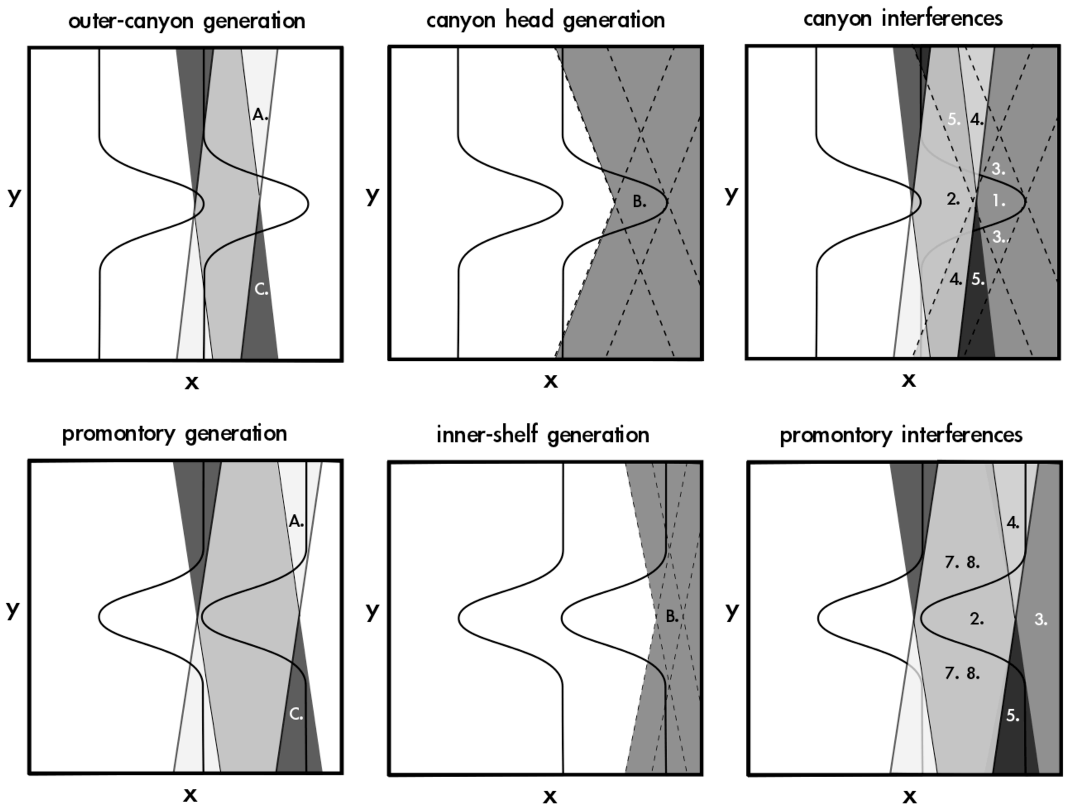

Figure 9. Schematic diagrams of the different interference regions at each shelf-width anomaly. For each configuration the two 180º out-of-phase internal tidal trains (generated in the outer-canyon rim and at the faces of the promontory) are represented by bands A. and C. A third wave train is generated with a quarter cycle lag over the canyon head and in smaller scale at the promontory inner-shelf. The diagonal propagation paths make each of these trains to intercept in different regions. Numbers identify each particular wave combination (interference) and help the interpretation of the next figures.

[22] Interference processes dominate the wave pattern solution and result from almost face-to-face generation slopes and an out-of-phase generation cycle (Figure 9). With small aperture angles, canyons and promontories scatter internal tide waves mainly in the along-shelf direction. The fact that the generating slopes are not aligned to each other originates diagonal travelling paths (towards the opposed rim) and creates a geometric interference so-called "diamond" pattern solution (discussed next). This solution is observed in the interior domain of each feature, bordered by IT generation slopes (rims), and corresponds to converging wave interference (geometric sum of opposite along-shelf wavenumber signs). When two near point sources radiate waves with equal frequency and wavelength, the convergent crests interfere to produce a standing mode of equal frequency and wavelength. The resulting amplitude doubles the amplitude of the incident waves and numerous nodal points (non oscillating nodes) are formed, with a number of nodes functions of the section width. (Figure 7 and Figure 8). In the present case study both opposite slopes have small differences in orientation, which interference solution creates a standing wave component in the along-shelf direction and a progressive wave component in the cross-shelf direction.

c. Diamond patterns

[23] Both canyon and promontory features generate over their interior domain internal wave (IW) diamond patterns (where wave crests form a quadrilateral polygon). This interference configuration results from the crossing over of the two generated wave trains, travelling in diagonal directions. This geometric solution becomes visible for wide features, when distances between the opposite generation slopes are larger than one IW wavelength. Diamond aperture (smaller distance between two opposite polygon vertices) is function of the difference in the propagation directions of the two incident wave trains. Near-rectangular canyons (or promontories), where both rims would share similar orientations, the diamond patches will become very squeezed. While triangular canyons mouths (or promontory's plateaus), with ~90º aperture angle, will generate square patches.

[24] An interesting result from this interference process is the generation of a standing wave component in the cross-canyon (and cross-promontory) y-direction and the generation of new propagating internal wave mode in the along-canyon (along-promontory) x-direction (Figure 10.a). These new IW modes propagate as the crossing crests interceptions transit in time along this cross-shelf direction, from canyon head region to offshore and inversely from outer-shelf to the inner-plateau region for the promontory configuration (as the promontory shape is reversed from the canyon). This geometric advection enables this new IW mode to propagate with lower phase speeds for apertures lower than 90º, or with higher phase speeds for apertures higher than 90º).

Consequently the wavelength will be function of the diamond patch aperture, as the frequency is the same as the original wave trains. It is important to notice that the nodal points generated by the standing mode component create null oscillation cross-shelf section, as they are continuously distributed along this direction (see Figure 7.b and Figure 8.b). Alongside these invariant cross-shelf solutions, the anti-nodes double the amplitude of the incident waves and transport this energy across-shelf (Figure 10.a).

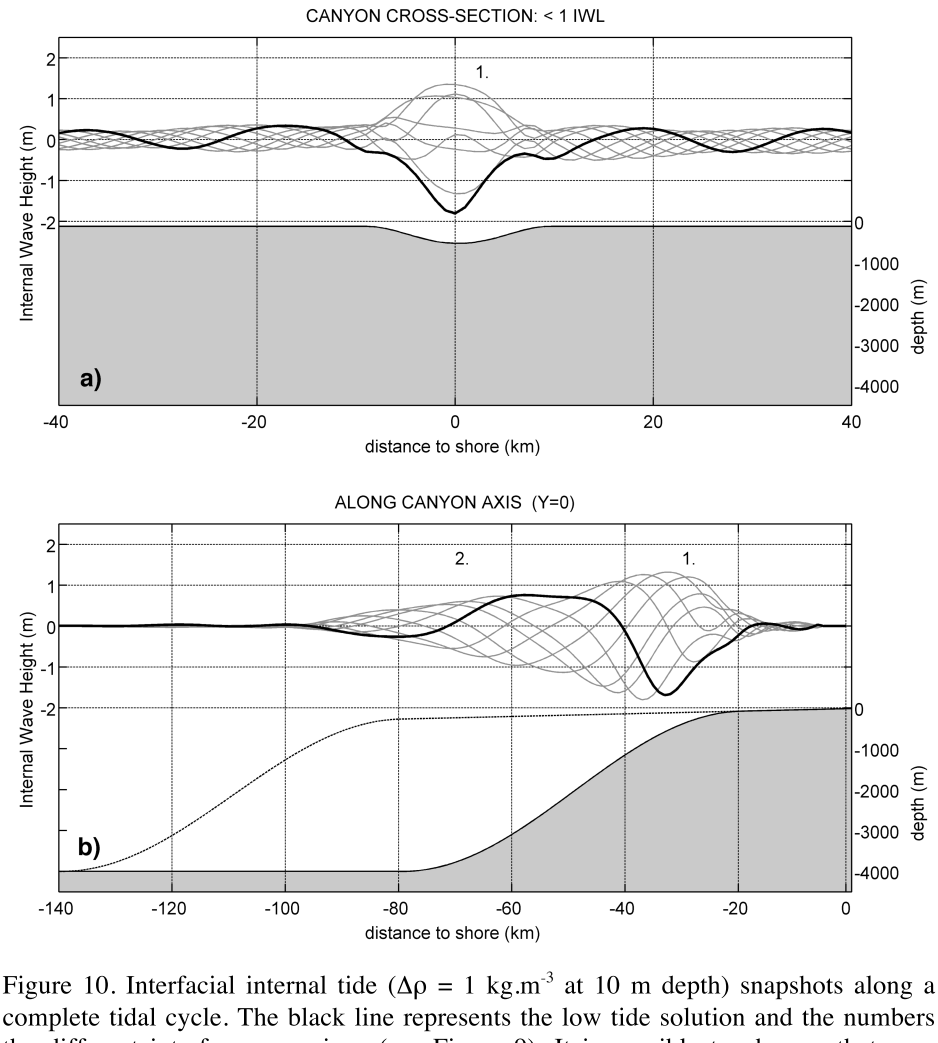

Figure 10. Interfacial internal tide ($\Delta\rho$ = 1 kg.m^{-3} at 10 m depth) snapshots along a complete tidal cycle. The black line represents the low tide solution and the numbers the different interference regions (see Figure 9). It is possible to observe that over cross-canyon head sections shorter than one Internal Wave Length (IWL), the interface plunges until the low tide instance. Along the canyon axis the interference solution generates a progressive internal wave with the same phase velocity but different wavelength (trapped wave).

d. "Ring-like" internal tide signatures

[25] A major difference is observed in the IW behaviour at small cross-feature's sections, between the canyon and the promontory configurations. With BFT in phase around the canyon head and cross-canyon distances less than one wavelength, the vertical displacement of the isopycnal interface is amplified by geometric contribution of multiple positive "tide-topography interaction" regions. In other words, the convergent flow (during mid-ebb tidal phase), or divergent flow (during mid-flood tidal phase), magnifies the interface plunging, or rising, focusing the BFT in the restricted canyon-head region (Figure 10.b). This process transforms small concave shelf features, such as canyon heads, in strong generation "hot-spots". Serpette & Mazé (1989) called this mechanism a "ring-like" generation, as they observed internal tide front as small circle shapes "radiating" from a canyon head. Quaresma et al. (2007) proposed a similar generation mechanism to strong internal tide solitons over the upper Nazaré canyon rim (mid-shelf region), where the reduction of the cross-canyon section creates a concave valley. This mechanism is not observed in the convex promontory configurations since the opposite BFT phases (destructive interference) inhibit the internal tide generation focusing

e) Progressive modes

[26] Outside the two topographic features, numerical results show progressives waves with different spatial variations in amplitude. The promontory presents an almost symmetric solution, while the canyon shows asymmetry. These results are interpreted next as the result of simple geometric interferences.

[27] With convex shapes, projecting continental shelves offshore, **promontories** also scatter interfacial IW towards the open ocean. These waves are generated with opposite phase at each point source of the promontory (southern and northern faces), where the BFT is also in reverse phase (Figure 4). The solution shows an offshore decay of the internal tide amplitude due to radial dispersion. However, this region also reveals intercalated along-shelf sections, where the amplitude is either amplified or damped symmetrically to the promontory axes (Figure 7.b). This wave pattern results from another geometric interference process, now with internal waves of equal amplitude and wavelength, propagating in similar direction (sharing equivalent along-shore wavenumber).

[28] The internal tides generated at each point source and crossing the interior domain of the shelf features will encounter on the opposite side another point source generating waves in opposite phase. Destructive interference (Figure 11.b) occurs then at the along-shelf tracks, superposing promontory's sections (y-direction) measuring multiple IW wavelengths (λ, 2λ, …). Conversely, constructive interference (Figure 11.a and 11.c) occurs along promontory's sections half-wavelength wider or narrower than the previous ones (3/2 λ, 5/2 λ, …). This interference configuration is summarized in a schematic diagram in Figure 9 and the corresponding wave pattern can be verified in the amplitude distribution of the internal tide, calculated by harmonic analysis in the vicinity of the promontory feature (Figure 7). The solution also shows wave refraction processes undergone by coastal incident internal tides, after crossing the promontory's plateau and intercepting these shallow depths in diagonal directions (Figure 7.a).

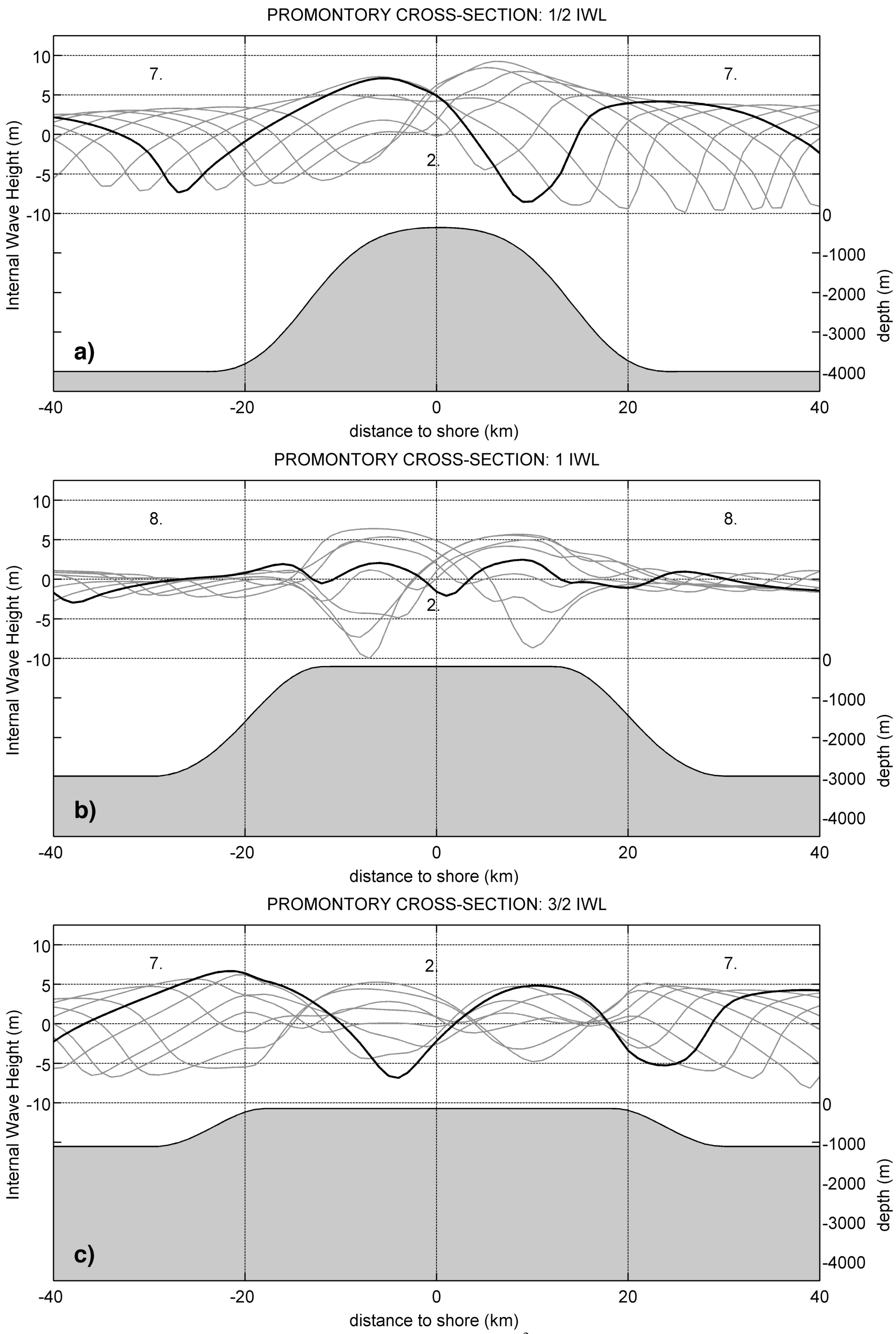

Figure 11. Interfacial internal tide ($\Delta\rho$ = 1 kg.m^{-3} at 30 m depth) snapshots over different y-section crossing the promontory at several instants along the tidal cycle. The black line represents the mid-ebb solution and the numbers the different interference regions (see Figure 9).

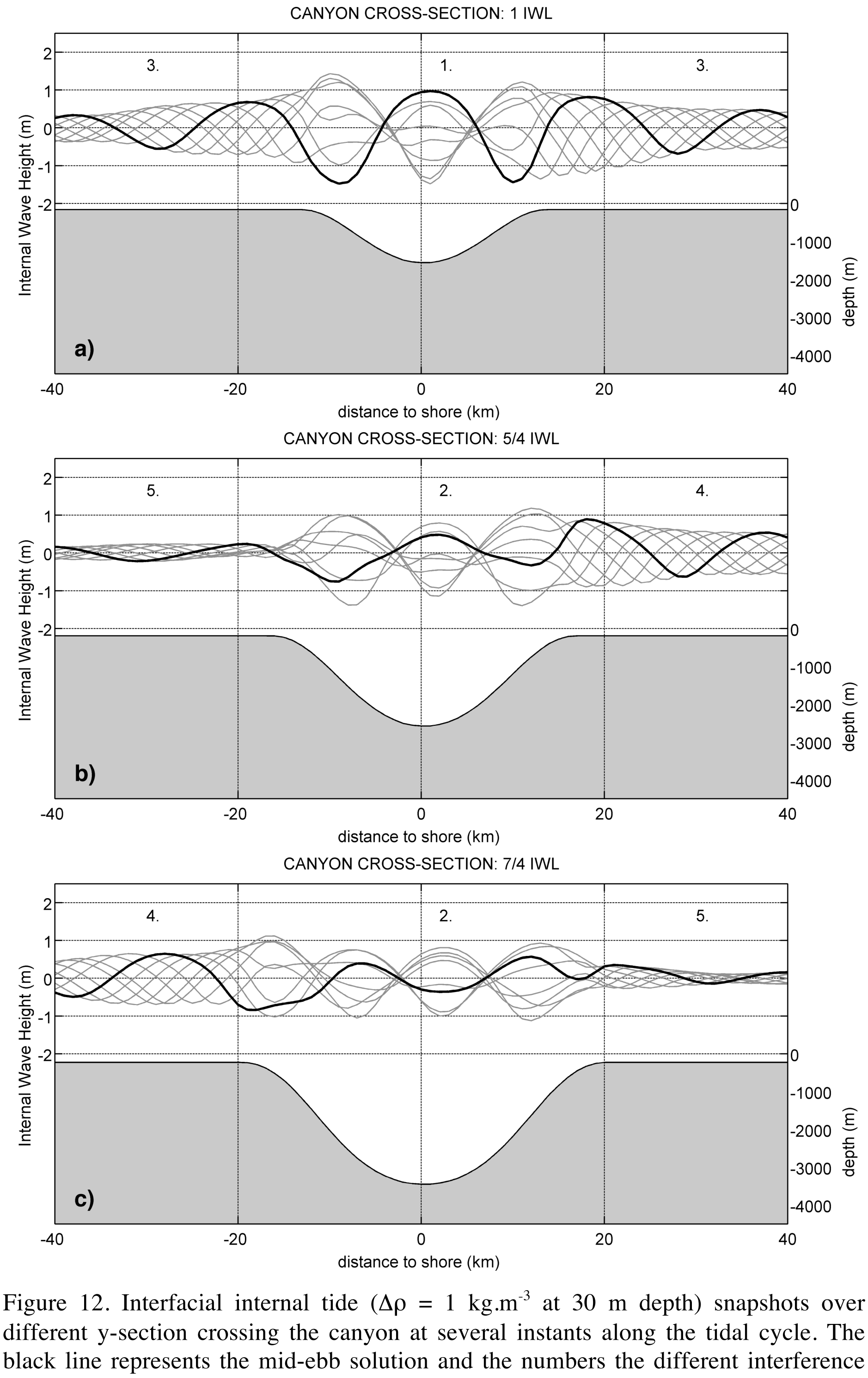

Figure 12. Interfacial internal tide ($\Delta\rho$ = 1 kg.m^{-3} at 30 m depth) snapshots over different y-section crossing the canyon at several instants along the tidal cycle. The black line represents the mid-ebb solution and the numbers the different interference regions (see Figure 9). Observe over the canyon head the internal tide is release into the shelf at mid-ebb phase, while at the southern outer-rim this release occurs earlier and in the northern outer-rim later.

[29] The canyon configuration shares the same interference and refraction mechanisms but differs in the scattering directions. With a concave shape, intercepting the continental shelf, **submarine canyons** spread out interfacial tides into the shelf (towards the coast). As they propagate shoreward, the wave amplitude decays by wave radial dispersion and the wave crests rotate to become almost parallel to the coastline, by refraction process (Figure 8.a). Contrary to the promontory configuration, internal tides generated at each point source of the canyon head will encounter on the opposite side another point source generating waves in phase (Figure 9). Constructive interference (Figure 12.a) occurs then at the along-shelf tracks superposing canyon's sections (y-direction) measuring one IW wavelength (λ) and destructive interference would be expected along canyon's sections half-wavelength wider, in an alternated amplification and damping of the internal tide at each new half-wavelength cross-section (like in the promontory configuration). However, in the outer canyon rim, where the barotropic forcing is in opposite phase between facing slopes, a new wave pattern configuration is established. Here the intercalated along-shelf sections become asymmetric, showing amplitude amplification at one side and damping on the opposite shelf (Figure 8.b). This curious result comes from a third progressive wave (propagating either to north or to south as function of the distance between the point sources and the phase lag between different generation instances), produced by two standing waves settled inside the inner promontory region (discussed next).

f. Asymmetric interference

[30] Here the analysis focuses on the asymmetric interference solutions existing outside the canyon (Figure 8.b). This outer-canyon region corresponds to a different *BFT* configuration from the canyon head (Figure 5), where internal waves (IW) are scattered with reverse phases and one could expect to observe similar interference solution as in the promontory's case (Figure 7.b). We will see next that this wave pattern results from the presence of multiple point sources generating internal tides with different phase lags (Figure 9). Firstly, the diagonal IW paths make the interference in this region function of the *BFT* phase verified in the entire canyon domain. Maximum *BFT* values are reached at each quarter-of-tidal cycle, alternating from opposite sign to synchronized IW generation (Figure 5). During mid-ebb and mid-flood phases IWs are generated in phase in the upper canyon region and during high tide and low tide other IWs are generated at the southern and northern canyon rim, in opposite phase. Each desynchronized internal tide generation creates its own standing wave in the interior domain of the canyon. This special case gives rise to a new interference solution, where a third progressive wave is generated by geometric sum of the two previous standing waves, as it will be demonstrated next.

[31] Let us take a linear wave train travelling to the north (positive y-direction), $\eta_1 = a\cos(\omega t + ky)$, encountering a second wave train travelling in the opposite direction with similar amplitude, frequency and wavelength, $\eta_2 = a\cos(\omega t - ky)$. Since both wavenumbers differ in sign, the solution becomes a standing wave of double the amplitude and with the same frequency as the propagating waves: $\eta_3 = 2a\cos ky \cos\omega t$. If the standing wave forced during high-tide and low-tide phases is formulated by η_3, one should represent the other standing wave forced one-quarter cycle out of step in time, at mid-flood and mid-ebb phases, by $\eta_4 = 2a\cos ky \sin\omega t$.

[32] Along cross-sections of one and half wavelength (or multiples of this) the previous standing wave becomes: $\eta_4 = 2a\sin ky \sin\omega t$. Once these two standing waves oscillate inside the canyon a third progressive wave (η_5) become a product of this interference by: $\eta_5 = \eta_3 + \eta_4 = 2a\cos(\omega t - ky)$. This means that the new IW will propagate in only one direction, enabling a constructive (or destructive) interference of η_1, or η_2, if the new wave η_5 arguments are in phase with the original η_1, or η_2, progressive waves (Figure 12.b and 12.c). The propagation direction of this new IW is very sensitive to the cross-shelf width, as for each difference of one quarter IW wavelength both standing waves formulation, change to $\eta_3' = 2a\sin ky \cos\omega t$ and $\eta_4' = 2a\cos ky \sin\omega t$, to obtain $\eta_5' = \eta_3' + \eta_4' = 2a\sin(\omega t + ky)$ and the resulting progressive wave propagates with opposite wavenumber (opposite direction). In the canyon topography these interactions become visible in the resulting outer-shelf wave pattern (Figure 8.b).

[33] A similar effect on smaller scale is also reproduced in the promontory's inner shelf (Figure 7.a). This, results from a phase reversal in the BFT, at mid-ebb and mid-flood instants, focused on the interception of the promontory with the regular shelf (figure 4).

5. Internal tidal beams

[34] In this section, continuous stratification replaces the previous sharp upper-ocean pycnocline (strong stratification) to express a mean ocean profile, where density varies weakly, continuously from surface to bottom of the ocean. If winter density profiles are taken to represent the permanent deep ocean stratification near mid-latitude continental shelves, a mean gradient slope can be approximated by $N = 10^{-3}$ s^{-1} (weak stratification), which varies by less than a factor of 2 in climatological profiles. An exception is verified in the North-eastern Atlantic Ocean where Mediterranean water mass entrainments, between 600 to 1500m depths, can increase these values by a factor of 3 (moderate stratification). Ten regular-sized isopycnal layers, displaced from surface (z = 0) to the abyssal bottom (z = 4000m), replace the previous two-layers configuration. Their densities are chosen to verify the adopted buoyancy value (constant stratification), and their number to let energy dissipate to higher baroclinic modes and consequently generate oblique internal tidal beams. The first density interface is placed beneath the shelf-break, at 400m depths, intercepting near-critical walls (Figure 6). This option will restrict IW to propagate into the deep ocean and filter the respective ascending ray pairs. This somehow reproduces the mixing-layer blocking effects during winter conditions and simplifies results interpretation.

a. Beam scattering

[35] The weak stratification profile ($N = 1.0 \times 10^{-3}$ s^{-1}) reduces the critical slope region to a topographic narrow belt that contours the rim and foot of the strong along-shelf slopes forced by both abrupt shelf-features (Figure 6). Consequently, internal tide waves are generated above maximum *BFT* value slopes and scattered as oblique energy beams detached from critical gradient isobaths, with tangent angles ($\tan \theta$).

[36] The convex shape of the promontory radiates, from each facing along-shelf critical shelf-break belt, offshore propagating waves with opposite phase (Figure 13, left). This behaviour is in phase with the BFT solution (Figure 4). Notice that the 400m depths upper-layer interface limits the IW generation to the outer rim of the promontory, where the BFT sign is opposite for each slope. The energy is radiated perpendicular to the isobaths of origin, towards the deep-ocean (Figure 13, left). At the bottom, IT beams are reflected further way from the promontory, following the same direction of origin if reflecting bottom is flat (the sloping bottom reflection is discussed in the next section). The sinusoidal shape of the promontory's rim causes the perpendicular rays to become divergent at the promontory head (deeper rim) and base (shallower rim near the regular continental shelf). This configuration defocuses the internal wave beams generated over these separated regions and preserve a major energy path radiated from the mid-rim (Figure 14.a).

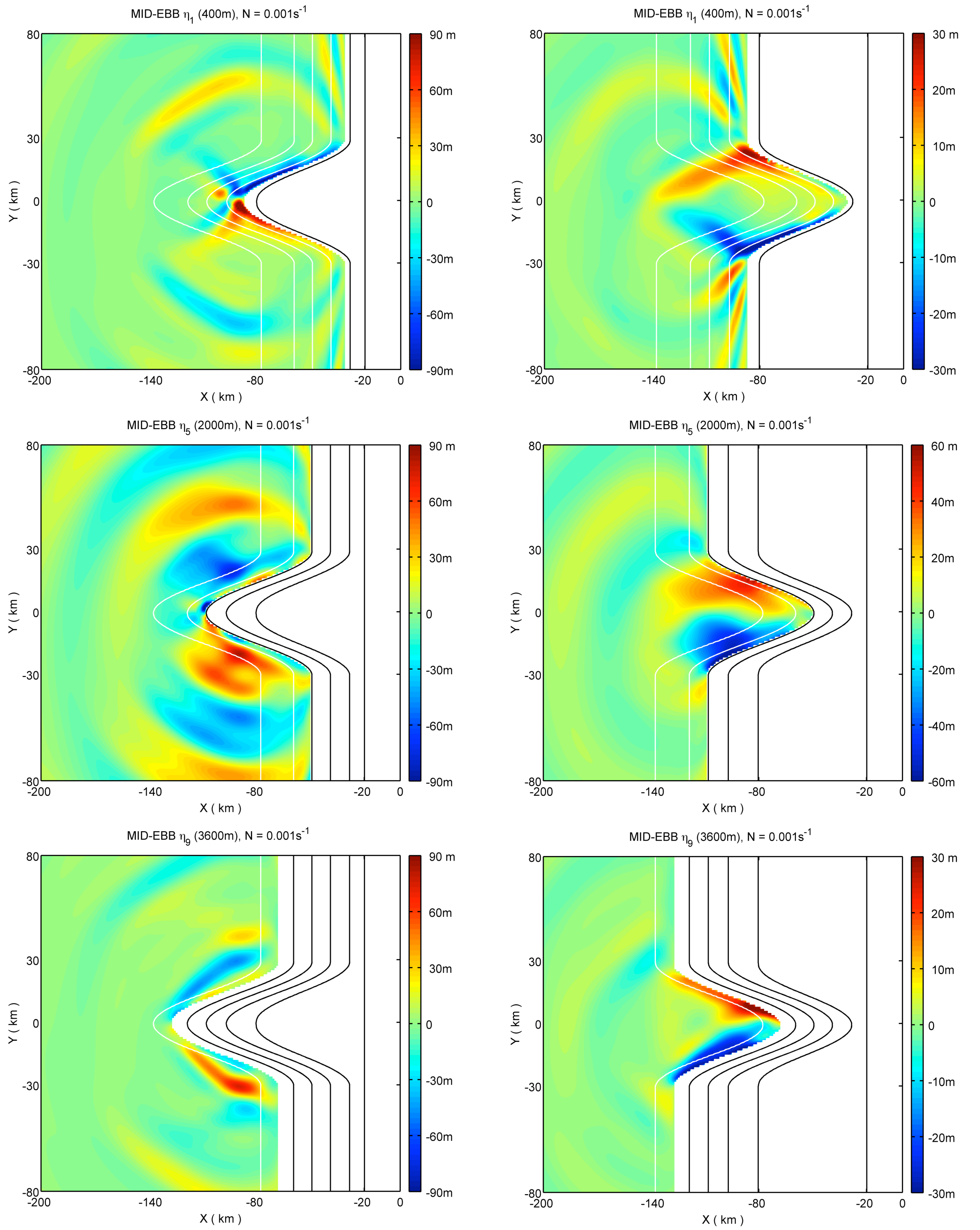

Figure 13. The scattering solution of an internal tidal, under continuous stratification of constant buoyancy frequency N = 0.001 s^{-1}, over idealized abrupt shelf features: submarine promontory (left) and submarine canyon (right). The three represented interfaces correspond to the 1) top; 5) middle and 9) bottom pycnoclines. Color-contours map the isopycnal height (η_1, η_5, η_9) at med-ebb tidal phase. The geomorphic features are represented by the following isobaths contour lines: 80, 278, 1000, 2000, 3000 and 4000m.

[37] Another well-known result is the Saint Andrews cross signature observed in the outer promontory cross-shelf slope (Figure 13.a, left), which becomes a sill for the along-shelf propagating Kelvin wave. As the critical slopes plunge into deeper regions, the adopted stratification structure enables the radiation of the ascending beam pairs from adjacent points placed at each side of the “sill” (promontory head). With constant characteristic slope, *c*, each ascending beam outcrops the first density interface at the opposite promontory’s side of its generation (Figure 15.b, left).

[38] The concave shape of the submarine canyon radiates internal tidal beams from the critical shelf-break belt into its deep interior (Figure 13, right). Waves are generated from each facing slope, mainly in the canyon’s outer region. Again the 400m depths upper-layer interface limits the IW generation to the deeper rim of the canyon, where the BFT sign is opposite for each slope (Figure 4). The energy is radiated perpendicular to the isobaths of origin towards the facing canyon wall (opposed along-shelf slope). Multiple sloping bottom reflections are expected but simulation results show the generation of a cross-canyon (y-direction) standing mode, which occupies the entire canyon domain (Figure 13, right). In the next section it will be demonstrated that the previous behaviour results from 3D beam reflections over a sloping bottom. In the outer-canyon region, over the abyssal plain, internal tides are scattered radially from the canyon’s mouth. Similarly to the promontory’s configuration, internal wave beams are focused in particular paths that correspond to the perpendicular directions to the opposite outer canyon’s rim. The beam ray tracing will show next that these paths correspond to internal waves generated at the outer canyon’s rim, which are reflected in the flat bottom of the ocean, keeping their propagation direction toward the open ocean (Figure 14.b).

b. 3D bottom reflection

[39] The internal tide solution, scattered from both geomorphic features, shows wave fronts that seem to refract over strong sloping bottoms (Figure 14). A similar behaviour was already been identified in the two-layers tide solution, which interfacial mode refracts due to phase velocity changes, when propagating diagonally towards the coast. When considering a continuous stratified ocean, a refracted solution cannot be simply explained by the change in phase velocity of the different baroclinic modes. The major reason lies in a false hypothesis of flat bottom solutions if the method of vertical mode decomposition is adopted over such abrupt features. Instead, the internal tidal beam behaviour should be considered by a method of characteristics. When considering the three-dimensional reflection problem of an internal tidal beam over a sloping bottom, the reflected energy does not lie in the same vertical plane as the incident beam (exception for beams intercepting the bottom in the horizontal perpendicular direction of its isobaths). To verify this statement, an algorithm is formulated in the present work to reproduce 3D internal wave paths through sloping bottom topographies. The formulation is developed in two different dimensions. In the vertical plane, the superposition of different baroclinic modes produce beam structures, where energy density propagates obliquely along internal tide characteristics (beams). The respective beam slope, c , or the angle θ that it makes with the horizontal plane, is given by (3) where ω = 1.4 x 10 $^{-4}$ rad.s $^{-1}$ is the M_2 frequency, f = 1.0 x 10 $^{-4}$ rad.s $^{-1}$ is the Coriolis frequency at mid-latitude and N the buoyancy frequency (N = 1.0 x 10^{-3} s^{-1}). The continuous stratified ocean is a wave-guide to propagating IW beams, reflecting them at the sea-surface and at the bottom of the ocean (Figure 14).

[**40**] By taking N as constant through the water volume, the beam slope also becomes constant all over the domain (even over sloping bottoms) and can be represented by a wavenumber vector $\vec{k} = (k, m, l)$, normal to the group velocity vector (representing the energy path). When internal tidal beams are reflected from flat bottoms, or from the sea-surface, the vertical wavenumber k changes sign and the horizontal wavenumber, $K_H{}^2$ = m^2 + l^2, is conserved. However, when the beam is reflected at a sloping bottom the horizontal wavenumber K_H will change and local refraction is produced. In the horizontal plane, the refracted solution follows a dispersion equation where the incident, ϕ_i , and reflected angles , ϕ_r , relative to the upslope bathymetry gradient vector are function of the bottom slope value (Mass 2011),

$$sin\,\phi_r = \frac{sin\,\phi_i\,(1 - S^2)}{S^2 + 2S\,cos\,\phi_i + 1} \qquad (4)$$

where S ≡ γ/c express the critical reflection condition (Figure 6).

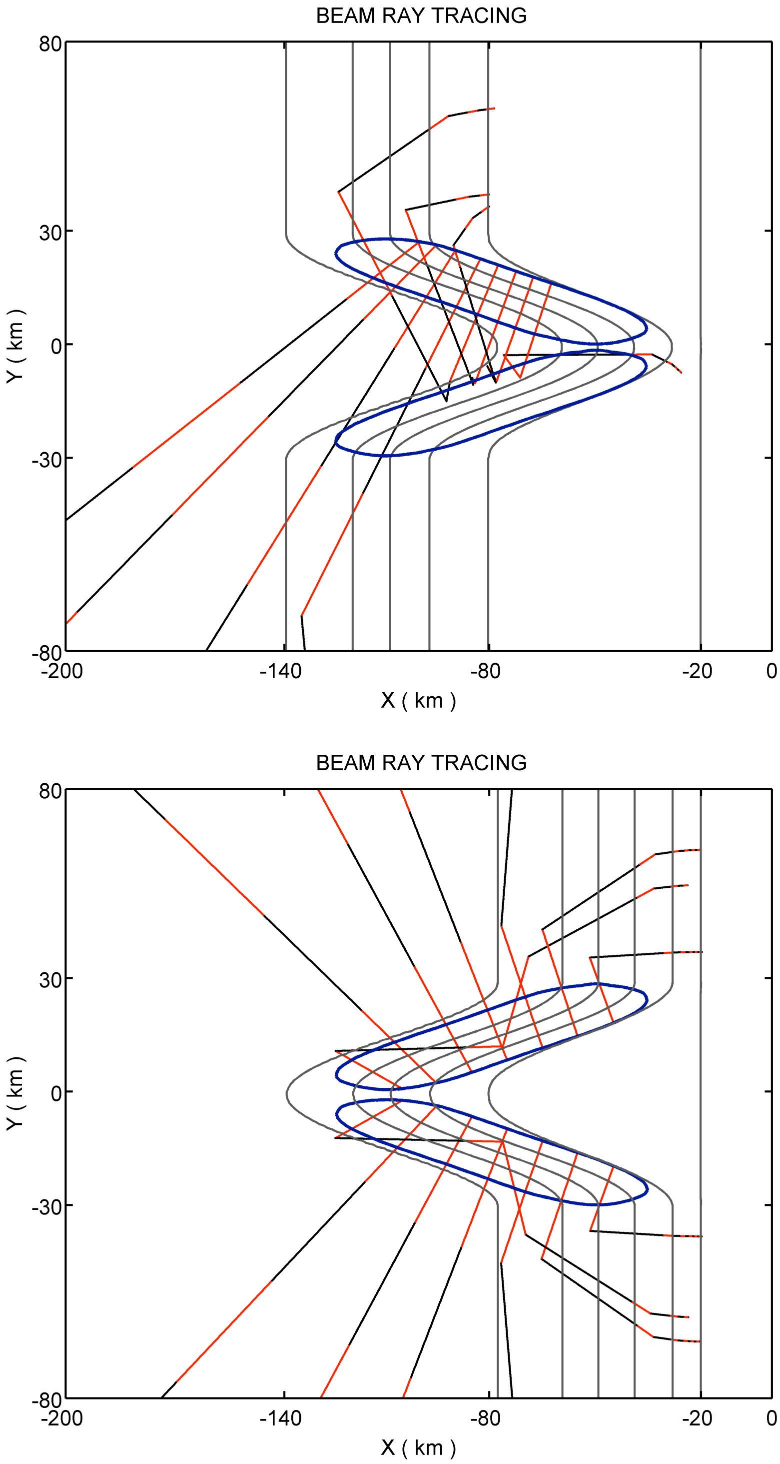

Figure 14. Ray tracing of the initially descending internal tidal beams over abrupt shelf features (2D view): a) submarine canyon (north face generated ensemble) and b) submarine promontory (both north and face emanated internal beams). The wave characteristic slope, *tan* α, is negative in red and positive in black. The sign will change whenever the internal beam is reflected at the bottom of the ocean or at the sea-surface (ocean wave guide).

[41] Ray models are commonly used to trace the propagation path of the internal wave group velocity along continuously stratified vertical planes. Multiple rays can illustrate the wave field that emerges from different point sources in limited areas (Broutman et al., 2004). Equations (3) and (4) are used to trace several beam rays from different point sources placed along each feature's rim (Figure 14), emanating from critical isobaths gradients near regions of high BFT values. As expressed in each solution (Figure 13), the outer-rims of the promontory and canyon topographies radiate downward beam rays that will preserve their direction since they are vertically reflected by the flat bottom. The correspondent ascending energy beam pairs (not considered here), emanating from real ocean stratification condition will preserve the same behavior, as they will be reflected firstly at the surface (no refraction mechanism) and then further way by the same flat abyssal bottom. However, the energy beams emanating from the inner-rims will experience horizontal refraction once they are reflected at the continental slope or abrupt walls (Figure 15).

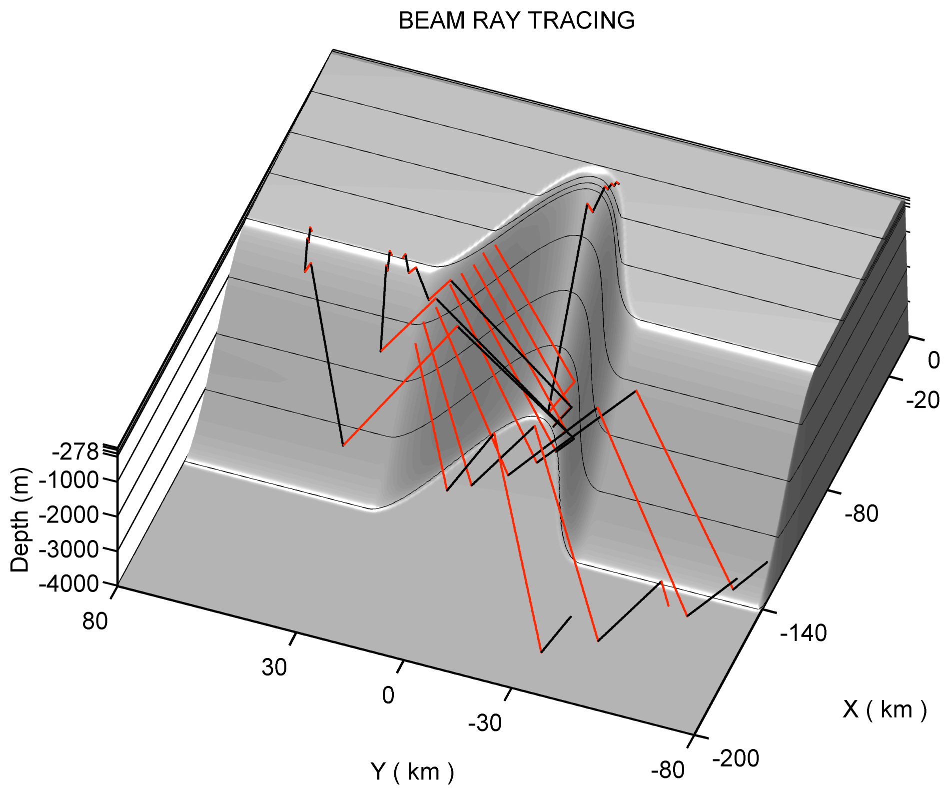

Figure 15a. Ray tracing of the initially descending internal tidal beams generated along the canyon's northern rim (3D view)

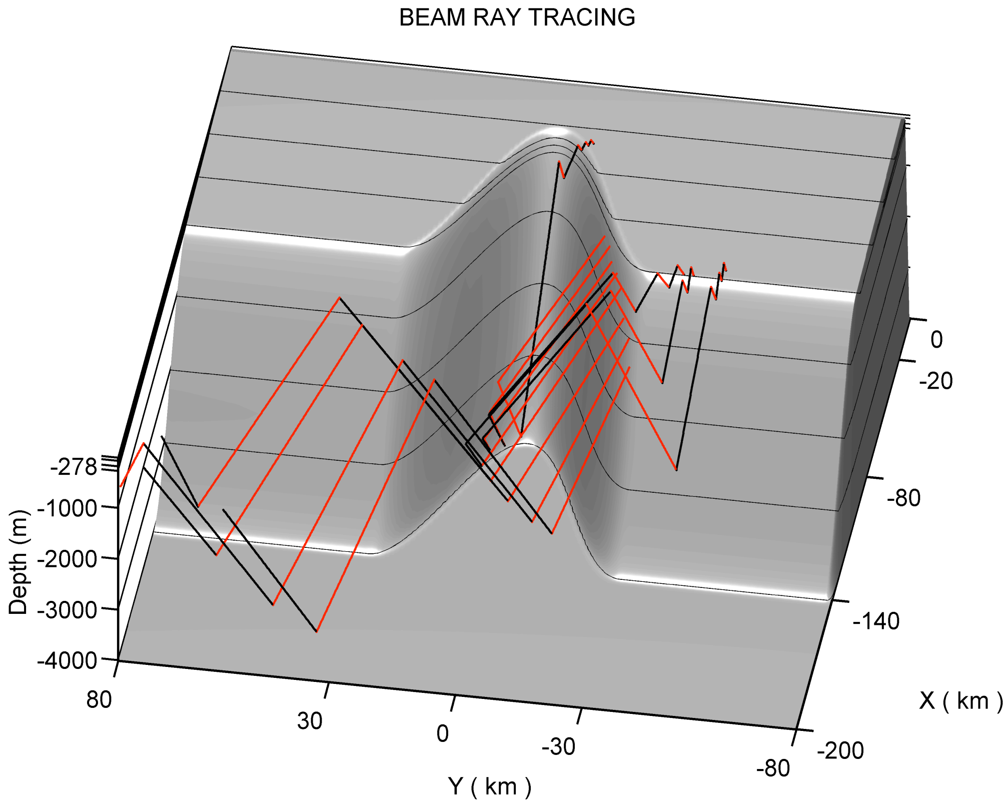

Figure 15b. Ray tracing of the initially descending internal tidal beams generated along the canyon's southern rim (3D view)

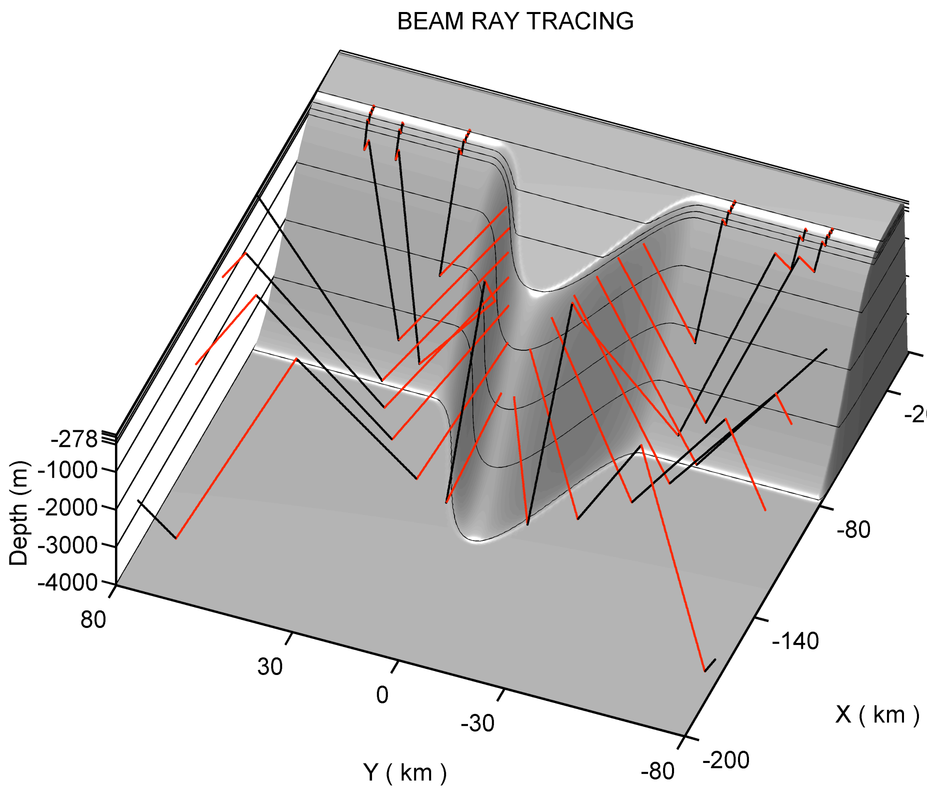

Figure 15c. Ray tracing of the initially descending internal tidal beams generated along the promontory's rim (3D view).

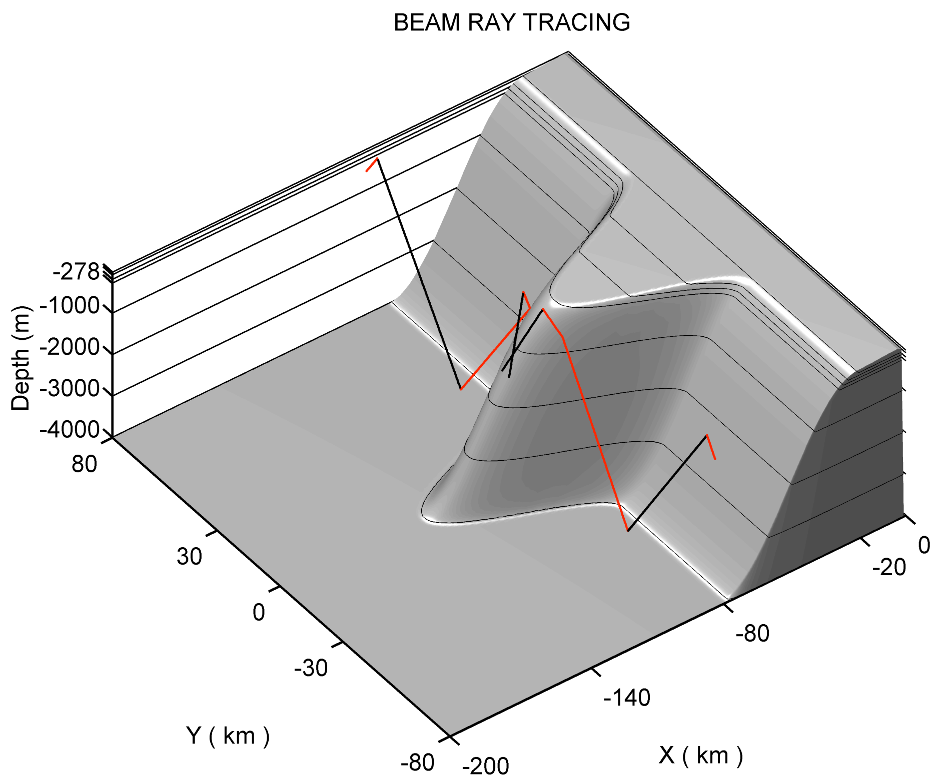

Figure 15c. Ray tracing of the initially ascending internal tidal beams generated over the outer sill of the promontory (3D view).

6. Summary

[42] Abrupt shelf features, such as submarine canyons and promontories, sets up important along-shelf bathymetry gradients that modify drastically the tide solution along narrow continental margins. Important distortions of along shelf propagating tide waves magnify the barotropic forcing term over these topographic steps, making these regions efficient internal tide generation "hot-spots". Each opposite shelf width anomaly establishes distinct surface tide modulation. The promontory reveals higher *BFT* (maximum values at high tide and low tide periods) due to stronger tidal current amplification and phase opposition between its two faces (opposite *BFT* sign). On the contrary, the canyon shows lower *BFT* strength, in phase around the canyon head during mid-ebb and mid-flood instants and reverse phase in its outer-rims at high tide and low tide periods. Different stratifications originate different internal wave patterns.

[43] When considering interfacial internal waves, generated at multiple point sources and propagating with different directions, interference processes must be taken into account. This mechanism gives rise to standing mode solutions in the interior domain of each topographic feature and to amplified or attenuated progressive modes in its outside region. These patterns can become even more complex in real continental margins, where intricate canyon or promontory bathymetries create multiple generation sites and phase, giving rise to numerous propagation paths.

[44] When continuous stratification is taken in consideration over intricate bathymetries, refraction of internal tide beams (at each bottom reflection face) will enhance the 3D internal wave pattern and trap the baroclinic energy path along the topography. The generation region and the propagation behaviour are very sensitive to slopes set up by these topographic features. Super-critical slopes ($\gamma/c > 1$) enable the baroclinic energy to propagate to deeper regions of the domain while sub-critical slopes ($\gamma/c < 1$) reflect beam energy to upper ocean layers and consequently shelf-ward.

References

Baines, P. G., 1982: On the internal tide generation models. *Deep Sea Research*, 29, 307-338.

Baines, P. G., 1983: Tidal motions in submarine canyons – a Laboratory Experiment. *Journal of Physical Oceanography*, 13, 310-328.

Bleck, R., and L. Smith, 1990: A Wind-Driven Isopycnic Coordinate Model of the North and Equatorial Atlantic Ocean 1. Model Development and Supporting Experiments. *Journal of Geophysical Research*, 95, 3273–3285

Carter, G. S., 2010: Barotropic and baroclinic M2 tides in the Monterey bay region. *Journal of Physical Oceanography*, 40, 1766-1783.

Carter, G. S., M. C. Gregg, and R. C. Lien, 2005: Internal and solitary-like waves, and mixing on the Monterey Bay shelf. Cont. Shelf Res., 25, 1499–1520.

Gerkema, T., 1994: Nonlinear dispersive internal tides: generation models for a rotating ocean, PhD-thesis, Universiteit Utrecht.

Gerkema, T., 2008: An introduction to internal waves, Lecture notes, Royal NIOZ.

Jachec, S. M., O. B. Fringer, M. G. Gerritsen, and R. L. Street, 2006: Numerical simulation of internal tides and the resulting energetics within Monterey Bay and the surrounding area. *Geophys. Res. Lett.*, 33, L12605, doi:10.1029/2006GL026314.

Kunze, E., L. K. Rosenfeld, G. S. Carter, and M. C. Gregg, 2002: Internal waves in Monterey Submarine Canyon. *Journal of Physical Oceanography*, 32, 1890–1913.

Martini, K. I., M. H. Alford, J. Nash, E. Kunze, and M. A. Merrifield, 2007: Diagnosing a standing wave in Mamala Bay, *Oahu. Geophys. Res. Lett.,* 34, L17604, doi:10.1029/2007GL029749.

Maas, L., 2011: Wave attractors. Lecture notes, Royal NIOZ.

Mazé R., 1987: Generation and propagation of non-linear internal waves induced by the tide over a continental slope. *Continental Shelf Research*, 7, 1079-1104.

Morel, Y., R. Baraille, A. Pichon, 2008: Time splitting and linear stability of the slow part of the barotropic component. Ocean Modell. 23 (3–4), 73–81.

Petruncio, E. T., L. K. Rosenfeld, and J.D. Paduan, 1998. Observations of the internal tide in Monterey Canyon, J. Phys. Oceanogr., 28, 1873–1903.

Petruncio, E. T., J.D. Paduan, and L. K. Rosenfeld, 2002. Numerical simulations of the internal tide in a submarine canyon, Ocean Model., 4, 221–248.

Quaresma, L.S., Vitorino, J.,Oliveira, A., DaSilva, J., 2007. Evidence of sediment resuspension by nonlinear internal waves on the western Portuguese mid-shelf. Marine Geology 246, 123–143.

Quaresma, L. S., Pichon, A., 2011: Modelling the barotropic tide along the West-Iberian margin, J. Mar. Syst., doi:10.1016/j.jmarsys.2011.09.016

Rattray, M., 1960: On the coastal generation of internal tides. *Tellus*, 12, 54-62

Serpette, A., R. Mazé, 1989: Internal tides in the Bay of Biscay: a two-dimensional model*, Continental Shelf Research*, 9, 795-821, 1989.

Wunsch, C., 1967: Progressive internal waves on slopes. *Journal of Physical Oceanography*, 35, 131-144.

Wunsh, C., 1975: Internal tides in the ocean. Reviews of Geophysics and Space Physics, 13, 1, 167-182.

Annex A

Three-dimensional reflection

The three-dimensional beam scattering problem, over irregular topography, must take into account the fact that its horizontal propagation direction can be modified after bottom reflection. This effect results from the changing in the internal tide propagation vertical plane, whenever an internal wave beam intercepts a slopping bottom in diagonal direction (Figure 1). To formulate this behaviour let us follow Gerkema (2008) and Maas (2011) in the manipulation of the dispersion relation of internal wave beams upon bottom reflection. The focusing and de-focusing of the beam will not be considered here, simplifying the analysis to the variation of the horizontal wave-number angle, ϕ, (Figure 1, *Part III chapter 1*). Where ϕ' will represent next the same angle variation relatively to the bathymetry gradient vector ($0 \leq \phi' \leq \pi$). Two major conditions must be met at the reflection point ($z = H$):

1) Invariance of the beam slope ($\tan\theta = const$);
2) Vanishing of the normal-to-bottom-slope velocity component ($\mathbf{u}\perp = 0$).

Near the reflecting point, the solutions for the vertical velocity component associated with the incident (w*i*) and reflected (w*r*) waves cab be expressed are in the form:

$$\begin{aligned} wi &= Wi \ \exp\left\{ i\,(kx + ly + mz - \omega t) \right\} \\ wr &= Wr \ \exp\left\{ i\,(Kx + Ly + Mz - \omega t) \right\} \end{aligned} \qquad (33)$$

Where W is the vertical velocity component, (k, l, m) and (K, L, M) the respective wave-number components projected in Cartesian space (x, y, z). At the reflection point, one can trace a tangent surface to the bottom, expressed by zonal and meridional slopes, respectively s and d, as

$$z = s\,x + d\,y \qquad (34)$$

The bottom boundary condition 2) states that the component normal to this surface of the total velocity, $wi + wr$, must be null. Equivalent, one can project the incident (w*i*) and reflected (w*r*) vertical velocities on this surface using (34), as

$$\begin{aligned} \underline{\underline{wi}} &= (...) \exp\left\{ i\,(kx + ly + m\,[sx + dy] - \omega t) \right\} \\ \underline{\underline{wr}} &= (...) \exp\left\{ i\,(Kx + Ly + M\,[sx + dy] - \omega t) \right\} \end{aligned} \qquad (35)$$

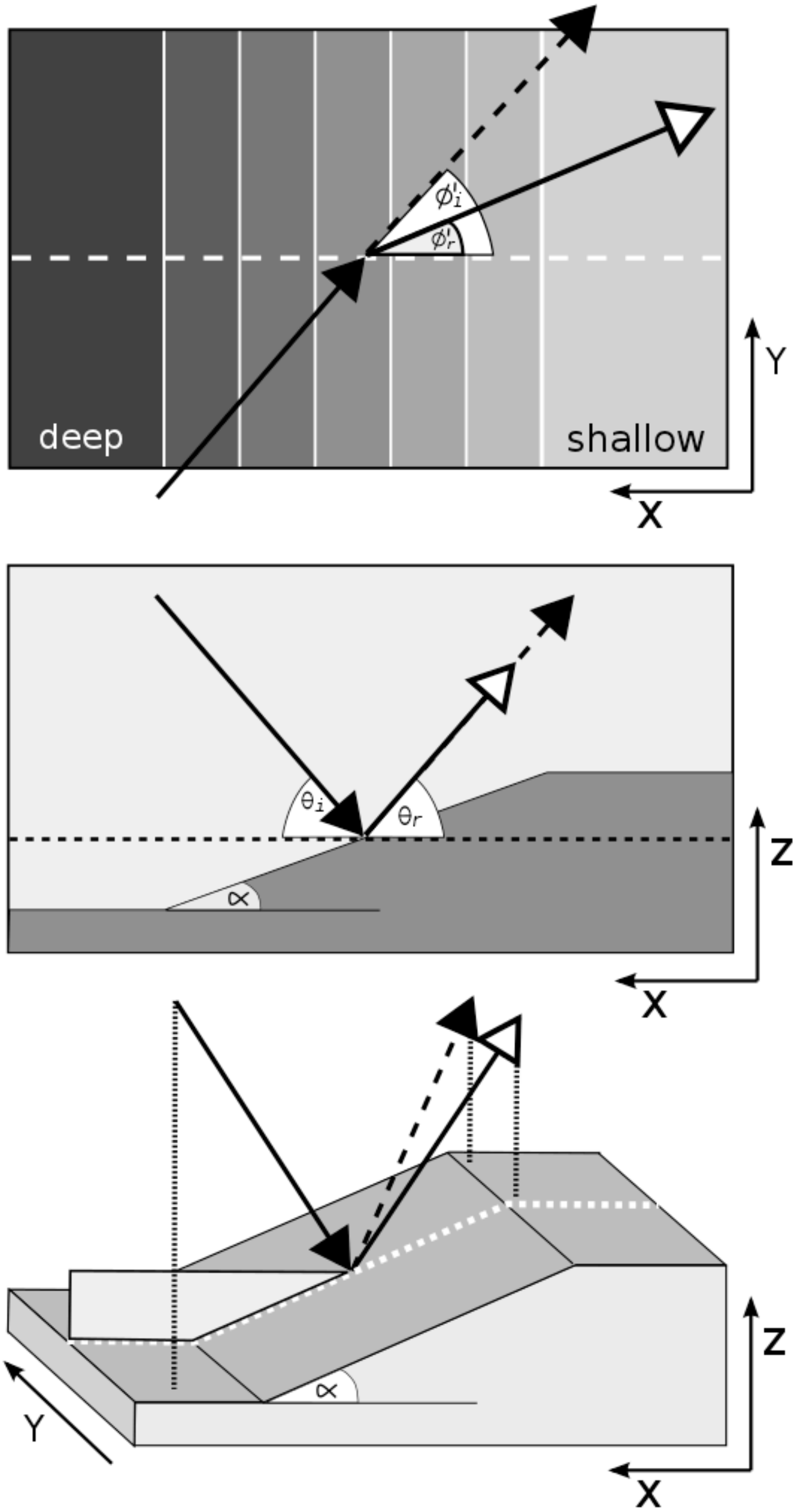

Figure 1. Different perspectives of a downward propagating internal wave beam, making an angle θ_i with the horizontal plane and ϕ'_i with the bottom slope vector (pointing to the shallower isobaths). The reflected beam share the same vertical angle, $\theta_i = \theta_r$ but differs in the horizontal angle ϕ'_r , which value is modified taking the reflected beam to be reoriented towards the shallow region.

And make the total projected velocity to be null by

$$(...)\exp\left\{ i\,([k+sm]\,x\ +[l+dm]\,y\ -\omega t)\right\}\ +\ ...$$
$$....\ +\ (...)\exp\left\{ i\,([K+sM]\,x\ +[L+dM]\,y-\omega t)\right\}\ =\ 0 \qquad (36)$$

For this to hold, guaranteeing that at the bottom these two waves share the same space-time dependence at any tidal instant, one must verify the following equivalences:

$$[k+sm]=[K+sM]\quad ,\quad [l+dm]=[L+dM] \qquad (37)$$

Maas (2011) simplified this problem assuming the invariance of the beam slope along any horizontal directions (isentropy of the *f*-plane approach). Then, one can focus the analytical solution to a sloping bottom invariant along one of the orthogonal horizontal direction (e.g. $d = 0$), reducing the bottom slope to $z = s\,x$, with a gradient slope pointing (positive) to the shallow isobaths. Equation (37) gets,

$$K=k+s\,(m-M)\quad ,\quad l=L \qquad (38)$$

Both incident (i) and reflected (r) beams share the same group velocity ($\boldsymbol{C_g}$) unit vector angle θ and wave-number (**K**) angle β, since these slopes (c and γ respectively) depend only on the forcing frequency and stratification (constant along the domain). Notice that both vectors $\boldsymbol{C_g}$ and **K** share the same vertical plane. For convenience lets us take β as the invariant angle of reference:

$$\gamma i^2=\gamma r^2= tan^2\beta=\frac{N^2-\omega^2}{\omega^2-f^2} \qquad (39)$$

Equivalently, this slope can be decomposed by wave-number components taking the identity (38)

$$\gamma^2\ =\ \frac{M^2}{K^2+l^2}\ =\ \frac{m^2}{k^2+l^2} \qquad (40)$$

The sign of m for the incident wave (or M for the reflected wave) expresses the descending ($m > 0$) or ascending ($m < 0$) of the energy along the beam (Figure2, *Part III chapter I*). From (38) the wave-number l is shared by both incident and reflected wave, so any change in vertical wave-number must be compensated by the orthogonal wavenumber k (and vice-versa) in a relation:

$$K^2m^2-k^2M^2=0 \qquad (41)$$

By subtracting and adding a term k^2m^2 to (41) and using relation (38) to eliminate K, this expression can be factored as

$$(M - m)\ [(M + m)k^2 + (2ks + (m - M)s^2)\, m^2] = 0 \qquad (42)$$

Equations (42) can be verified if one of the next conditions is established:

1. [$M = m$], which imply from (40) that also [$K = k$]. Since upon reflection one of these two wave-numbers must change sign, the only physical configuration resulting from this solution is a reflected wave in phase opposition, propagating backwards in the same direction as the incident wave. This means, that they will be annihilate by each other.
2. The other possible solution comes when the second term (in brackets) is null.

The second term can be divided by m^3 and (39) used to obtain,

$$\frac{M}{m}(\gamma^{-2} - s^2) = -2\frac{k}{m}s - s^2 - \gamma^{-2} \qquad (43)$$

Now, to make disappear the wave-number slope, one can multiply (43) by γ^2, which will scale the topographic slope s by γ ($S \equiv s\gamma$) and normalize m by γ ($Ai \equiv m/\gamma$) and M by γ ($Ar \equiv M/\gamma$). Taking $(k, l) = k_h$ (cos ϕ, sin ϕ) and Ai = k from (40) one can rearrange (43) to obtain

$$\frac{Ar}{Ai} = \frac{1 \pm 2S\,cos\phi + S^2}{S^2 - 1} \qquad (44)$$

Equation (40) can be expressed as $Ar^2 / Ai^2 = -K_h^2 / k_h^2$, expressing that at each reflection one of the wave-numbers m or k_h must change sign and equation (38) as $L = K_h \sin\phi_r = l = k_h \sin\phi_i$. Finally, these two relations can be replaced in (44) to obtain a general formulation (45) expressing the angles that the incident and reflected wave number projections, on the horizontal plane, make with the upslope direction (see Figure 1).

$$sin\,\phi_r = \frac{sin\,\phi_i\,(1 - S^2)}{1 \pm 2S\,cos\phi_i + S^2} \qquad (45)$$

Discussion and perspectives

During the past years, I spent most of my time trying to interpret internal wave signals near irregular shelves, using current and temperature profile measurements. Before giving up, I realized the importance of remote sensing in helping us getting a spatial distribution of the upper-ocean internal wave distribution, in the vicinity of our study region. A new window had opened: surface pictures where now supporting my one-dimensional interpretation. Artificially, we are tempted to assemble single point time series to surface snapshots, always dispersed in time, to create a three-dimensional conceptual model of the internal wave activity in small regions of interest. Yet, many questions do not have answers under such approach. Here, starts my last attempt to dig a little bit further in the interpretation of the complex three-dimensional internal wave solution, observed in nature.

Other research groups are looking into this same problem using different perspectives and tools. While, some focus their study on the internal tide dissipation and breaking into turbulent micro scales, others focus their research in the generation of such density perturbations. In the middle there is a "jungle" of priceless research studies, pointing specific puzzle pieces, that one day will naturally get connected to unveil the internal tide oceanic process.

The present thesis is my small contribution to link some of the theory already published, and validated, to my personal in situ observation experience along with a numerical model approach. So, my starting point was the choice of a numerical tool that could be either used in realistic or academic configuration, as well as in pure barotropic or in vertical discretized layer configurations, to achieve the final goal of internal tide modelling. The Hybrid-Coordinate Ocean circulation Model (HYCOM) was the elected, fulfilling all requirements and by convenience being currently developed and validated by the SHOM to become a tidal predicting hydrodynamic model.

Working in close collaboration with Dr. Annick Pichon, whose experience in this subject is vast and of great value, I started to build a realistic simulation of the west-Iberian continental margin. This task became more complicated than expected, since it brought me to build up a new bathymetry DTM for the study region. Taking the advantage to be working with two national Hydrographic offices, making available high quality bathymetry data, an accurate one-arc minute DTM was assembled (WIBM2009). This model ensures now a more realistic relief of the Portuguese and Galicia margins, where abrupt shelf discontinuities and complex coastline coexist in shallow-water regions. Foreseeing accurate barotropic tide solutions, several studies were performed to achieve the best possible correlation between simulations and numerous tide-gauge and current profiler datasets. Based on the harmonic independence of the eight principal tide components, a polychromatic tidal spectrum was built from two different global tide solutions, and used as boundary-forcing conditions. The best semi-diurnal correlations were obtained when forcing the model with NEA2004 (K2 constituent was the exception) and the best diurnal by forcing TPXO7.2. The corresponding results attest an accuracy improvement from previous literature references. The spatial analysis of the tide solution, reveal energetic sub-inertial modes propagating poleward along the Portuguese and Galician coasts, already observed by other authors but never studied in detailed. This is a very interesting subject that should be adressed in a specific study, which may use the present thesis academic model configurations to study the impact of irregular narrow shelves (such as the west-Iberian) on the triggering and shape of this continental shelf waves.

Nevertheless, the originality of the published tide solution is the identification of a surprising super-inertial tide wave distortion, “trapped” along the west-Iberian shelf. The frequency domain and the wavelength of such features put aside any possible coastal bounded wave mode, steering to topographic effects that intensify and invert semi-diurnal tidal ellipses, over mid-latitude abrupt geomorphic structures such as submarine canyons and promontories. This result gave a major twist to the working plan sketch of my thesis: If the barotropic solution shows itself a complex behaviour over the expected internal wave “hotspot” sites, how can we proceed with the realistic modelling of the internal tide without understand the physical mechanism behind this solution? My PhD advisors and co-directors agreed with me that a new researching axis was worth to be followed.

This new element, made me put the "realistic modelling of the internal tide solution along the Portuguese margin" in a bookshelf and return to the barotropic forcing problem. After some dead end attempts to developed 2D analytical solutions of the bounded surface tide, over abrupt 2D-slopes, I decided to used HYCOM model in linear equation configuration to study this super-inertial "topographic" mode. Taking the hypotheses that this mode is locally "trapped" over each shelf feature, one can find (and force) one-dimensional cross-shelf solutions, away from the obstacle and let the model solve the corresponding solution. An idealized regular margin (monotonous along-shelf) was then shaped by single sinusoidal shelf-width anomalies in the middle of a right-bounded numerical domain. As a result, a submarine canyon is built by a negative shelf-width anomaly and a positive one builds a promontory. This approach enables the forcing of a "smooth-shelf" tidal solution at the open-boundary, placed several tidal excursions length, away from each geomorphic feature.

When a super-inertial tidal harmonic is forced, topographic trapped waves are settled. Since they outcome from linear approximation, these modes are interpreted as the result of an angular momentum conservation upon the water stretching and squeezing, forced by the driving Kelvin tide wave flow over the abrupt along-shelf slopes. This curious solution intensifies the tidal currents over the promontory plateau and diverts them over the submarine canyon. In result, complex barotropic forcing configurations (changing location, strength and phase along the tidal cycle) will determine the generation of barocline modes, in a different arrangement between the canyon and the promontory.

The final step in this research strategy was the inclusion of different stratification configurations into the previous idealized simulations, and the forcing of the same monochromatic super-inertial surface tide. As expected, such complex barotropic tidal forcing originates even more intricate baroclinic solutions. But, starting now from a known forcing configuration, one can uncover the internal wave patterns using interference solutions, for the interfacial mode, or 3D bottom reflection effects when considering a continuous stratified medium. Other topographic and stratification configurations were tested and are currently been analysed, such as case of internal tide solutions inside straight submarine canyons or the reinforcement of the mid-water stratification by the influence of Mediterranean water masses.

After this academic approach, allowing the identification of the physical processes behind the complex internal tide patterns over irregular narrow margins, we are now in conditions to recover the realistic west-Iberian model configuration and pursue with the original internal tide study. Simplified or realistic stratification can then be forced into this larger domain, where multiple geomorphic features are present and will contribute to the complete realistic solution. This research topic is an ongoing project that I will focus my attention in the following years. Sea experiments were already conducted in the area to collect high-frequency sampling data, in particular over the promontory of Estremadura and inside the Nazaré submarine canyon.

Another interesting research axis is the study of possible sub-inertial internal wave bounded solutions, namely internal Kelvin waves and coastal trapped waves that one can foresee to exist along such irregular continental slope, as it is the Norwest Iberian ocean border. Important density gradients are established here, due to the presence of different deep-water masses (e.g. Mediterranean veins), flowing poleward and intercepting strong bathymetry slopes. Equivalent approach can be followed using idealized bathymetry configurations and sub-inertial forcing to help the interpretation of realistic modelling and/or in situ observation.

Many other research ideas were accumulated during this 3 years work with Dr. Annick Pichon and Dr. Yves Morel. One is the use of a non-hydrostatic model, with the same idealized configuration, to study the critical changing behaviour from sinusoidal tide waves (at the origin) to non-linear solutions, such as the non-linear internal solitons. These small-scale features seem to be formed in the trough of the linear internal tide, but will exibt a distinct dispersion mechanism when formed. To reproduce such features, whose signatures are observed in SAR imagery and interpreted as localizers of the internal tide wave front, one must adopt non-hydrostatic codes. Again, topographic impacts and bottom friction must play a crucial role in this wave shoaling.